2014

Impact on new aerodynamic solutions for the front-end on the engine bay thermal performance

Federico De Medio
University of Windsor

Impact of new aerodynamic solutions for the front-end on the engine bay thermal performance

By

Federico De Medio

A Thesis

Submitted to the Faculty of Graduate Studies through

the Department of Mechanical, Automotive and Materials Engineering

in Partial Fulfillment of the Requirements for

the Degree of Master of Applied Science

at the University of Windsor

Windsor, Ontario, Canada

2014

IMPACT OF NEW AERODYNAMIC SOLUTIONS FOR THE FRONT–END ON THE ENGINE BAY THERMAL PERFORMANCE

BY

FEDERICO DE MEDIO

APPROVED BY:

_____

D. Ting,
Department of Mechanical, Automotive and Materials Engineering

_____

E. Tam,
Department of Civil and Environmental Engineering

_____

R. Carriveau, Advisor
Department of Civil and Environmental Engineering

13 August 2014

DECLARATION OF ORIGINALITY

I hereby certify that I am the sole author of this thesis and that no part of this thesis has been published or submitted for publication.

I certify that, to the best of my knowledge, my thesis does not infringe upon anyone's copyright nor violate any proprietary rights and that any ideas, techniques, quotations, or any other material from the work of other people included in my thesis, published or otherwise, are fully acknowledged in accordance with the standard referencing practices. Furthermore, to the extent that I have included copyrighted material that surpasses the bounds of fair dealing within the meaning of the Canada Copyright Act, I certify that I have obtained a written permission from the copyright owner(s) to include such material(s) in my thesis and have included copies of such copyright clearances to my appendix.

I declare that this is a true copy of my thesis, including any final revisions, as approved by my thesis committee and the Graduate Studies office, and that this thesis has not been submitted for a higher degree to any other University or Institution.

ABSTRACT

This work investigates the impact of an innovative aerodynamic solution for the front-end of a vehicle on the engine bay thermal performance. Starting from a production series automobile, an alternative aerodynamic configuration was studied, with the aim of improving the overall aerodynamic behavior without excessively penalizing the thermal aspect, and by keeping into account all the involved constraints. The aero-thermal performances were evaluated through a co-simulation approach which exploits a CFD and a thermal computational solver.

The main driver for this research was the increasing demand for fuel efficient vehicles. Nowadays, in order to comply with more and more severe regulations, the car manufacturers are trying to study solutions able to guarantee the achievement of emissions and fuel consumption targets mandated by law. This thesis focuses on one possible way to achieve such targets in the short term on a model already in production.

DEDICATION

To mom and dad,

For their unconditional love, support and constant source of motivation.

ACKNOWLEDGEMENTS

This year has been an incredible adventure, made of huge ups and downs, big difficulties alternated to incredible satisfactions. Here, now, it's time to express my utmost and sincere thanks to all those people who supported me in all ways, in particular:

First and foremost, my parents, who supported me in any way even being 6,851.525 km far away, and who believed in me even when I had crazy ideas and plans.

My sister, with whom I would have liked to spend much more time during these years (even if she military occupied my bedroom while I was away).

My grandparents, especially my *nonno Giuseppe*, I miss you.

My Italian friends whom I had the chance to call few times during this year, I miss you all guys! In particular, I would like to thank Pino and Giulia, with whom I had the chance to chat a lot (you guys know what it means to be abroad!), Gabry and Bomba for their contagious happiness, Fabia, and Giulio.

Also, I would like to thank my friends from Politecnico, in particular that bloody geek Simone, Pablo, and Edo. Among my friends from Politecnico, I would like to thank my five mates of this program for the

wonderful time we spent together, especially my floor-mates Luca and Fra for withstanding me for the entire year (which was far from being easy!).

My Canadian friends with whom I had a great time: Kyle, Tom, Ashley, and Pheebs. By the way: thanks to Tom for challenging me to skate (still waiting for him to ski), and special thanks to Luca and Kyle for their "support" while learning how to skate!

My academic advisor from the University of Windsor, Rupp Carriveau, for the great way we were able to handle all the difficulties of this project and for the time and patience he had for me, I really appreciated that.

My academic advisor from Politecnico di Torino, Renzo Arina, for his prompt help and support any time I had a request despite the distance.

My Chrysler advisor Richard Sun, who always supported me and who gave me plenty of his time, despite of his extremely tight schedule. I will always remember and appreciate the timeliness of his responses, which should be an example for most people.

My CRF advisor Enrico Ribaldone and his group, especially Michele Citti and Matteo Giusti, whom I bothered so much I still have to figure out how they could still reply to my e-mails; I really appreciated your strong support for the technical side, we were able to overcome all the difficulties notwithstanding the huge distance.

My counselor Raffaella from Politecnico, whose advices were always helpful.

Mojie, for bearing me and helping me realize my plans.

Andy, my *Lucius Fox*, for being able to withstand me, realize all my impossible requests and help me develop all my ideas.

All the people at ARDC who helped me, especially Owais, whom I bothered so much for understanding how things worked in a totally new environment.

Mike Huston, who always helped us Italians for any issue we had.

The Canadian border officers: they made us feel home any time we came back!

The US Environmental Protection Agency for being an extremely valid, clear and resourceful source of information.

The Centro Ricerche Fiat for allowing using their material for this thesis purposes.

TABLE OF CONTENTS

DECLARATION OF ORIGINALITY iii

ABSTRACT iv

DEDICATION v

ACKNOWLEDGEMENTS vi

LIST OF TABLES xii

LIST OF FIGURES xiii

LIST OF APPENDICES xxiv

LIST OF ABBREVIATIONS/SYMBOLS xxv

1. CHAPTER 1 INTRODUCTION 1

1.1. MAIN DRIVERS FOR THE RESEARCH 1

1.2. OBJECTIVES 5

1.3. THE AERODYNAMICS SIDE 7

1.3.1. CURRENT SCENARIO 7

1.3.2. FUTURE DEVELOPMENTS 15

1.4. THE THERMAL MANAGEMENT SIDE 18

1.4.1. CURRENT SCENARIO 18

1.4.2. FUTURE DEVELOPMENTS 27

1.5. THE PROBLEM 33

1.5.1. PROBLEM DEFINITION & METHODS FOR ADDRESSING IT 33

1.5.2. STATE-OF-THE-ART APPROACH 37

1.5.3. USED CO-SIMULATION PROCEDURE 43

1.6. RESEARCH DEVELOPMENT AND THESIS ORGANIZATION 47

2. CHAPTER 2 AERODYNAMIC ANALYSIS 51
2.1. CAR VIRTUAL MODEL – GEOMETRY DESCRIPTION 51
2.1.1. EXTERIOR BODYWORK 51
2.1.2. UNDERHOOD PACKAGING 56
2.2. CFD SIMULATION 64
2.2.1. TESTING CONDITIONS 64
2.2.2. CONVERGENCE PLOTS 65
2.2.3. AERODYNAMIC RESULTS 70
2.2.4. PRESSURE DISTRIBUTION MAPS 75
2.2.5. VELOCITY FIELD MAPS 95

3. CHAPTER 3 THERMAL ANALYSIS 122
3.1. CAR VIRTUAL MODEL – GEOMETRY DESCRIPTION 122
3.1.1. EXTERIOR BODYWORK MESH 123
3.1.2. ENGINE BAY MESH 127
3.2. THERMAL SIMULATION 129
3.2.1. TESTING CONDITIONS 129
3.2.2. CONVERGENCE PLOTS 130
3.2.3. THERMAL ANALYSIS RESULTS 130
3.2.4. TEMPERATURE DISTRIBUTION MAPS 131
3.2.5. SUMMARY OF THERMAL RESULTS 149

4. CHAPTER 4 FINAL CONSIDERATIONS & RECOMMENDATIONS 153
4.1. OVERALL CONTRIBUTION 153
4.2. MANUFACTURING ISSUES 154

4.3. WORKFLOW OPTIMIZATION 157

5. REFERENCES/BIBLIOGRAPHY 159
5.1. SOURCES IN THE TEXT 159

6. APPENDICES 162
6.1. Appendix A 162
6.2. Appendix B 162
6.3. Appendix C 163
6.4. Appendix D 166
6.5. Appendix E 173
6.6. Appendix F 178
6.7. Appendix G 182
6.8. Appendix H 193

7. VITA AUCTORIS 197

LIST OF TABLES

Table 1.1 – Output power, heat rates and residual enthalpy percentage distribution for light driving conditions for SI and CI engines. [3] _____ 21

Table 1.2 - Examples of design factors for DOE-based design development. [6] _____ 40

Table 2.1 - Aerodynamic results: comparison between drag and lift coefficient for the baseline and modified versions._____ 70

Table 2.2 - Cooling air mass flow rates through the front inlet vents and to the HEXes._____ 71

Table 2.3 – Distribution of cooling air mass flow rates through the front inlets. _____ 72

Table 2.4 - Average absolute total pressures over inlet and outlet faces of the HEXes. _____ 73

LIST OF FIGURES

Figure 1.1 - Contribution of different categories to overall USA greenhouse gases emissions due to transportation in 2010. [2] Data from U.S. Environmental Protection Agency, 2010 U.S. Greenhouse Gas Inventory. 1

Figure 1.2 - CO_2 emissions per kilometer, historical and forecasted performances. [24] 2

Figure 1.3 - CO_2 emissions per kilometer travelled over time, historical and forecasted data for different Countries. [24] 3

Figure 1.4 - Average fuel consumption (in km/L) for different Countries fleets, normalized to US cycle. [24] 4

Figure 1.5 - FIAT 500L, the object of the thesis research. [16] 5

Figure 1.6 - Historical evolution of passenger car drag coefficient. Today, to further reduce it, it's necessary to focus on the internal flows. [24] 8

Figure 1.7 - Main powertrain and cooling system components crossed by the incoming cooling airflow. [2] 9

Figure 1.8 - Extreme operating conditions: on the left: high load and speed, ram effect best exploited: on the right: low speed and load, poor ram effect, backflow, buoyancy, higher temperatures. [2] 9

Figure 1.9 - Airflow pattern around a Nissan GT-R. It is possible to visualize the cooling airflow and its interaction with the rest of the flow. [8] 10

Figure 1.10 - Cooling airflow drag experimental measurement procedure. Open and closed air vents configurations. [2] 10

Figure 1.11 - Cooling airflow drag computational measurement procedure through CFD. Open and closed air vents configurations. [9] 11

Figure 1.12 - Cooling airflow drag of various cars from the 70s (N=sample size). [2] 11

Figure 1.13 - Percentage contribution to total drag of different parts for a recently developed passenger vehicle. [18] The cooling package has the highest share of drag. 12

Figure 1.14 - Possible alternative radiator arrangements for reducing cooling airflow drag. [2] 13

Figure 1.15 - Typical positioning for cooling airflow inlet and outlet on a current generation vehicle. [10] 14

Figure 1.16 - Cooling inlet design, historical evolution for Opel Kadett. [2] 15

Figure 1.17 - Ferrari F12 Berlinetta front brake cooling ducts in open and closed position. They improve the aerodynamic behavior of the car by reducing the internal flow when not necessary. [11] 16

Figure 1.18 - Porsche 911 Turbo S active front spoiler. [14] 16

Figure 1.19 - AGS system for the Dodge Dart. It currently represents one of the main areas of interest for automotive aerodynamicists. [12] 17

Figure 1.20 - Typical passenger vehicle cooling system architecture. [15] 18

Figure 1.21 - Basic functioning scheme of a typical automotive cooling system. [16] 19

Figure 1.22 - Percentage contribution of different factors to total input power introduced through the fuel over engine operating speeds for a GM 1.6L Diesel engine at full load. 21

Figure 1.23 - Typical performance curve for a passenger car braze-welded aluminum radiator. A specific operating point is highlighted. [3] 22

Figure 1.24 - Characteristic curve for a 500 W automotive cooling fan with 380 mm blades. [3] 23

Figure 1.25 - Air-side pressure loss as a function of air speed for various radiator geometries (size: length x width x depth). Al-m: aluminum mechanical radiator; Al-b: aluminum-brazed radiator. [3] 24

Figure 1.26- Automotive cooling system design flow chart. [3] _____ 25
Figure 1.27 - Architecture of a LT/HT cooling system [3]. _____ 29
Figure 1.28 - Audi TFSI 1.8L featuring an integrated exhaust manifold [3]. _____ 30
Figure 1.29 - Opel Insignia compact cooling module [3]. _____ 30
Figure 1.30 - Dual-cooling system scheme. [2] _____ 31
Figure 1.31 - Temperature distribution map of a V8 engine heads obtained through CFD analysis. [19] _____ 36
Figure 1.32 - Examples of aerodynamic and thermal maps which can be obtained through virtual CFD simulation. [5] _____ 36
Figure 1.33 - Co-simulation process flow-chart. Data between CFD and thermal solvers are exchanged until convergence is reached. [5] _____ 37
Figure 1.34 - Velocity field in the vertical mid-plane section of a vehicle. By studying the flow, it is possible to identify ways to conveniently manage the cooling airflow in the engine bay. [24] _____ 39
Figure 1.35 - Modular design analysis. Each module represents a design factor in the DOE-based optimization algorithm developed at Ford. [6] _____ 40
Figure 1.36 - Morphing of a virtual model to be optimized through DOE. [6] _____ 41
Figure 1.37 - Co-simulation flow-chart used for the aero-thermal analysis. [22] _____ 44
Figure 1.38 - Detailed flow-chart of the used co-simulation process. [22] _____ 45
Figure 1.39 - Temperature assignment to exhaust line components (heat sources). This setup is similar to the one used in the warm simulation performed for the model under analysis. [22] _____ 46

Figure 2.1 - FIAT 500L NAFTA MY 2014 virtual model in Star-CCM+ environment. The picture shows a discretized volume mesh of the model with around 44 million volume cells. 52

Figure 2.2 - Other views of the CFD model. Notice the accuracy of details in the underhood and on the exhaust line. 53

Figure 2.3 - Volume mesh of the CFD model, vehicle exteriors. 54

Figure 2.4 - Volume mesh of the space surrounding the vehicle and the engine bay (XZ mid-plane, with coordinates y=0). Notice the prism layer extrusion representing the boundary layer. 54

Figure 2.5 - Volume mesh of the space surrounding the vehicle and the engine bay (XY section plane, with coordinates z=0). Again, notice the prism layer extrusion representing the boundary layer. 55

Figure 2.6 - Volume mesh of the underbody. Notice how fine is the mesh on the components of interest from the aero-thermal viewpoint. 55

Figure 2.7 - Volume mesh detail of the front end. It is possible to see the meshed HEXes behind the inlet grilles. 56

Figure 2.8 - Front inlets to the engine bay. The main central grille is the one which will be shuttered by the AGS at speed. 57

Figure 2.9 - Front grilles, highlighting the cooling air inlets. 57

Figure 2.10 - Cooling system HEXes. RAD: radiator; COND: A/C condenser; ITC: intercooler. 58

Figure 2.11 - Engine air inlet. Notice the unfavourable positioning with respect to the inlet opening. 58

Figure 2.12 - Battery position in the engine bay. 59

Figure 2.13 - Engine positioning in the underhood. 59

Figure 2.14 - Gearbox location in the engine bay. 60

Figure 2.15 - Exhaust line. Surface temperatures will be assigned to its component as heat sources in the warm CFD simulation. 60

Figure 2.16 - Fuel line from filler cap to engine inlet. 61

Figure 2.17 - Electrical system components. 61
Figure 2.18 - Cooling module conveyor. 61
Figure 2.19 - Fan and relative frame positioning in the engine bay. 62
Figure 2.20 - Typical wind tunnel experimental setup. Also in the case under study the wheels were rotating on drums. [23] 64
Figure 2.21 - CFD simulation residuals plot. Top: baseline version; bottom: modified version. 66
Figure 2.22 - Drag coefficient convergence plots for the baseline (top) and modified (bottom) models. The ordinate axis values are hidden for confidentiality reasons. 67
Figure 2.23 - Cooling air mass flow rates through the front inlet vents. Top: baseline version; bottom: modified version. 68
Figure 2.24 - Convergence plot of cooling air mass flow rates to the HEXes. 69
Figure 2.25 - Detail of front inlet vents. The PIDs match the one reported in Table 2.3. 72
Figure 2.26 - Normalized drag force development over the longitudinal x direction for the two vehicle configurations. 74
Figure 2.27 - Normalized drag force development over x, detail of the central part of the vehicle. 74
Figure 2.28 - Pressure distribution over the vehicle body, front-end. Left: baseline; right: modified. 76
Figure 2.29 - Detail of pressure distribution over the front-end for the baseline (left) and modified (right) versions. 77
Figure 2.30 - Detail of Cp distribution over the front-end. Notice the different extension of the high pressure area (in red) between the baseline (left) and modified (right) configurations. 77
Figure 2.31 - Detail of underbody Cp distribution as seen from the front-end. 77

Figure 2.32 - Underbody pressure distribution. Top: baseline; bottom: modified. 78

Figure 2.33 - Detail of pressure distribution over the front part of the underbody. Left: baseline; right: modified. 79

Figure 2.34 - Pressure distribution over the car body. Top: baseline; bottom: modified. 79

Figure 2.35 - Pressure distribution over the vehicle body, top view. Top: baseline; bottom: modified. 80

Figure 2.36 - Pressure distribution over the front-end, detail of the inlet vents. Top: baseline; bottom: modified. 81

Figure 2.37 - Pressure distribution map, detail of the engine bay. The two visible rectangles are the A/C condenser (top) and the intercooler (bottom) inlet faces. Top: baseline; bottom: modified. 82

Figure 2.38 - C_p distribution in the engine bay, detail of A/C condenser and intercooler outlet faces. Top: baseline; bottom: modified. 83

Figure 2.39 - Pressure distribution over the inlet face of the radiator. Note the big difference between the baseline, top, and the modified version, bottom. 84

Figure 2.40 - Radiator outlet face pressure distributions for the baseline (top) and modified (bottom) cases. 85

Figure 2.41 - Pressure distribution map - detail of inlet to the cooling fan. Top: baseline; bottom: modified. 86

Figure 2.42 - Pressure distribution in the engine bay downstream of the cooling module. Top: baseline; bottom: modified. 87

Figure 2.43 - Pressure distribution over the longitudinal vertical mid-plane with coordinates y=0 mm. Top: baseline; bottom: modified. 88

Figure 2.44 - Pressure distribution in the engine bay. Detail of the longitudinal vertical section plane with coordinates y=+200 mm. Top: baseline; bottom: modified. 89

Figure 2.45 - C_p distribution over the horizontal section plane with coordinates z=+10 mm. Top: baseline; bottom: modified. 90

Figure 2.46 - Pressure distribution over the horizontal plane with coordinates z=-90 mm, detail of the HEXes. Top: baseline; bottom: modified. 91

Figure 2.47 - Pressure distribution over the horizontal section plane with coordinates z=0 mm, detail of the HEXes. Top: baseline; bottom: modified. 92

Figure 2.48 - Pressure distribution over the horizontal section plane with coordinates z=+60 mm, detail of the HEXes. Top: baseline; bottom: modified. 93

Figure 2.49 - Pressure distribution over the horizontal section plane with coordinates z=+310 mm, detail of the HEXes. Top: baseline; bottom: modified. 94

Figure 2.50 - Velocity distribution over the horizontal section plan with coordinates z=0 mm. Top: baseline; bottom: modified. 96

Figure 2.51 - Velocity distribution map over the horizontal plane with coordinates z=+60 mm. Top: baseline; bottom: modified. 97

Figure 2.52 - Velocity distribution over the horizontal section plane with coordinates z=+260 mm. Top: baseline; bottom: modified. 98

Figure 2.53 - Velocity distribution over the horizontal section plane with coordinates z=-140 mm. Top: baseline; bottom: modified. 99

Figure 2.54 -Velocity distribution over the vertical longitudinal mid-plane (y=0 mm). Top: baseline; bottom: modified. 100

Figure 2.55 - Velocity distribution over the longitudinal vertical section plane with coordinates y=+100 mm. Top: baseline; bottom: modified. 101

Figure 2.56 - Velocity distribution over the longitudinal vertical section plane with coordinates y=+600 mm. Top: baseline; bottom: modified. 102

Figure 2.57 - Velocity distribution in the engine bay, vertical longitudinal mid-plane (y=0 mm). Top: baseline; bottom: modified. ___ 103

Figure 2.58 - Velocity distribution in the engine bay, vertical longitudinal section plane with coordinates y=+300 mm. Top: baseline; bottom: modified.___ 104

Figure 2.59 - Velocity distribution in the engine bay, vertical longitudinal section plane y=+300 mm. The colors indicate the magnitude of the x component of the vector of the local velocity. Top: baseline; bottom: modified.___ 105

Figure 2.60 - Velocity distribution in the engine bay, detail of the x component of the local velocity vector. Vertical longitudinal mid-plane (y=0 mm). Top: baseline; bottom: modified. ___ 106

Figure 2.61 - Velocity distribution in the engine bay, vertical longitudinal section plane with coordinates y=+400 mm. Top: baseline; bottom: modified.___ 107

Figure 2.62 - Velocity distribution in the engine bay, vertical longitudinal section plane with coordinates y=-300 mm. Top: baseline; bottom: modified.___ 108

Figure 2.63 - Velocity distribution over the horizontal section plane z=+60 mm, detail of the engine bay. Top: baseline; bottom: modified.__ 109

Figure 2.64 - Velocity distribution over the horizontal section plane z=-140 mm, detail of the engine bay. Top: baseline; bottom: modified. ____ 110

Figure 2.65 - Velocity distribution (colors indicate the magnitude of x component of the local velocity vector) over the horizontal section plane z=+10 mm. Top: baseline; bottom: modified. ___ 111

Figure 2.66 - Velocity distribution (colors indicate the magnitude of x component of the local velocity vector) over the horizontal section plane z=+60 mm. Top: baseline; bottom: modified. ___ 112

Figure 2.67 - Velocity distribution over the horizontal section plane z=0 mm, detail of the HEXes. Top: baseline; bottom: modified. _____ 113
Figure 2.68 - Velocity distribution over the horizontal section plane z=+60 mm, detail of the HEXes. Top: baseline; bottom: modified. _____ 115
Figure 2.69 - Velocity distribution over the horizontal section plane z=-40 mm, detail of the HEXes. Top: baseline; bottom: modified. _____ 116
Figure 2.70 - Velocity field in the heat exchangers. Top: baseline; bottom: modified._____ 117
Figure 2.71 - Velocity distribution over the A/C condenser inlet face. Top: baseline; bottom: modified. _____ 118
Figure 2.72 - Velocity distribution over the intercooler inlet face. Top: baseline; bottom: modified. _____ 119
Figure 2.73 - Velocity distribution over the A/C condenser inlet face. Top: baseline; bottom: modified. _____ 119
Figure 3.1 - Example of patch creation starting from individual cells grouped together. [24]_____ 124
Figure 3.2 - Virtual model of the vehicle in the RadTherm environment._____ 124
Figure 3.3 - Detail of the underbody geometry as modelled in RadTherm._____ 125
Figure 3.4 - Detail of the mesh of the RadTherm vehicle model. ___ 125
Figure 3.5 - Detail of the mesh of the front-end of the vehicle in RadTherm._____ 126
Figure 3.6 - Detail of the mesh of the underbody in RadTherm._____ 126
Figure 3.7 - Detail of the engine bay discretization in the RadTherm virtual environment. _____ 127
Figure 3.8 - Detail of the engine bay mesh._____ 127

Figure 3.9 - Detail view of the engine bay mesh. Notice the cables and cooling module discretization, still fine enough not to lose any relevant thermal information. 128

Figure 3.10 - Detail of the front-end mesh, aesthetic parts and detail of the engine bay. 128

Figure 3.11 - Convergence plot for the thermal simulation. Left: baseline; right: modified. 130

Figure 3.12 - Temperature distribution map of the complete vehicle. Top: baseline; bottom: modified. 132

Figure 3.13 - Temperature distribution map of the complete vehicle, view of the upper part of the vehicle body. Top: baseline; bottom: modified. 133

Figure 3.14 - Temperature distribution map, view of the underbody. Top: baseline; bottom: modified. 134

Figure 3.15 - Temperature distribution map, detail of the engine bay. Top: baseline; bottom: modified. 135

Figure 3.16 - Temperature distribution map, detail of the fan assembly. Top: baseline; bottom: modified. 136

Figure 3.17 - Temperature distribution map, detail of the engine bay. Top: baseline; bottom: modified. 137

Figure 3.18 - Temperature distribution map, detail of the engine bay from the front. Top: baseline; bottom: modified. 138

Figure 3.19 - Temperature distribution map, detail of the fuel line. Top: baseline; bottom: modified. 140

Figure 3.20 - Temperature distribution map, detail of the engine air intake line. Left: baseline; right: modified. 141

Figure 3.21 - Temperature distribution map, detail of the fuse-box. Left: baseline; right: modified. 141

Figure 3.22 - Temperature distribution map, detail of the battery. Left: baseline; right: modified. 141

Figure 3.23 - Temperature distribution map, detail of the front lockary and underbody shields. Top: baseline; bottom: modified. 142

Figure 3.24 - Temperature distribution map, detail of the vehicle body frame. Left: baseline; right: modified. 143

Figure 3.25 - Temperature distribution map, detail of the brakes system. Left: baseline; right: modified. 143

Figure 3.26 - Temperature distribution map, view from above of the vehicle body frame. Top: baseline; bottom: modified. 144

Figure 3.27 - Temperature distribution map, detail of the gearbox assembly. Left: baseline; right: modified. 145

Figure 3.28 - Temperature distribution map, detail of the engine assembly. Left: baseline; right: modified. 145

Figure 3.29 - Temperature distribution map, detail of the exhaust line. Top: baseline; bottom: modified. 146

Figure 3.30 - Temperature distribution map, detail of the cooling module. Left: baseline; right: modified. 147

Figure 3.31 - Temperature distribution map, detail of the cooling module. Left: baseline; right: modified. 147

Figure 3.32 - Temperature distribution map, detail of the cooling module. Left: baseline; right: modified. 148

Figure 3.33 - Temperature distribution map, detail of the suspensions sub-group. Top: baseline; bottom: modified. 148

Figure 3.34 - Temperature distribution map, detail of the suspensions sub-group. Left: baseline; right: modified. 149

Figure 3.35 - Temperature distribution map, detail of the steering assembly. Left: baseline; right: modified. 149

LIST OF APPENDICES

6.1. Appendix A _____ 162

6.2. Appendix B _____ 162

6.3. Appendix C _____ 163

6.4. Appendix D _____ 166

6.5. Appendix E _____ 173

6.6. Appendix F _____ 178

6.7. Appendix G _____ 182

6.8. Appendix H _____ 193

LIST OF ABBREVIATIONS/SYMBOLS

A/C: Air Conditioning

ACEA: Association des constructeurs européens d'automobiles

ACS: Advanced Cooling System

AGS: Active Grille Shutters

ARDC: Automotive Research and Development Center

CAC: Charge Air Cooling

CAD: Computer Aided Design

CAE: Computer Aided Engineering

C_D: drag coefficient

C_DA: drag area

CFD: Computational Fluid Dynamics

CI: Compression Ignition (engine)

C_L: lift coefficient

C_p: pressure coefficient

CPU: Central Processing Unit

CRF: Centro Ricerche FIAT

CTC: Chrysler Technical Center

DOE: Design Of Experiment

EPA: Environmental Protection Agency

EU: European Union

FCA: FIAT Chrysler Automobiles

GUI: Graphical User Interface

H: Heat transfer coefficient (convective)

HEX: Heat Exchanger

ICE: Internal Combustion Engine

IT: Information Technology

MPV: Multi-Purpose Vehicle

MY: Model Year

NAFTA: North American Free Trade Agreement

OEM: Original Equipment Manufacturer

PID: Part Identification

SAE: Society of Automotive Engineers

SI: Spark Ignition (engine)

T: Temperature

WOT: Wide Open Throttle

Do not be ashamed when you wish to be
taught what you do not know;
To know something is praiseworthy, blamable is to
not want to learn anything.

Marcus Porcius Cato, Disticha IV, 29

1. CHAPTER 1

INTRODUCTION

1.1. MAIN DRIVERS FOR THE RESEARCH

Environmental friendliness and sustainability are becoming today the principal drivers for many technological innovations in different industrial fields. More specifically, in the automotive sector the key problem is to improve the overall efficiency in the utilization of the resources which are necessary for personal mobility. In an effort to reduce the environmental impact of human transportation, in the past decades several organizations have tried to establish more and more severe regulations in terms of vehicles emissions and fuel consumption. Regulatory institutions from all over the world have developed and still work to define new standards for several different categories of vehicles, especially passenger cars, whose share of market is high enough to represent a significant contribution to the overall emissions of main pollutants. Recently, this tendency has even more intensified, involving organizations from all over the world. More specifically, both the European Union and the United States of America are leading benchmarks for such a strong intensification of the restriction limits. The European Commission and the US Environmental Protection Agency (EPA) respectively are pushing the car manufacturers towards the development of cleaner technologies year by year,

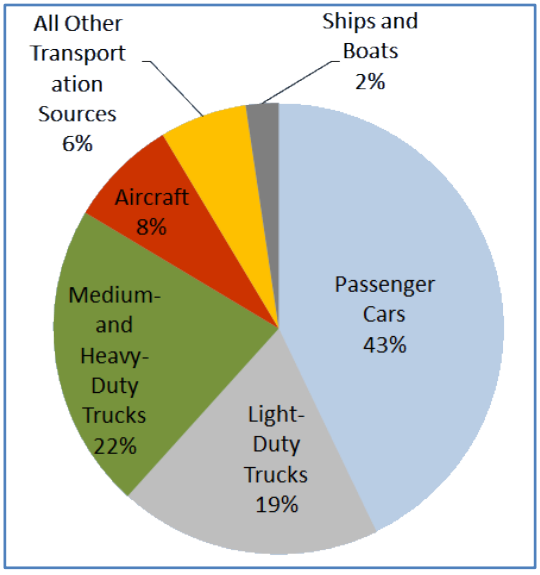

Figure 1.1 - Contribution of different categories to overall USA greenhouse gases emissions due to transportation in 2010. [2] Data from U.S. Environmental Protection Agency, 2010 U.S. Greenhouse Gas Inventory.

through the enforcement of more and more stringent regulations. In the next years, Euro VI and EPA Tier 3 emission standards will be introduced (see Appendix A), which mandate for even lower emission levels compared to the current scenario. In addition to the regulatory standards to be satisfied by law, voluntary agreements between manufacturers, e.g. the ACEA agreement in Europe, determine the CO_2 reduction trend which can be seen in Figure 1.2.

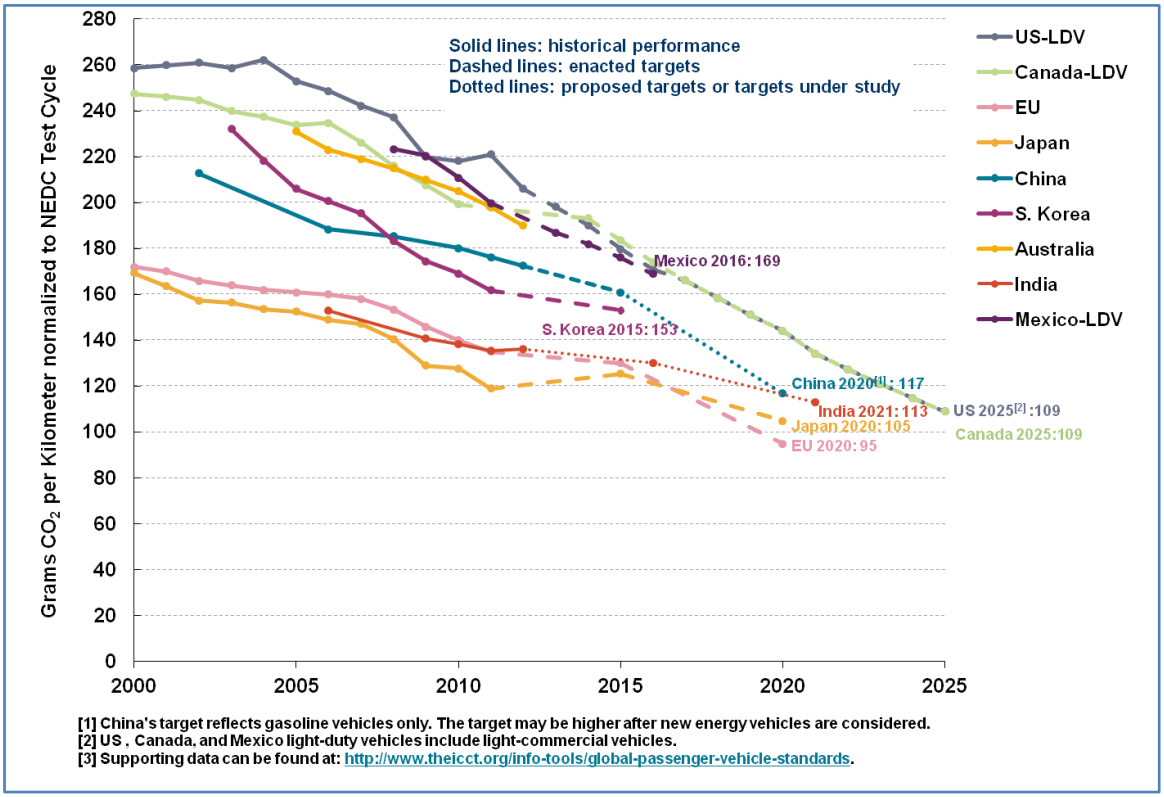

Figure 1.2 - CO_2 emissions per kilometer, historical and forecasted performances. [24]

These agreements, though not compulsory by law, are nonetheless important from a brand image point of view, and they contribute to set and quantify targets that all the best manufacturers of a given market try to achieve in order to satisfy step by step the official regulations. In particular, these limits have to be considered in this specific context because of the presence of FIAT, which represents one of the main members of ACEA.

All of this has an important reverberation on the technological aspect, because for the car manufacturers it is crucial today to study and develop

innovative ideas to be implemented in the next generation of vehicles in order to fulfill the aforementioned requirements. A direct result of the push towards more environmentally efficient vehicles is clearly visible in Figure 1.3, where the historical and forecasted evolution of passenger cars in terms of CO_2 emission per distance travelled is plotted over time.

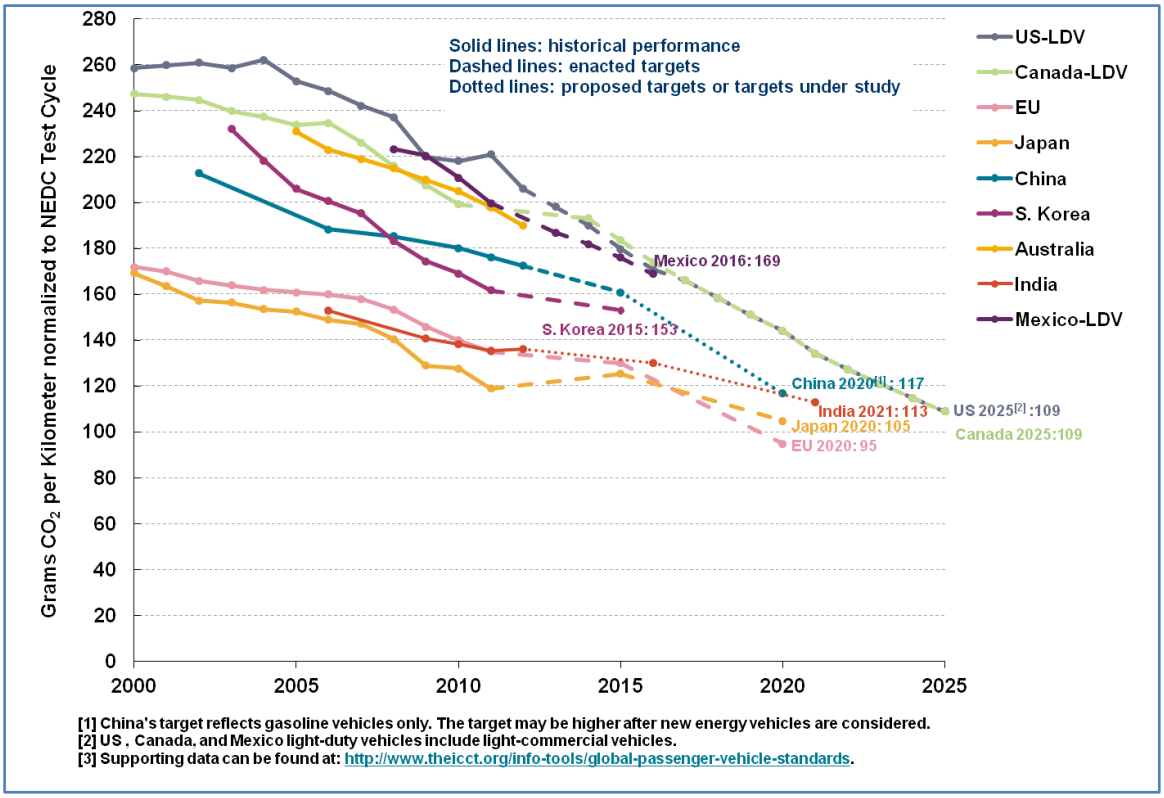

Figure 1.3 - CO_2 emissions per kilometer travelled over time, historical and forecasted data for different Countries. [24]

This trend directly results in improved fuel economy, being CO_2 a direct indicator of fuel consumption. This is immediately noticed in the following plot, which shows the fuel consumption average of the fleet of different Countries over the world, normalized to the US and European test cycles:

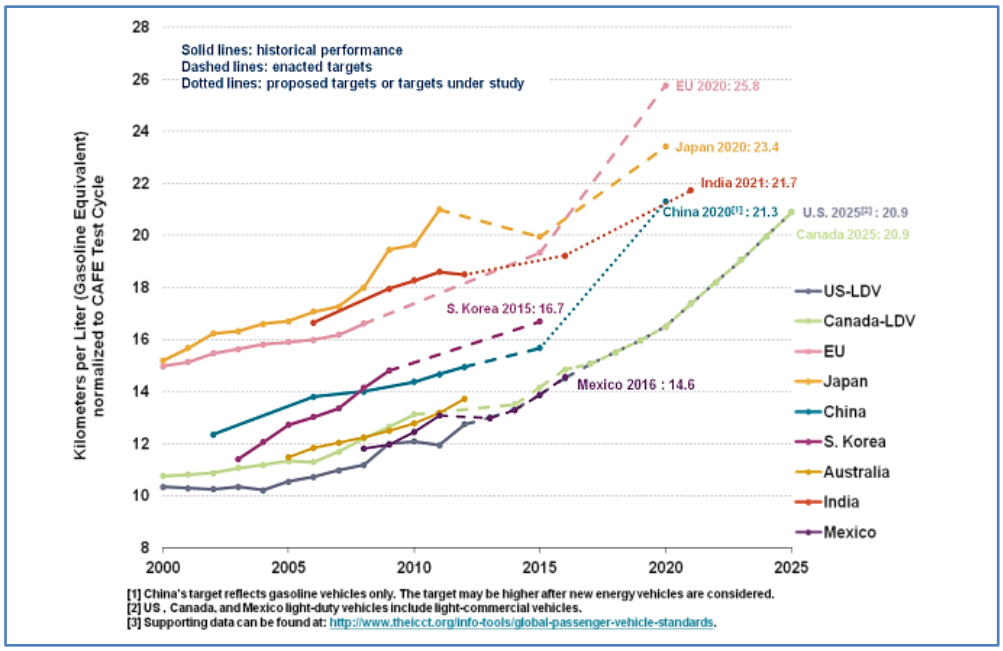

Figure 1.4 - Average fuel consumption (in km/L) for different Countries fleets, normalized to US cycle. [24]

In particular, the challenge today is to achieve the emissions and fuel consumption targets through an economically feasible technology implementable in the short term, possibly taking advantage of all the new CAE-assisted engineering design tools available nowadays. Here are some examples of possible solutions to achieve emissions and fuel consumption limits:

- Hybrid/electric powertrain
- Energy recovery systems (e.g. Kers)
- Lightweight materials (e.g. Al alloys, composites…)
- New approaches to engine design (e.g. downsizing, turbocharging…)
- Alternative fuels (e.g. biofuels)
- Aerodynamics improvements
- Optimized thermal management

If considering the above list, it becomes immediately evident how the first items require an extensive study and development to get significantly improved, either because the technology is not currently fully available or engineeringly advantageous, or for cost reasons associated to its implementation on a large

scale production. In addition, also the time required to develop and implement a given solution must be accounted for, so that the most viable choice today is to focus on the last two items, namely aerodynamics improvements and optimized thermal management. As a matter of fact, improvements in these areas can guarantee significant fuel consumption and emissions reductions within a remarkably lower time if compared to the other technologies. As a result, it becomes now clear why the automotive industry is concentrating on these two aspects, and what is the purpose of this research project.

1.2. OBJECTIVES

The following thesis aims at identifying and developing new aerodynamic solutions for the front-end of a vehicle and at evaluating their impact on the thermal performances in the engine bay. The starting point is represented by the FIAT 500L model, a mini-MPV launched in 2012.

Figure 1.5 - FIAT 500L, the object of the thesis research. [16]

From a technical point of view, this vehicle is a 5-door hatchback with front engine and front-wheel-drive architecture (a *Trekking* version featuring AWD layout has been commercialized at the end of 2013). The version the research work will focus on is the NAFTA 1.4L Turbo MultiAir, featuring a 1368 cc gasoline engine capable of delivering 160 hp @ 5,500 rpm and a peak torque of 250 Nm @ 2,500 rpm. The starting point will be the analysis of the current aero-thermal behavior of the model. On the basis of such an investigation, innovative solutions will be studied for the front-end of the vehicle in order to improve the behavior of those areas which will be considered critical from the thermal viewpoint. These ideas will then be modelled in the virtual CAD environment and simulated in the thermal solver in order to evaluate the efficacy and the extent of the potential improvement on the thermal aspect, while at the same time the engineering team of the Company will quantify their impact from an aerodynamic perspective. The final target is to identify new aerodynamic configurations for the front-end which optimize the thermal management in the engine bay by also minimizing the overall vehicle drag by acting on the cooling airflow drag. The possibility to work together with the analysis and design teams of FIAT and Chrysler will guarantee the possibility to take advantage of all the know-how and all the resources available for achieving this target.

Two main fields of engineering are involved in this work: aerodynamics and thermal management. In addition to these, other constraints will be mandated by vehicle packaging for the engine bay, style needs, and pedestrian safety issues. In the next paragraphs the current aerodynamics and thermal management scenario is presented with the state-of-the-art practices used in the automotive industry, along with a basic technical background to allow the reader get confident with the parameters of interest for the problem. Then the expected future developments will be highlighted to understand in which direction is the development of the aforementioned approaches and procedures going.

1.3. THE AERODYNAMICS SIDE

1.3.1. CURRENT SCENARIO

The starting point for an aero-thermal simulation is represented by the aerodynamic part. The main target of the aerodynamic design of a medium-size passenger vehicle like the one we focus on is the search for a configuration able to guarantee the minimum drag, and, as a consequence, to reduce as much as possible the impact of aerodynamic power request on the total power delivered by the engine through the fuel. To put it differently, lower drag results in lower fuel consumption and emissions, which are the main drivers of this research for innovation.

Today aerodynamics plays a major role in improving the overall fuel efficiency of a vehicle. Extensive studies in the automotive field have been carried out from an experimental point of view in the last decades, in which different body shapes and conformation of car body details were devised and tested in order to identify the most aerodynamic shapes. Recently, the results of such an extraordinary investigation have been implemented on large production vehicles by most manufacturers, due to the extremely stringent requirements in terms of emissions and fuel consumption. As a consequence, from an external aerodynamics point of view the vast majority of the automobiles within the same segment look very similar, the only differences being mostly associated to style issues required by the market or minor niceties. The result of this is that much less freedom is allowed to the designers, who have to devise a body shape by being restricted by style issues, structural limits, interior packaging, powertrain requirements, thermal needs and active, passive and pedestrian safety constraints.

The direction undertaken by those car manufacturers which aim at making a difference with respect to competitors, therefore, is to concentrate on internal aerodynamics, in order to minimize the drag without impacting too much on the other constraints mentioned above. As a matter of fact, as low as it can be, the drag associated to the cooling airflow has become a significant portion of the overall drag of a car today. Therefore, this is the reason why a viable way for further reducing the aerodynamic resistance of a vehicle nowadays is to focus on the internal flows.

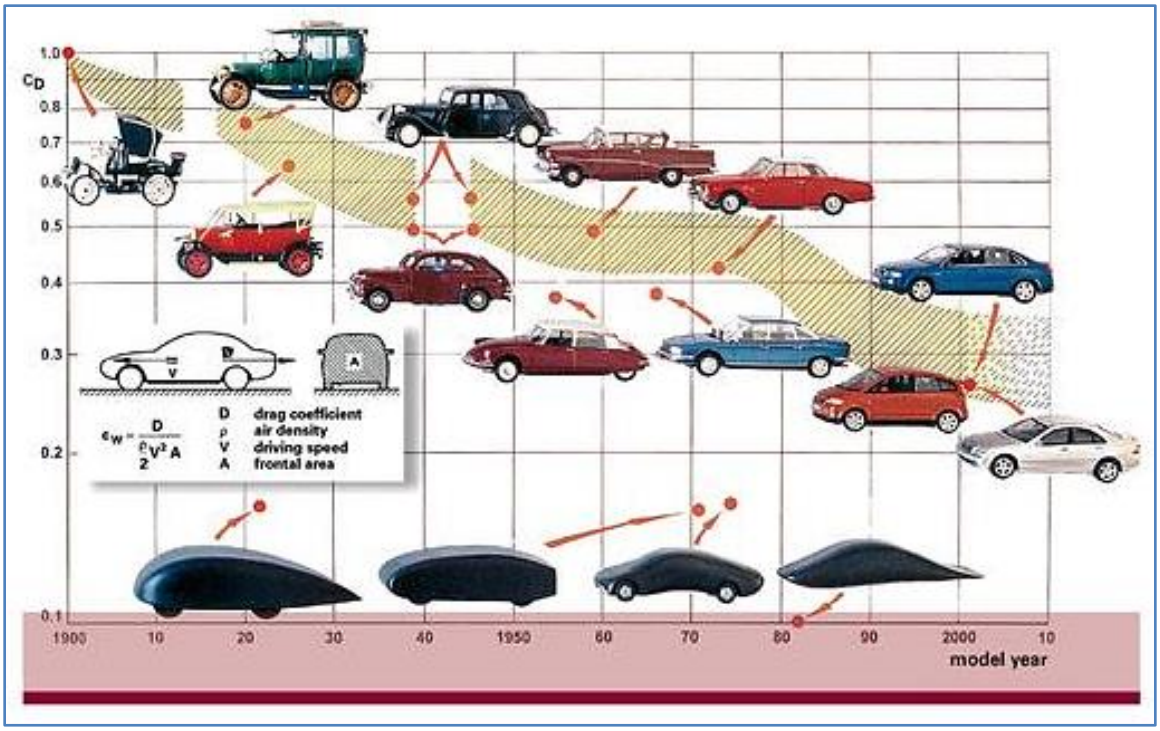

Figure 1.6 - Historical evolution of passenger car drag coefficient. Today, to further reduce it, it's necessary to focus on the internal flows. [24]

Before proceeding, it is necessary to define what is the cooling airflow and its associated drag. Cooling airflow is that part of incoming airflow that, when the vehicle is moving, enters the engine bay through the air vents at the front-end and, by exploiting the pressure differential between that inlet and the outlet (typically located in the underbody), it crosses all the cooling system, HVAC and powertrain components that need to be cooled down.

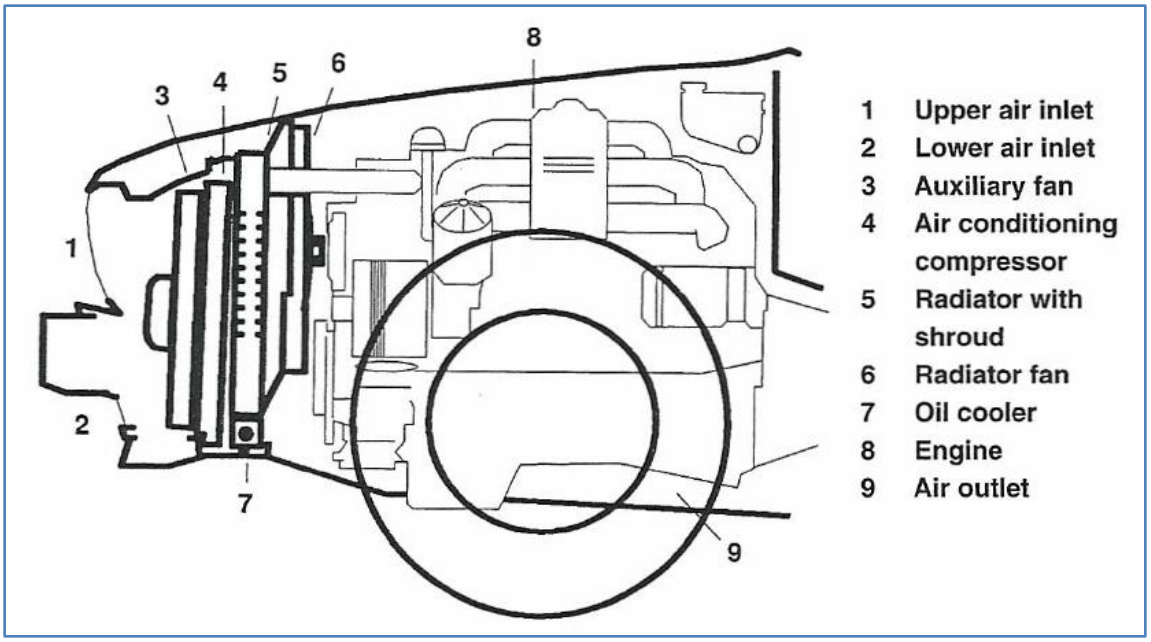

Figure 1.7 - Main powertrain and cooling system components crossed by the incoming cooling airflow. [2]

This advantageous exploitation of a favorable pressure gradient is called *ram air effect* (or simply *ram effect*). Unfortunately, it is not always possible to fully exploit it due to the operating conditions of the vehicle. For instance, if the car is moving at low speed and it is in idle, highly inhomogeneous cooling results due to the effects of high backflow and buoyancy, resulting in higher operating temperatures for the components.

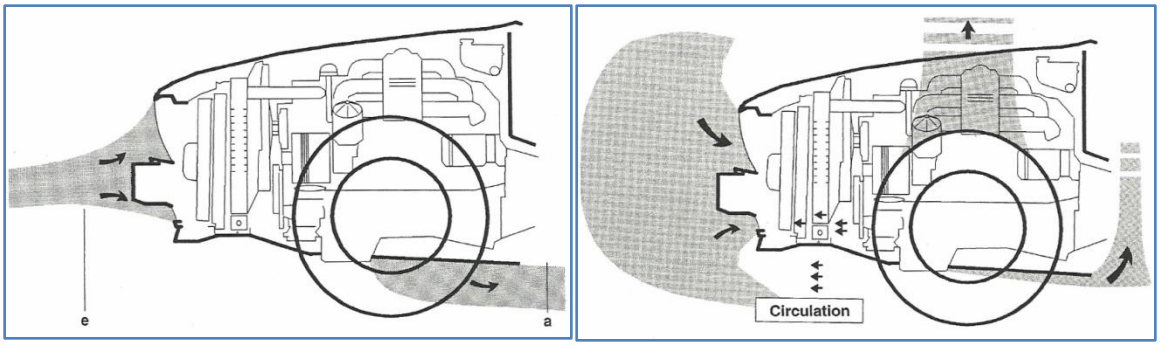

Figure 1.8 - Extreme operating conditions: on the left: high load and speed, ram effect best exploited: on the right: low speed and load, poor ram effect, backflow, buoyancy, higher temperatures. [2]

In addition to the cooling performances, an important aspect associated to the cooling airflow is its aerodynamic impact. Cooling drag is defined as the contribution of the cooling airflow to the total drag of the vehicle, and it is due to

two different components: *cooling-air drag*, associated to the pressure loss between inlet and outlet, and *interference drag*, associated to the change in flow pattern due to airflow deviation.

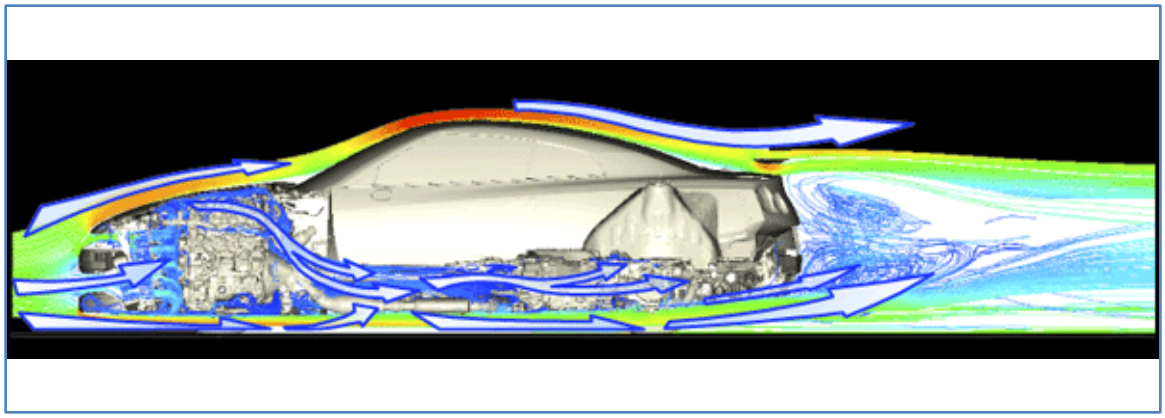

Figure 1.9 - Airflow pattern around a Nissan GT-R. It is possible to visualize the cooling airflow and its interaction with the rest of the flow. [8]

While these two components are conceptually different, they are not easily separable from an experimental point of view. Consequently, they are generally accounted for together by considering the difference between total vehicle drag with open and closed air vent, an approach which is used both in experimental testing and in computational simulation.

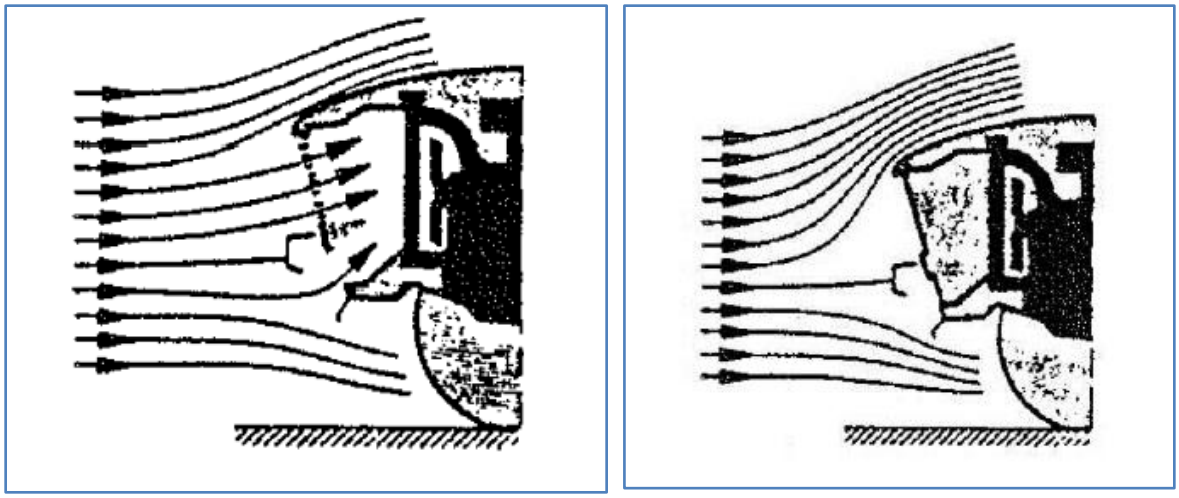

Figure 1.10 - Cooling airflow drag experimental measurement procedure. Open and closed air vents configurations. [2]

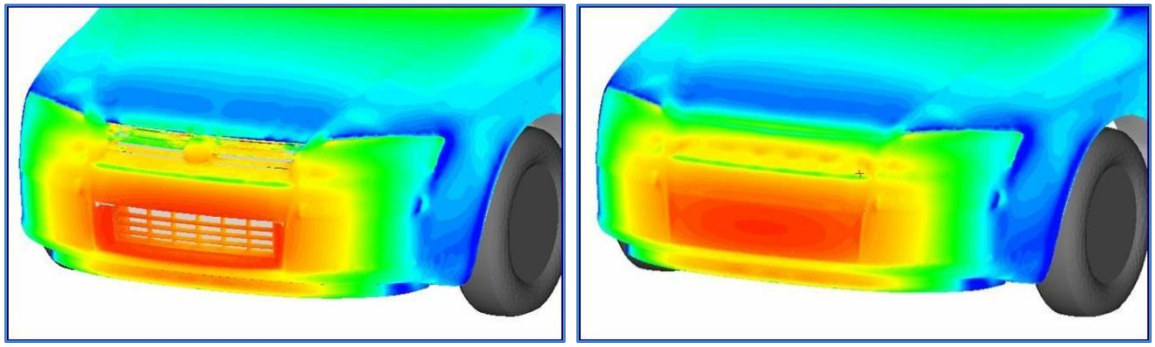

Figure 1.11 - Cooling airflow drag computational measurement procedure through CFD. Open and closed air vents configurations. [9]

In order to understand and quantify the importance of this factor, it is possible to see in Figure 1.12 some figures of cooling airflow drag obtained by experimentally testing a relevant sample of cars. As can be noticed, the contribution of this factor in terms of C_D can easily be as high as 0.04, thus being a noteworthy factor to focus on for vehicle aerodynamic optimization.

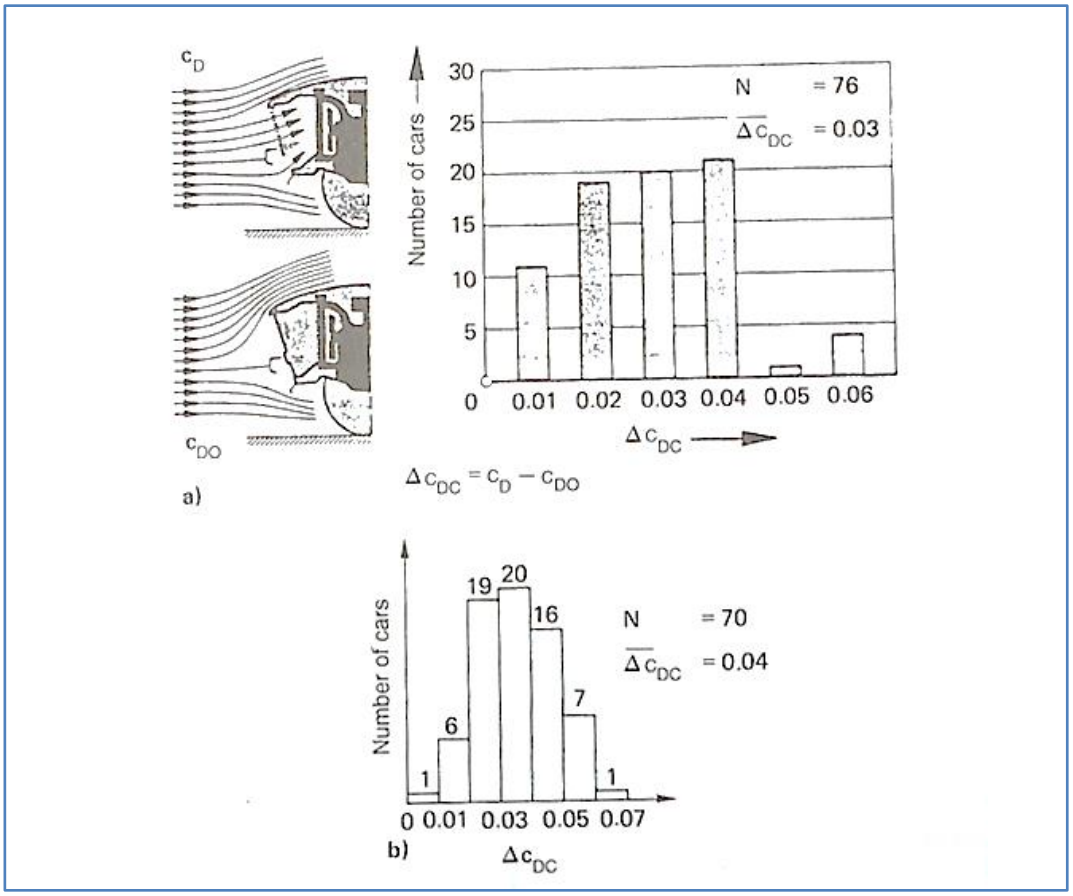

Figure 1.12 - Cooling airflow drag of various cars from the 70s (N=sample size). [2]

As a note to the reader, it must be said that the figures shown above are representative for a sample of cars from the Seventies, however they are not too far from the ones of the current generation of passenger vehicles. This statement is validated by several other sources, including a SAE paper [1] by Baeder, Indinger, Adams, and Unterlechner which attribute to the cooling air about 10% of the total vehicle drag. Some other researchers assign an even higher share of drag to cooling airflow, according to the specific model under test; these include Dr. Simone Sebben (Volvo), who discussed in a SAE paper frequently cited in the literature about an un-named vehicle with a total drag coefficient of 0.29. For this vehicle, the total contribution of cooling drag to the total one corresponds to approximately a third, about the same as the external flow one. This puts in evidence once more that a strong effort must be done today to minimize this term so as to ameliorate the aerodynamic performances of passenger vehicles.

Parts	Percentage of Total Drag
Cooling package (including radiator, intercooler, oil cooler, etc)	33.4%
Exterior	31.7%
Front wheels	13.1%
Rear wheels	6.9%
Floor	6.9%
Rear Axle	3.1%
Engine	3.1%
Front Suspension	1.4%
Exhaust	0.7%

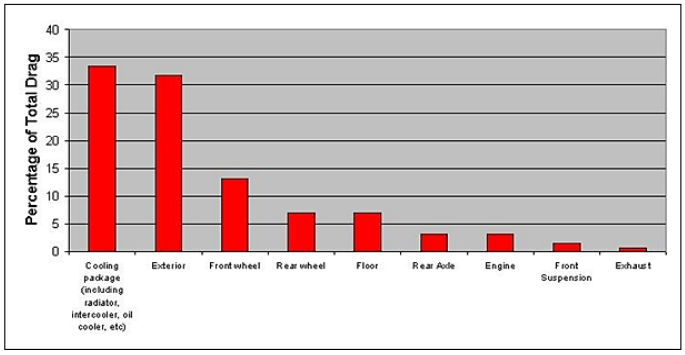

Figure 1.13 - Percentage contribution to total drag of different parts for a recently developed passenger vehicle. [18] The cooling package has the highest share of drag.

Following the Oil Crisis, in the Seventies several experimental tests were carried out in various wind tunnels in order to diminish the overall vehicle drag thus trying to lessen the fuel consumption. Hucho [2] provides a very interesting insight about such experiments and their results, which are still used as general guidelines by most aerodynamicists in several companies nowadays, even though they refer to specific cases and, as with any aerodynamic result, have no general validity and applicability. When considering internal flows, examples include re-positioning of the radiator and modifications in the layout of the engine bay, as shown in Figure 1.14.

Today these studies are widely available to the designers in the automotive industry, and they represent a valuable source of data which can be used while devising new models. As a matter of fact, in recent years the application of these good practices in the design phase has resulted in very similar layouts for the engine bay of current vehicles, as well as very close designs of the front-end. The vast majority of passenger vehicles, in fact, are characterized today by inlets for the cooling airflow very close to the stagnation point in front of the car, where a high static pressure area is available to drive the flow across all the main components within the engine bay by exploiting the ram effect. The outlet is generally located in the underbody, which is becoming smoother and smoother in order to avoid flow separation due to exposed protruding parts which negatively affect drag.

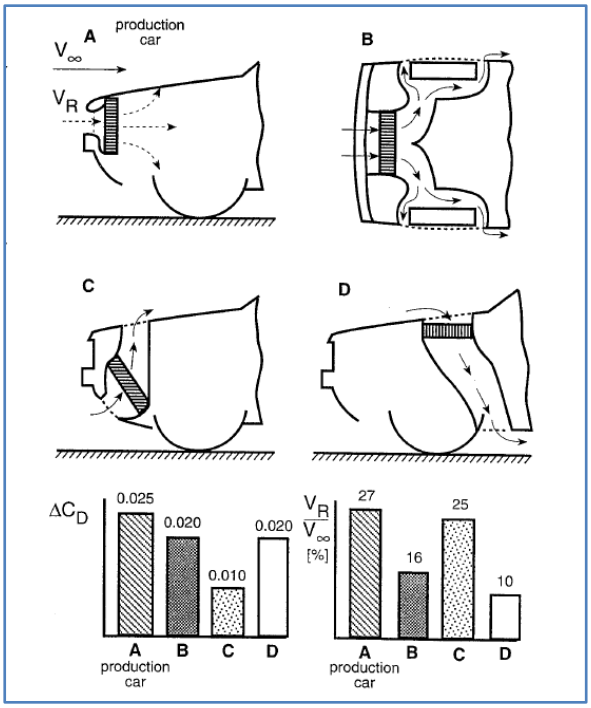

Figure 1.14 - Possible alternative radiator arrangements for reducing cooling airflow drag. [2]

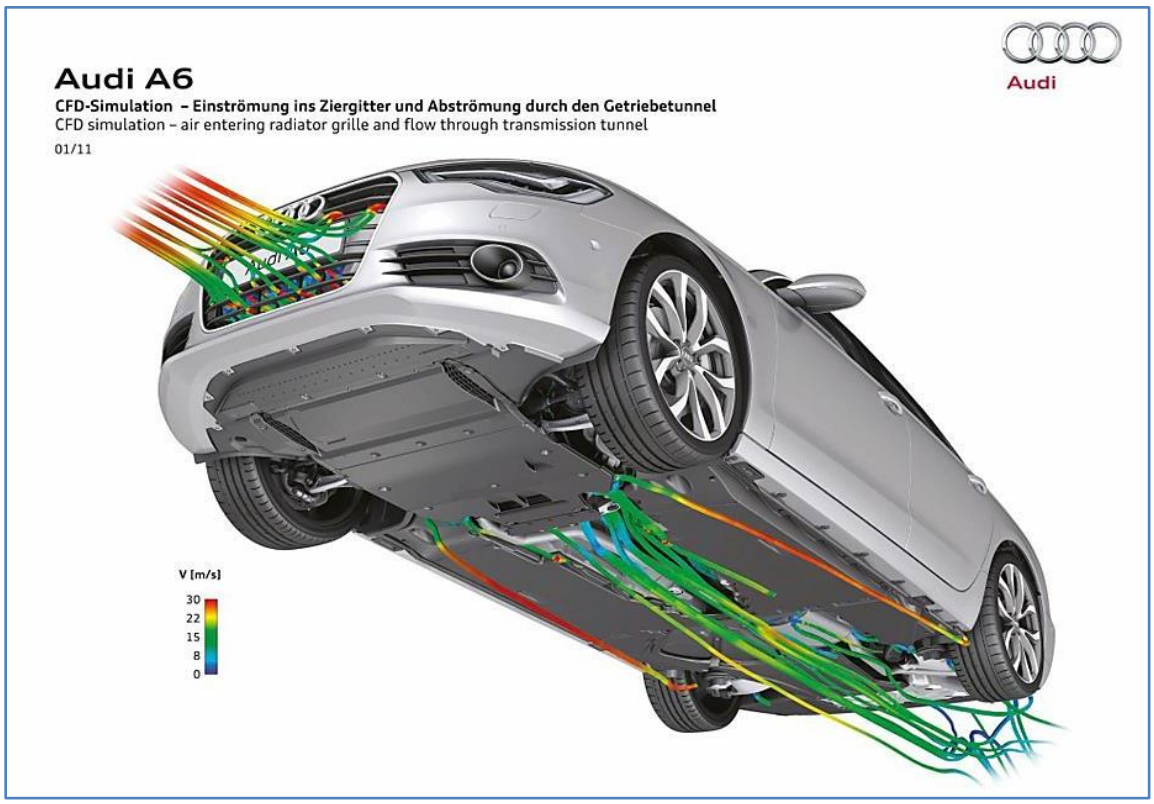

Figure 1.15 - Typical positioning for cooling airflow inlet and outlet on a current generation vehicle. [10]

Another feature that makes recent automobiles distinguishable from their predecessors is the size of the inlet of the front vents, which is getting smaller and smaller to reduce the drag. This, as will be discussed later, has a strong impact on the thermal management of a vehicle, because all the restrictions to the flow limit the air flow rate so that other measures are needed to dispose of the heat generated by the powertrain. In any event, most of the manufacturers have now become able to achieve optimal trade-offs for their models, and today the research is towards extreme solutions for further restricting the inlets when cooling flow is least needed, as will be discussed later. This trend becomes evident if considering the same model produced by a given company over the years, as for instance is the case with the Opel Kadett model shown in Figure 1.16.

Figure 1.16 - Cooling inlet design, historical evolution for Opel Kadett. [2]

After having considered the current practices employed in the design of the front-end and the engine bay layout, it is now interesting to focus on those developments that are currently under research and that represent the state-of-the-art in the field.

1.3.2. FUTURE DEVELOPMENTS

In order to limit as much as possible the cooling drag contribution to the total drag, innovative solutions are being developed nowadays by most carmakers. They range from very basic ideas fairly easy to implement on a real model to extremely complex configurations requiring a complete re-design of the

front-end, the engine bay and the underbody. The vast majority of these ideas are first implemented in top-level cars in which the final cost to customer is not a big concern. Examples include, but are not limited to, internal diffusers in the engine bay for better static pressure recovery, active flaps for cooling ducts to specific components, e.g. brakes, active grille shutters (AGS) to limit the volume flow rate of cooling air when least needed, variable-height front air dam, etc.

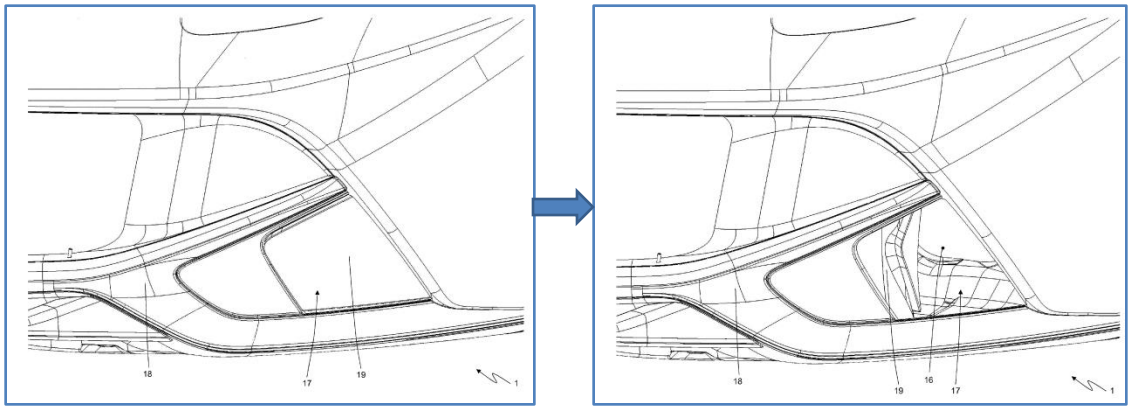

Figure 1.17 - Ferrari F12 Berlinetta front brake cooling ducts in open and closed position. They improve the aerodynamic behavior of the car by reducing the internal flow when not necessary. [11]

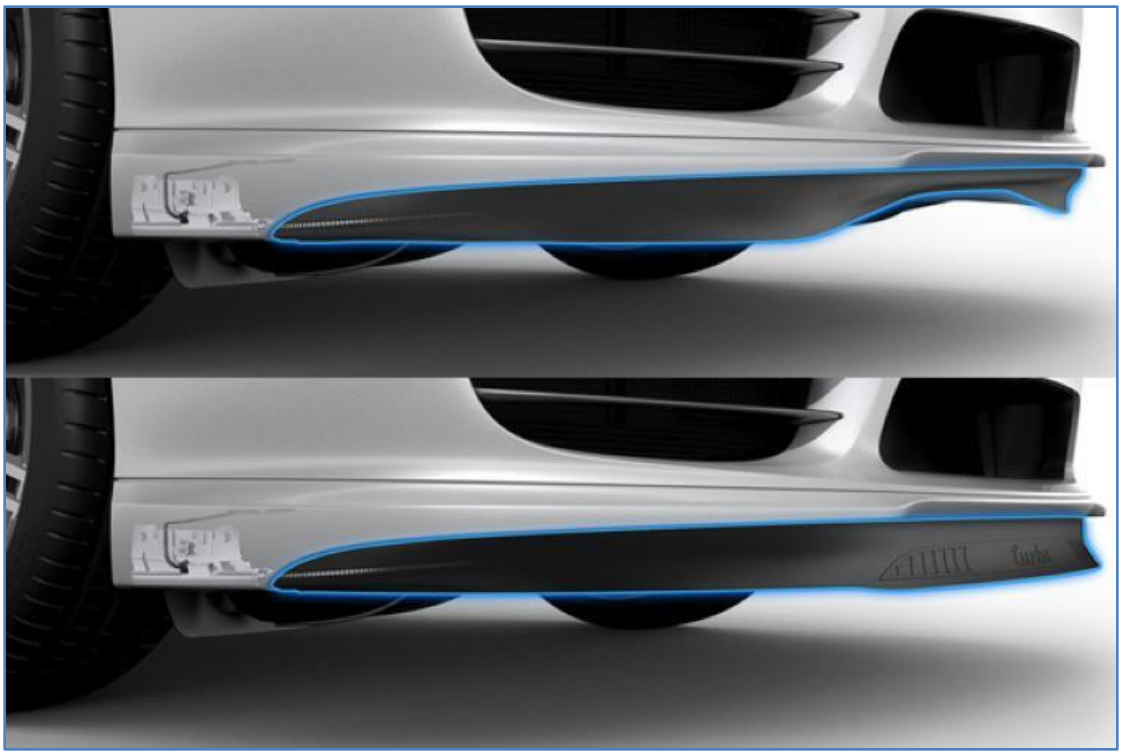

Figure 1.18 - Porsche 911 Turbo S active front spoiler. [14]

Some of these technologies are getting more common even on medium-size passenger cars, as can be seen in the following figure, which shows the AGS system for a Dodge Dart.

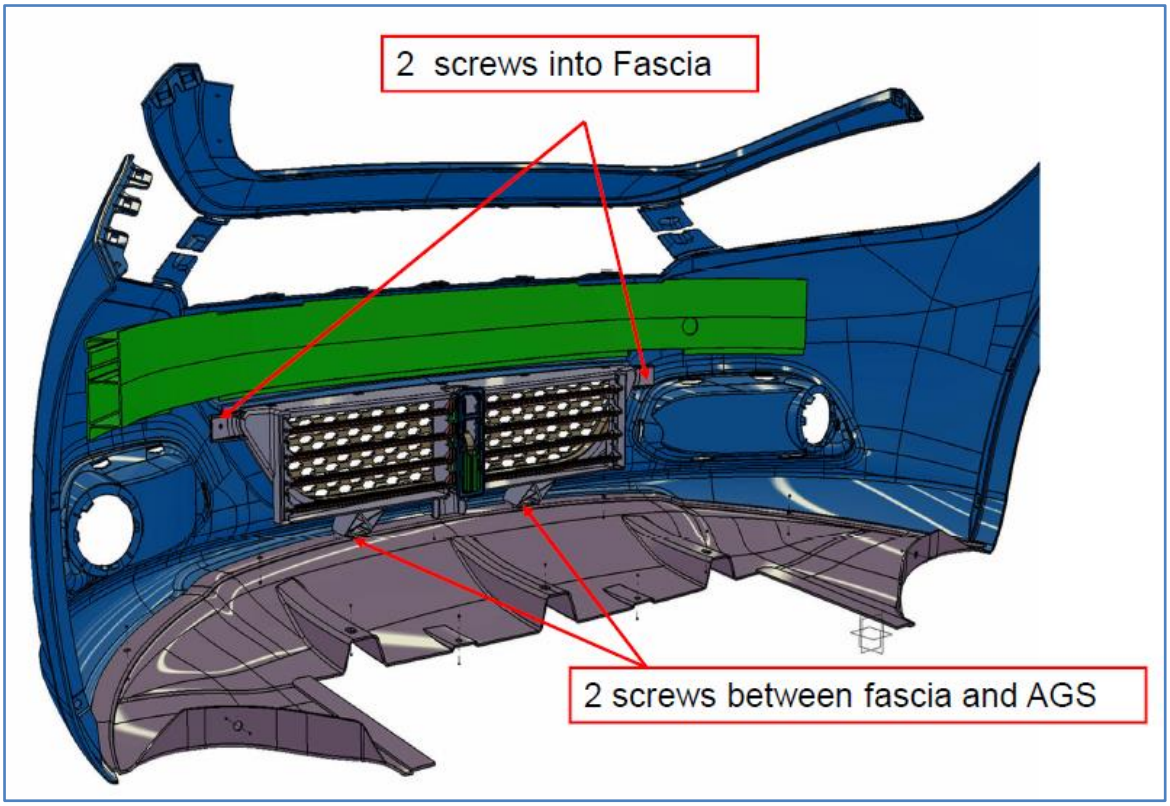

Figure 1.19 - AGS system for the Dodge Dart. It currently represents one of the main areas of interest for automotive aerodynamicists. [12]

Today the target for car manufacturers and their designers is to make these innovative solutions available on the large scale production, so as to improve fuel consumption and emissions performances of those vehicle segments for which those parameters are most crucial. Of course, when implementing such improvements on lower segment vehicles the main challenge for the designer consists in finding the best compromise between efficacy, cost, weight, and complexity. In particular, for a mini-MPV vehicle like the FIAT 500L the cost is probably the main constraint, due to the characteristics of the market segment it addresses, so that this will strongly affect and influence the amount of modifications that can be carried out on the baseline version.

1.4. THE THERMAL MANAGEMENT SIDE

1.4.1. CURRENT SCENARIO

Any aerodynamic device among all the ones mentioned above has a strong influence on the thermal performances of a vehicle. Therefore, even though significant benefits may come from the aerodynamic point of view, there might be thermal drawbacks which make a given solution not suitable for a given model. This is the reason why a proper aerodynamic and thermal co-design is required when developing a new model or when making modifications to an existing one, so that the best trade-off can be identified which guarantees the most efficient configuration which achieves the best aero performances without too high a penalization on the thermal side.

This chapter aims at providing an overview of the current scenario for the thermal management of passenger vehicles, and shows the current solutions adopted by most manufacturers in this area.

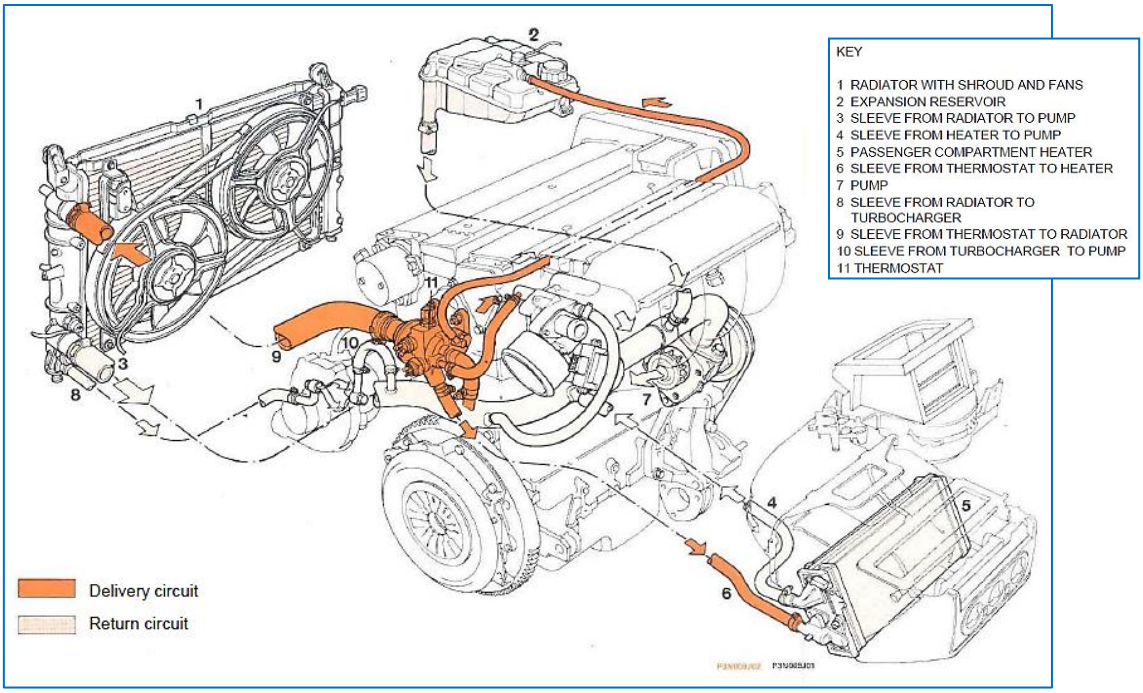

Figure 1.20 - Typical passenger vehicle cooling system architecture. [15]

Figure 1.20 shows the typical cooling system architecture currently adopted on the vast majority of low to medium passenger vehicles. The main components are radiator, cooling fan, coolant pump, thermostat, heater core for passenger compartment, expansion tank and pressure cap, water jackets inside the engine head and block, the coolant itself and all the plumbing system. The basic functional scheme of the cooling system is shown in Figure 1.21, with all the aforementioned components.

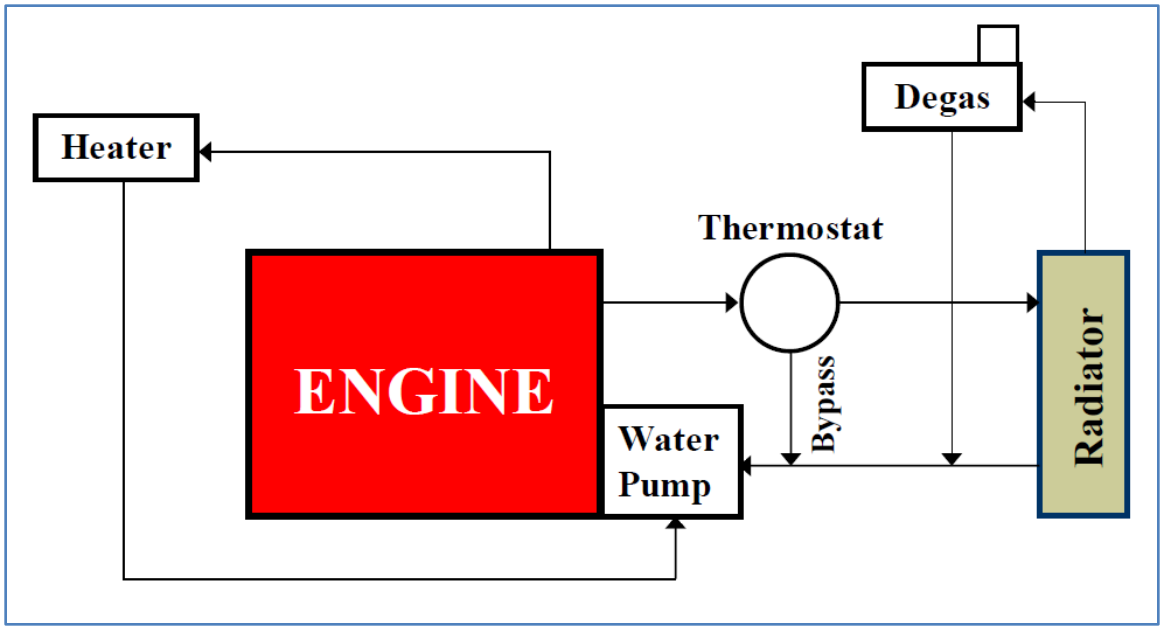

Figure 1.21 - Basic functioning scheme of a typical automotive cooling system. [16]

Here is a list of objectives which must be fulfilled by the cooling system:

- Remove excess heat from the engine
- Ensure adequate cooling to all components under all operating conditions
- Avoid too high thermo-structural stresses on components
- Ensure correct thermal balance even under severe operating conditions
- Maintain optimal operating temperature for the engine (highest efficiency)
- Achieve optimum operating temperature in the shortest possible time

These performance needs must be satisfied by also guaranteeing the following requirements:

- Minimize power request from fuel
- Minimize the impact on aerodynamic drag
- Ensure vehicle proper functioning in all environmental conditions
- Satisfy durability and reliability requirements

As mentioned above, one of the main points to be satisfied by a cooling system is to maintain a correct thermal balance in all the possible operating conditions which can be experienced by the vehicle. Below is the governing equation determining such balance [3]:

$$\dot{m}_f Q_{LHV} = P + \dot{Q}_{cool} + \dot{Q}_{oil} + \dot{Q}_{amb} + \dot{H}_{inc} + \dot{H}_{exh} \qquad (1)$$

where:

$\dot{m}_f$ = fuel mass flow rate to the engine
Q_{LHV} = lower heating value of the fuel
} $\dot{m}_f Q_{LHV}$ = fuel energy rate at engine inlet

P = engine brake power
$\dot{Q}_{cool}$ = heat transfer rate to the cooling medium
$\dot{Q}_{oil}$ = heat transfer rate to the oil
$\dot{Q}_{amb}$ = heat rate directly rejected by convection and radiation to the surrounding ambient
$\dot{H}_{inc}$ = exhaust enthalpy loss due to incomplete combustion
$\dot{H}_{exh}$ = exhaust enthalpy loss due to high temperature of exhaust gases

For the thermal management engineer it is interesting to understand the contribution of each factor to the total power absorbed by the fuel inlet into the engine. Different parameters affect such a distribution, like engine type (SI or CI),

engine speed and load, weather conditions, etc. However, in order to give an idea of the involved values, the following table shows how the power input in the engine through the fuel gets distributed among the above mentioned factors in moderate weather conditions and low to medium engine speeds and loads

Table 1.1 – Output power, heat rates and residual enthalpy percentage distribution for light driving conditions for SI and CI engines. [3]

	P	$\dot{Q}_{cool}$	$\dot{Q}_{oil}+\dot{Q}_{amb}$	$\dot{H}_{inc}$	$\dot{H}_{exh}$
	(percentage of fuel heating value)				
SI engine	25-28	17-26	3-10	2-5	34-45
CI engine	34-38	16-35	2-6	1-2	22-35

(e.g. city traffic) for both SI- and CI-engine-equipped vehicles:

The graph below shows the contribution of the different factors as a function of the engine speed at full load. As can be seen, no big variations are displayed over the engine operating speed range, even though bigger changes usually occur when varying the load.

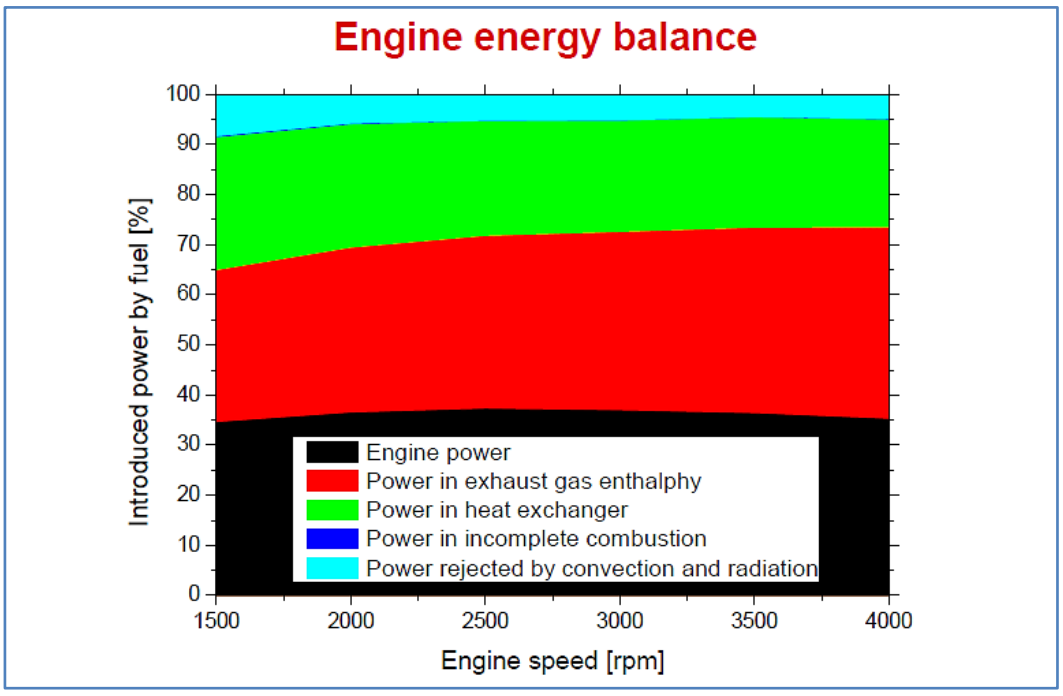

Figure 1.22 - Percentage contribution of different factors to total input power introduced through the fuel over engine operating speeds for a GM 1.6L Diesel engine at full load.

The basic working principles of a typical automotive cooling system are assumed to be known by the reader, so no deep detailing on such aspect will be discussed. On the contrary, the focus will be more on the variation of thermal performances due to those aerodynamic parameters which are involved.

First of all, in a traditional system one of the main parameters of interest to properly design and control a cooling system is the ram air which enters the engine bay through the front inlet vents located on the vehicle front-end. This has a huge impact on the thermal performances of the underhood components, especially the radiator, the cooling fan and all the other potentially present HEXs. In turn, this affects in a significant way the power request from the pump, which must adapt its discharge to the demand of the cooling system.

A typical curve for automobile radiator performances is shown in Figure 1.23, which illustrates how an increase of cooling air mass flow rate significantly improves the heat transfer coefficient for a common braze-welded aluminum radiator (size: 580x305x18 mm, width x height x depth).

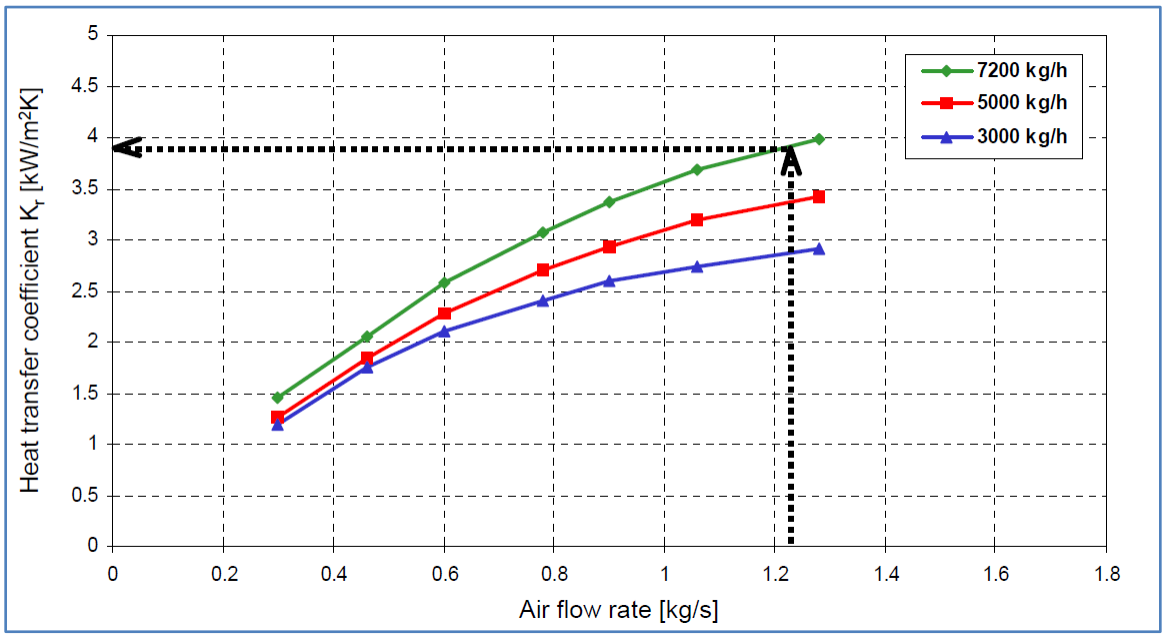

Figure 1.23 - Typical performance curve for a passenger car braze-welded aluminum radiator. A specific operating point is highlighted. [3]

As can be seen, the air speed plays a big role in the heat transfer which takes place in the radiator. However, this parameter cannot be modified or acted upon through the use of the cooling system control system, since it depends on the weather and vehicle operating conditions. As a consequence, in the development phase it is necessary to suitably design the cooling system so as to allow its proper functioning in all the possible vehicle operating conditions. Similar plots can be obtained for all the other heat exchangers in the engine bay, e.g. HVAC condenser, intercooler, transmission oil cooler, etc. As for the cooling fan, the typical characteristic curve is shown in Figure 1.24. In this case, however, the cooling air mass flow rate is mostly dictated by the cooling needs when the vehicle is stopped or at low speeds, so that it is the heat dissipation requirement for the specific vehicle operating condition that determines the minimum airflow rate required for a proper functioning of all the powertrain components and assemblies.

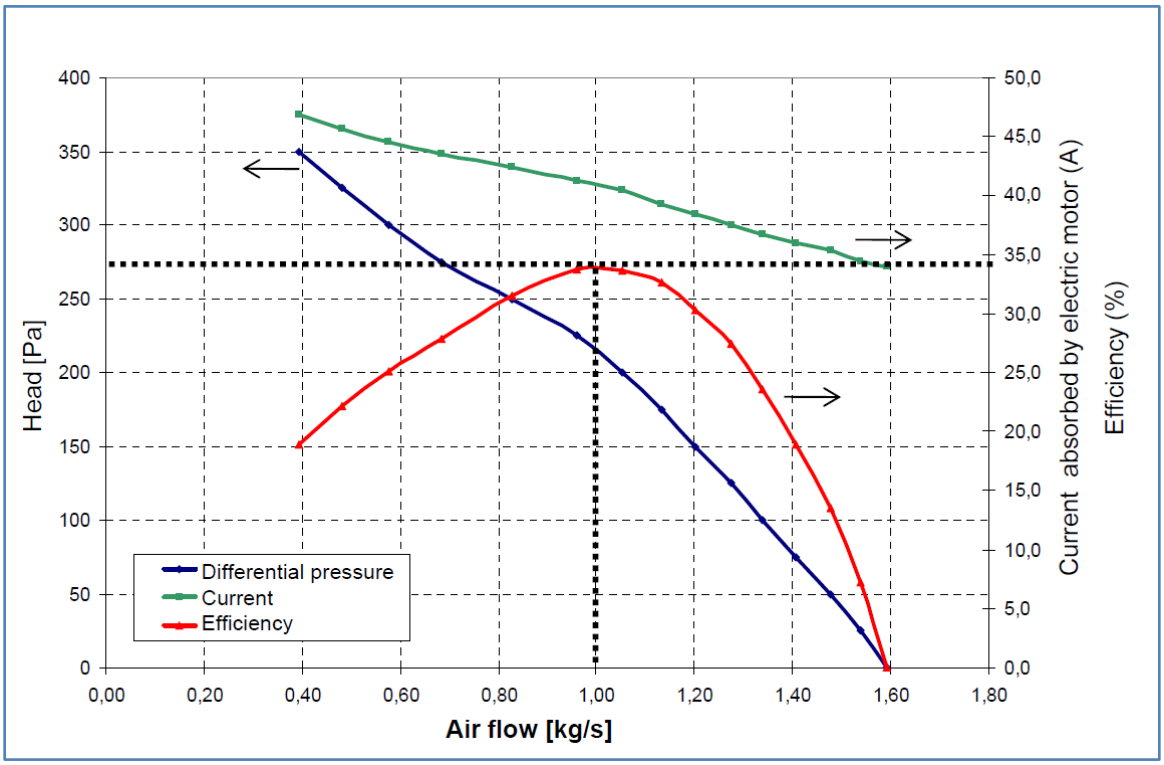

Figure 1.24 - Characteristic curve for a 500 W automotive cooling fan with 380 mm blades. [3]

When considering the performances of the cooling system, it is important to take into account the fact that two conflicting requirements are involved: on one hand, the heat exchange process efficiency, on the other hand the aerodynamic efficiency. Therefore, the pressure losses associated to the air side must be carefully accounted for in order to minimize the impact on drag deriving from the thermal needs. A typical curve representing the pressure losses on the air side for various radiator geometries is shown in Figure 1.25.

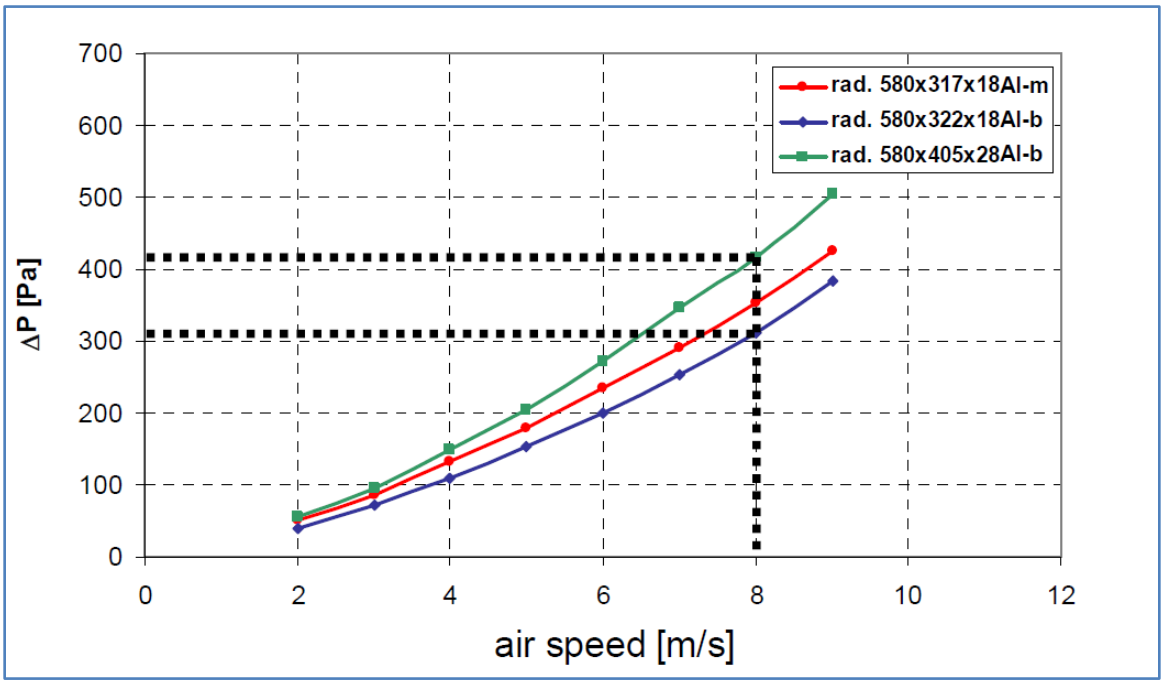

Figure 1.25 - Air-side pressure loss as a function of air speed for various radiator geometries (size: length x width x depth). Al-m: aluminum mechanical radiator; Al-b: aluminum-brazed radiator. [3]

The incoming cooling air mass flow rate, though being one of the most crucial parameter in the system, is not the only variable affecting the thermal performances of the vehicle. In fact, based on the specific operating condition, an exact coolant mass flow rate must correspond to a given air mass flow rate based on the heat rate dissipation required by the engine. Similar curves for the one shown above for the air side can be plotted for the coolant side. Other components are involved in the analysis and dimensioning of the system on the coolant side, including thermostat, coolant pump, plumbing system, etc. For all

of them it is necessary to take into account the mechanical, hydraulic and friction power requirements so as to achieve the most efficient operating condition in the entire range of use.

When designing a cooling system, it is necessary to go through a sequence of steps in order to achieve the aforementioned result. For the cooling system engineer, two important parameters need to be defined which will determine the performances of the system in its various operating conditions. These parameters are the air-to-boil temperature (ATB) and the external temperature difference (ETD). The former is defined as:

$$ATB = T_a + T_b - T_{ri} \quad (2)$$

where T_a is the ambient temperature, T_b the boiling temperature of the coolant at the specific operating pressure, and T_{ri} the radiator coolant inlet temperature. The ETD is defined as:

$$ETD = T_{ri} - T_{ai} \quad (3)$$

where T_{ai} is the radiator air inlet temperature.

The flow chart below (source: D'Ambrosio, S., *Internal Combustion Engines and their application to vehicle*, lecture notes [3]) represents the approach followed in the design and dimensioning of an automotive cooling system with the various requirements mandated to the designer.

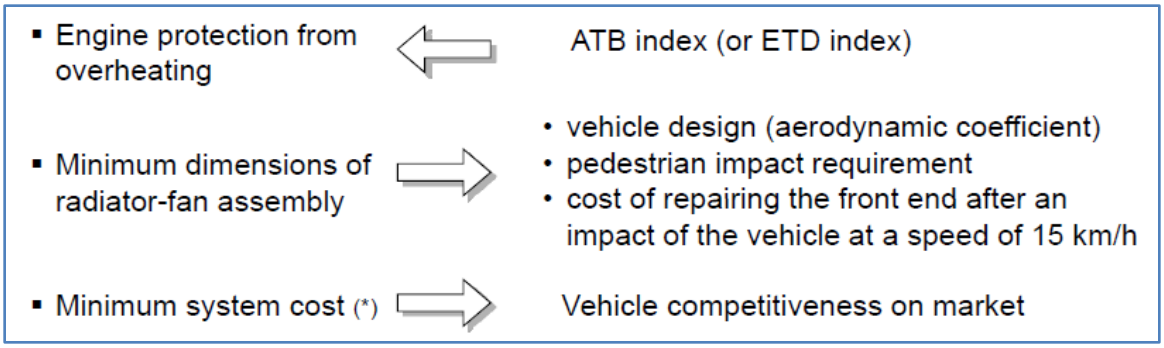

Figure 1.26- Automotive cooling system design flow chart. [3]

The work this thesis focuses on, however, does not represent a design problem, rather an analytical one, where the effects of aerodynamic improvements on the thermal performances must be evaluated. For this type of problem, the following inputs are required [3]:

- Coolant flow rate
- Heat disposed by the engine
- Heat disposed by the oil heat exchanger
- Heat transfer coefficient of the radiator
- Fan performance curve
- Radiator and HVAC condenser pressure drop
- Dimensions and pressure drop of air grids
- Heat disposed by HVAC condenser
- Engine power and torque curves
- Vehicle style features (CAD detailed geometry description, external shape and underhood compartment)
- Gearbox and differential ratios
- Tyre rolling radius

Starting from these items, it is possible through a virtual co-simulation procedure to evaluate the air speed and temperature distribution on the cooling module components surfaces and to check the ATB and ETD indices, which should be:

$$ATB > ATB_{limit} \quad (4)$$

$$ETD < ETD_{limit} \quad (5)$$

Of course, not all the above parameters will be necessary as inputs in this thesis work, due to the fact that the optimization procedure will not focus on all the possible operating conditions. Therefore, some of them will not be taken into strong consideration, e.g. the cooling fan performance curve will not be analyzed

because of the fact that it is in the "off" condition at the considered speed. However, in order to design a suitable control system for, e.g., an AGS system, this factor must be absolutely accounted for in order to find the most efficient operating control algorithm. Also, for this work (and, in general, in the co-simulation approach) the engine load and rpm are already known from the specific testing air speed condition, so that it will not be necessary to go through the various transmission ratios and tyres rolling radius to evaluate them.

In the following paragraph some of the state-of-the-art advancements in the thermal management field are discussed. While some of them are still a prerogative of high-market-end models, some others are getting more and more common even on mid- and small-size vehicles like the one this thesis focuses on.

1.4.2. FUTURE DEVELOPMENTS

The word "thermal management" was introduced few years ago to identify a procedure used in the automotive field to address all the thermal problems associated to a vehicle, from the cooling system to the HVAC management, from the thermo-structural analysis of powertrain components, to passenger comfort studies. More specifically, this word is usually associated to recent development in the cooling system management of the vehicle, which underwent significant improvements in recent years in order to minimize the emissions and improve the efficiency of modern engines, as well as speeding up the warm-up time. These improvements were so remarkable that the so-called Advanced Cooling Systems (ACS) were devised thanks to the collaboration between OEMs and suppliers. Essentially, thanks to improvements in each and every area of the cooling system components, it was possible to evolve from a discrete-wise control system to a continuous one, in which the values of the main parameters

vary in the continuum so as to allow optimum working conditions in the entire operating range. The consequences of this resulted in higher operating temperatures for the engine and the underhood components, thus achieving higher efficiencies and lower fuel consumptions, a reduction of warm-up times, thus improving the cold start emissions, nowadays crucial in the testing and homologation procedures, as well as the human thermal comfort in the passenger compartment, and optimal management of the engine heatstroke.

The innovations which allowed achieving such improvements include [3]:

- Metal temperature measurement probes
- Electric water pump
- Electric thermostat
- Low-temperature/high-temperature (LT/HT) cooling loops
- Water charge air cooling (WCAC)
- Integrated exhaust manifold
- Split cooling

As can be seen, most of the above items directly result from an improvement either in the sensor technology or in the control system approach, where the implementation of electronically-controlled devices allows to better set the operating conditions of the components involved. Also, thanks to the growing demand for turbocharged engines, systems featuring LT/HT cooling loops and WCAC are getting more and more common even in mid- and small-size vehicles. A scheme of such systems layout is shown in Figure 1.27. The advantages offered by this strategy lie in the fact that a more compact system can be used with higher performances with respect to a traditional cooling system. The flexibility offered by this system allow to position the HEXes closer to the components that need to be cooled down, thus reducing the volume and the friction associated to the bends and the hoses in the plumbing. This reduction in charge air pressure

losses results in a decrease in the transitory turbo-lag, even though a slight increase in weight results from the use of a WCAC. Also, the use of coolant to cool down the compressed air exiting the compressor improves the efficiency and the performances of the engine compared to the traditional air-cooled intercoolers. The possibility to control separately the HT and LT cooling loops, also, allows a better management of the warm-up phase, as well as the steady-state operation. Overall, fuel consumption reductions of significant value can be expected by the implementation of such a system.

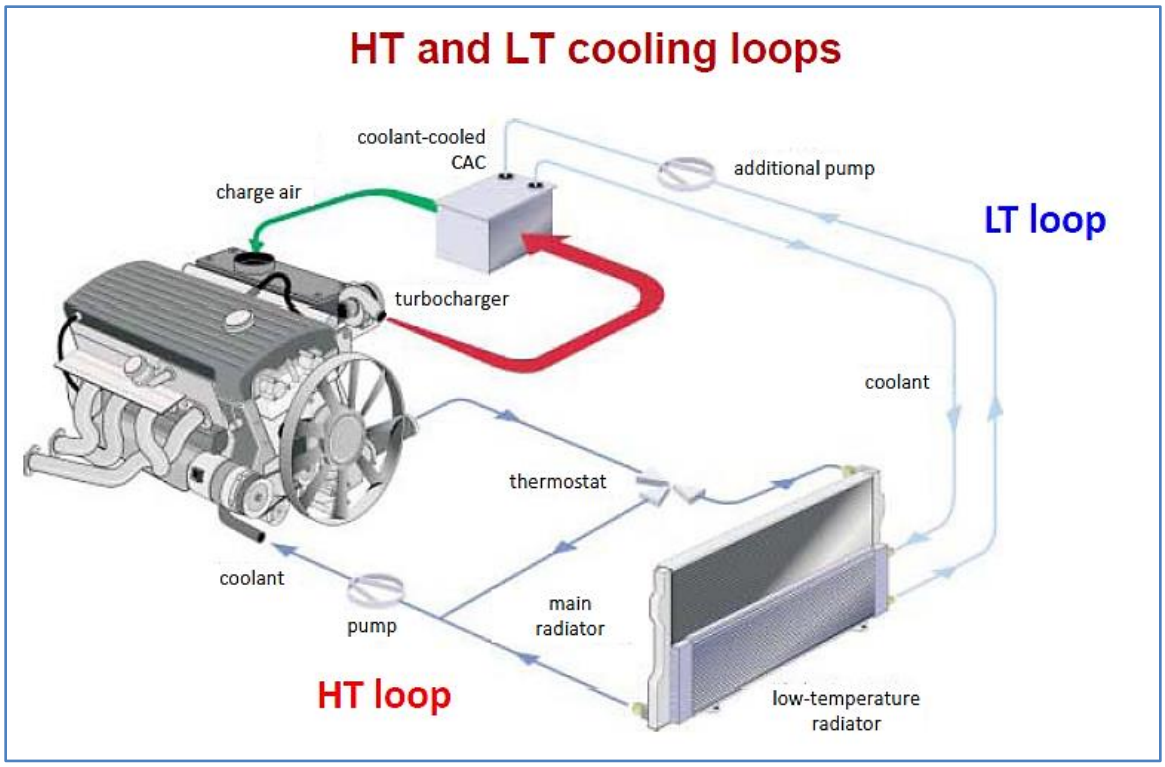

Figure 1.27 - Architecture of a LT/HT cooling system [3].

Other improvements in the thermal management of a vehicle are associated to advancements in the manufacturing technology used to produce components and assemble groups of components into modules. This is the case, for instance, for the integrated exhaust manifold and the cooling module single-unit architecture. The former guarantees advantages in terms of time required for the catalytic converter to reach the light-off temperature, with better emissions and

fuel consumption in both the start-up and steady-state phases. The latter allows weight reductions as well as a more compact architecture, which is essential when considering the engine bay packaging.

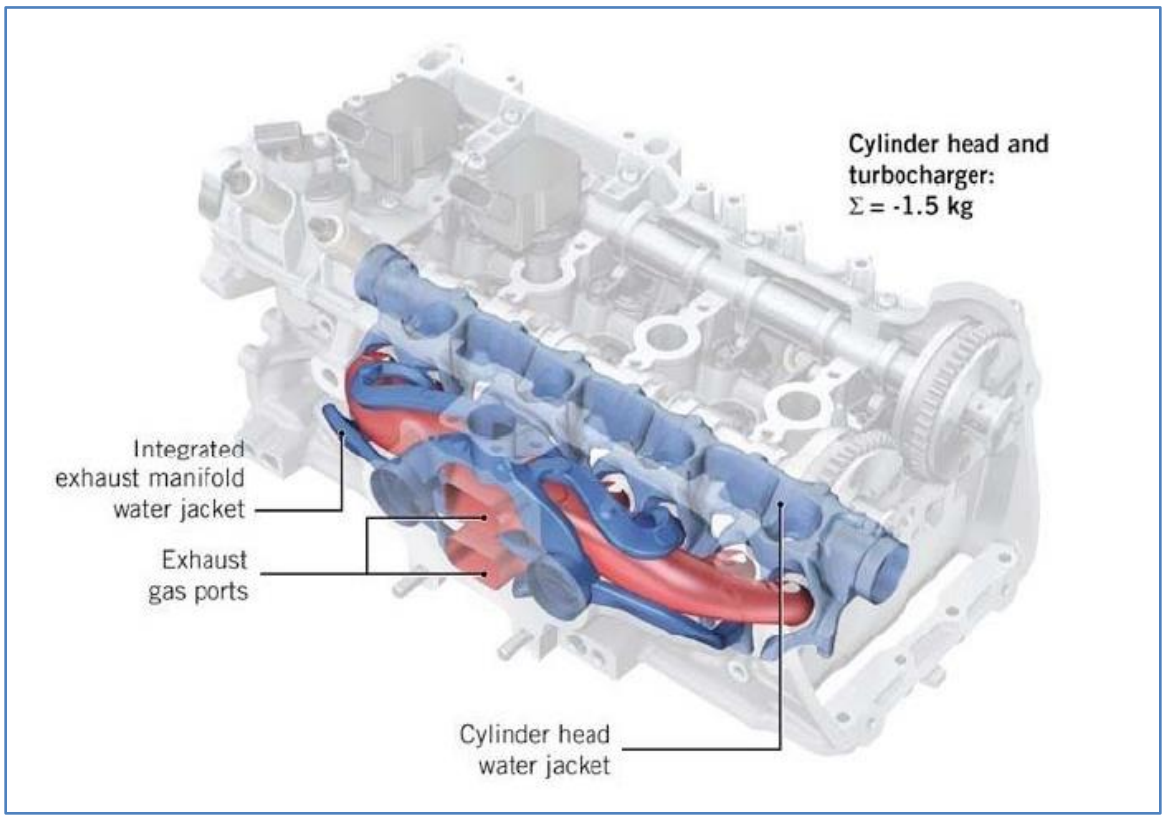

Figure 1.28 - Audi TFSI 1.8L featuring an integrated exhaust manifold [3].

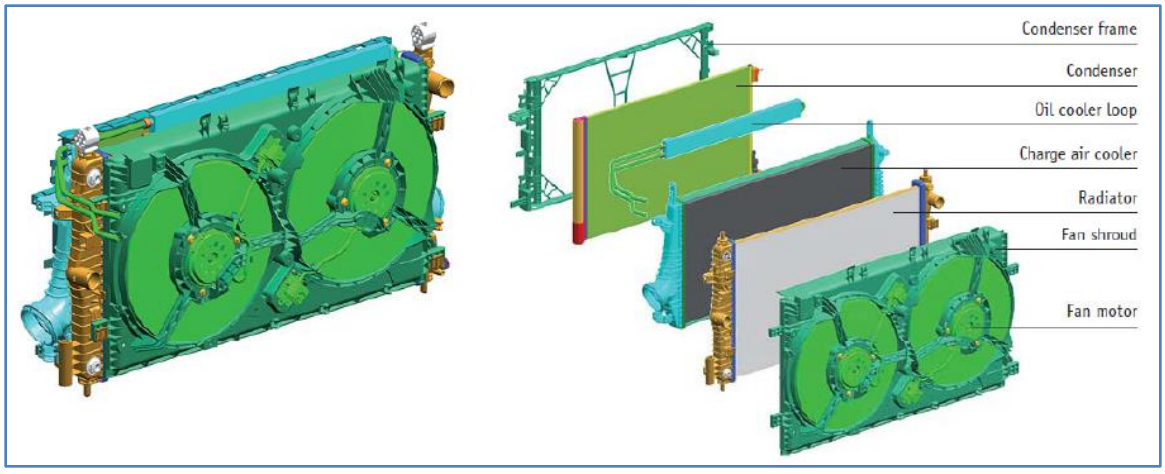

Figure 1.29 - Opel Insignia compact cooling module [3].

In addition to improvements in the components field, advancements in terms of thermal management have been achieved from a global system point of view. Different new architectures have been devised to further improve cooling systems. These innovations completely redefine the typical cooling system layout and/or use different working principles. The implementation, development and commercialization of these systems on passenger vehicles, however, has not become widespread yet due to the big extent of the involved changes.

One of such systems is the so called "split-cooling" or "dual-cooling", where two cooling loops are present to solve two conflicting requirements: speed up the warm-up phase to minimize cold-start emissions and consumption and provide heat to the cabin in a fast way. A scheme describing such a system is shown in Figure 1.30. This architecture is currently adopted in some high-end market segment vehicles like the Audi A6 with second generation 3.0L Diesel engine.

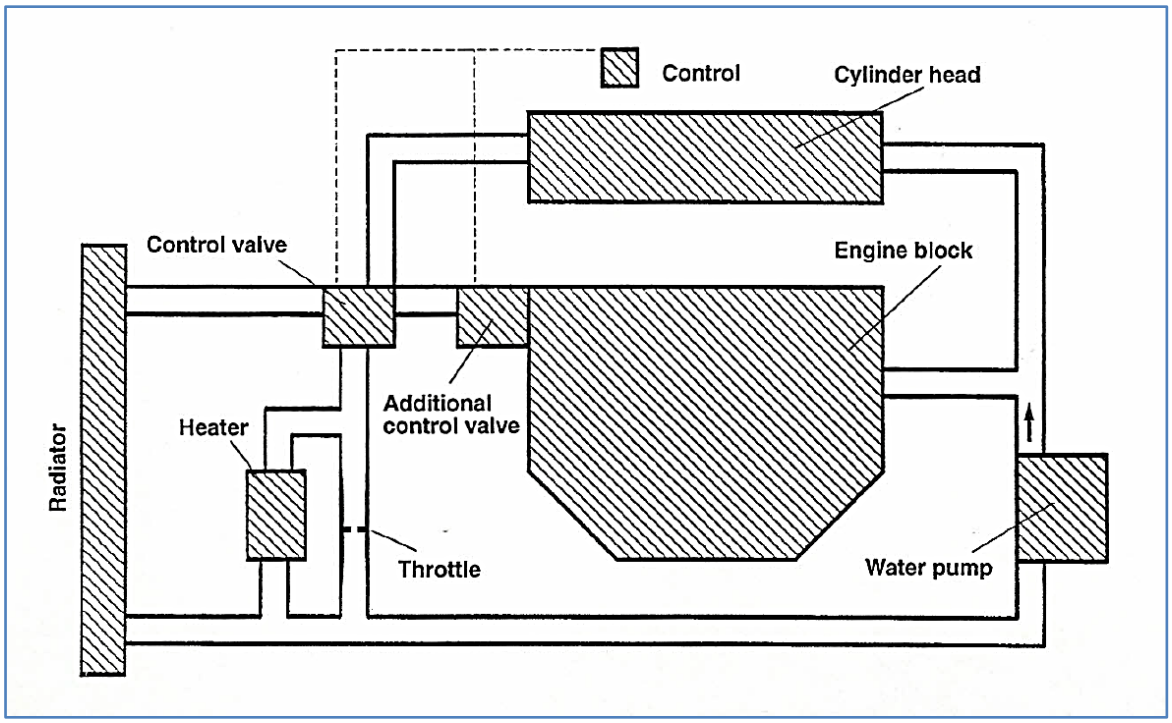

Figure 1.30 - Dual-cooling system scheme. [2]

Another improvement in the thermal management of passenger vehicles is represented by high-temperature cooling. This approach consists in operating the engine at higher temperatures compared to the traditional ones thanks to the development in coolants chemical composition, which can be now operated at temperatures as high as 140°C. If components are designed to function efficiently from a thermo-structural perspective, this strategy allows operating the engine at better efficiencies with lower emissions and fuel consumptions ([2], after [4]). This method is only effective with Diesel-engined vehicles due to the fact that higher engine operating temperatures have a detrimental effect on the volumetric efficiency, as well as on the knock limit. As a consequence, it will not be of direct interest for this thesis work, if not for providing the reader with some hints about possible future developments in this field.

A further development for cooling systems is represented by *phase-change cooling* systems (PCC), where phase changes of the coolant are used in the HEXes in order to dispose of the heat from the powertrain. This approach exhibits some advantages, like the possibility to circulate a lower mass of coolant, thus allowing the use of a smaller pump in terms of size and delivery rate, as well as more uniform components temperature distribution. [2]

Most of the innovative systems or components presented above are currently under research and development in various laboratories of several universities and car manufacturers worldwide. The first commercial applications are currently seen mainly on top-level vehicles for which the cost to the final customer is not one of the main constraints in the definition of the project. Most of the research for the manufacturers, however, still focuses on details optimization, in order to exploit the current technology employed for automotive thermal management at its best. In order to achieve this result, the use of virtual simulation tools can provide the designers with a huge support. This topic is the object of the next paragraph.

1.5. THE PROBLEM

After having discussed about the engineering disciplines involved in the research work, it is necessary to identify the problem that the vehicle engineers face when developing the aero-thermal aspects of a car.

1.5.1. PROBLEM DEFINITION & METHODS FOR ADDRESSING IT

The development phase of an automobile from an aero-thermal point of view is a complex process where several trade-offs have to be achieved in order to find the best balance available among all the explored concepts. As can be expected after considering the previous chapters, conflicting requirements appear when dealing with the aerodynamic and thermal design and optimization of a vehicle. To put it in a nutshell, on the aerodynamic side drag reduction is the main driver for the design of a passenger vehicle. At the same time, thermal power dissipation from the engine bay must be sufficient enough to avoid engine overheating and the consequent thermo-structural degradation of the components, as well as all the other issues already mentioned before. As a consequence, different iterations must be performed and the design and optimization phase in order to achieve a satisfactory result in terms of both aerodynamic and thermal performances, by also keeping into account additional requirements like passive and pedestrian safety, esthetics needs, weight and cost issues. Therefore, different departments are involved which together contribute to define the final configuration to be sold on the market.

In order to find this optimum trade-off configuration, different paths can be followed. Each of them requires different resources in terms of staff, time, facilities, and tools, and, accordingly, each of them provides more or less

accurate results. Also, each strategy has its own advantages and disadvantages based on the required resources. A brief overview will be now given about these methods with their relative main pros and cons.

The first, rudimentary way to address any aero-thermal problem consists in using the differential equations at the base of the heat exchange process. This approach, however, has way too many drawbacks to be considered a viable alternative for automotive designers. First of all, numerous and complex differential equations are involved when dealing with 3D-space geometries of each component of a vehicle cooling system, so that it would be extremely time consuming to evaluate the thermal behavior of a concept in such a way. Also, in order to properly use this method, several unknowns must be measured prior to the calculations, so that a physical functioning model is needed. Analogously, the analytical approach cannot be applied in the aerodynamic field, so that it is necessary to resort to another method.

A more feasible engineering alternative for evaluating the aero-thermal behavior of a vehicle under development would be to physically build prototypes and test them in the wind and climatic tunnels. Of course, this approach is extremely demanding in terms of economic and time expenditures, because a significant number of functioning prototypes have to be built and tested before getting to the optimal trade-off. Indeed, this strategy was followed in the past, when virtual engineering was not yet developed and accurate to such a remarkable extent as it currently is. Therefore, significantly higher costs of development resulted from the fact that many concepts had to be constructed with exactly modelled features in terms of external shape, cooling system and HVAC components which would have equipped the production model. On top of this, the optimization process followed with this approach was only driven by the designers' experience and insight. The engineering team, in fact, could optimize a newly developed concept only by testing the different prototypes and

by improving them based on previous data gathered from past experience on different car models of the same manufacturer. In other words, this method followed a trial-and-error approach rather than a consistent and systematic engineering procedure.

In order to overcome this limit, and thanks to the huge developments in the numerical computation field, the computational fluid dynamics (CFD) approach was developed and implemented in various industrial fields, including the automotive sector. This method consists in designing a CAD model of the vehicle to be developed with all its detailed geometric features of interest, to be then discretized into small volume elements where the basic fluid dynamic equations can be numerically solved. Without going too deep into the details, by integrating the results over the entire volume of interest, it is then possible to evaluate both the bulk characteristics and the local properties of the fields of interest (e.g. velocity, pressure, temperature, etc.). This approach, originally focused especially on external aerodynamics, has now been extended to other fields, like, for instance, internal flows and thermal management. By using the same principle, in fact, it is possible to evaluate the thermal properties of a given model by imposing the proper boundary conditions in the software. The level of accuracy achieved today with commercial solvers widely available in the field is so high that in many cases this is the only method used, with the designers team not even testing a single prototype concept in the climatic tunnel in the development stage (with the only exception of the final production version). Over the past years, the diffusion of the CFD for aerodynamics and thermal calculations has been intense, with the vast majority of carmakers currently adopting this approach all over the world. The advantages of this methodology are immediately evident: no need to construct physical prototypes requiring extensive economic and manpower resources, extremely faster development process (a new configuration can be developed, studied and selected within three

weeks), which guarantees the possibility to go through several optimization iterations, and the possibility for the designers to easily visualize field maps and identify critical areas where to focus in order to achieve the desired improvements. Of course, as usually occurs in the engineering field, this method also has some drawbacks: in fact, very powerful workstations are required to perform accurate models calculations, which are enormously demanding in terms of computational memory, number and speed of CPUs. However, once the hardware and software tools expenditures are done, the number of cases to which the approach can be applied has no limit, so that in the long term the investment is much more convenient with respect to any other aforementioned method.

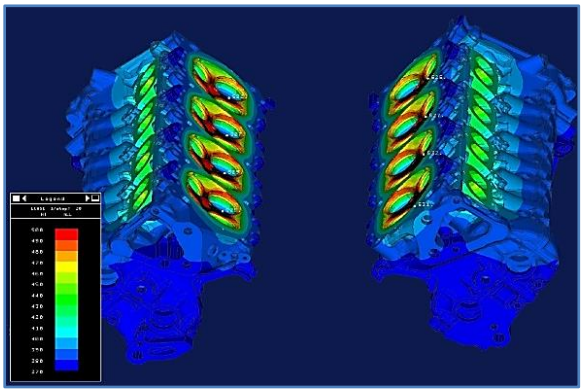

Figure 1.31 - Temperature distribution map of a V8 engine heads obtained through CFD analysis. [19]

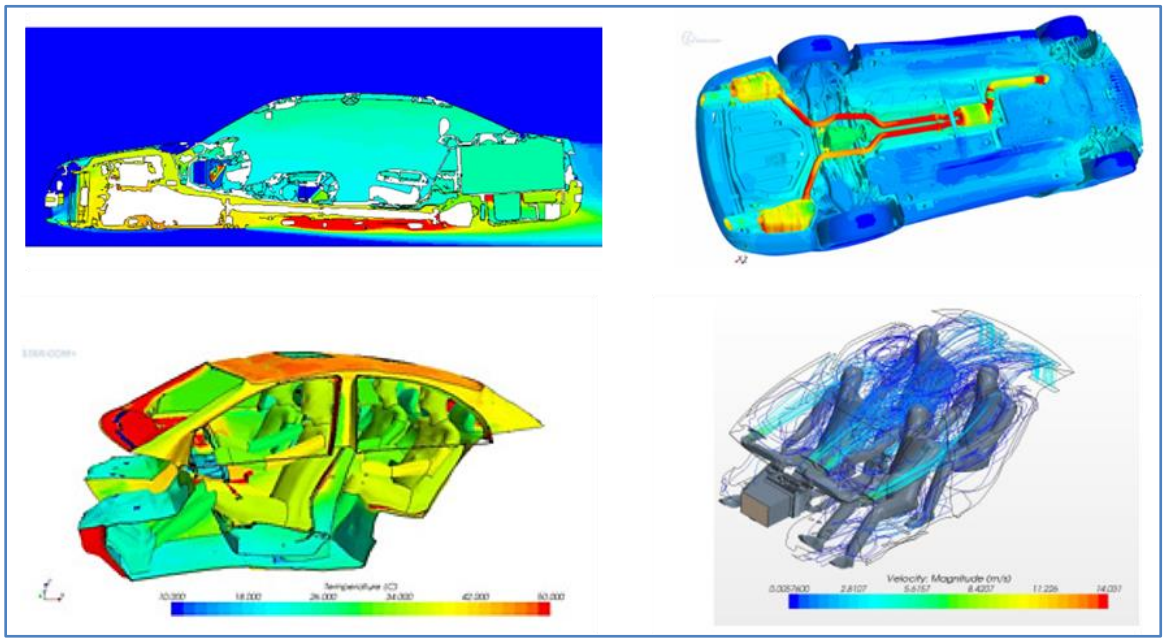

Figure 1.32 - Examples of aerodynamic and thermal maps which can be obtained through virtual CFD simulation. [5]

1.5.2. STATE-OF-THE-ART APPROACH

As already mentioned, the numerical computation approach currently represents the best method to address the automotive aero-thermal design and optimization. The challenge today is no more focused just on the increase in model size which can be reasonably handled by the solver, which is remarkably big (in some high-performance automotive external aerodynamics application the model size can be as high as 130 million cells), rather on the possibility to adopt and improve the so-called co-simulation method. While in the recent past the aerodynamic and thermal problems were separately addressed for a given vehicle, today the tendency is to couple them into a single process involving an exchange of information between the CFD and the thermal solver. The basic idea is shown in Figure 1.33, taken from the SAE paper 2012-01-0635 by Reister and Bauer. [5] In this example a single commercial code is used, while in this thesis work two different codes will be used (Star-CCM+ and RadTherm).

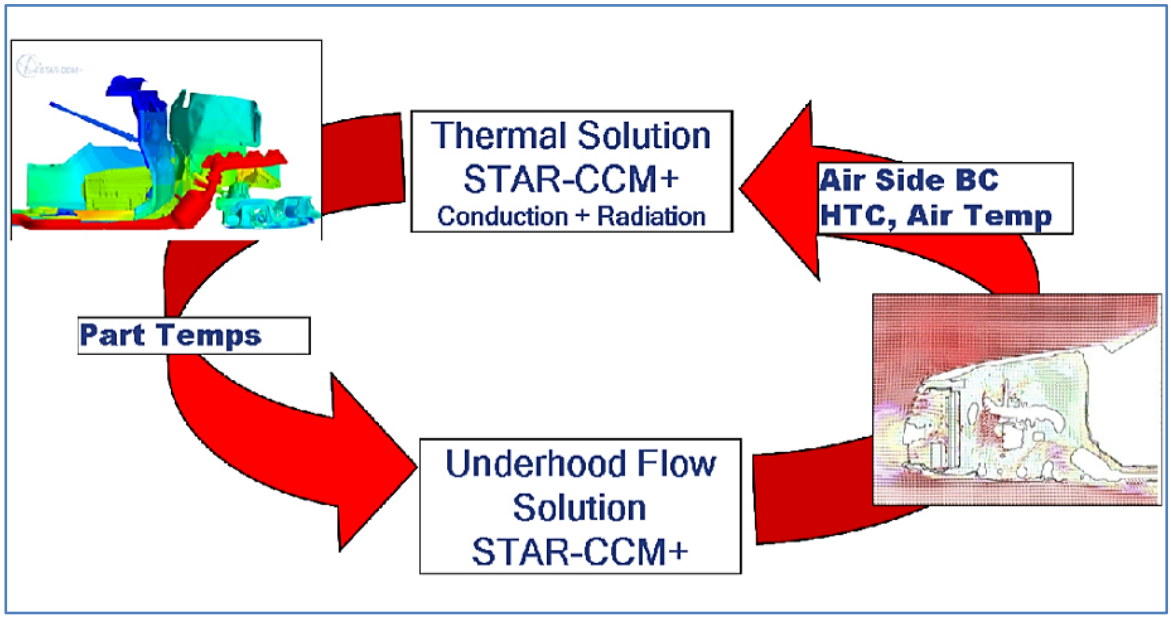

Figure 1.33 - Co-simulation process flow-chart. Data between CFD and thermal solvers are exchanged until convergence is reached. [5]

As can be seen, the CFD solver is in charge of calculating the aerodynamic parameters of the problem, as well as the convective heat exchange ones (essentially convective heat transfer coefficient h and fluid wall temperatures T for the components of interest, typically the exhaust line ones, at high temperature). Once the latter values are known, they are exported to the thermal solver in order to create a map on the model where the local temperatures and h coefficients are locally associated to each single part of the model. Then, the thermal solver calculates the remaining thermal part of the problem by considering the other heat transfer modes, namely conduction and radiation. Once the temperatures, heat transfer coefficients, heat fluxes and all the other thermal parameters of interest are evaluated, these are input again in the CFD solver for the second iteration. The CFD re-calculates the wall T and h values to be then re-input in the thermal solver, and so on, until convergence is achieved to the desired level of precision. For passenger cars applications, one or two coupled co-simulation iterations are usually performed. However, in order to achieve more accurate and reliable results, up to five or ten coupled co-simulation steps are recommended to achieve the required precision.

The possibilities offered by the combined use of the two solvers help the designers visualize aspects which cannot be otherwise identified. Consider, for instance, the maps shown in Figure 1.34: thanks to the graphical interface, the engineers are now able to see how the flow field characterizes the behavior of a given configuration and its impact on the thermal management, and by acting on the most critical areas they can optimize simultaneously both the thermal and aerodynamic issues highlighted, thus achieving the optimal trade-off in a much shorter time. The potential of the combined use of these two powerful tools is now getting clearer and clearer to the automotive designers, and the co-simulation is gradually becoming the norm for this type of analysis.

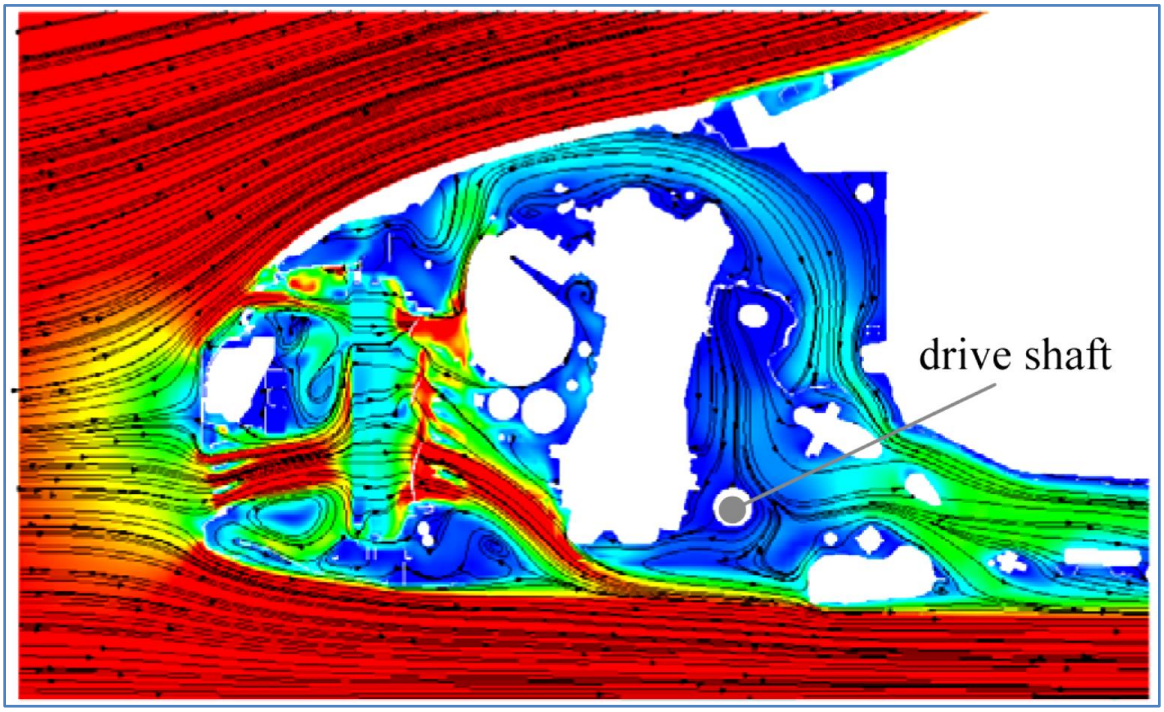

Figure 1.34 - Velocity field in the vertical mid-plane section of a vehicle. By studying the flow, it is possible to identify ways to conveniently manage the cooling airflow in the engine bay. [24]

A further development which can be expected for this procedure consists in automating it to a greater extent. In other words, while today the mapping and data exchange between CFD and thermal solvers is still to be done manually, the next step would be to develop an algorithm able to automatically accomplish this task, so as to decrease the manual pre-processing time, which corresponds to the lengthiest operation in the loop.

An interesting state-of-the-art approach currently being developed and studied only in the aerodynamic field is represented by the DOE-based optimization algorithm internally developed by some companies, including Ford. The latter, in fact, according to the SAE paper 2011-01-0169 [6], has developed an interesting process to automatically evaluate the best alternative in terms of aerodynamic behavior among different proposed configurations. This process consists of a few steps, from the creation of a preliminary surface envelope of a vehicle in the CAD environment, accurate enough to exhibit all the

relevant features, to the final evaluation of the optimal design in terms of drag. After generating the 3D model, the designer splits it into different modules, each of which represents a design factor to be analyzed.

Figure 1.35 - Modular design analysis. Each module represents a design factor in the DOE-based optimization algorithm developed at Ford. [6]

Table 1.2 - Examples of design factors for DOE-based design development. [6]

Windshield Angle	Front End Plan View Sweep	Decklid Height
Roof Height	Rear Pillar Curvature	Greenhouse taper
Tumblehome	Spoiler Length	Hood Length
Hood Height	Truck Box Plan View Taper	Side View Roof Taper
Hood Angle	Body side lateral position	Plan View Roof Taper
Rear Header Curvature	Rear Overhang	Box Cover
Tailgate Spoiler Length	Truck Box Height	Box Length
Box Width	Ride Height	Box Cover Length

After identifying the factors to act upon, different levels (i.e.: different values) are assigned to each factor, which then has a variability range constrained by different needs (esthetics, passive safety, pedestrian safety, thermal management, etc.). The combination of all the levels of each factor

identifies the entire design space defined by a matrix. Next, the morphing of the model takes place, where the different variables are mapped in the software to identify the design space.

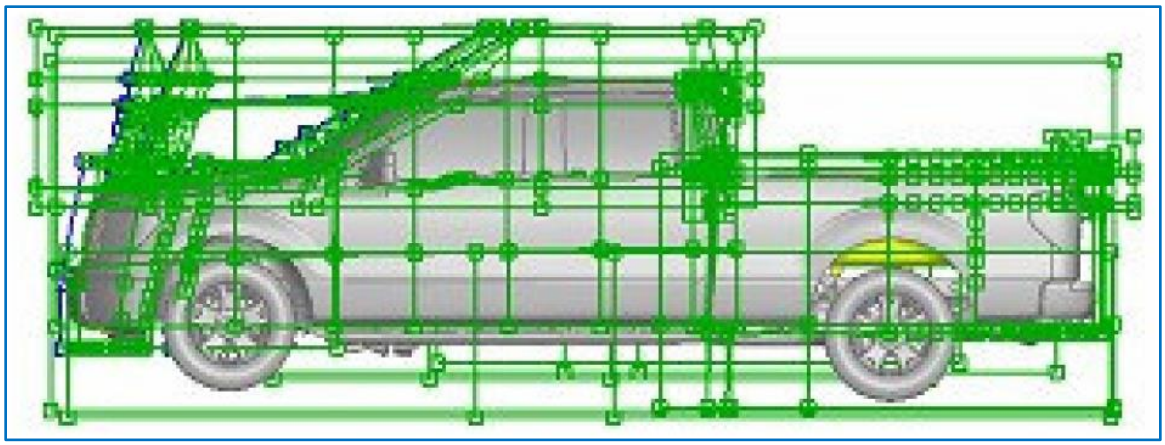

Figure 1.36 - Morphing of a virtual model to be optimized through DOE. [6]

Subsequently, the DOE method gets involved in order to minimize the correlation between different factors, to minimize the total number of simulations to be run, and to provide satisfactory data to perform a meaningful statistical analysis. Without getting too much into the mathematical and statistical aspects which go beyond the scope of this thesis, it suffices to say that the software is able to evaluate the level of dependency between factors and to minimize the correlation between them, so as reduce the design space from the original one to a much smaller one where few important factors with the highest contribution to total drag are considered within their variability range.

Based on the analysis of the factors to be studied, CFD simulations are run to cover the new, reduced design space by investigating all the corresponding aerodynamic configurations. The results of these simulations highlight the contributions of each factor to the total drag in its variability range. A sensitivity analysis can be then carried out and the Pareto principal factors can be found. Even more importantly, the solver generates a response surface which approximates the best aerodynamic configuration by connecting the various

modules in a realistic manner (e.g. by avoiding gaps or weird geometrical connections deriving from pure mathematical relations). In other words, the software is able to re-model the vehicle in such a way to get the most advantageous configuration with feasible shapes which can be manufactured. Thanks to this approach, the optimal aerodynamic configuration which minimizes the drag can be attained.

The advantages of this strategy are immediately evident to the reader: not only has the algorithm the ability to find the optimal aerodynamic design, but also it gives the designer extremely useful guidelines to understand the impact of each feature to the overall drag in its variability range. This, combined with the GUI which allows a user-friendly visualization of the results, gives the engineers a valuable tool for the aerodynamic design and optimization phase of a vehicle.

The next technological challenge would be to extend this approach to the thermal problem. In other words, the DOE-based method should not be limited just to the aerodynamic field. In order to exploit the numerical computation approach at its best the entire co-simulation should be carried out through a DOE-based approach able to give guidelines for optimization to the developers. No such evolution is currently mentioned in the literature, but this technology advancement is to be envisioned and expected in the near future thanks to the progress in terms of computing power and degree of automation. From a conceptual point of view this step is not as complex as it may seem: the differences with respect to the current approach lie in the fact that the equations involved are different, being related to the thermal aspect and not to the aerodynamic one. The implementation of those equations in the algorithm loop, however, is far from being straightforward. Analogously, the automatic mapping and exchange of data between CFD and thermal solver and the DOE design space reduction process are inherently characterized by a level of complexity

which must be properly managed in order to be fitted to the process, which requires an extensive effort for both software developers and users of the code.

1.5.3. USED CO-SIMULATION PROCEDURE

After having discussed about the ways to analyze the aero-thermal behavior of a vehicle, it is now time to highlight the actual procedure that will be used for this specific thesis work.

The virtual simulation approach has been chosen for understanding the potential benefit and drawbacks of fitting an AGS system onboard by comparing the aerodynamic and thermal performance at highway speeds and loads (details are provided later on). The co-simulation procedure selected is the one currently adopted in the Company on the FIAT side, consisting in the combined use of Star-CCM+ as a fluid solver and RadTherm as a thermal solver.

The development of this co-simulation procedure is shown below. First, a "cold" aerodynamic simulation of the model has to be run in Star-CCM+, which evaluates the main aerodynamic parameters like drag, lift and air mass flow rates of interest of the vehicle in its "cold" state, i.e. without having any temperature or thermal dissipation power assigned to any component. This is done in order to match the operating conditions of the physical wind tunnel test, where the model is not running (just the wheels are rotating on the moving belt, so as to replicate the actual road aerodynamic behavior). Second, starting from the values measured on the physical model tested in the climatic tunnel, the main thermal parameters are assigned to the aerodynamic model in the so-called "warm" Star-CCM+ simulation, including thermal power to be dissipated by the HEXes and the exhaust line skin surface temperatures. Next, the convective heat transfer coefficients and the local fluid wall temperatures calculated through Star-CCM+

are mapped on the RadTherm model. The automated procedure internally developed and currently under improvement at FIAT has been used for this purpose. In order to take full advantage of this automatic mapping and in order to use the scripts and macros developed for this purpose, the parts IDs of the Star-CCM+ and the RadTherm models must match, so that it took some time for the co-simulation set-up and pre-processing. Details about this will be provided later. After running the RadTherm simulation in order to get the new values of the thermal parameters of interest, a new warm Star-CCM+ simulation is run with the new skin surface temperatures of the components calculated by RadTherm. The new fluid h and T values are then calculated and the aero-thermal analysis of the results can be carried out.

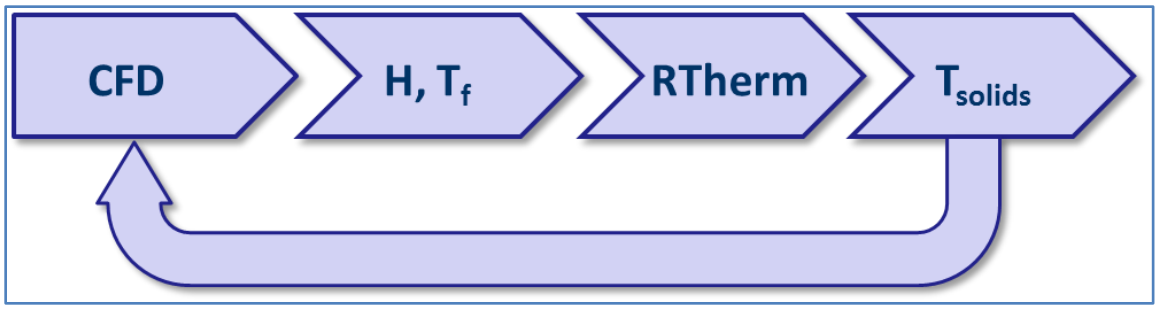

Figure 1.37 - Co-simulation flow-chart used for the aero-thermal analysis. [22]

A more detailed flow-chart with the sub-activities split-up is shown in Figure 1.38. This entire methodology has been developed over the past two years at CRF, and is getting more and more reliable and robust. In particular, the level of accuracy of the simulation thermal results compared to the measurements on the physical model is a point currently under study. The procedure used for this thesis work corresponds to the one developed in 2013, where average temperatures constant over the surface are assigned to each passive component in the mapping of the RadTherm model in steady-state analysis. In other words, average temperature values are mapped in RadTherm to passive components (i.e. not heat sources) starting from the fluid (air) temperatures in their proximity, which are previously calculated by the CFD code cell by cell for each

component. Therefore, instead of mapping a temperature distribution variable over these surfaces, just an average value is considered on the convective heat transfer side. During the last and current years, several developments and improvements have been done in order to overcome the limits of such an approach. In fact, in some cases for critical components the temperature differences between the physical tests and the simulation runs could be too high and provide no meaningful information, so that just trends can be extrapolated from the results. As a matter of fact, this procedure is still the state-of-the-art for the majority of manufacturers for this type of analysis. However, a further

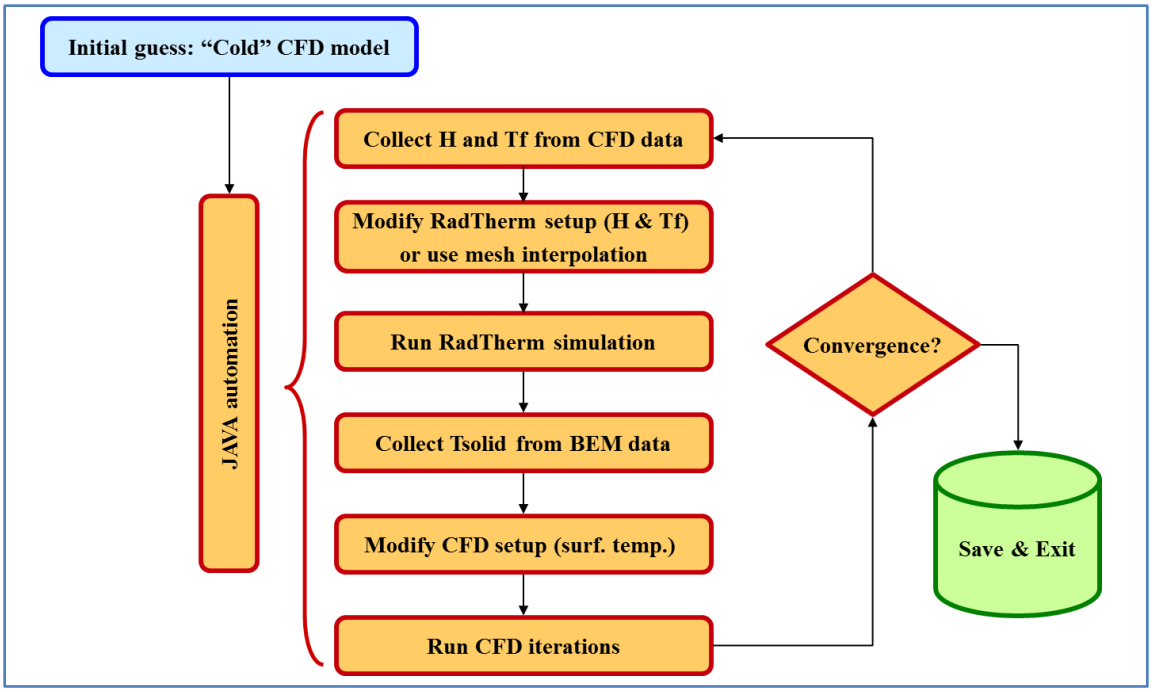

Figure 1.38 - Detailed flow-chart of the used co-simulation process. [22]

optimization of this method has already been studied (always at CRF) where not only the temperature distribution over a single components is accounted for, but also a time-history curve of the component temperature is assigned, even in the steady-state analysis. In fact, even if the testing phase to be simulated is in itself a steady-state one, some components may not reach their thermal equilibrium in that phase time-frame. Therefore, by imposing a time-evolution curve describing

the thermal behavior over time of a given part, the accuracy of the results can be substantially improved. The only drawback of such a technique lies in the fact that measurements have to be taken on the real vehicle model, so that in case of a concept development these time-evolution trends may not be available due to the absence of a physical prototype, and consequently they have to be inferred from similar models/platforms.

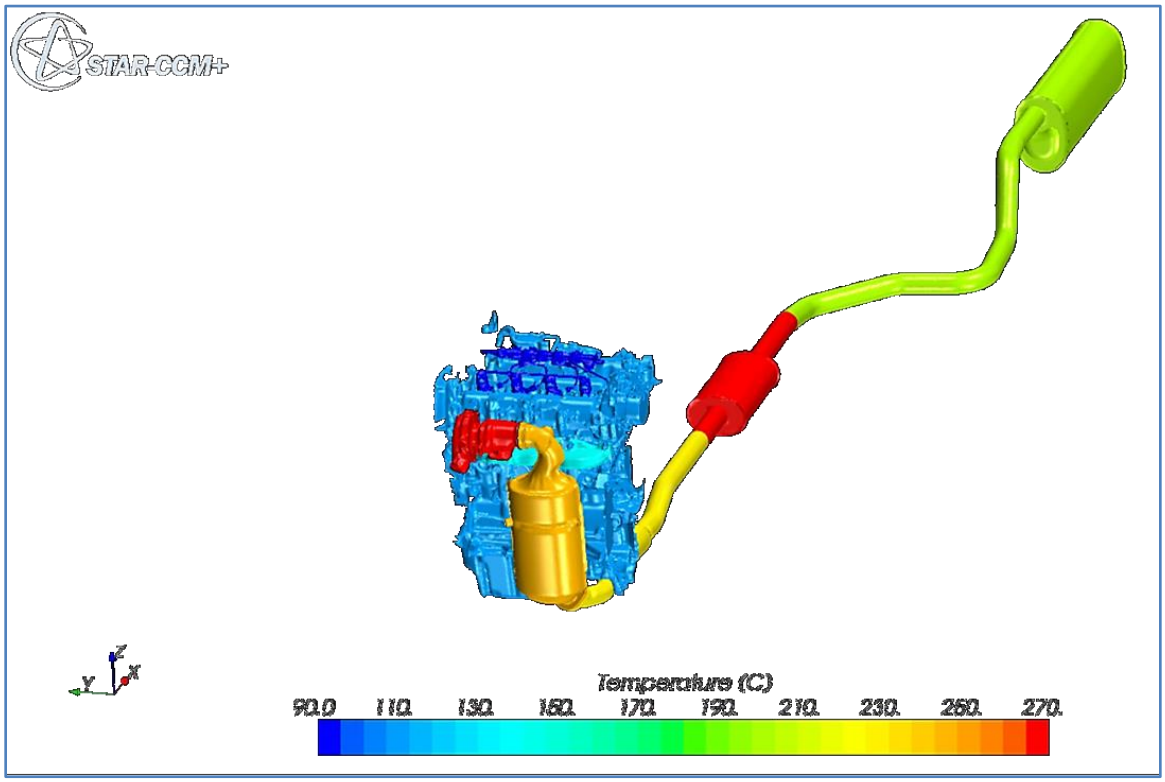

Figure 1.39 - Temperature assignment to exhaust line components (heat sources). This setup is similar to the one used in the warm simulation performed for the model under analysis. [22]

However, for this thesis work, the "traditional" approach has been chosen where constant surface temperatures are assigned to the exhaust line components. This has been dictated by the fact that the new procedure is still under extensive development and requires further validations. Additionally, no time-history evolution of the exhaust line of the specific model under study was readily available, so that average and constant values over the passive components surfaces were imposed. Finally, the time required to implement this

methodology for this thesis work was too high compared to the time frame allowed by the program, so that it was chosen to adopt the current procedure and to focus not just on the improvement of the process but especially on the optimization of the vehicle. Being the procedure new to Chrysler, however, this work aimed also at extending and offering an overview of this procedure to the US-Canada aero-thermal group, as part of the harmonization process taking place in the newly established FCA group.

1.6. RESEARCH DEVELOPMENT AND THESIS ORGANIZATION

After reviewing the current and state-of-the-art technologies involved in the aero-thermal design and development of a passenger vehicle, it is now possible to focus on the analysis of the specific model which is the object of this thesis work. Before getting into the technicalities, here is a brief overview of how the research has been organized and how the thesis work is structured.

The FIAT 500L 1.4 MultiAir NAFTA version MY 2014 has been chosen by the Company as the vehicle to work on. Due to resources and time constraints, the research work has been limited to the analysis of the aero-thermal impact of one device only, the AGS system. Due to the fact that several simulations had to be performed for each configuration and that this type of analysis had not been performed for the baseline model, it was chosen to limit the study to two cases only: a baseline version, which simulates a fully-open shutter system, and a fully-closed AGS configuration. This was dictated by the resources and time constraints imposed by this project work, as well as by the fact that two different computational solvers were to be learnt by the author, which required a significant amount of time in order to master the programs. Also, the need to perform a meaningful comparison between different configurations constrained

the analysis to be focused on a device whose effect at a given speed and load, in the specific test phase of interest, did not affect (either positively or negatively) the performances at different operating conditions. Therefore, even though several potential improvements were suggested based on the results of the aero-thermal analysis of the baseline version, only the AGS system was studied. By so doing, it was possible to directly compare the aero-thermal results at high speed without concerning about the low speed or idle behavior, as the AGS is fully-open in the latter conditions. In fact, when the vehicle is still or at low speed, the AGS blades are fully open, so that the effect of the presence of the system is negligible from an aero-thermal viewpoint, and the vehicle can be treated as the baseline model without AGS. In this way, it is possible to focus just on a high-speed-conditions analysis since the effect of the AGS does not affect in a meaningful way the low-speed, idle or heat-stroke conditions thermal performances.

For each configuration, hereafter referred to as "baseline" and "modified", three different numerical simulations had to be performed. First, a "cold" CFD simulation was run on each model, to evaluate the aerodynamic performances of the vehicle in a manner consistent to what is done in the wind tunnel tests (details are provided later). Then, a thermal power to be dissipated by the heat exchangers in the engine bay and the external skin temperatures of the exhaust line were imposed to the CFD model in order to perform a "warm" CFD simulation, where the thermal convection parameters are accounted for. The air temperature in this simulation was taken equal to the one in the corresponding physical test procedure, so as to replicate the same operating conditions. The values obtained from this simulation were then exported to the thermal solver RadTherm through a macro developed at CRF and used to map the thermal model. Afterwards, the coupled aero-thermal simulation was run and the final aerodynamic and thermal parameters were computed. Following each

simulation, the analysis of the obtained results was carried out that will be shown in the next sections, whose details are provided in the following.

Chapter 2 focuses on the aerodynamic performances of both the baseline and modified versions of the vehicle. It is organized in such a way that a direct analysis is carried out in parallel on both the production model and the version equipped with the fully closed AGS system by focusing on the same parameters each time. Based on the results of the simulations, a comparison between the two configurations is provided in order to highlight the differences in terms of aerodynamic performances.

Chapter 3 is structured in a similar way, with the only exception that it deals with the thermal side of the research. More specifically, the thermal management aspects are considered, which show the thermal behavior of the main components in the engine bay and on the exhaust line for both the baseline and the modified versions. In such a way it is possible to highlight critical areas and quantify the deterioration of thermal performances deriving from the adoption of the AGS system.

Chapter 4 includes few final recommendations deriving from the analysis for a successful implementation of this technology into the production model.

Finally, Chapter 5 includes all the references used as part of the literature review to get familiar with the issues faced when dealing with this type of problem and analyses in the automotive sector.

According to the laws of aerodynamics, the bumblebee can't fly, but the bumblebee doesn't know the laws of aerodynamics, so it goes ahead and flies.

Igor Ivanovich Sikorsky

2. CHAPTER 2

AERODYNAMIC ANALYSIS

2.1. CAR VIRTUAL MODEL – GEOMETRY DESCRIPTION

As already mentioned in the introduction, the vehicle model under analysis is the FIAT 500L NAFTA version MY 2014, which is the latest release of the car for the North America market. It is equipped with a 1.4L, 4-cylinder, 16 valves MultiAir in-line engine with peak power equal to 160 hp @ 5,500 rpm and a peak torque of 250 Nm @ 2,500 rpm. The geometrical description of the vehicle model in the virtual environment is developed with ANSA in FIAT. In other words, an ANSA model representation of the vehicle is used to describe its geometrical features in the CAD environment. This model is the used for several purposes, including aerodynamics (both external and internal), thermal management and structural analysis. The ANSA CAD model was then exported in a format importable in Star-CCM+ (version: 8.06.007) and in RadTherm (version 11.1.0) in order to perform the aero-thermal simulations. The following paragraphs highlight the model features in terms of exterior bodywork and underhood packaging, and show the corresponding Star-CCM+ and RadTherm meshes.

2.1.1. EXTERIOR BODYWORK

Figure 2.1 shows the geometrical description of the vehicle under analysis. As it can be seen, the virtual model replicates all the features of the real physical model, with the only exception of the interiors. Specifically, the model is built for the specific purpose of performing an external aerodynamic analysis and a

thermal analysis focused on the engine bay and exhaust line, so that all the interiors (the cockpit area) is not strictly required. This allows a huge saving of computing time and power by considerably reducing the size of the mesh. For the model under analysis, the overall surface mesh size is over 219 million elements, subdivided as follows in the different regions:

- Condenser: 1,054,910 faces
- Intercooler: 168,472 faces
- Radiator: 764,999 faces
- Region 1 (rest of vehicle and wind tunnel): 217,184,649 faces

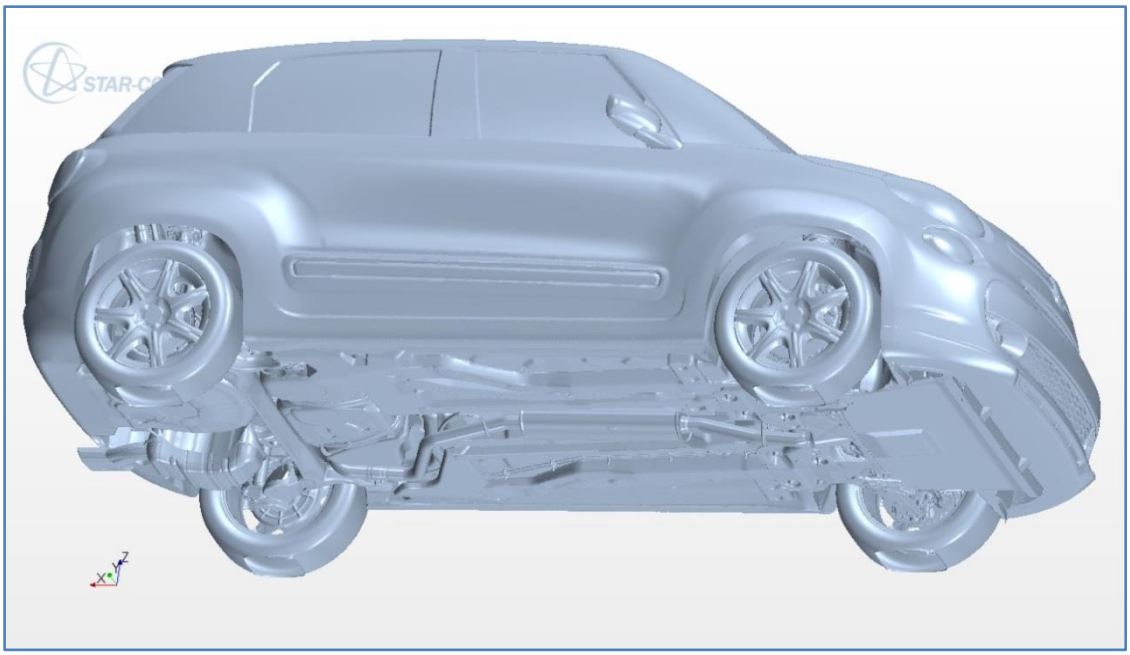

Figure 2.1 - FIAT 500L NAFTA MY 2014 virtual model in Star-CCM+ environment. The picture shows a discretized volume mesh of the model with around 44 million volume cells.

As for the discretized volume space, the volume mesh size corresponds to approximately 44 million cells, subdivided as follows in the different regions:

- Condenser: 368,270 cells
- Intercooler: 58,445 cells
- Radiator: 265,719 cells
- Region 1 (rest of vehicle and wind tunnel): 42,930,536 cells

The need to have different, separated regions for the cooling system heat exchangers derives from the different characteristics to be assigned to them. In particular, they are defined as "porous" regions, where air can pass through but a certain resistance to motion is present due to both inertia and viscous forces which are different from the ones in free-stream conditions or within other areas of the vehicle. In order to replicate the effect of these resistances on the model, some values experimentally measured on the baseline version were assigned to the resistances in the three main directions.

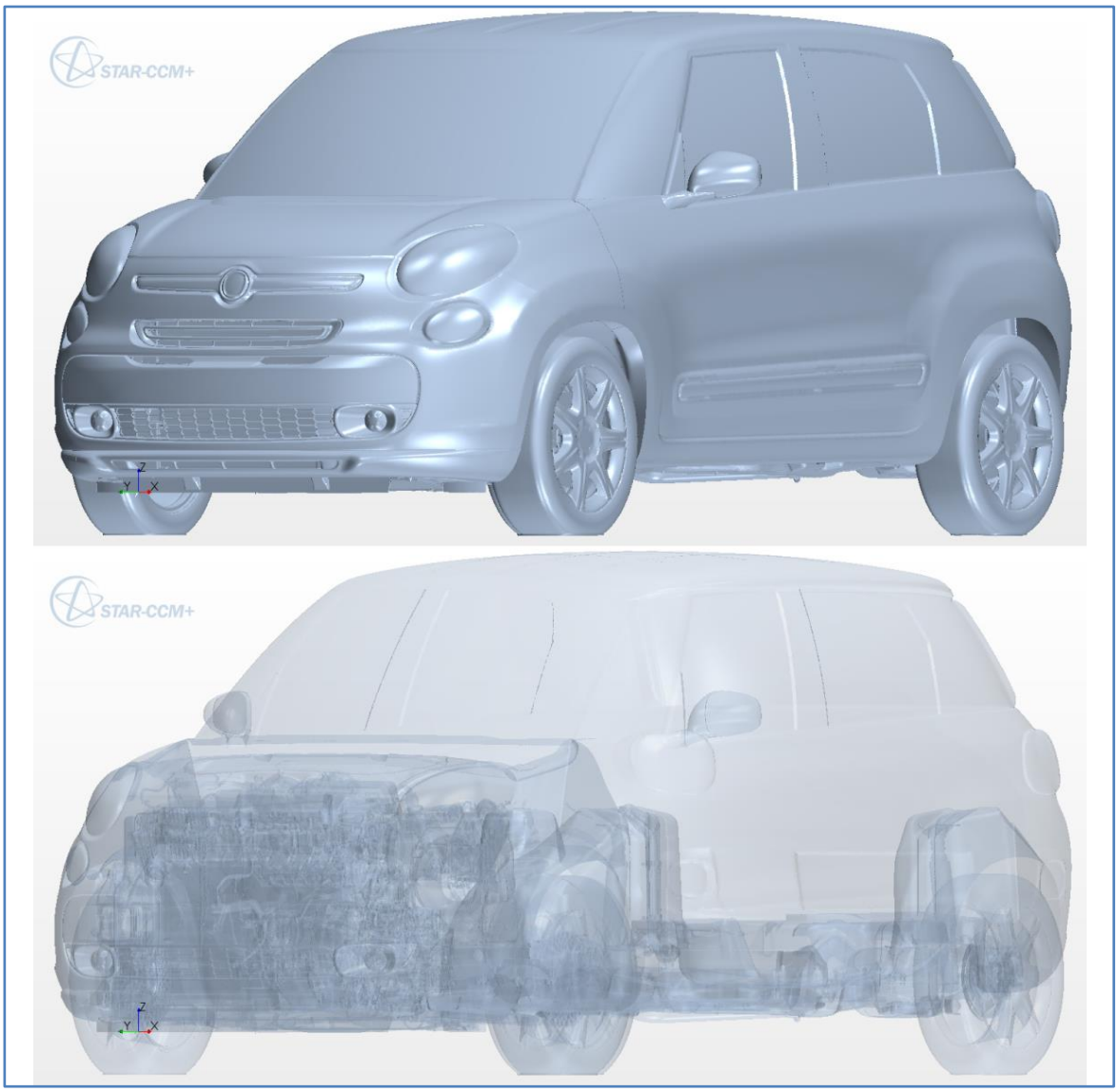

Figure 2.2 - Other views of the CFD model. Notice the accuracy of details in the underhood and on the exhaust line.

Other views of the CFD model are shown in Appendix C. The following figures highlight the volume mesh of the model. A polyhedral volume mesh is used to discretize the volume and allow the solver computing the fluid equations cell by cell. An extruded prism layer is used in the code to replicate the boundary layer over the various surfaces. Since only constant thickness can be imposed in the commercial code used, different thicknesses have to be imposed to the different components of the model, as can be seen from the pictures below. The imposed values derive from experimental measurements collected in the wind tunnel so as to replicate in the best possible way the flow conditions in the CFD environment.

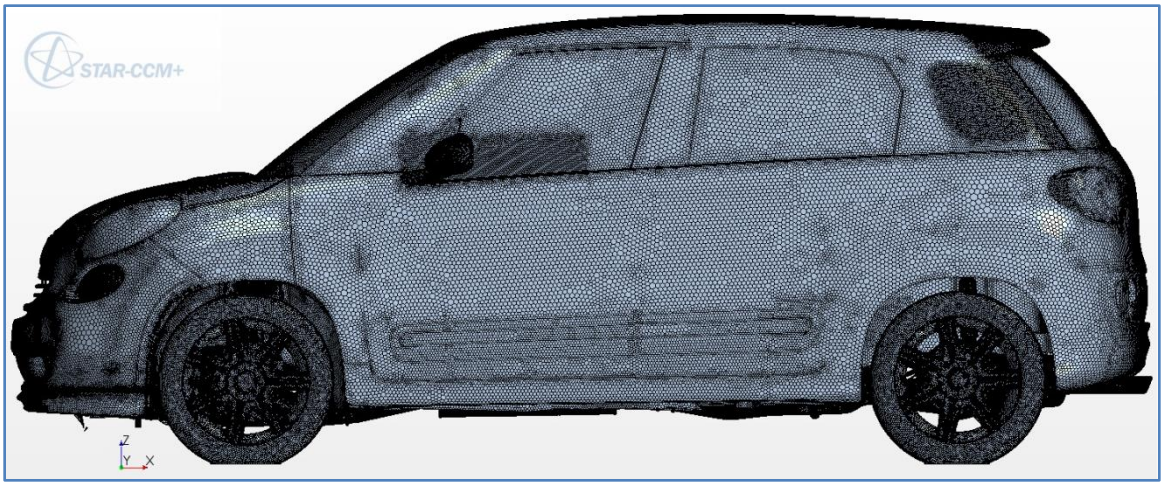

Figure 2.3 - Volume mesh of the CFD model, vehicle exteriors.

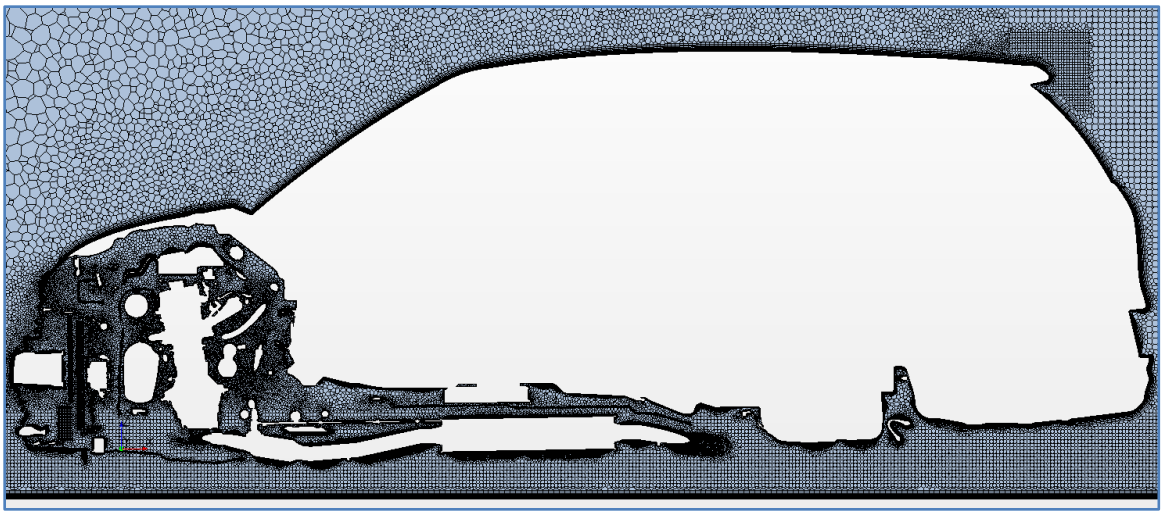

Figure 2.4 - Volume mesh of the space surrounding the vehicle and the engine bay (XZ mid-plane, with coordinates y=0). Notice the prism layer extrusion representing the boundary layer.

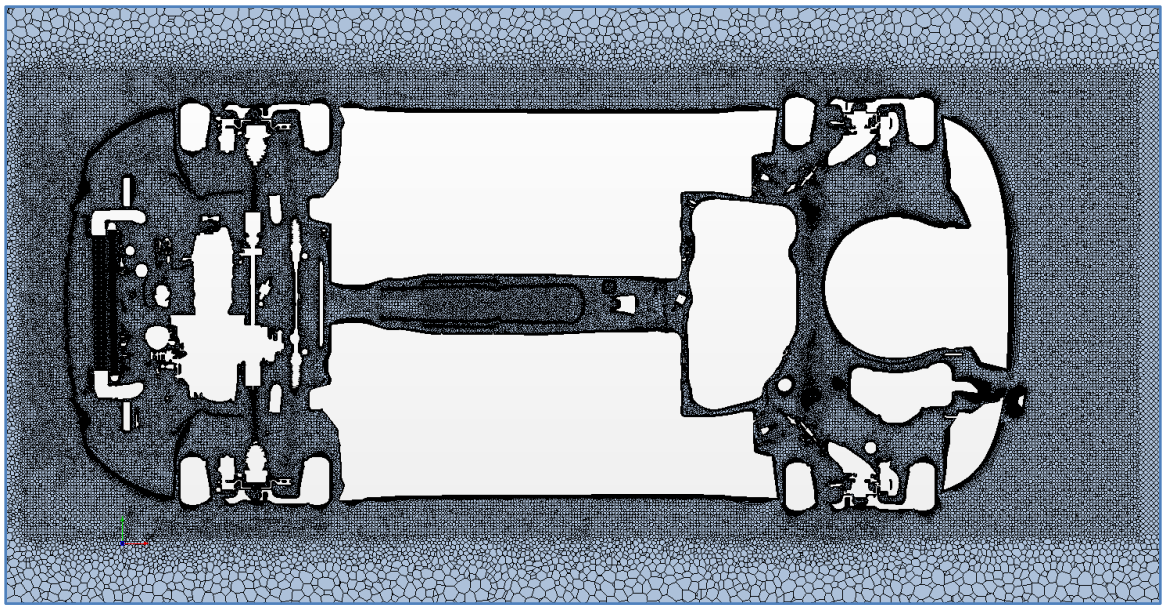

Figure 2.5 - Volume mesh of the space surrounding the vehicle and the engine bay (XY section plane, with coordinates z=0). Again, notice the prism layer extrusion representing the boundary layer.

As can be seen in Figure 2.6, all the components where a higher accuracy is required to properly describe the flow conditions are characterized by a very fine mesh, much finer than the one where less details are present or required, like, for instance, the external body shell. This allows getting a more accurate and precise mapping of the flow field characteristics and, in turn, better results matching with the experimental tests.

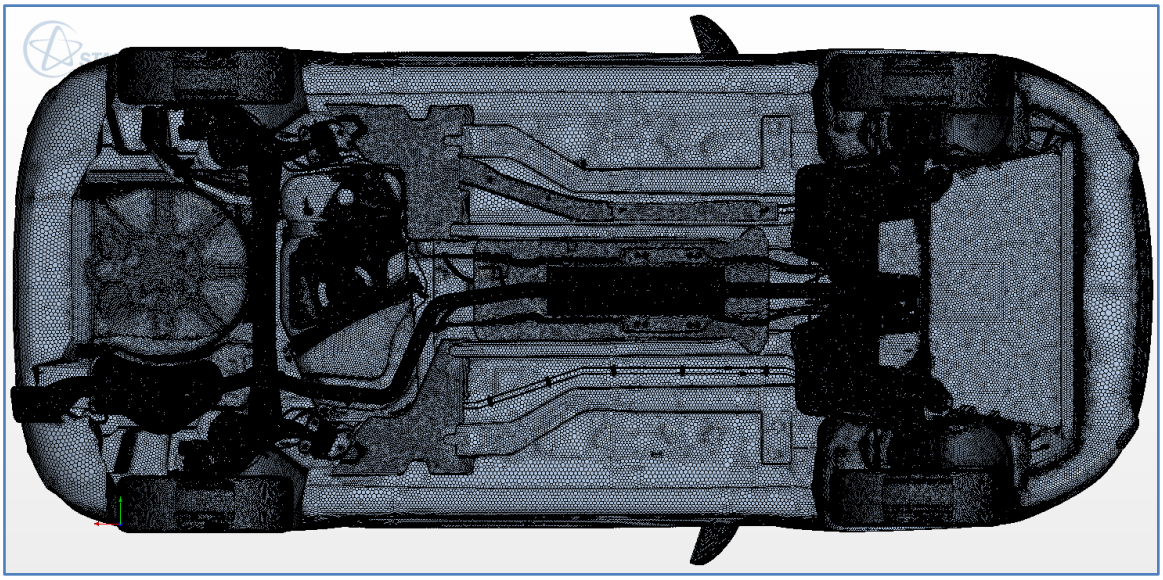

Figure 2.6 - Volume mesh of the underbody. Notice how fine is the mesh on the components of interest from the aero-thermal viewpoint.

Other pictures of the volume mesh of the CFD model are reported in Appendix D. It is interesting to highlight how fine is the mesh of the front grilles, which is an area of extreme interest for this thesis purposes. In fact, this is the location where the design modification will take place, therefore in order to catch the variation in aerodynamic performance in a meaningful way, it is crucial to have a high level of detailing.

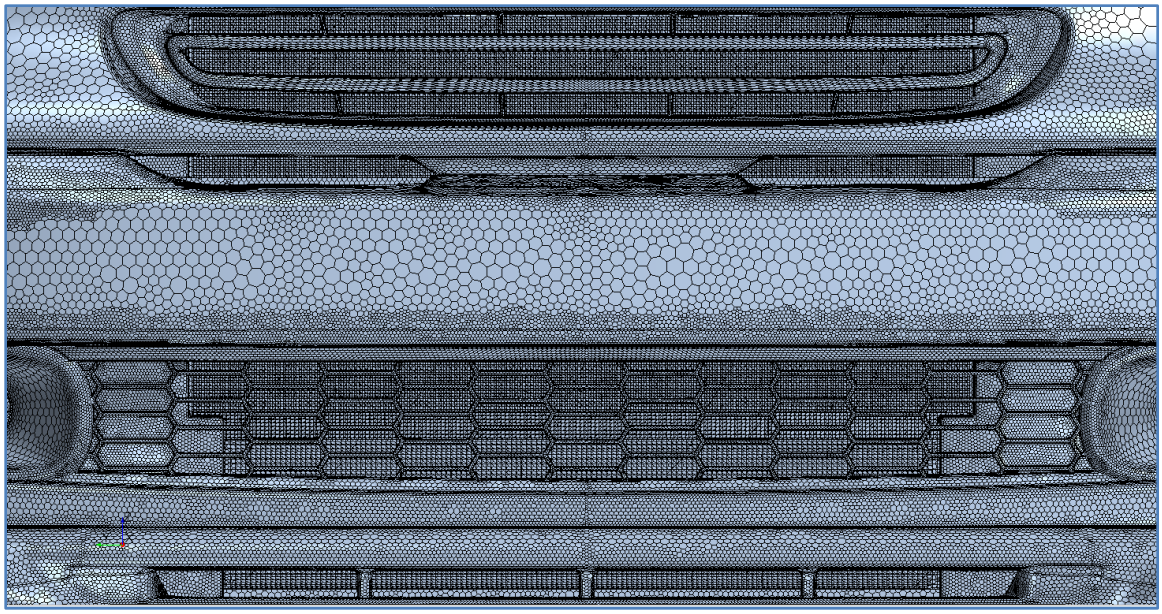

Figure 2.7 - Volume mesh detail of the front end. It is possible to see the meshed HEXes behind the inlet grilles.

2.1.2. UNDERHOOD PACKAGING

The engine bay represents the main focus of this thesis. This is the area where the design changes mostly affect the performances in terms of both aerodynamic and thermal behavior. Consequently, the level of detailing is very high, as will be shown later. The following pictures show the underhood packaging of the FIAT 500L NAFTA version MY 2014. The virtual model replicates the real model features. As can be seen, the engine bay area is extremely compact due to the overall vehicle dimensions, dictated by its mission.

Therefore, the packaging of the engine bay components ix extremely dense and the available room for design modification is quite limited. However, a preliminary feasibility analysis showed that enough room for fitting an AGS system is available just behind the central main grille, labeled as "*Region 1: STY_centralGrilleLower_ts_I*" in the virtual model.

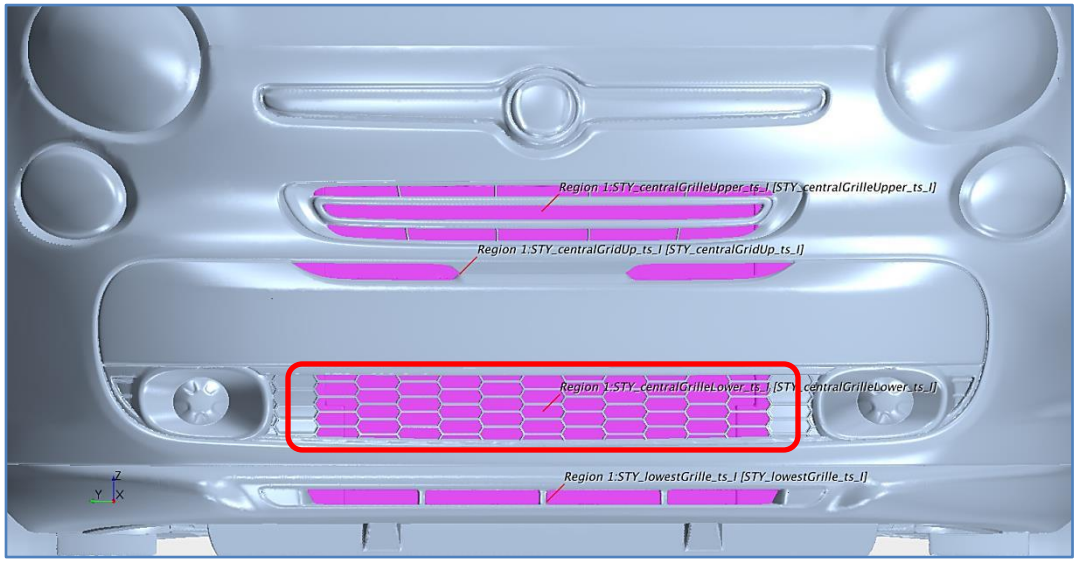

Figure 2.8 - Front inlets to the engine bay. The main central grille is the one which will be shuttered by the AGS at speed.

The following figures display the packaging of the underhood area, showing how the various sub-groups are positioned and their relative components.

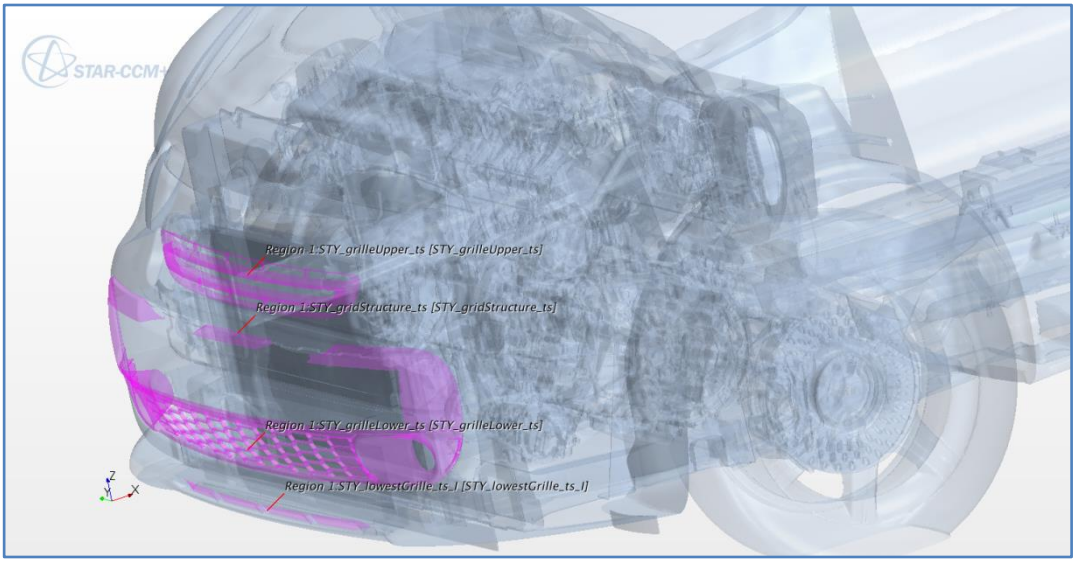

Figure 2.9 - Front grilles, highlighting the cooling air inlets.

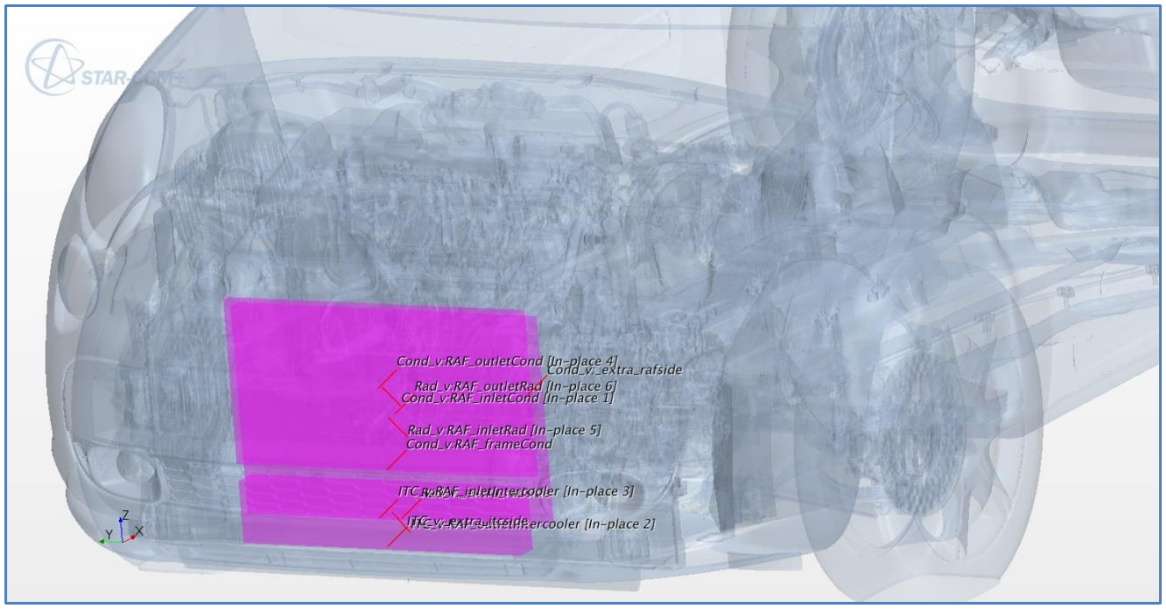

Figure 2.10 - Cooling system HEXes. RAD: radiator; COND: A/C condenser; ITC: intercooler.

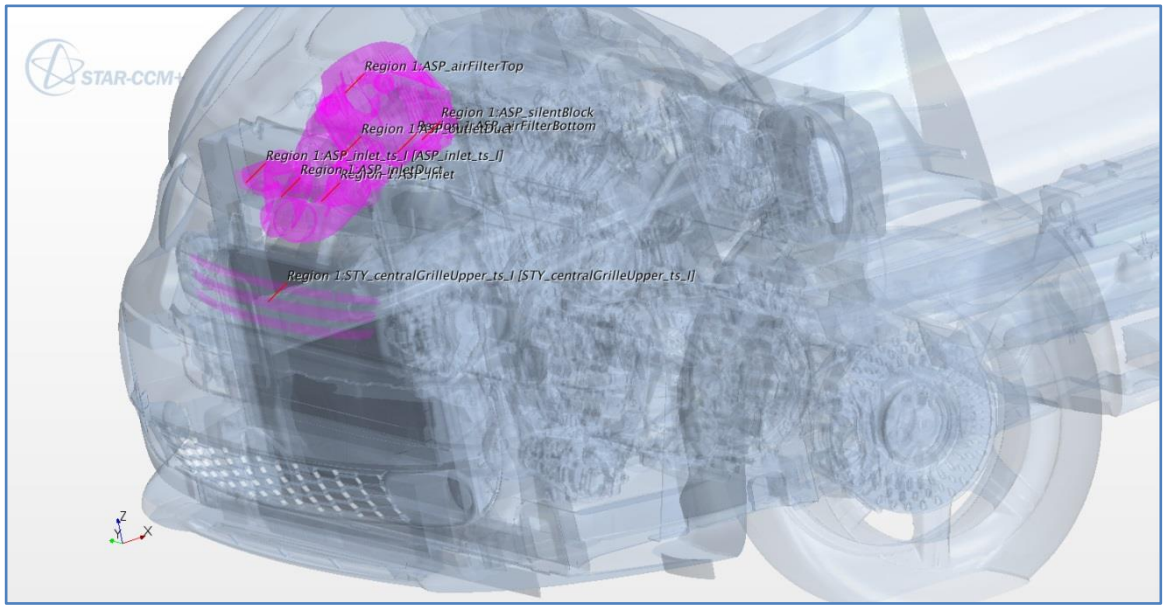

Figure 2.11 - Engine air inlet. Notice the unfavourable positioning with respect to the inlet opening.

Figure 2.11 shows the unfavorable positioning of the air scope in the underhood sucking the air necessary for the ICE operation. As can be seen, the engine air inlet is located above the cooling module conveyor which seals the area between the inlets and the cooling system HEXes in order to maximize the flow to the exchangers. This has a detrimental effect on the engine performances, however due to packaging constraints it was chosen to position this component

in such a way, thus achieving a necessary though difficult trade-off between conflicting requirements.

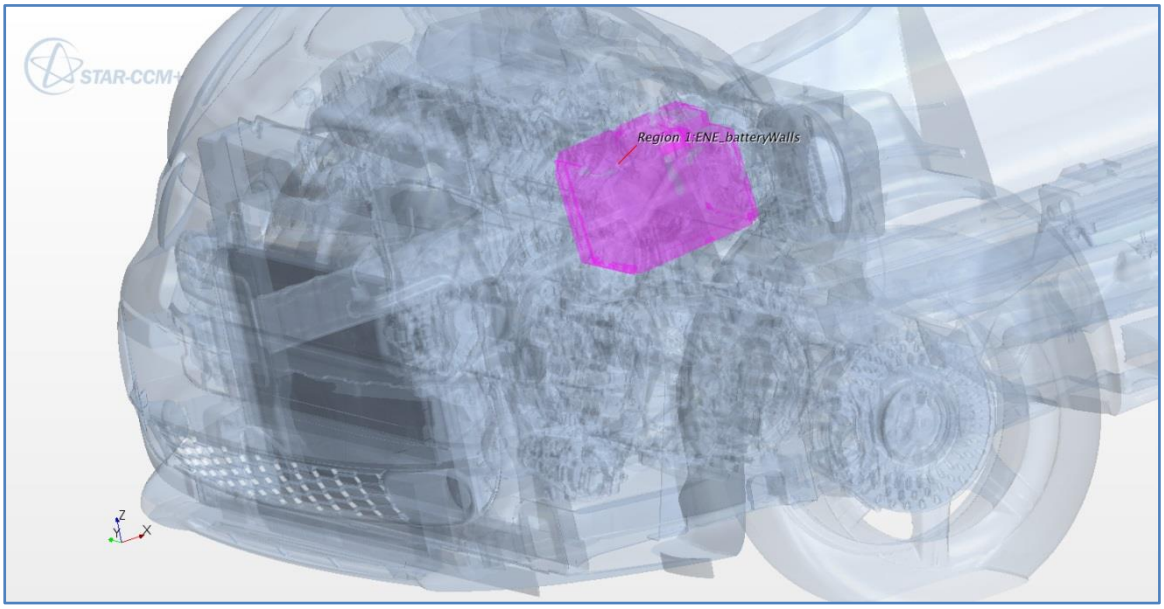

Figure 2.12 - Battery position in the engine bay.

Figure 2.13 - Engine positioning in the underhood.

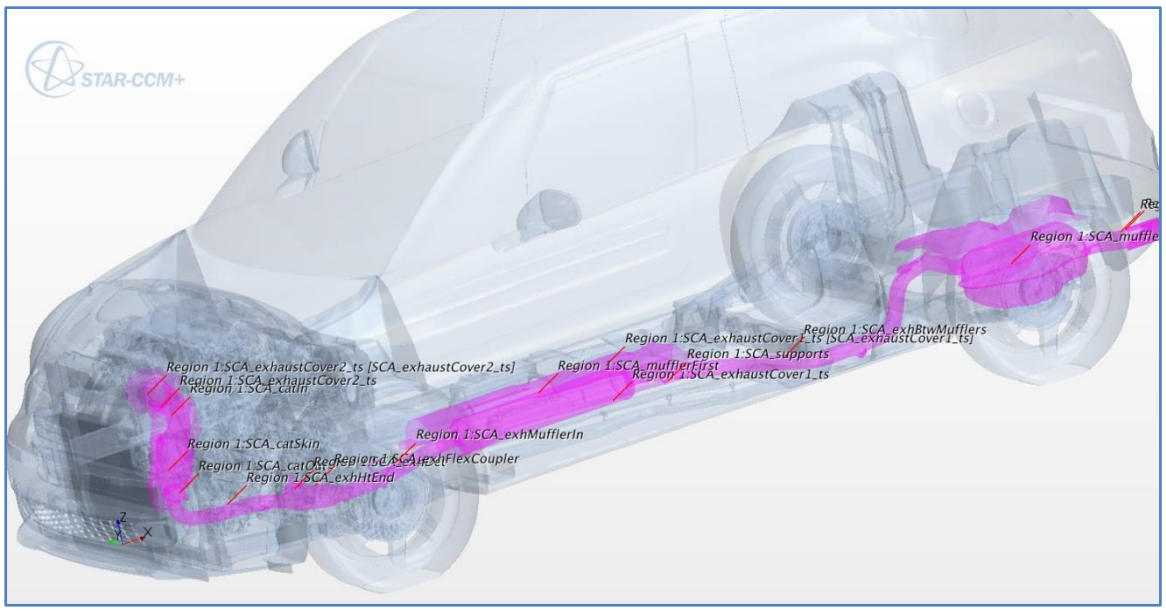

Figure 2.15 - Exhaust line. Surface temperatures will be assigned to its component as heat sources in the warm CFD simulation.

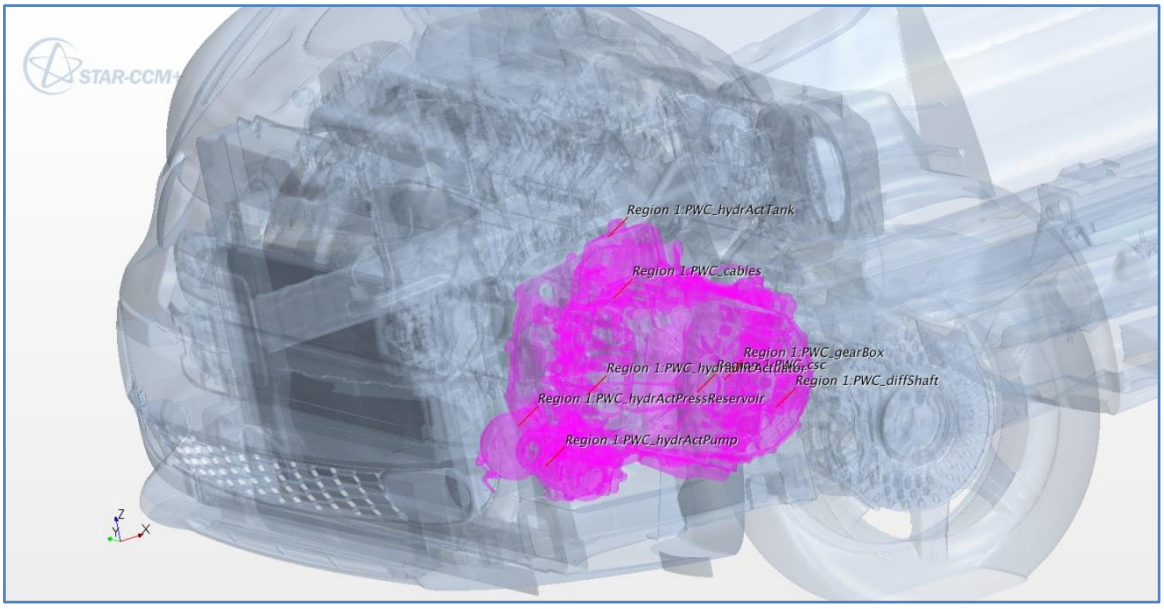

Figure 2.14 - Gearbox location in the engine bay.

As can be seen, only the main subgroups are highlighted in order to understand the engine bay layout and the relative positioning between them. The total number of parts in the CFD model is 352, grouped in 4 regions and 19 main sub-groups (e.g.: PWM for engine components, STY for aesthetic body parts, RAF for cooling system components, etc.).

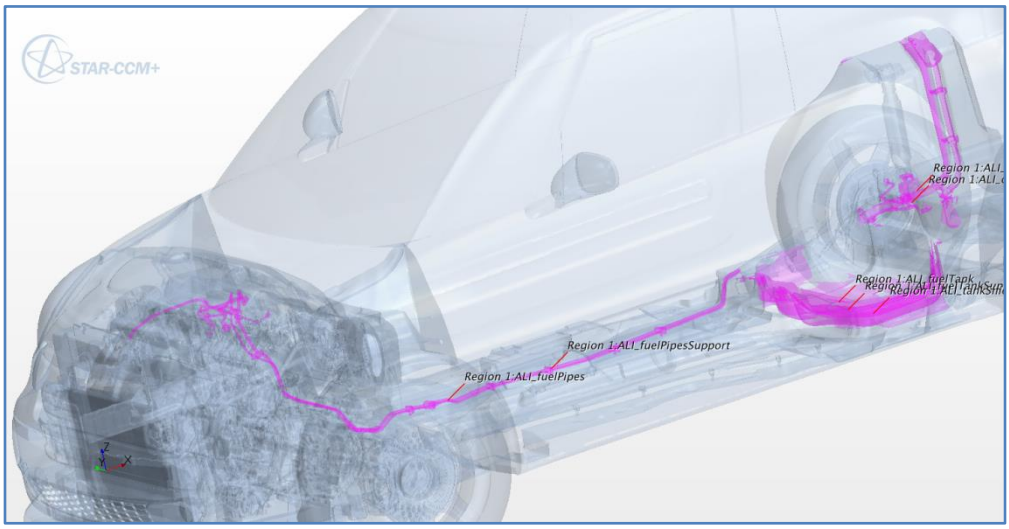

Figure 2.16 - Fuel line from filler cap to engine inlet.

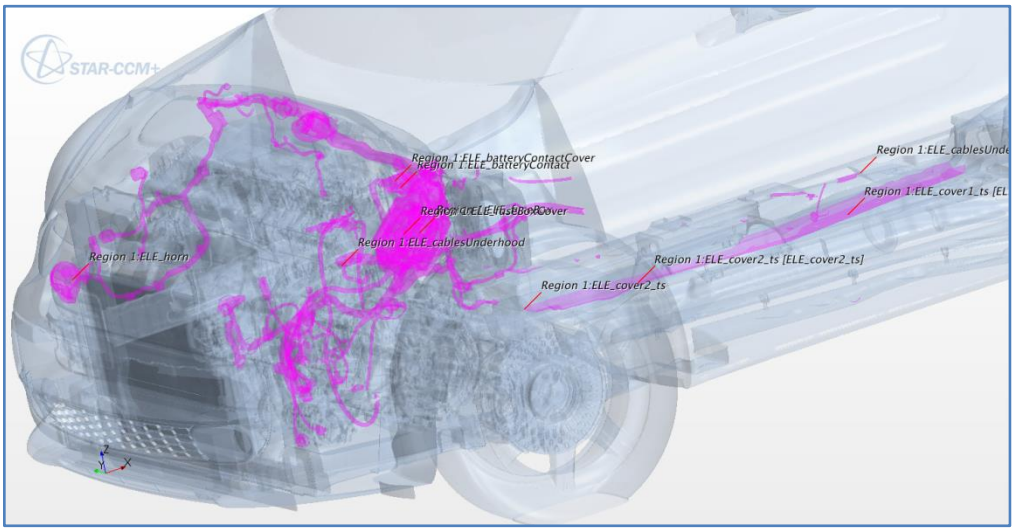

Figure 2.17 - Electrical system components.

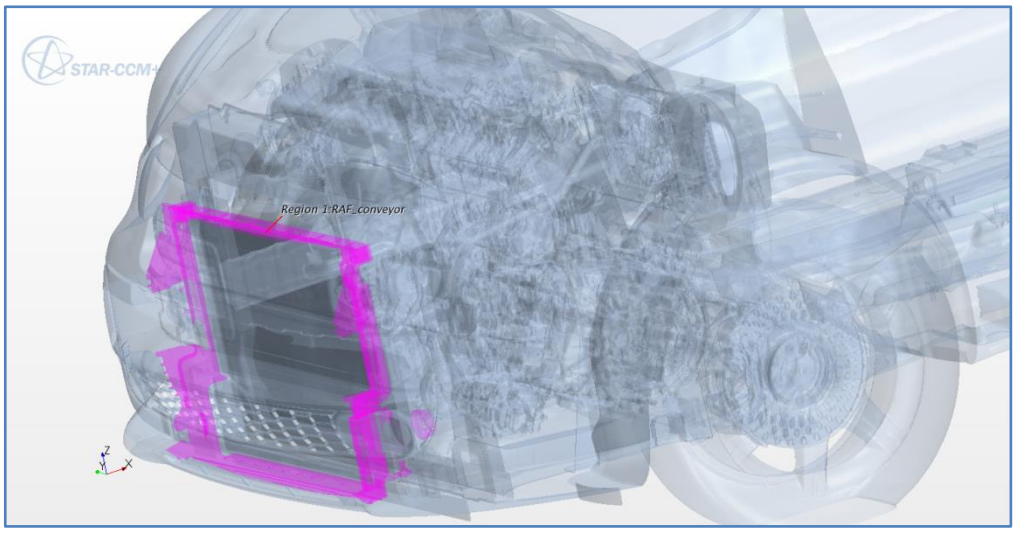

Figure 2.18 - Cooling module conveyor.

As can be seen in Figure 2.18, a cooling module conveyor is present in order to minimize the leakages and direct the (theoretically) entire incoming cooling air mass flow rate to the HEXes. Unfortunately, leakages and pressure losses are always present, but this fairly simple system allows minimizing such losses thus improving the overall thermal performances of the system.

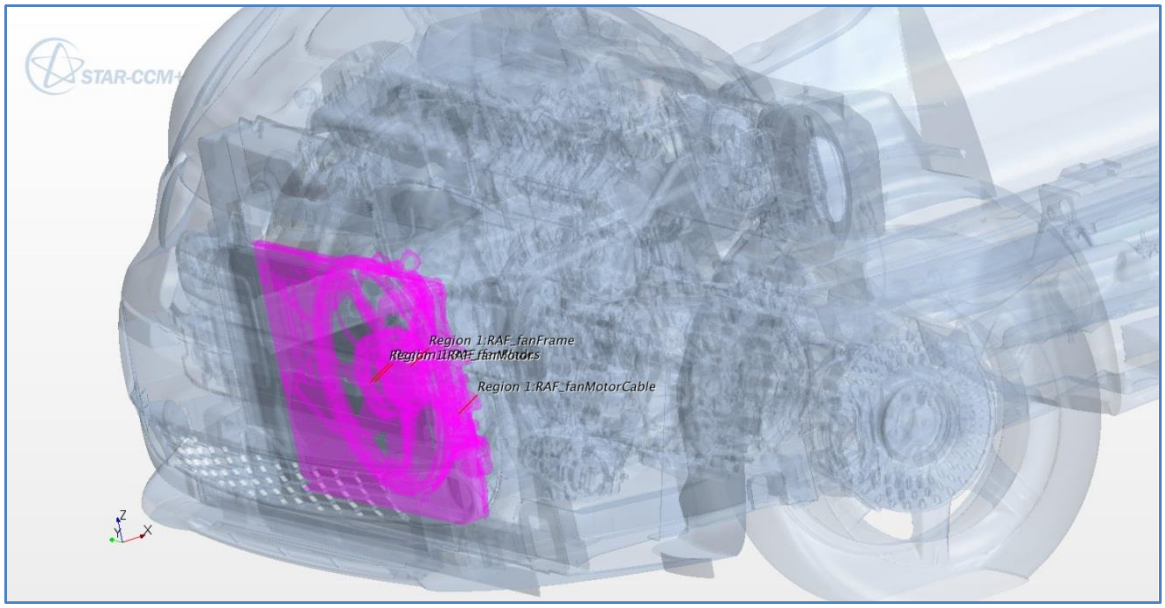

Figure 2.19 - Fan and relative frame positioning in the engine bay.

As a final remark, it must be said that the AGS system in its fully closed position was modelled in the virtual environment as an "ideal" closure, perfectly sealing the entire main central grille. This was done by simply converting the control surface *STY_centralGrilleLower_ts_l* into a baffle interface in Star-CCM+. This strategy, though being a fairly significant approximation, is nonetheless extremely fast in order to understand the impact of such system on the aero-thermal performances on a preliminary design stage basis, thus allowing deciding whether it is worthy carrying on with the system design or resorting to alternative solutions less detrimental in terms of thermal behavior. Therefore, the improvement in terms of aerodynamic performances evaluated through this CFD simulation were higher than in the real case, since in the real physical system

effects like leakages and pressure losses diminish the overall drag improvement guaranteed by the AGS.

After considering the underhood packaging of the model, it is now possible to consider the flow field around the vehicle, especially focusing on the underhood area, which is the one mostly affected by the design changes under analysis. The following paragraph shows the results of both the baseline and modified versions and compares them to each other in order to identify the differences and quantify the variation of the involved aerodynamic parameters.

2.2. CFD SIMULATION

2.2.1. TESTING CONDITIONS

Before getting into the details of the simulation, it is necessary to specify the testing conditions under which the aerodynamic measurements were taken. The wind speed was set equal to 38.9 m/s (140 km/h). The 1:1 scale production vehicle was positioned on a fixed-ground scale (i.e. with no moving belt) and the measurements were taken with engine off and rotating wheels (on drums). The experimental setup is similar to the one shown in Figure 2.20. These conditions were replicated in the CFD case and the boundary layers were included not just on the vehicle parts, but also over the wind tunnel walls. This allows a proper data correlation between the simulated and experimentally measured results.

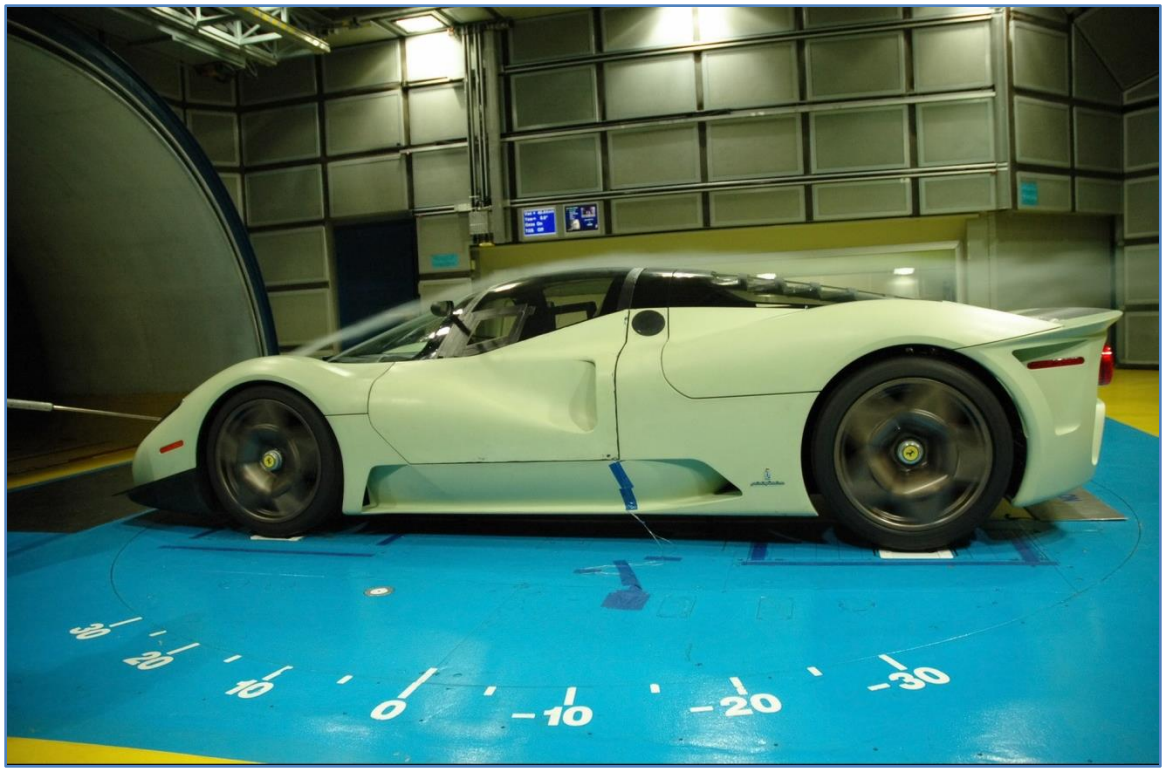

Figure 2.20 - Typical wind tunnel experimental setup. Also in the case under study the wheels were rotating on drums. [23]

2.2.2. CONVERGENCE PLOTS

Convergence plots represent the history of the various iterations necessary for a numerical solver to reach the final, converged solution of a problem. In this case, the commercial code used calculates cell by cell the average values of the required parameters of interest by approximating better and better, iteration after iteration the basic laws of fluid dynamics, namely conservation of mass, momentum and energy. The final solution, i.e. the one obtained when no meaningful variation between several subsequent iterations is appreciable, is the so called "converged" solution of the case. At this point, various aerodynamic parameters of interest can be studied and flow field maps can be collected on the GUI.

Following are some of the convergence plots created to evaluate convergence. They include residuals, Cx, Cz, and pressures over the inlet and outlet faces of the HEXes. As can be seen, all of them reached stable, converged values after approximately 3,000 iterations. However, in order to properly estimate average values so as to minimize the effect of minor oscillations in the convergence process, it was chosen to stop the computation at 4,000 iterations, and to average the results over the last 1,000 iterations. This procedure is very fast and straightforward to be applied, and it is the one currently adopted in the Company. Other convergence criteria may be applied based on other considerations, like, for instance, a given variation in the results between n consecutive iterations. However, the final goal is the same, i.e. to have results as stable as possible without requiring extremely long computational time and power. For the specific case under analysis, 48 CPUs were used in parallel for each simulation, and this allowed reaching convergence within one day.

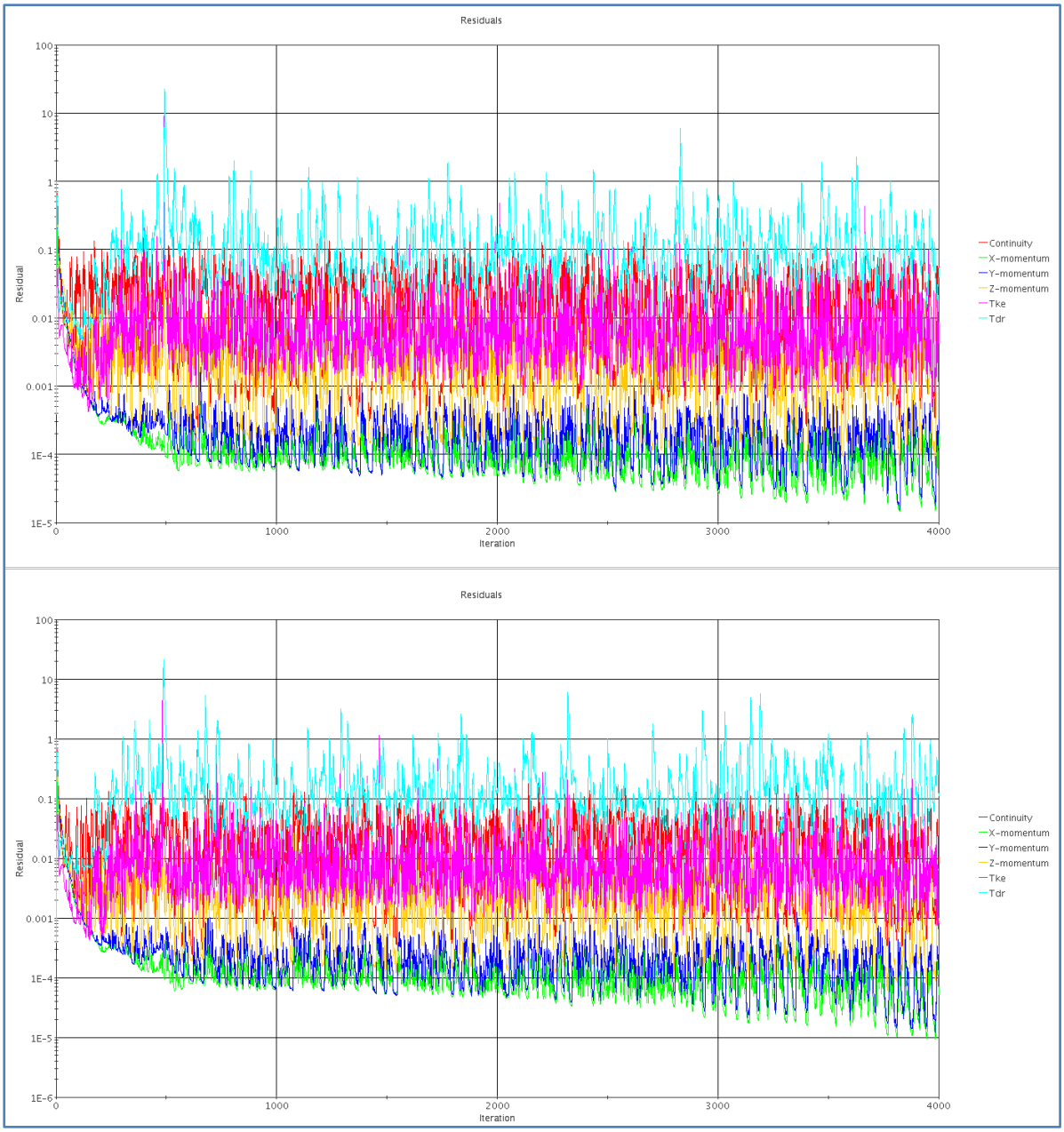

Figure 2.21 - CFD simulation residuals plot. Top: baseline version; bottom: modified version.

As can be seen in the above plots, the residuals show an oscillating behavior over the several iterations performed. This trend is normal and expected, as long as the values oscillate below unity and remain within stable variability ranges. These values represent simulation parameters related to the basic laws of fluid dynamics involved in the computation, and their primary function is to monitor the evolution of the simulations.

Figure 2.22 shows the drag coefficient evolution for both the baseline and modified models. Here the convergence is much more evident, and the oscillations are extremely small.

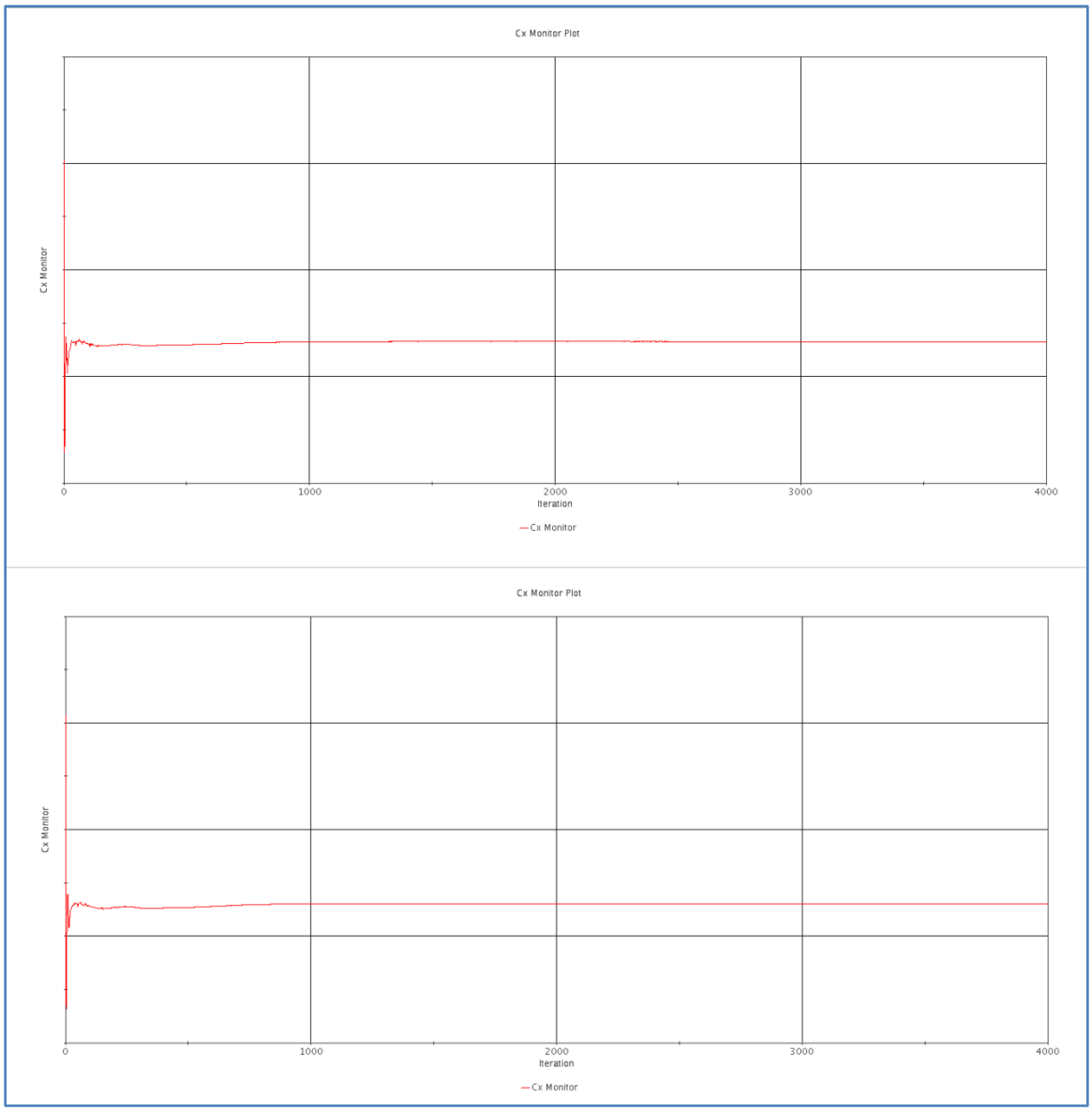

Figure 2.22 - Drag coefficient convergence plots for the baseline (top) and modified (bottom) models. The ordinate axis values are hidden for confidentiality reasons.

Figure 2.23 shows the convergence plot for the mass flow rates of incoming cooling air through the various front grilles (refer to Figure 2.8 for the corresponding PIDs). As will be discussed later, the results match the original

expectations, with the most part of the flow crossing the main central and upper inlets for the baseline case and mostly the upper inlet for the modified version.

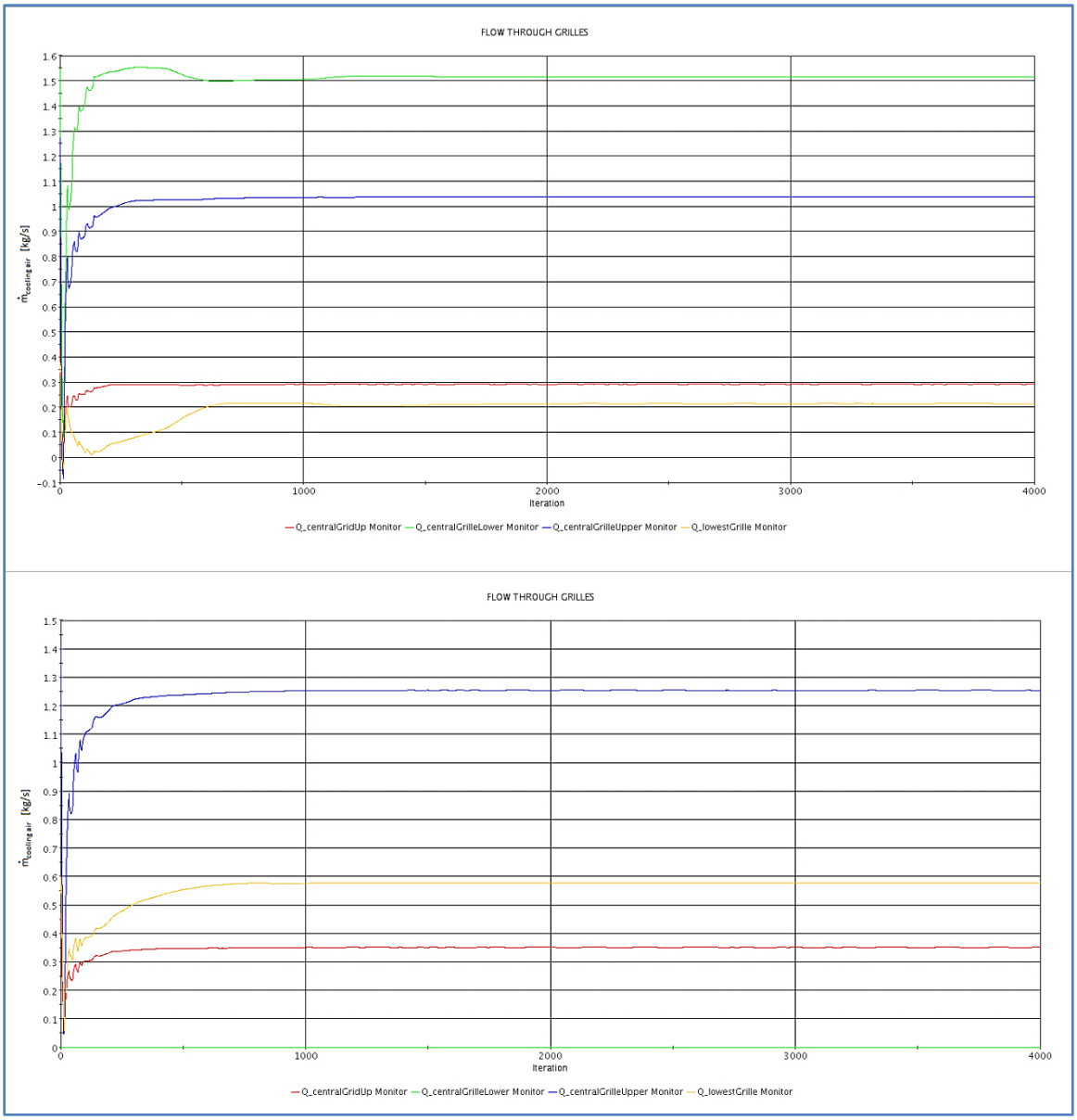

Figure 2.23 - Cooling air mass flow rates through the front inlet vents. Top: baseline version; bottom: modified version.

Figure 2.24 displays the convergence plot for the cooling air mass flow rates to the HEXes. Also in this case the trend is clearly visible, with the values stabilizing and finally reaching convergence.

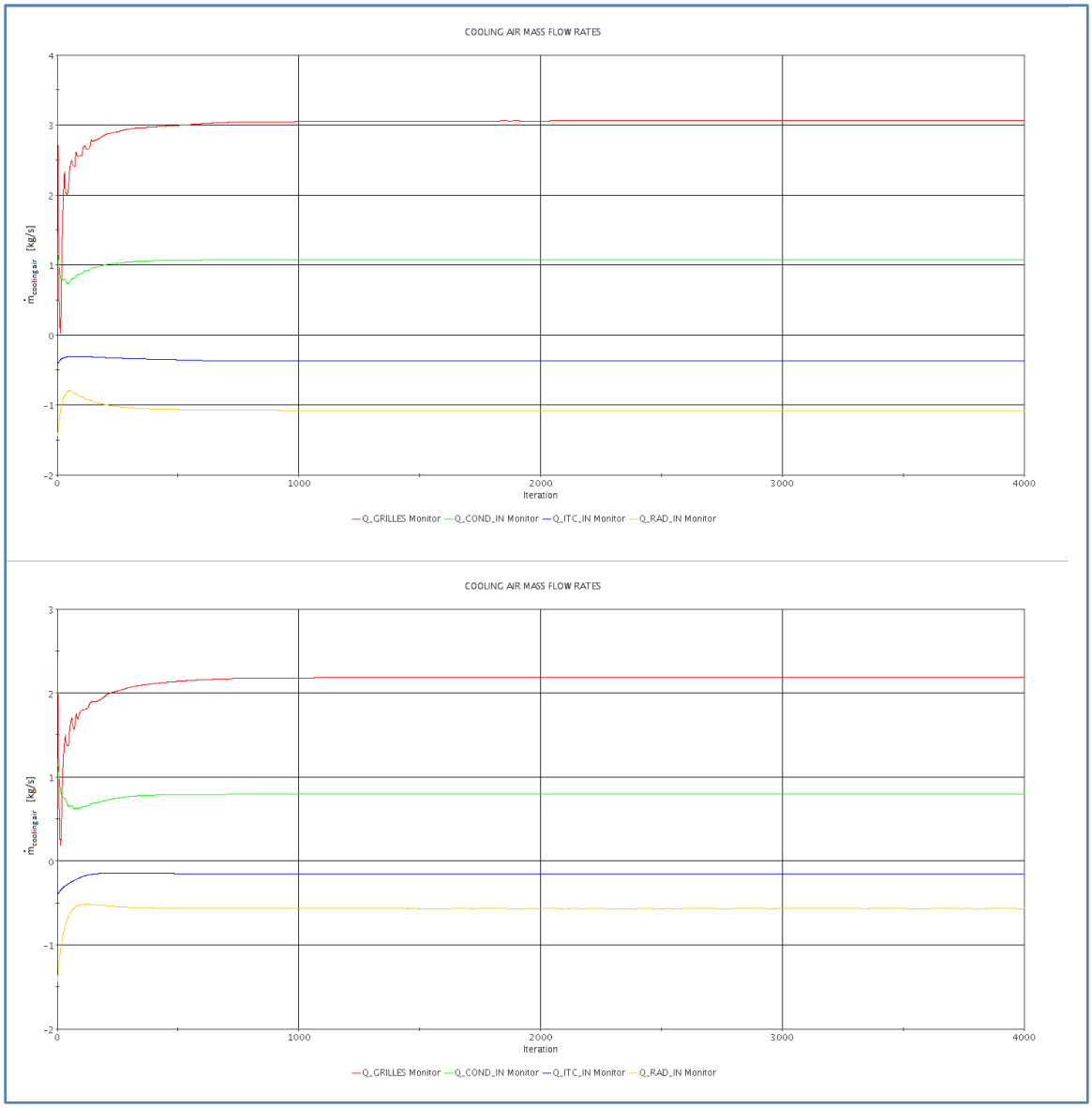

Figure 2.24 - Convergence plot of cooling air mass flow rates to the HEXes.

Similar trends to the ones shown above were obtained for the pressure values on the inlet and outlet faces of the heat exchangers, but for the sake of brevity they are here omitted. It is instead interesting to focus on the results to understand how the two versions behave in aerodynamic terms, and that is the purpose of the next paragraph.

2.2.3. AERODYNAMIC RESULTS

The main aerodynamic parameters of interest are reported in the following tables. They include drag and lift coefficient in terms of relative variation between baseline and modified versions, mass flow rates of cooling air, and pressures on the inlet and outlet faces of the HEXes. These indicators allow understanding how the operating conditions vary when applying the design modification. For the sake of readability, it was decided to report and analyze these parameters separately, subdividing them in four categories, namely aerodynamic results, mass flow rates to the HEXes, mass flow rates through the grilles, and pressure values.

Table 2.1 - Aerodynamic results: comparison between drag and lift coefficient for the baseline and modified versions.

	C_x [-]	C_z [-]
BASELINE	---	---
AGS 100% CLOSED	---	---
DELTA	-7.2%	-21.8%

The above values show that by closing the main central grille with an AGS system, it is possible to ideally decrease the drag by more than 7%. This figure is extremely remarkable even considering the ideal approach followed. As a matter of fact, a quick test with the same purpose was performed on the real scale wind tunnel model by shutting the main central inlet with tape, which showed an improvement higher than 4%. Even considering this figure, the improvement is still worthy and justifies the adoption of this system for aerodynamic purposes. However, the thermal impact must be accounted for before further developing the system design, and that will be discussed in Chapter 3. If considering the fact that the cooling air drag typically accounts for approximately 10% of the overall

vehicle drag, the amelioration achieved with this system is extremely meaningful. As for the lift coefficient variation, it can be seen that a significant lift reduction is observed, meaning that a very tiny lift is still present. All in all, the vehicle is essentially neutral from the lift force point of view, as it is customary with this type of automobiles.

Table 2.2 - Cooling air mass flow rates through the front inlet vents and to the HEXes.

	$\dot{m}_{GRILLES}$ [kg/s]	$\dot{m}_{COND\ IN}$ [kg/s]	$\dot{m}_{ITC\ IN}$ [kg/s]	$\dot{m}_{RAD\ IN}$ [kg/s]
BASELINE	3.059	1.076	0.373	1.081
AGS 100% CLOSED	2.182	0.799	0.156	0.569
DELTA	-28.7%	-25.7%	-58.1%	-47.4%

The above numbers show how negatively the AGS affects the cooling air mass flow rates to the heat exchangers. More specifically, the most critical component is the intercooler, which is just behind the main central grille which gets shut by the system. This decreases the cooling air flow rate by over 58%, thus significantly deteriorating the heat exchange capability of the exchanger. Similarly, the flow to the radiator gets reduced by over 47%, thus requiring countermeasures in order to avoid engine overheating. The thermal aspect will be better analyzed in the next chapter, but these figures already highlight the remarkable impact the system has on the cooling system performances. A more modest though relevant reduction of cooling air flow rate is observed on the A/C condenser, corresponding to approximately 26%. Overall, total flow rate of cooling air entering the engine bay through the front vents gets reduced by 28.7%. The target becomes therefore to properly address the thermal management problem by having almost one third less cooling air available for cooling purposes.

Table 2.3 – Distribution of cooling air mass flow rates through the front inlets.

	$\dot{m}_{centralGridUp}$ [kg/s]	$\dot{m}_{centralGrilleLower}$ [kg/s]	$\dot{m}_{centralGrilleUpper}$ [kg/s]	$\dot{m}_{lowestGrille}$ [kg/s]
BASELINE	0.292	1.515	1.038	0.214
AGS 100% CLOSED	0.351	0.000	1.254	0.577
DELTA	20%	-100%	21%	169%

Figure 2.25 - Detail of front inlet vents. The PIDs match the one reported in Table 2.3.

Table 2.3 shows how the total cooling air mass flow rate gets split into the different inlet vents in the two configurations. In particular, when shutting the main central grille (labelled *centralGrilleLower*), no flow crosses that inlet. As a consequence, an increase in flow rate through the other grilles is observed, even if the total flow entering the engine bay gets reduced by almost 29% from 3.06 kg/s to 2.18 kg/s, as shown in Table 2.2. As can be noticed, the highest increase in cooling air flow rate takes place in the lowest inlet (*lowestGrille*), essentially due to the close positioning of that vent to the shuttered central grille. In fact, as will be shown later, a high static pressure area exists over the shuttered inlet, in proximity of the stagnation point. This means that this high pressure zone pushes and deviates the incoming air towards the upper and lower portions of the front bumper, thus pumping more air into the three remaining open inlets. In

this perspective, the pumping efficiency of each of the remaining inlets increases, even though the overall available air flow rate into the engine bay for cooling purposes gets reduced.

Table 2.4 - Average absolute total pressures over inlet and outlet faces of the HEXes.

	$p_{COND\ IN}$ [Pa]	$p_{COND\ OUT}$ [Pa]	$p_{ITC\ IN}$ [Pa]	$p_{ITC\ OUT}$ [Pa]	$p_{RAD\ IN}$ [Pa]	$p_{RAD\ OUT}$ [Pa]
BASELINE	654.2	461.0	714.5	306.5	501.7	291.3
AGS 100% CLOSED	334.4	82.2	161.8	-102.4	80.0	-39.1
DELTA	-49%	-82%	-77%	-133%	-84%	-113%

In terms of pressures over the HEXes inlet and outlet faces, minor variations are observed if considering the total pressure values; however, if considering the relative pressure values, the two configurations are significantly different especially in terms of available static pressure, as will be visually confirmed in the pressure distribution maps of the engine bay in the next paragraph.

It is interesting to notice how the drag force develops over the longitudinal x direction over the vehicle. A comparison plot with the normalized drag force values for both the baseline and modified case is shown in Figure 2.26. Note that all the values have been normalized to the maximum drag of each configuration, i.e. the reference value for each version is different. This means that the maximum normalized drag force corresponds to unity for both cases but the actual total drag values are different for the two models.

A detail of the drag development over x for the central part of the vehicle is plotted in Figure 2.27. Here is where the biggest part of the aerodynamic improvement takes place, as opposed to the front part, where the drag values are higher due to the high static pressure caused by the closed surface shutting the main central grille.

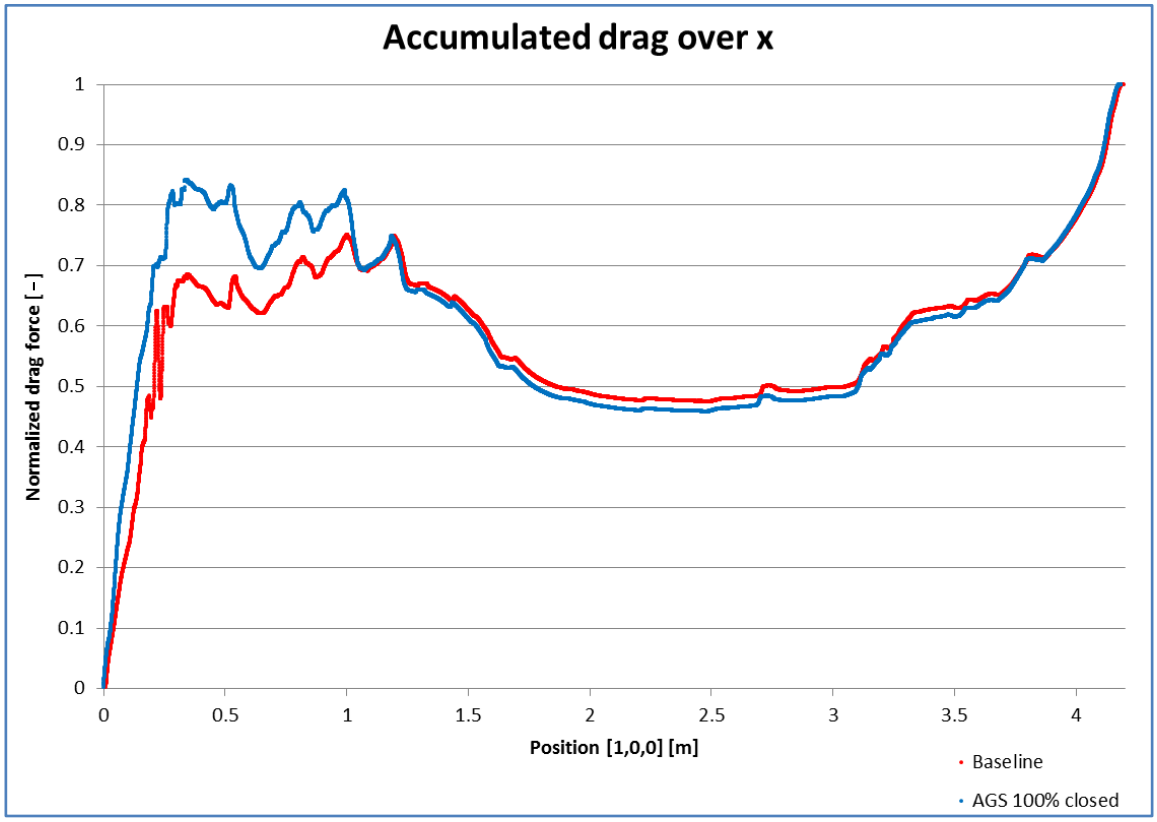

Figure 2.26 - Normalized drag force development over the longitudinal x direction for the two vehicle configurations.

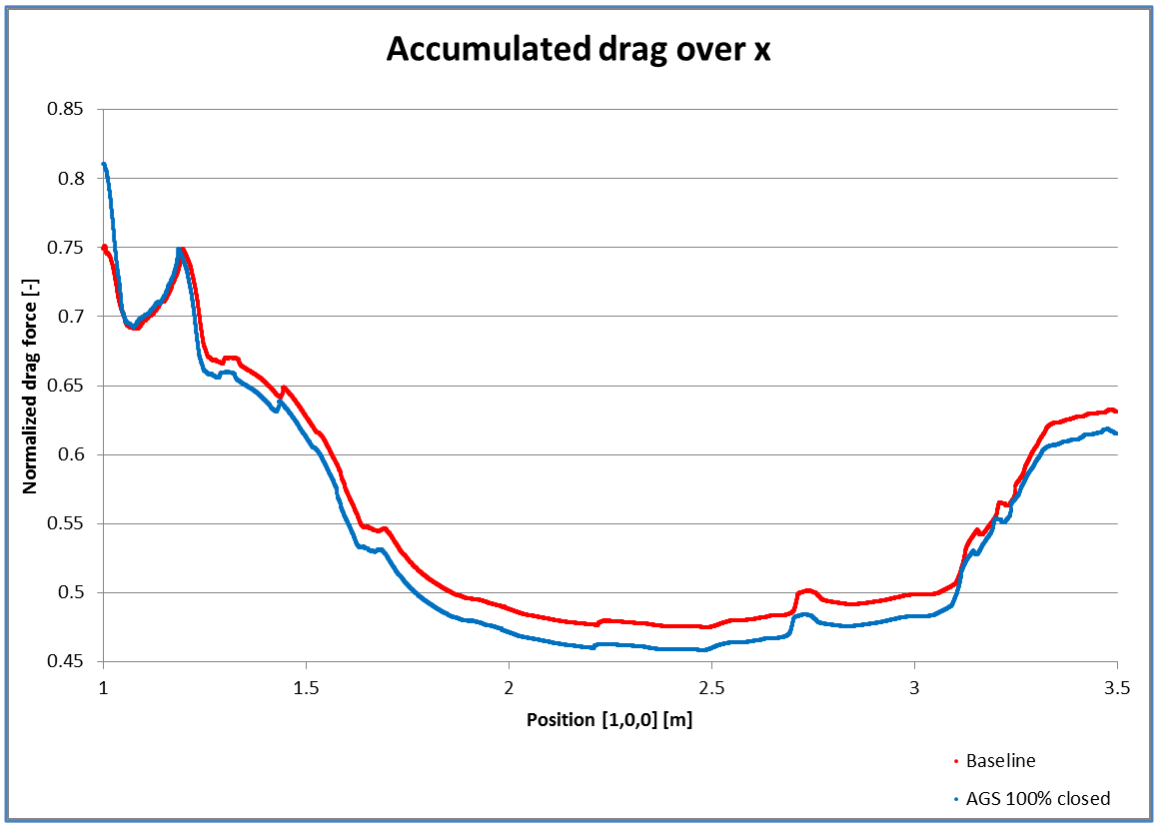

Figure 2.27 - Normalized drag force development over x, detail of the central part of the vehicle.

This high static pressure area causes the local drag to be higher, however the flow field around the entire vehicle is modified in such a way that overall a net reduction is observed when the system is closed. Notice how the drag force observed in the fully closed case around 0.25 m from the front end of the car corresponds to a thrust force in the baseline configuration. This is due to the flow characteristics around the cooling module, where low pressure areas and big recirculation vortices exist. With the only exception of this area, all the rest of the profile exhibits a very similar trend between the two configurations.

After outlining the numerical results of the aerodynamic simulation, it is now time to consider the flow field maps around the two vehicles to visually evaluate and understand the differences between the two versions. This is the object of the next two paragraphs, where all the main pressure and velocity maps are reported.

2.2.4. PRESSURE DISTRIBUTION MAPS

This paragraph deals with the pressure distribution maps over the vehicle body, slicing horizontal and vertical section planes, and details of the cooling system heat exchangers. The first part focuses on the external pressure field around the car body and over section planes, while the second one provides details of the pressure field within the engine bay.

2.2.4.1. EXTERNAL FLOW FIELD

Figure 2.28 shows the pressure coefficient ($C_{p)}$ distribution over the vehicle body. For incompressible flows, this parameter is defined as:

$$C_p = \frac{p - p_\infty}{\frac{1}{2}\rho_\infty v_\infty^2} \tag{6}$$

where p refers to pressure, ρ to density, v to velocity and the infinite subscript to the free-stream conditions (as opposed to the local ones). In this case, this relation holds true due to the low speed of the flow (below Mach number M=0.3), so that compressibility effects can be neglected. In case of steady, lossless flows, the above relation can be further reduced to:

$$C_p = 1 - \left(\frac{v}{v_\infty}\right)^2 \tag{7}$$

For the specific case under study, however, friction and viscous effects cause dissipation which cannot be neglected for an accurate prediction of fluid flow characteristics, so that it is necessary to resort to the numerical solver to account for them. However, the above relation is still extremely meaningful when analyzing the results because it gives a quick and intuitive relation to the analyst to understand the flow behavior at a given point.

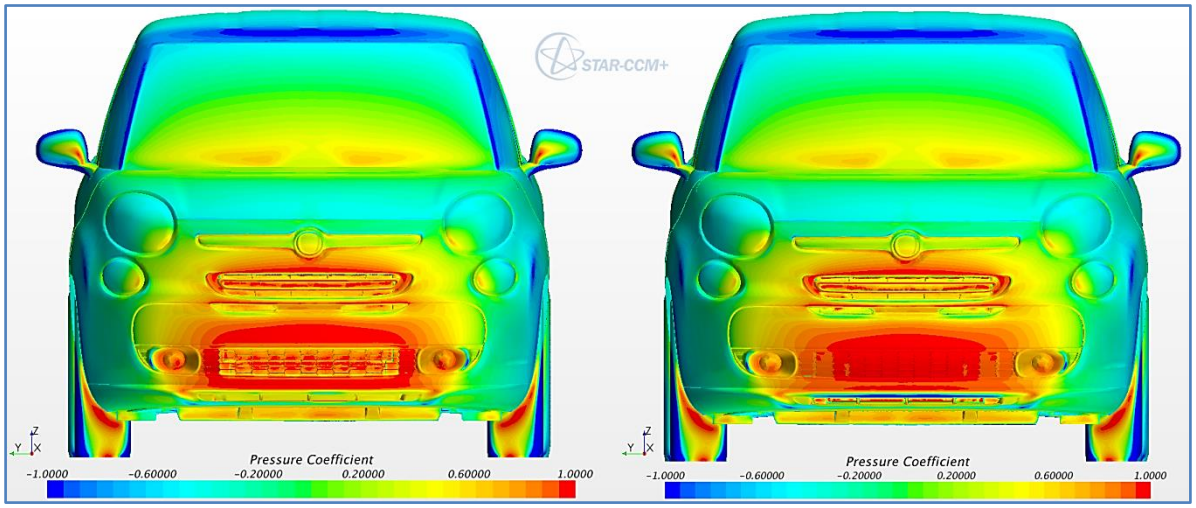

Figure 2.28 - Pressure distribution over the vehicle body, front-end. Left: baseline; right: modified.

Figure 2.28 highlights the differences between the baseline and modified configuration in terms of pressure distribution on the front-end. As can be observed, a large high static pressure area is present in proximity of the

shuttered grille for the modified version, where the flow comes to a halt at the stagnation point. This area, shown in red in the figures, is slightly more spread for the baseline case, as can be seen from the contours over the front bumper. However, for the modified case, the local drag force is higher in proximity of the shuttered inlet due the much wider surface area over which the air gets stopped.

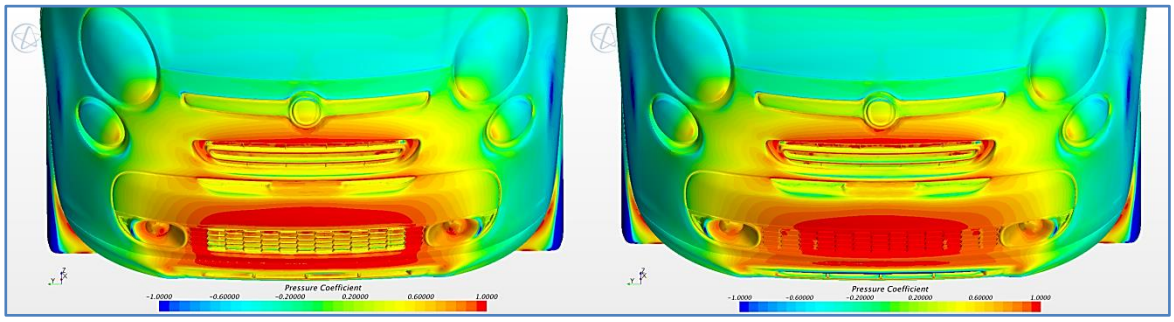

Figure 2.29 - Detail of pressure distribution over the front-end for the baseline (left) and modified (right) versions.

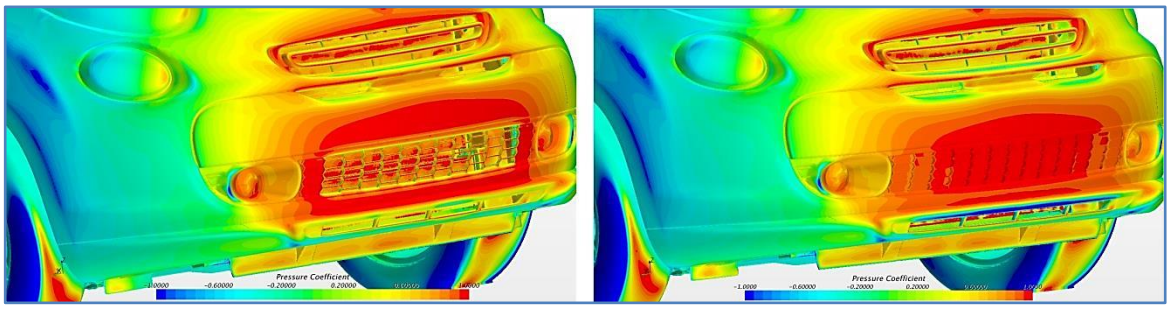

Figure 2.30 - Detail of Cp distribution over the front-end. Notice the different extension of the high pressure area (in red) between the baseline (left) and modified (right) configurations.

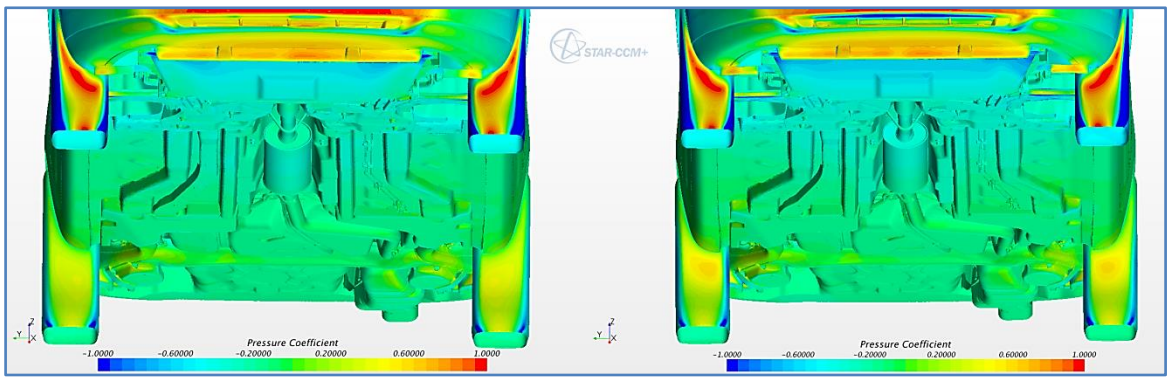

Figure 2.31 - Detail of underbody Cp distribution as seen from the front-end.

The pressure distribution over the underbody is basically unaffected from the presence of the fully closed AGS. However, Figure 2.31 shows that a low pressure, high speed flow exists in proximity of the lowest inlet when the AGS is closed, thus explaining the increase in flow rate discussed in the previous paragraph.

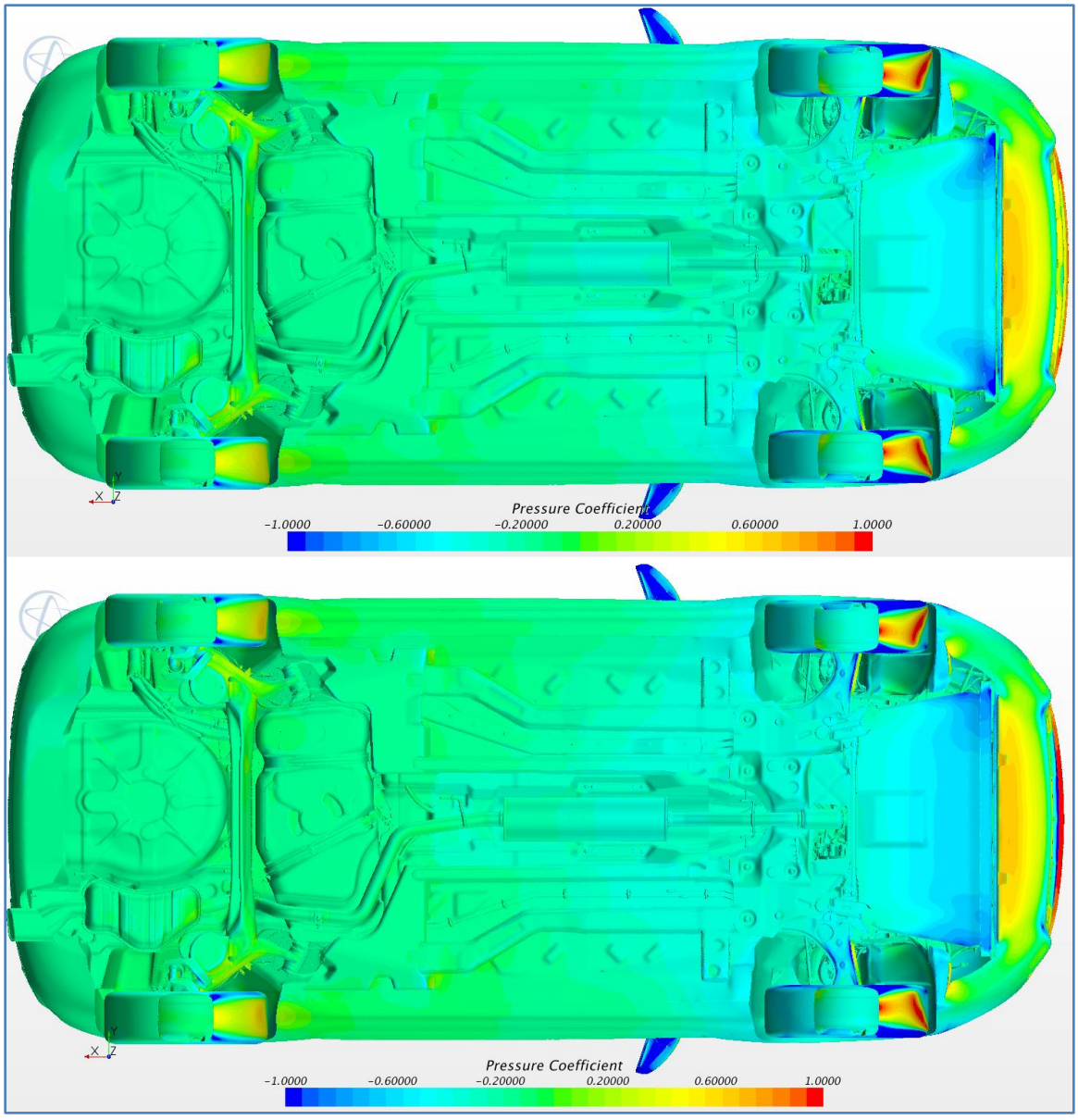

Figure 2.32 - Underbody pressure distribution. Top: baseline; bottom: modified.

As can be seen from Figure 2.33, a larger negative pressure area exists behind the front air dam when the AGS is fully closed. This local variation in the

characteristics of the flow field motivates the strong reduction of lift coefficient numerically found through the CFD simulation. In fact, even though higher negative peaks locally appear on the baseline version, overall a larger suction area is present for the modified one, so that the net effect is a reduction of total lift force.

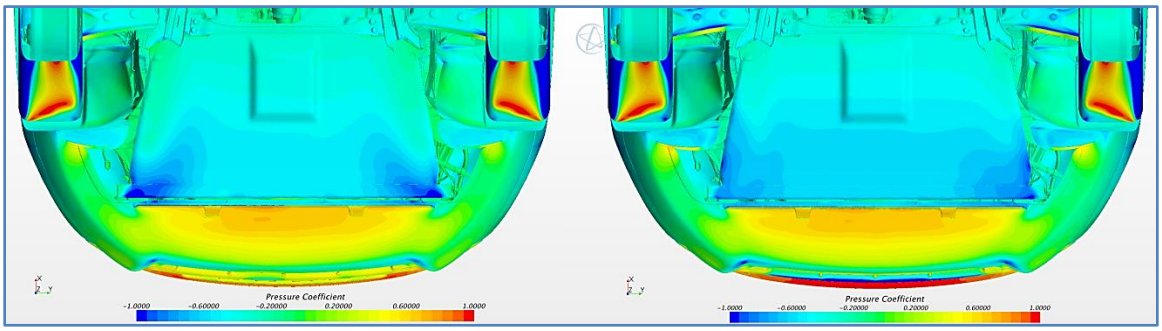

Figure 2.33 - Detail of pressure distribution over the front part of the underbody. Left: baseline; right: modified.

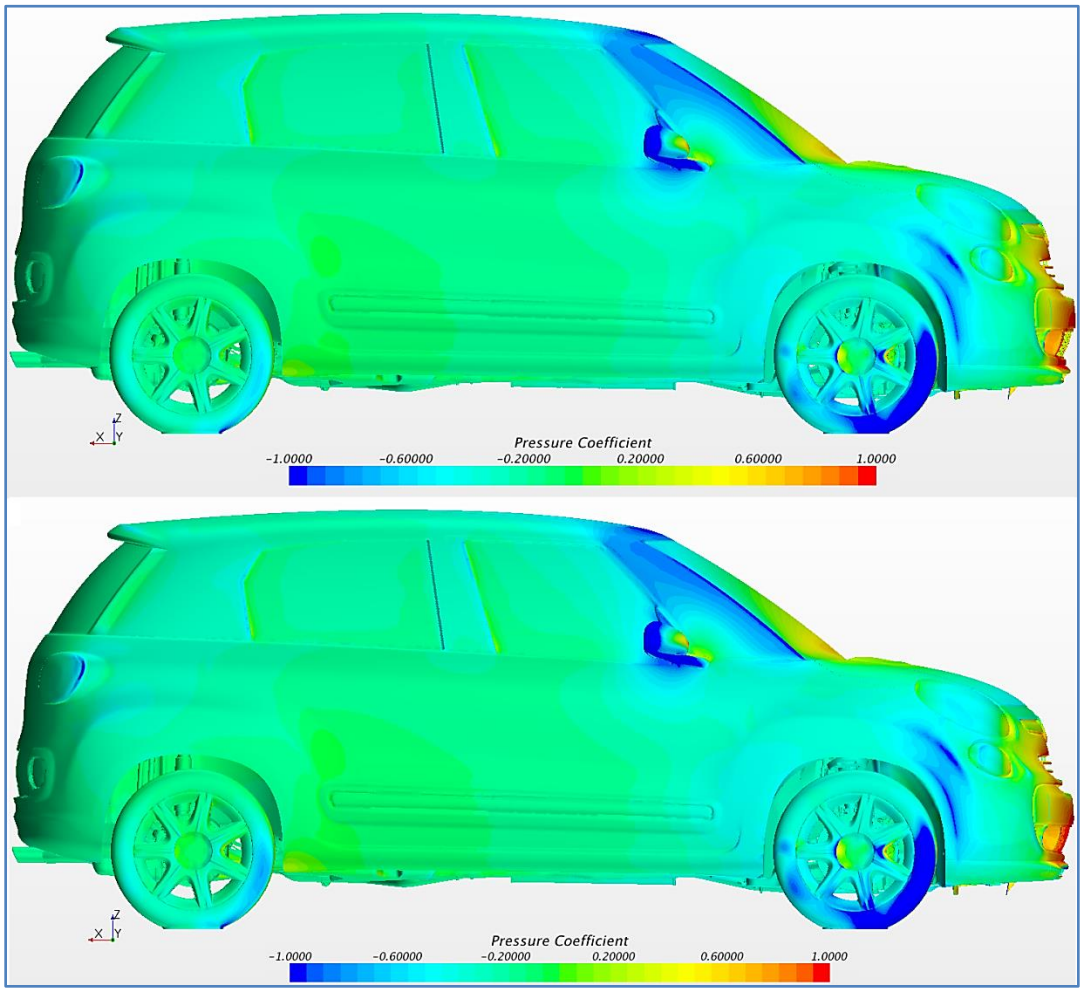

Figure 2.34 - Pressure distribution over the car body. Top: baseline; bottom: modified.

Figure 2.35 represents the top view of the model with the pressure distribution map. No significant differences are evidenced also in this case, thus confirming that the most significant influence of the AGS is on the front-end (in addition to the engine bay flow field, of course).

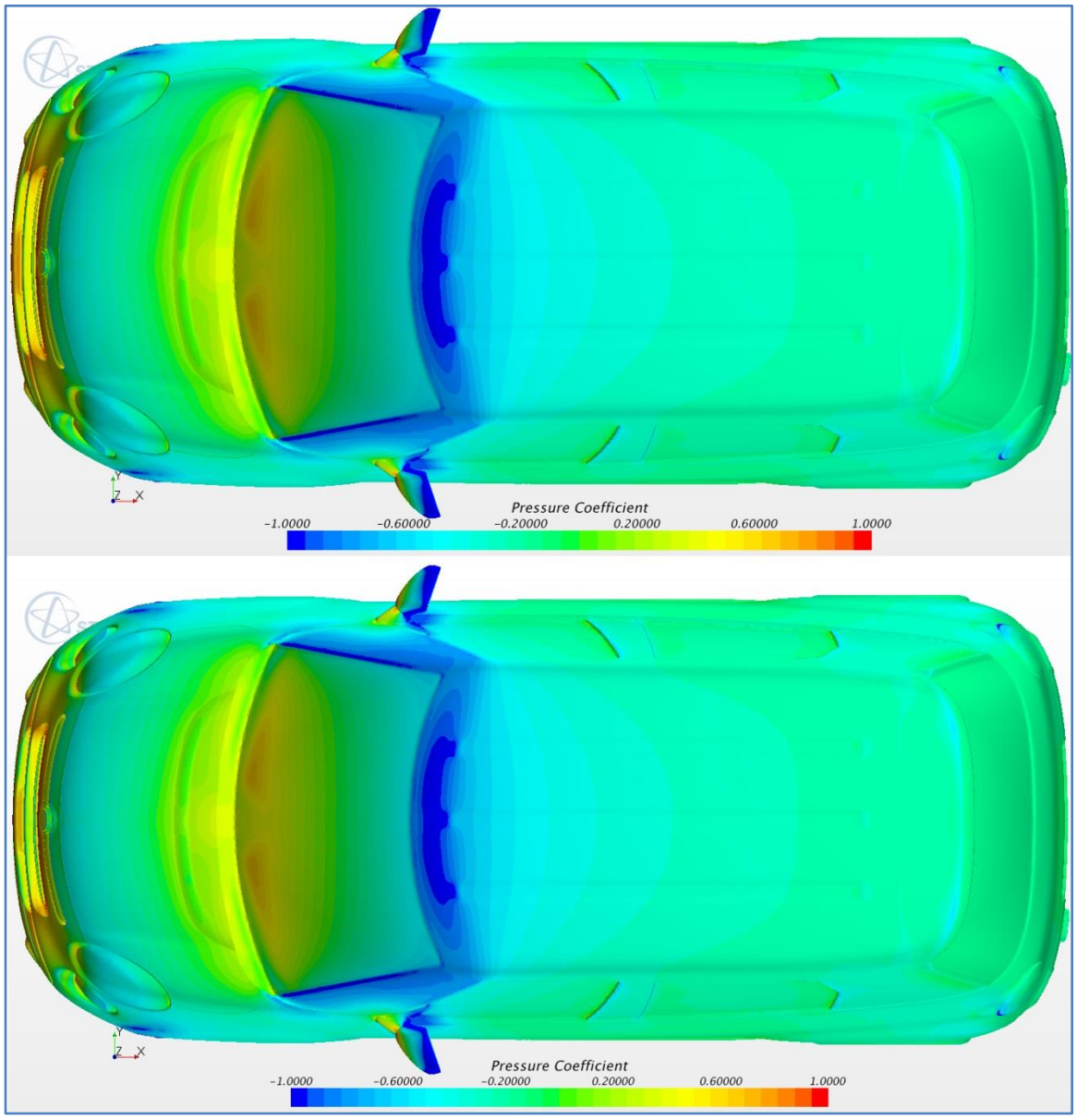

Figure 2.35 - Pressure distribution over the vehicle body, top view. Top: baseline; bottom: modified.

2.2.4.2. ENGINE BAY FLOW FIELD

As already mentioned in the previous paragraph, the area mostly affected by the presence of the AGS corresponds to the front-end. Here the flow field is altered by the inlet vent closure, and considerable differences are evidenced by the maps shown in the following figures.

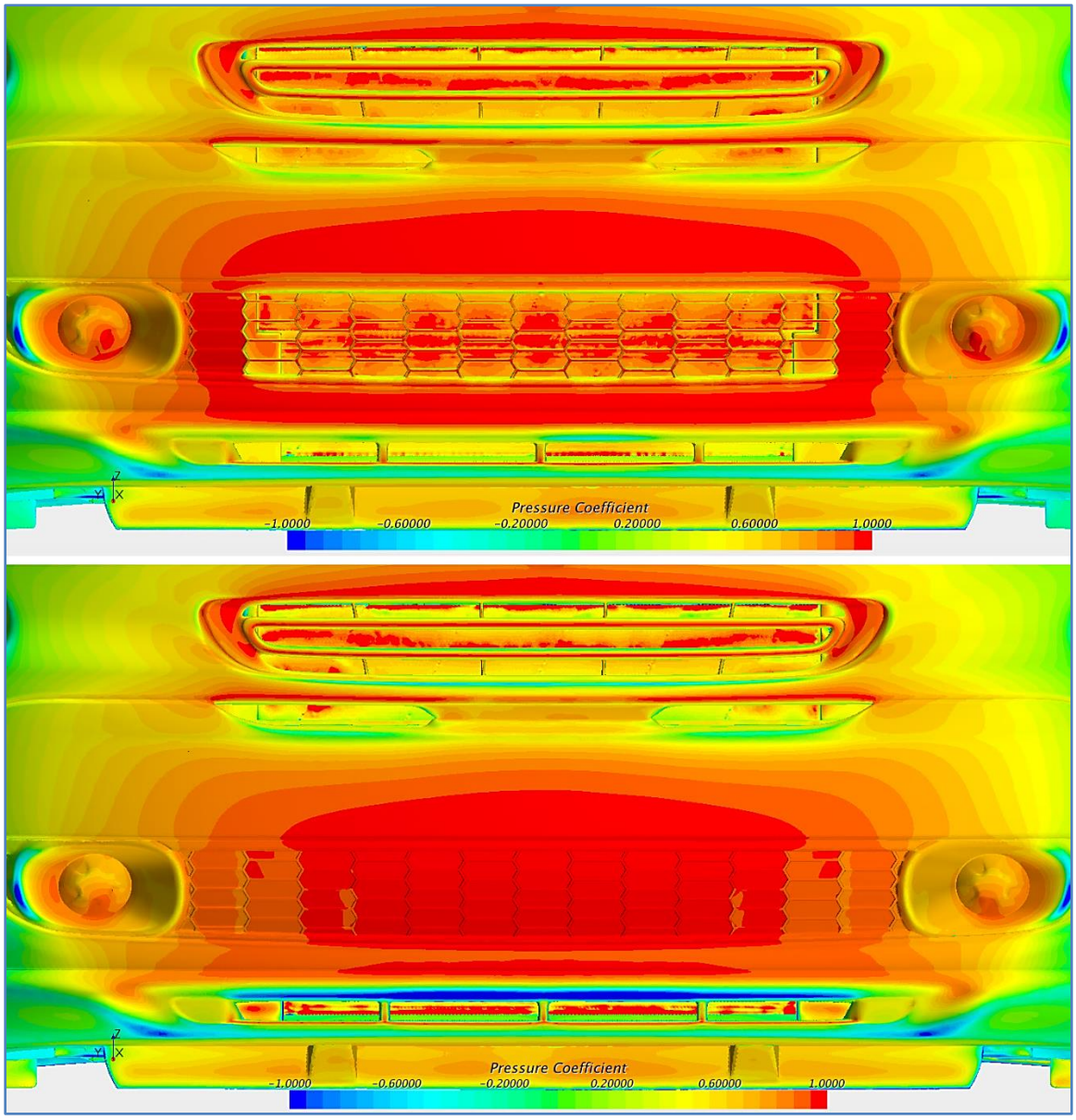

Figure 2.36 - Pressure distribution over the front-end, detail of the inlet vents. Top: baseline; bottom: modified.

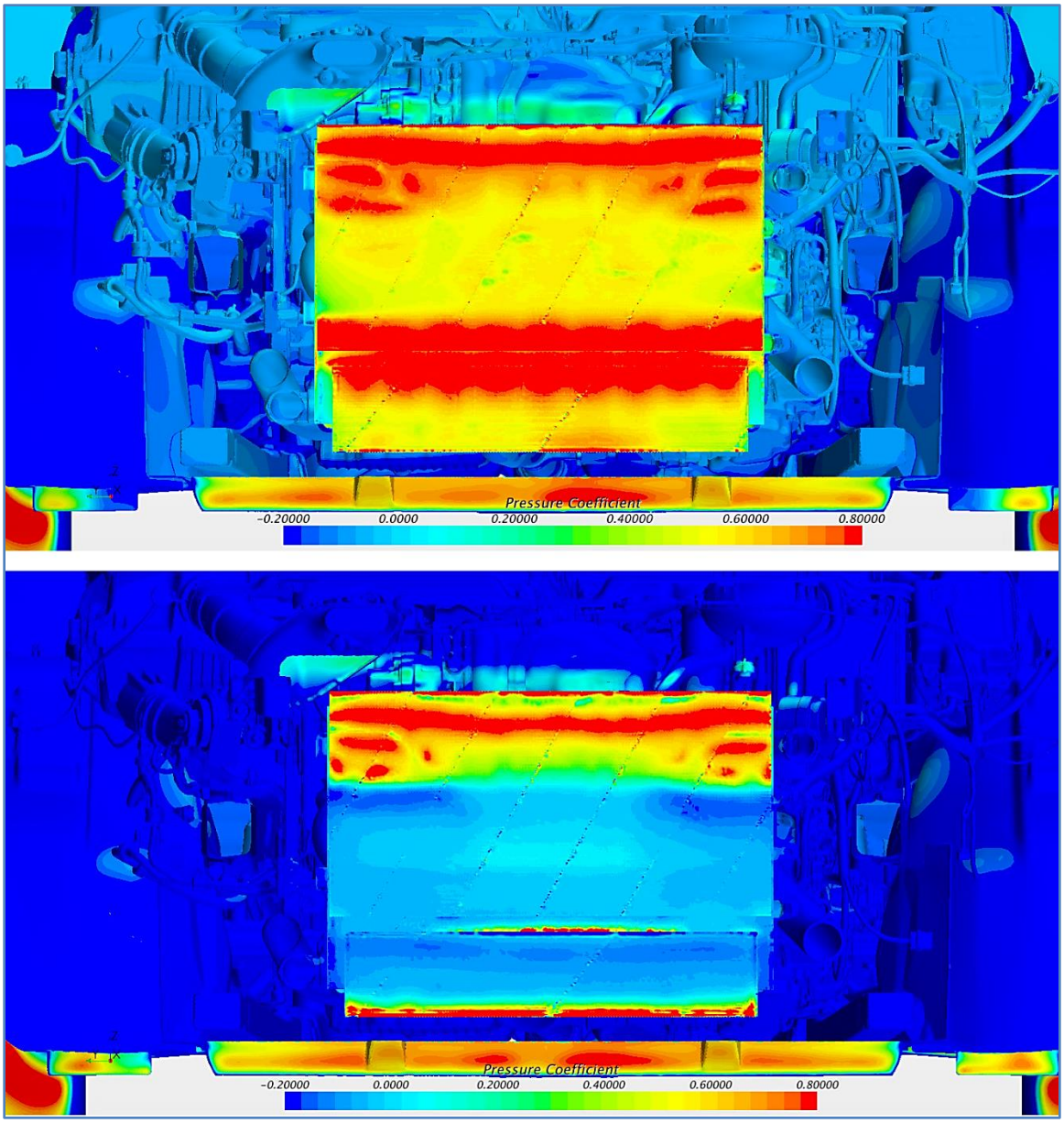

Figure 2.37 - Pressure distribution map, detail of the engine bay. The two visible rectangles are the A/C condenser (top) and the intercooler (bottom) inlet faces. Top: baseline; bottom: modified.

Figure 2.37 shows the engine bay pressure distribution map. The inlet faces of the air conditioning condenser (the upper rectangle) and of the intercooler (bottom rectangle) are clearly visible, as well as the differences between the two configurations. The range of C_p values has been reduced in order to underline the dissimilarities of the two fields. The presence of the shuttered inlet upstream of the two exchangers is immediately evident when considering the local pressures.

The wide blue areas on the HEXes in the modified case clearly show a reduction in pressure which negatively affects the heat exchange process. Also, the advantageous ram effect which could be exploited in the baseline case is strongly impaired in the modified case, this further impacting on the thermal performances of the system. This behavior extends all along the x direction within the cooling module, as can be seen in Figure 2.38, where the pressure distribution map on the outlet faces of condenser and intercooler are shown.

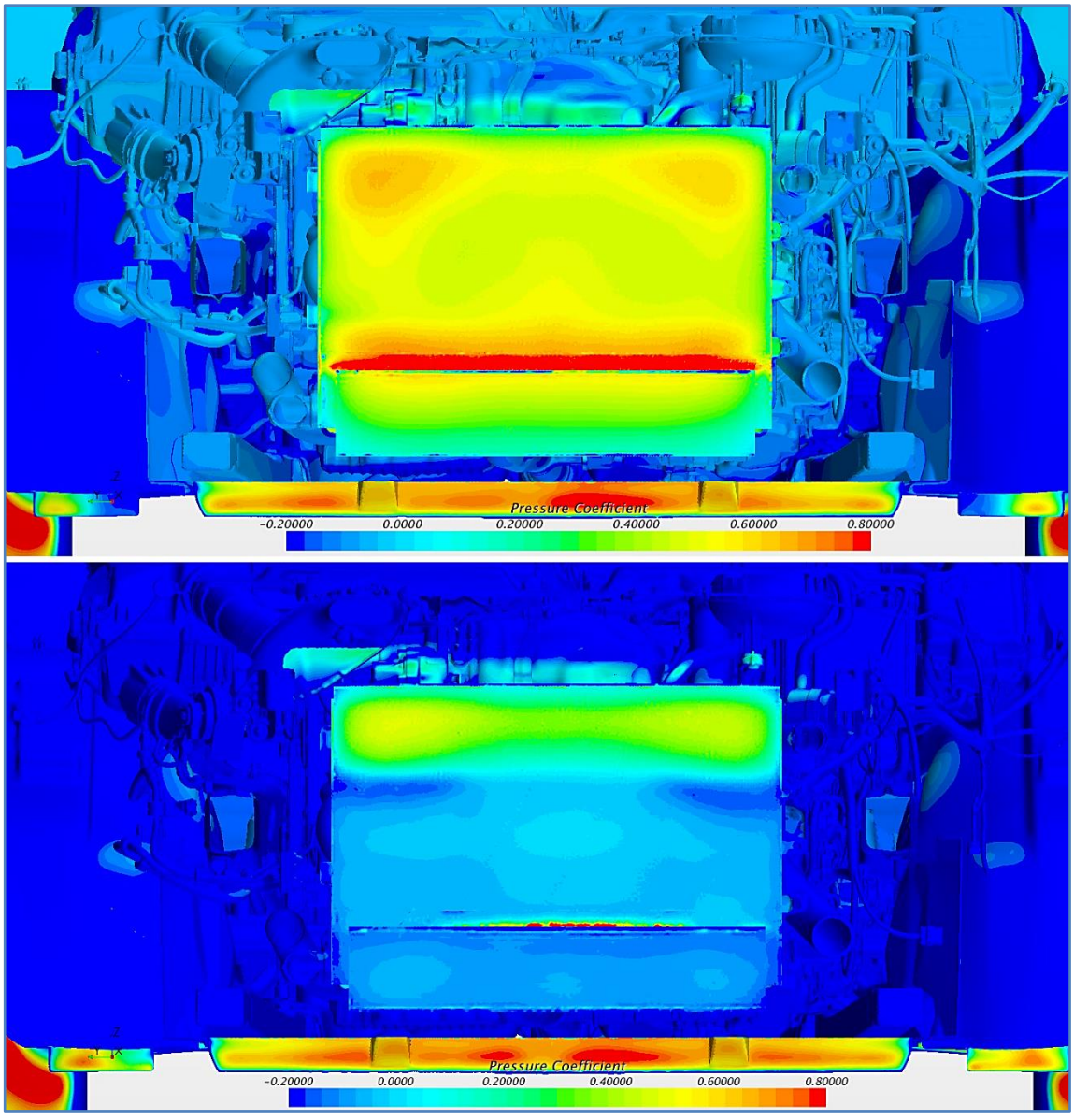

Figure 2.38 - C_p distribution in the engine bay, detail of A/C condenser and intercooler outlet faces. Top: baseline; bottom: modified.

It is interesting to notice how the pressure within the entire engine bay gets reduced. This is immediately evident when considering the dark blue areas beyond the exchangers, which are much more extended in the fully closed AGS case with respect to the baseline model.

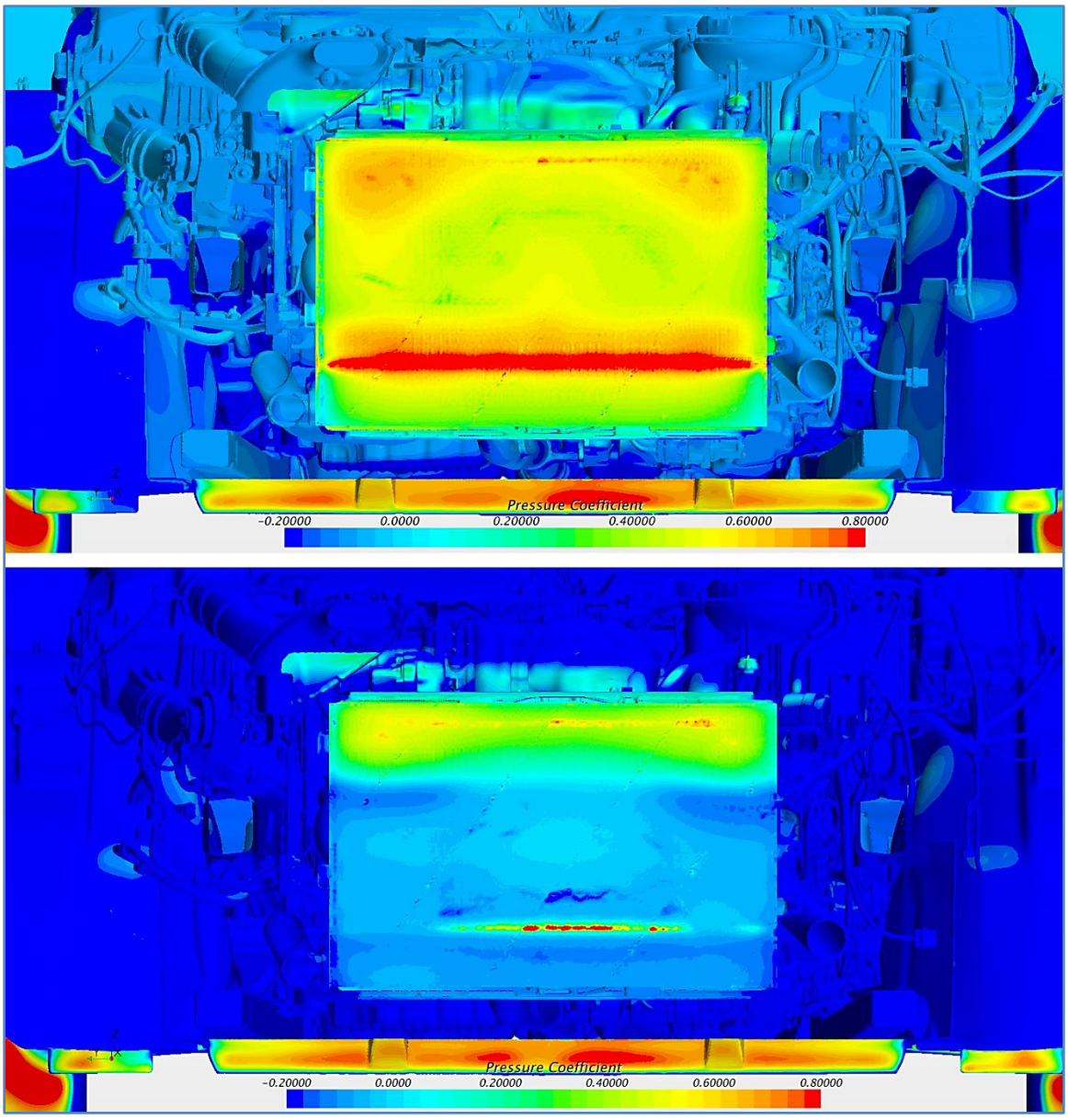

Figure 2.39 - Pressure distribution over the inlet face of the radiator. Note the big difference between the baseline, top, and the modified version, bottom.

Figure 2.40 displays the pressure distribution over the outlet face of the radiator, just ahead of the fan module, for the two versions.

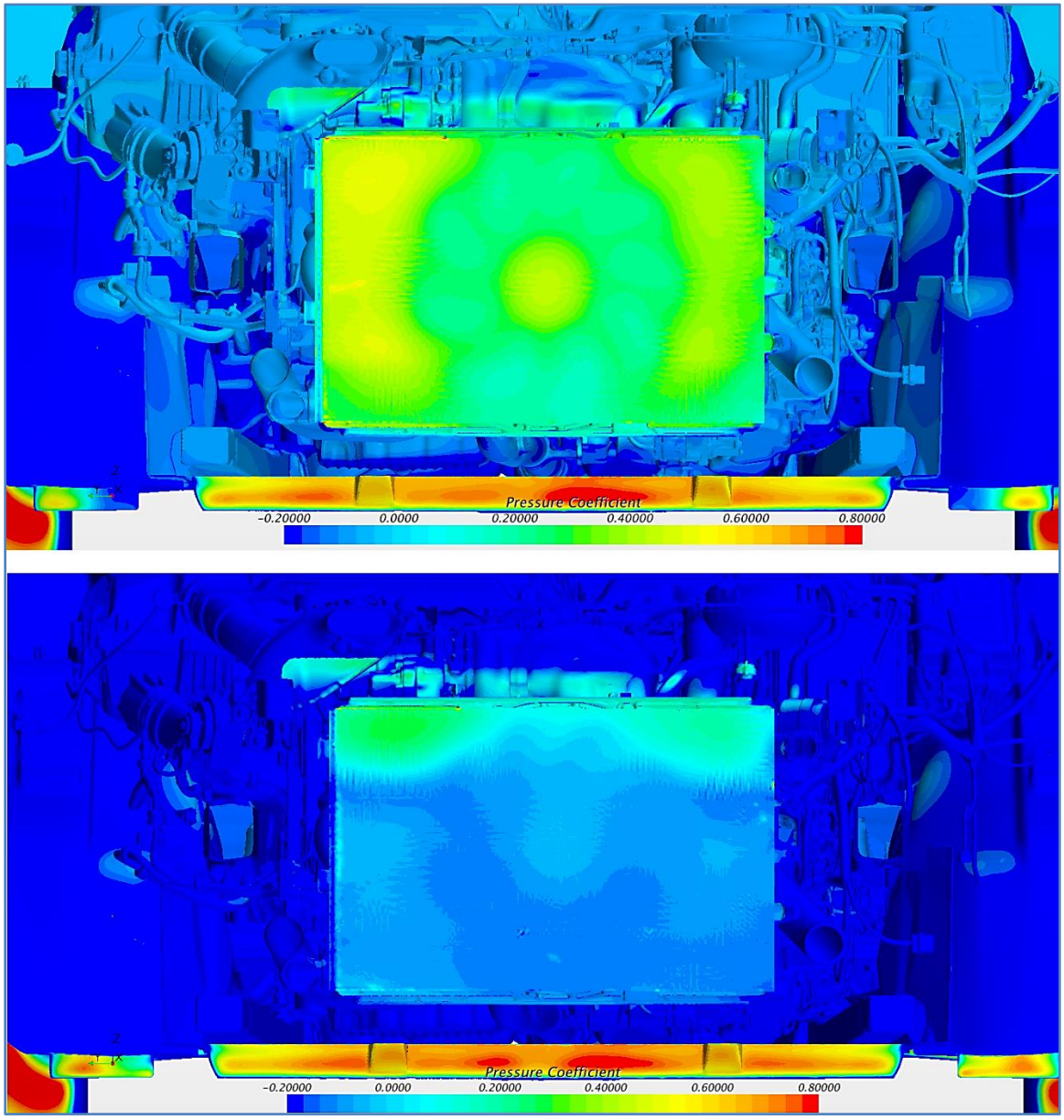

Figure 2.40 - Radiator outlet face pressure distributions for the baseline (top) and modified (bottom) cases.

Figure 2.41 shows the C_p map at the inlet of the cooling fan, which is stationary at the considered testing conditions. As can be seen, the strong effect of the closure propagates for a long distance downstream of the shutter itself, thus varying the entire flow field within the underhood compartment.

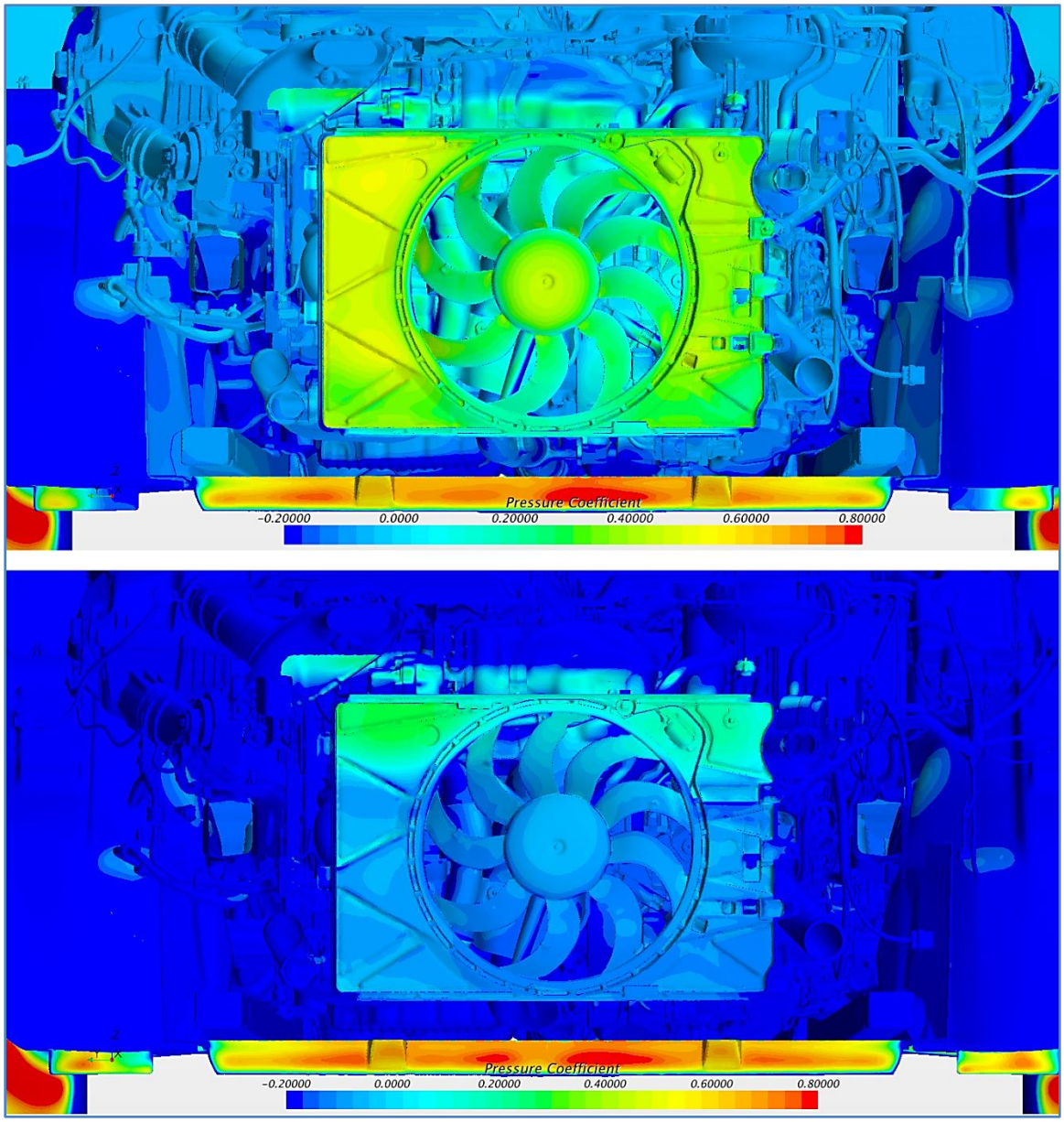

Figure 2.41 - Pressure distribution map - detail of inlet to the cooling fan. Top: baseline; bottom: modified.

A further visual confirmation for this comes from Figure 2.42, which shows how the pressure level in the region behind the cooling module is extremely different for the two cases. In particular, the lower pressure level inside the engine bay is directly responsible for the increased local drag figure in its proximity for the modified case. In fact, the higher pressure level on the external side and the lower pressure within the engine bay compared to the baseline case

both contribute to the higher local drag for the modified case already discussed in Figure 2.26 and Figure 2.27 (also in the non-normalized plot, not reported here for confidentiality purposes). The aerodynamic improvement in terms of drag reduction derives in fact from the flow downstream of the engine bay, as shown in the plot of drag development over x.

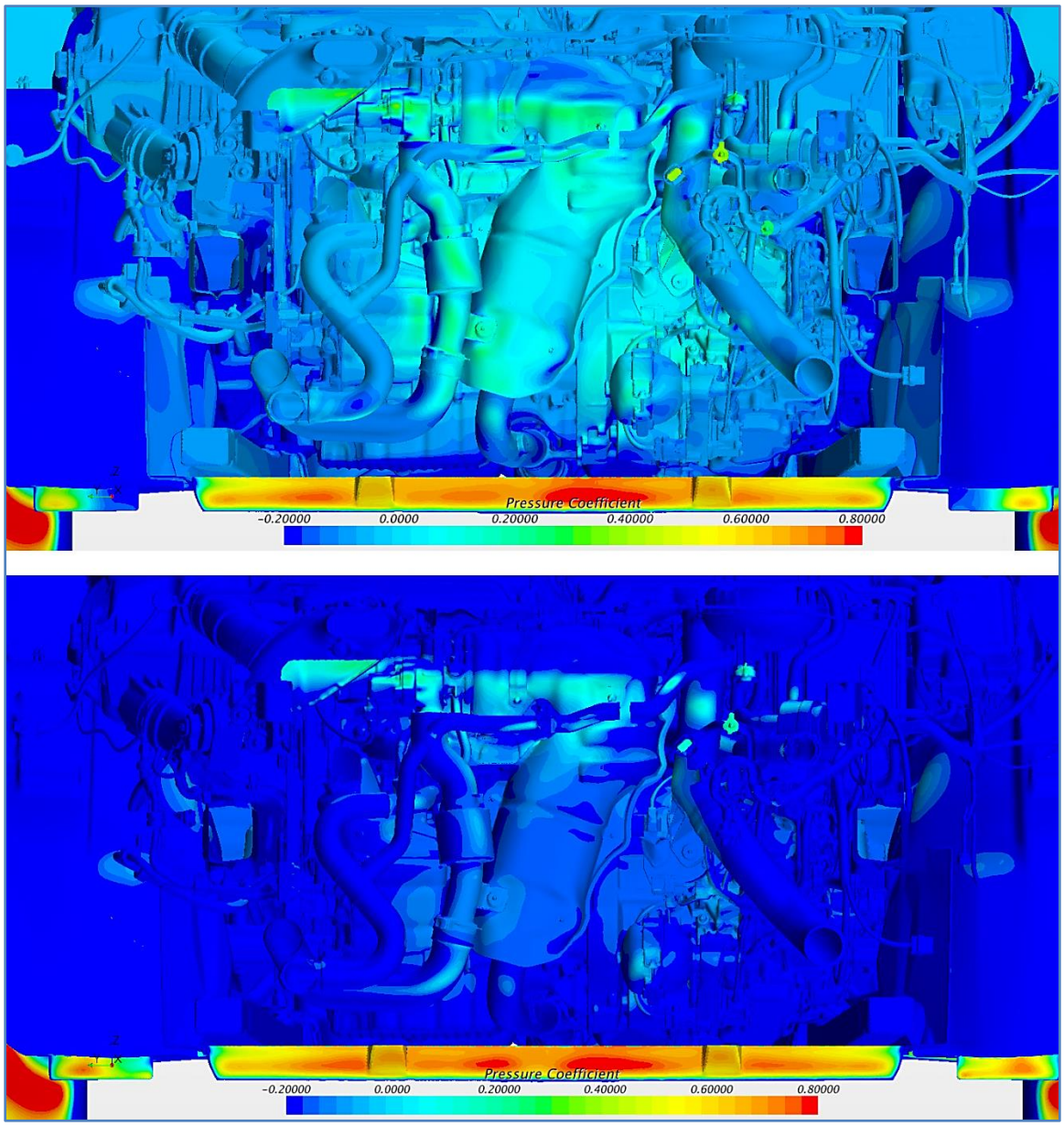

Figure 2.42 - Pressure distribution in the engine bay downstream of the cooling module. Top: baseline; bottom: modified.

Additional details of the HEXes pressure distributions are provided in Appendix E, where they are isolated from the other components to better highlight the variations between the two vehicle setups.

A very useful way for visualizing the flow field in the engine bay is provided by slicing section planes with the pressure distribution maps. The following figures show vertical (XZ) and horizontal (XY) section planes cutting the vehicle and all its underhood components with the corresponding pressure distribution. The differences between the two configurations are immediately clear, as the colors put in evidence. In particular, a significant reduction in the average pressure level in the engine bay for the modified case is observed, caused by the closure of the main central grille.

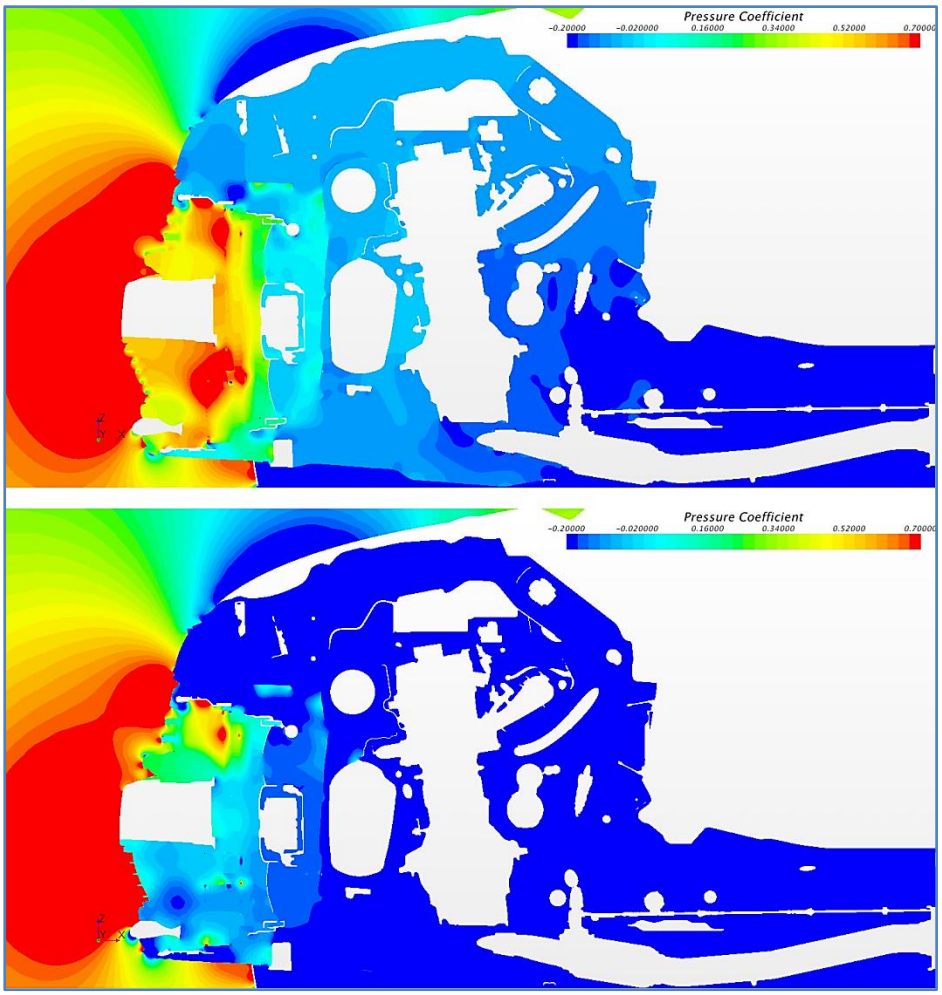

Figure 2.43 - Pressure distribution over the longitudinal vertical mid-plane with coordinates y=0 mm. Top: baseline; bottom: modified.

It is interesting to notice how the average relative pressure in front of the HEXes differs in the two configurations. In particular, the energy term associated to the static pressure for the modified case is much lower (in average) than in the baseline case. This implies that the ram effect which can be exploited to drive the flow across the exchangers is significantly more limited, thus worsening the thermal performances. This trend is confirmed if considering other vertical section planes along the y direction, like the one at y=+200 mm, shown below.

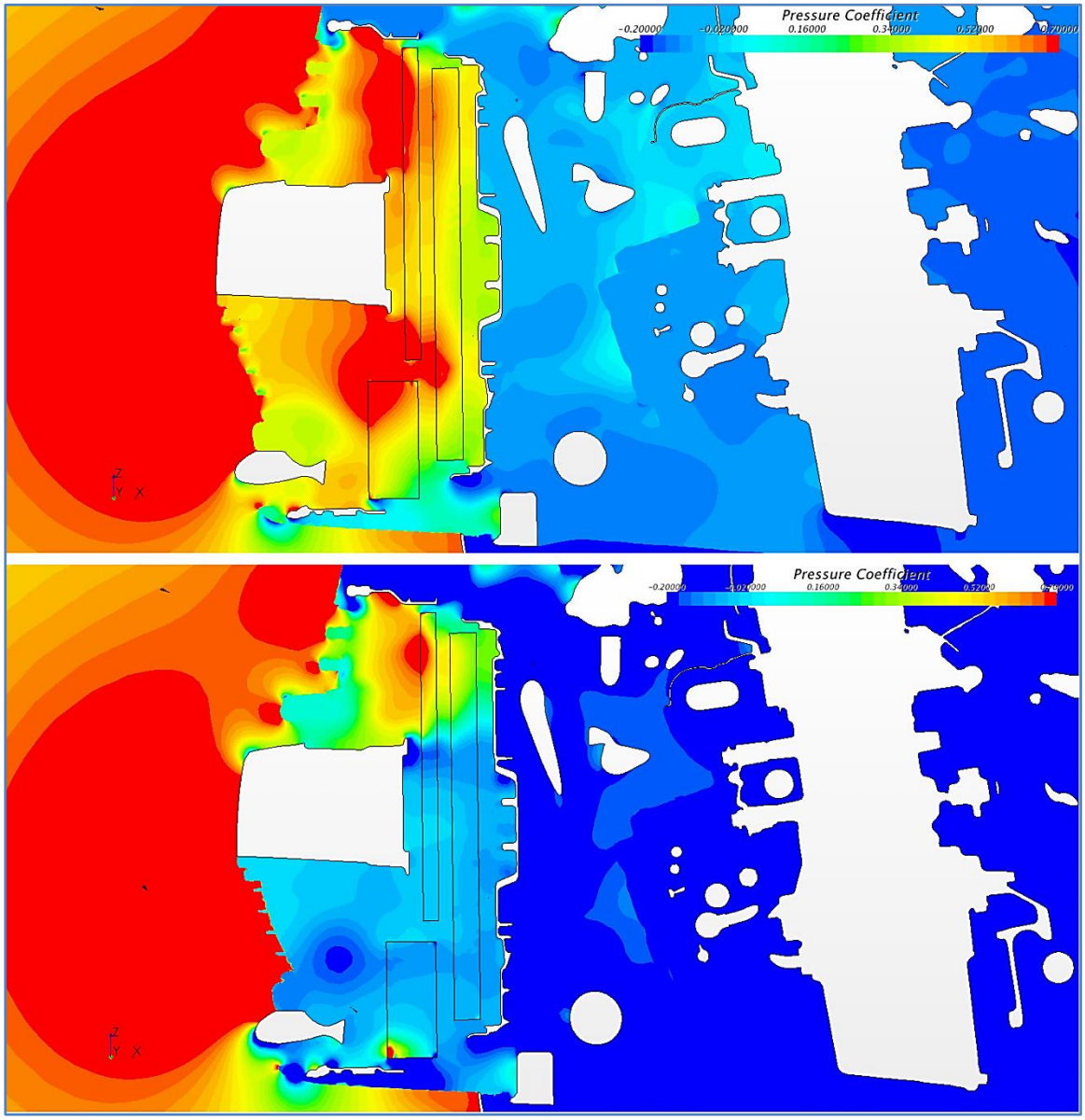

Figure 2.44 - Pressure distribution in the engine bay. Detail of the longitudinal vertical section plane with coordinates y=+200 mm. Top: baseline; bottom: modified.

This trend is evident also over the horizontal section planes. Figure 2.45 compares the C_p patterns for the two versions by considering the z=+10 plane. Here the effect of the closure is immediately visible. The AGS creates a large suction area just behind the closure, highlighted in blue in the bottom part of the figure below, as opposed to the orange-red zone of the baseline model.

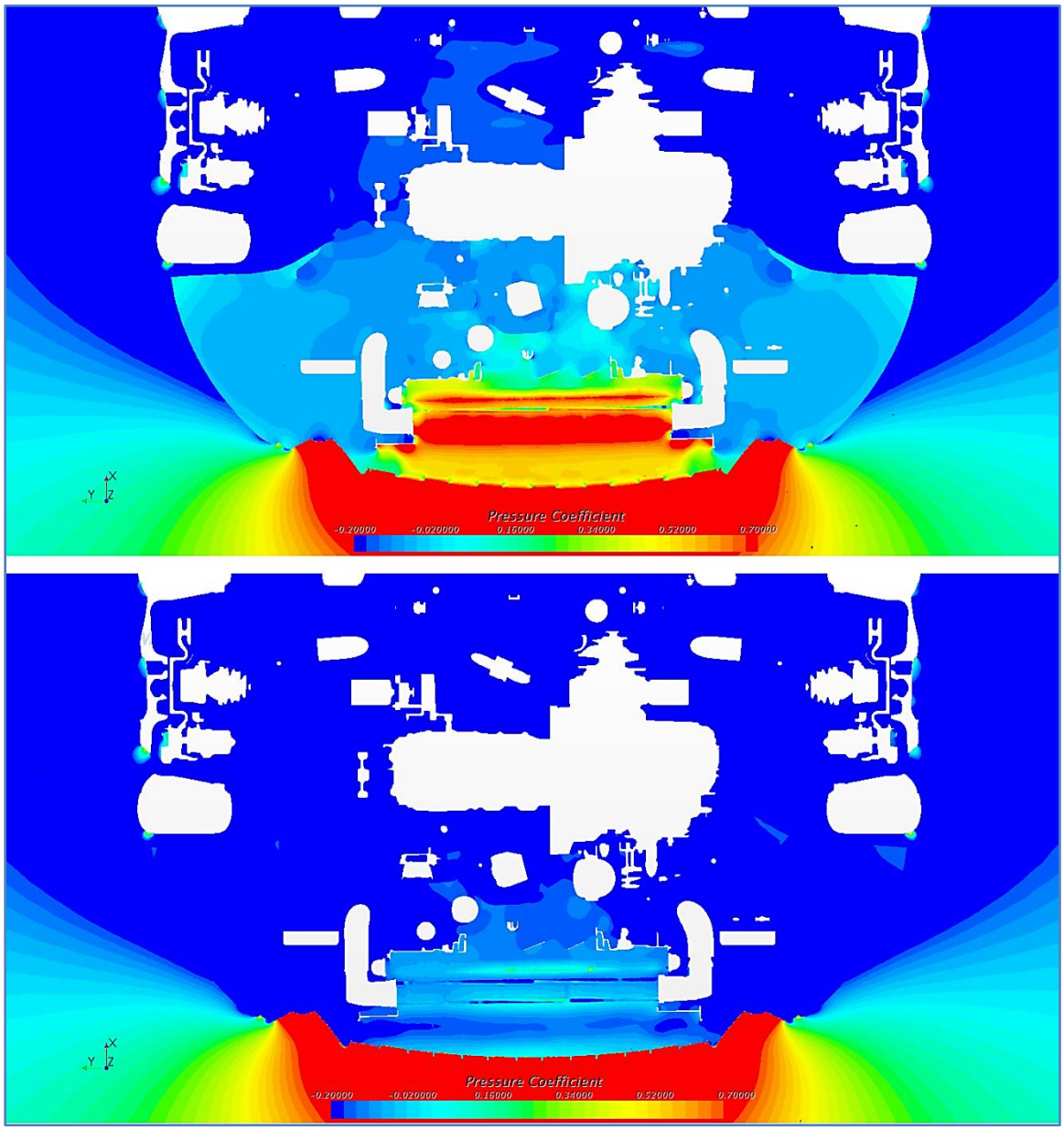

Figure 2.45 - C_p distribution over the horizontal section plane with coordinates z=+10 mm. Top: baseline; bottom: modified.

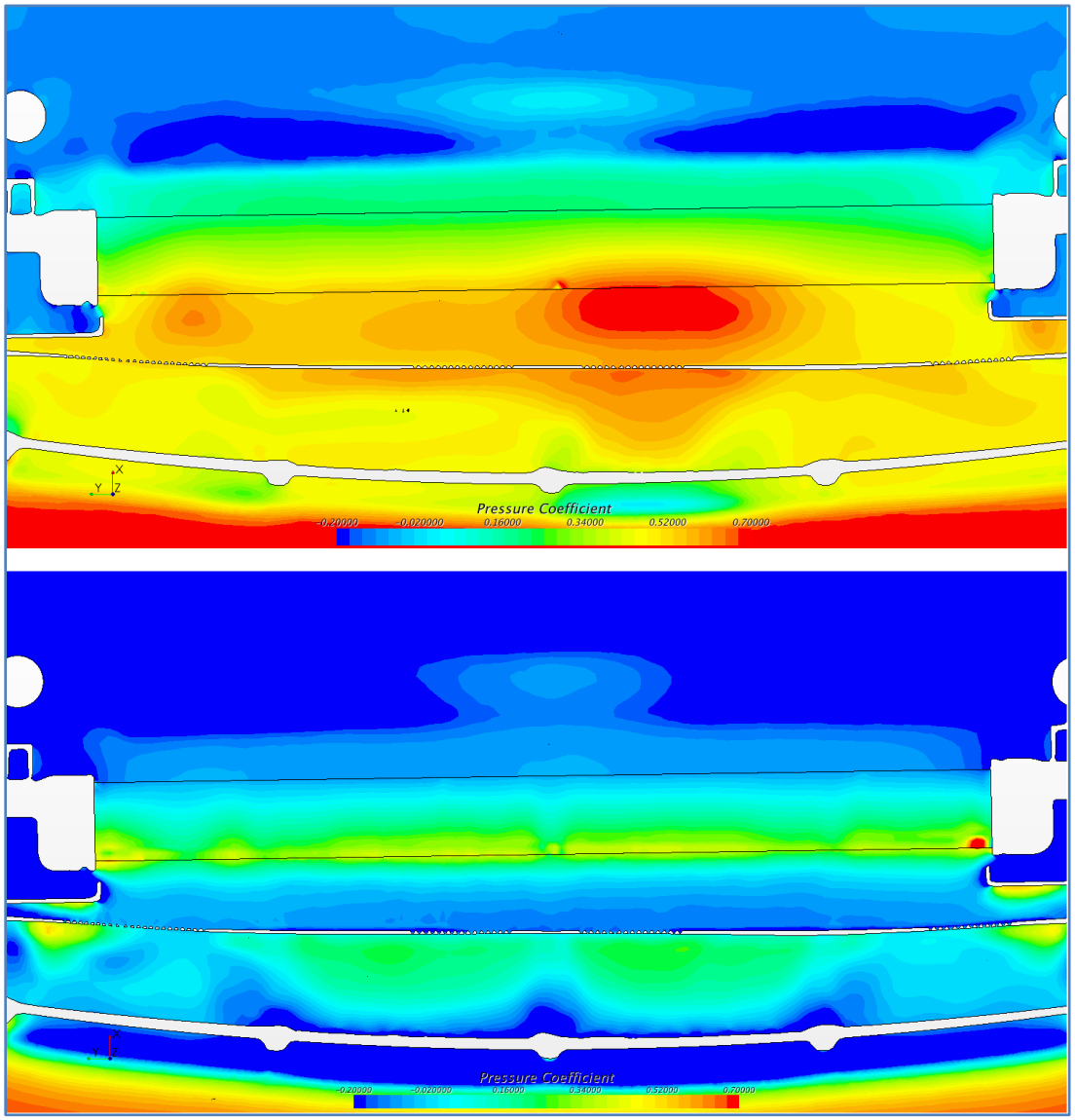

Figure 2.46 - Pressure distribution over the horizontal plane with coordinates z=-90 mm, detail of the HEXes. Top: baseline; bottom: modified.

The maps above show the detail of the pressure distribution in proximity of the cooling system HEXes. The entire flow field is altered and the reduction in pressure upstream of the exchangers will negatively impact on the thermal side. However, the margin allowed in the cooling system design is high enough that most luckily no alternative measures would be required to satisfy the heat dissipation request (as evidenced in experimental tests performed on cooling systems with similar performances by Fiat).

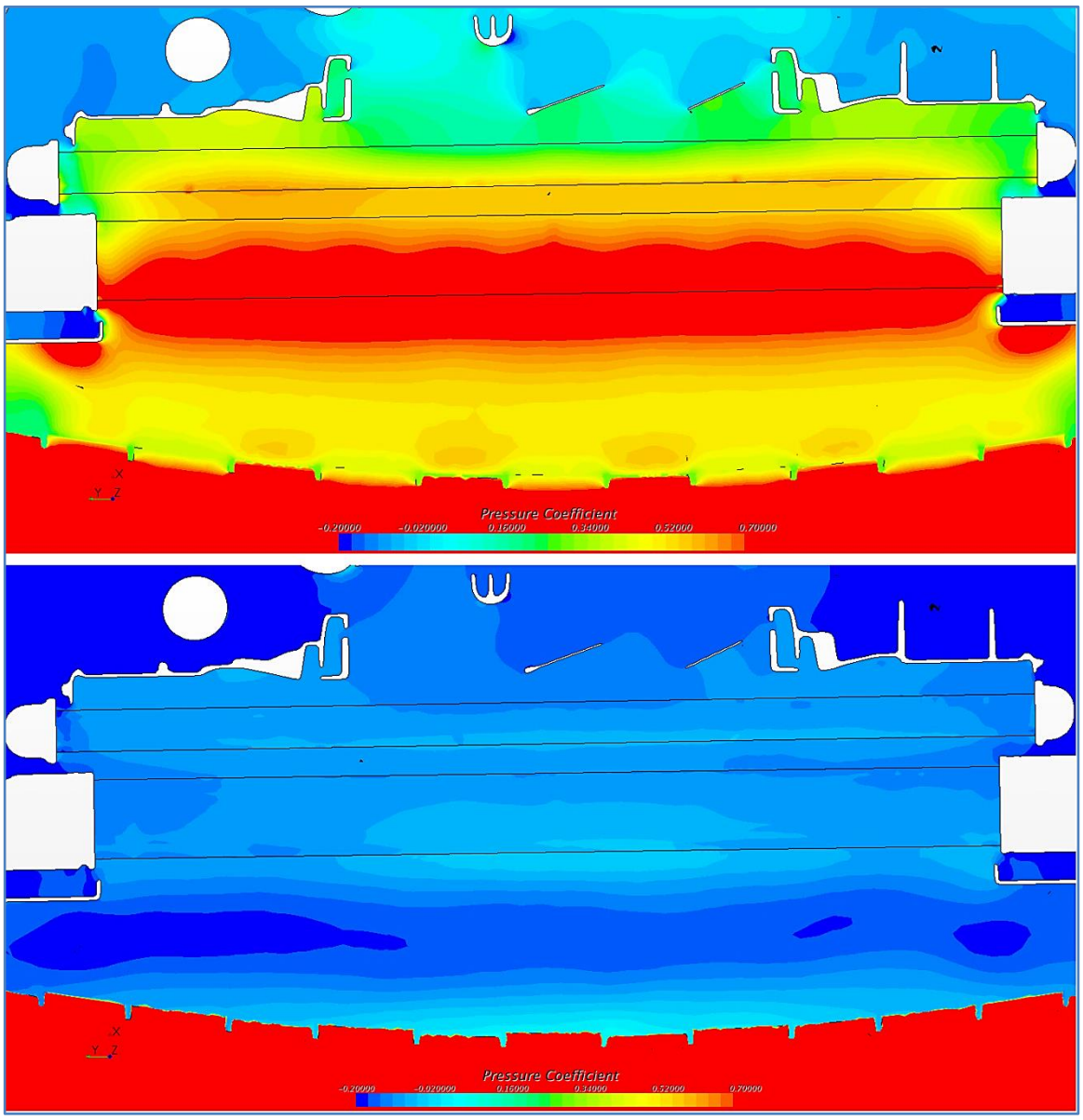

Figure 2.47 - Pressure distribution over the horizontal section plane with coordinates z=0 mm, detail of the HEXes. Top: baseline; bottom: modified.

Clearly, the influence if the closure on the HEXes is particularly intense immediately downstream of the closed AGS, but the effect also propagates and extends to the upper side of the cooling module due to the alteration of the entire flow field. This is evident if considering the horizontal section planes from z=-90 mm to z=+260 mm, where the biggest differences emerge between the two configurations.

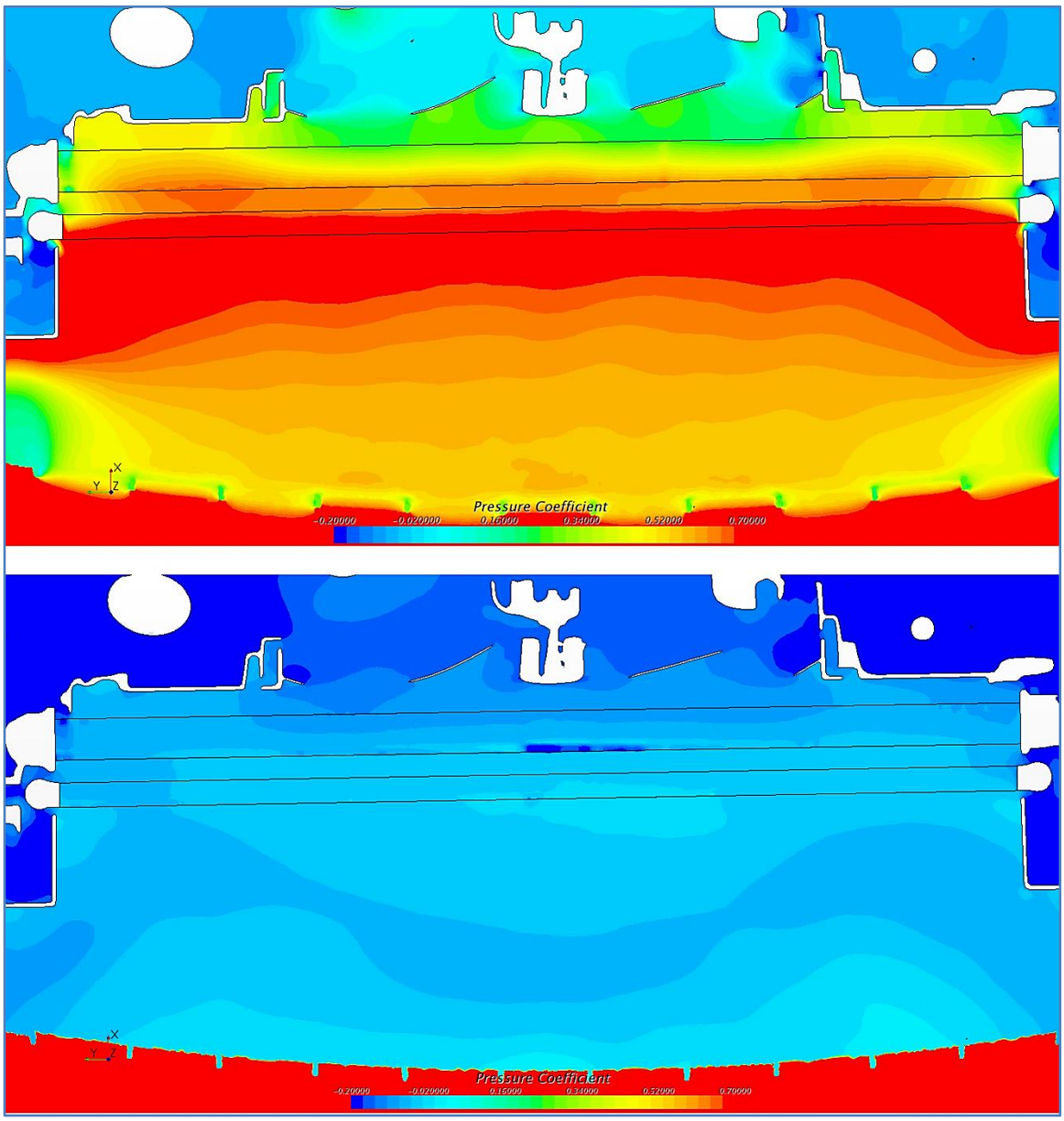

Figure 2.48 - Pressure distribution over the horizontal section plane with coordinates z=+60 mm, detail of the HEXes. Top: baseline; bottom: modified.

These dissimilarities in terms of pressure attenuate when moving upwards along the z direction. Around z=+310 mm, in fact, the flow field between the two configurations in terms of pressure becomes similar, thus implying that the impact of the AGS on this area, though not negligible, is less critical.

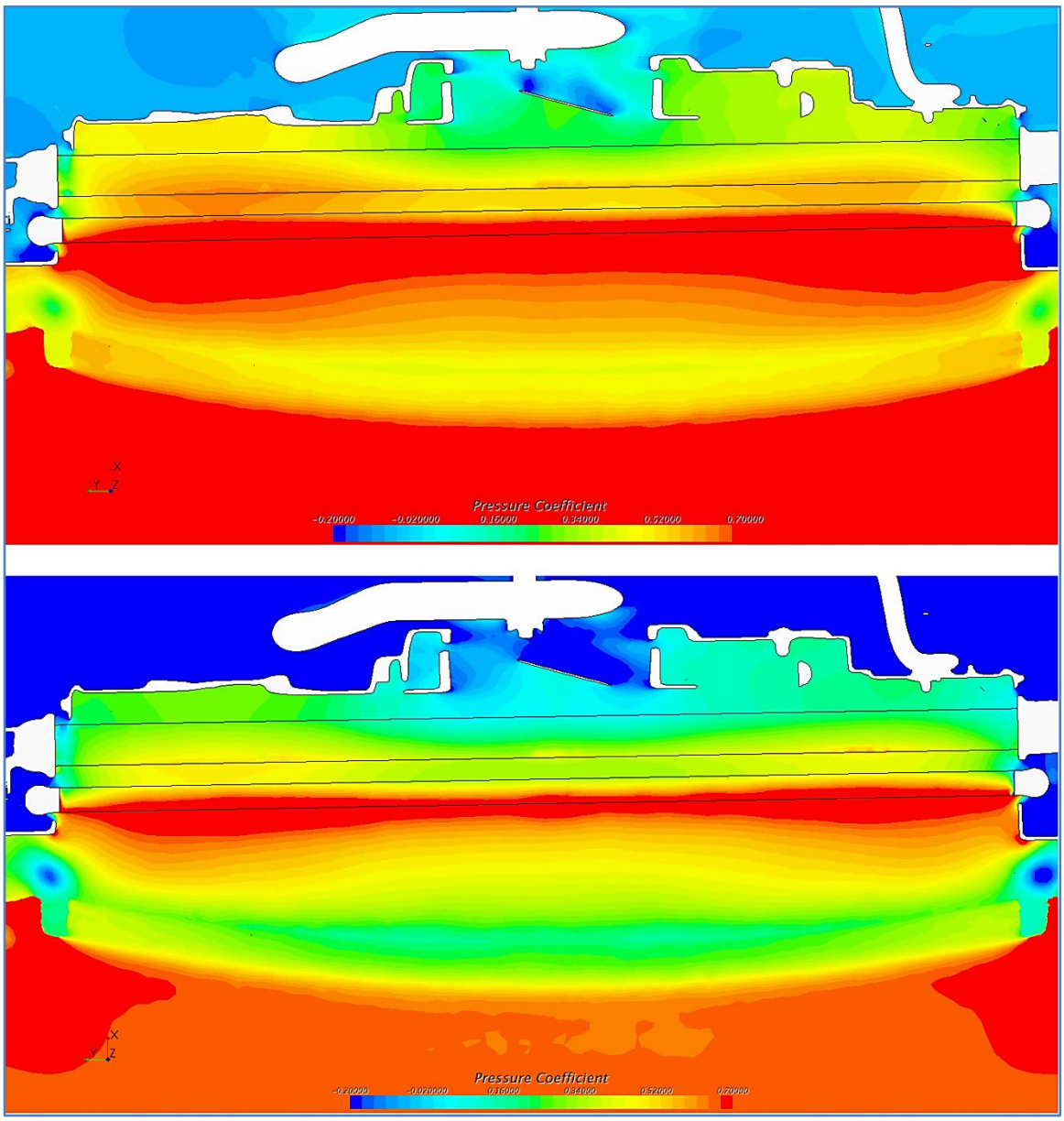

Figure 2.49 - Pressure distribution over the horizontal section plane with coordinates z=+310 mm, detail of the HEXes. Top: baseline; bottom: modified.

Appendix F shows additional maps of the pressure distribution within the engine bay, with details of the longitudinal vertical section planes slicing the underhood area.

2.2.5. VELOCITY FIELD MAPS

This paragraph focuses on the details of the flow field in terms of velocity maps. The local direction and magnitude of the air flow in proximity of the vehicle is analyzed in order to put in evidence aerodynamically critical areas. Two types of maps are presented: both of them represent the so called *line integral convolution* vector profiles of the local velocities of the air surrounding the vehicle surfaces. This technique allows visualizing streamlines all over a given surface, thus indicating the local flow direction in every part of the model. By using color bars with specified variability ranges, then, it is possible to understand the magnitude of the local velocities.

As mentioned above, two types of maps will be shown. In the former, only the absolute value of the local velocity is considered, i.e. it is of interest to consider just the magnitude of the local velocity vector. This is a useful indicator, for instance, in order to understand the magnitude of the local velocity across the heat exchangers. Here, in fact, what matters most is the magnitude of the velocity, which directly affects the heat exchange process effectiveness. On the other hand, for the remaining part of the engine bay, it is also important to understand the direction of the flow in order to identify recirculation areas where the flow direction reverses. This is important to know where the biggest momentum losses occur, which negatively affect the performances in terms of resistance to air (drag).

2.2.5.1. EXTERNAL FLOW FIELD

The following maps show the velocity field on vertical and horizontal section planes slicing the vehicle.

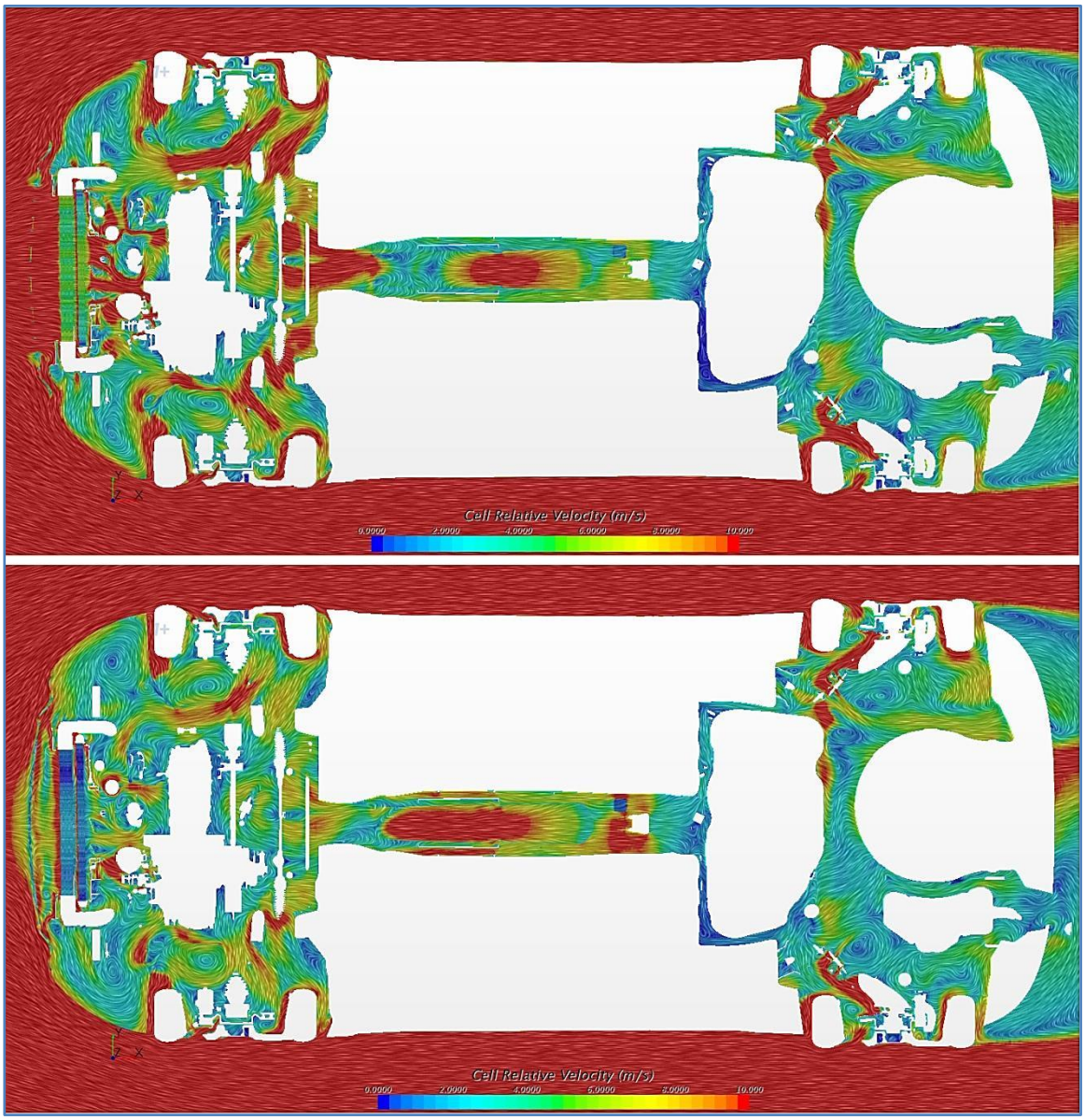

Figure 2.50 - Velocity distribution over the horizontal section plan with coordinates z=0 mm. Top: baseline; bottom: modified.

Substantial differences can be observed in the velocity distribution between the two versions. In particular, it is interesting to notice how the presence of the front grille closure has an important effect even significantly downstream of the inlet. On average, the flow in the underhood area is much slower when the AGS is in its fully closed position, and the red areas, corresponding to the portion of flow with speed higher than 10 m/s, get extremely reduced compared to the baseline case with the open inlet. On the contrary, the flow seems to accelerate

more in the underbody area under the central tunnel, thus showing how the presence of the AGS strongly alters the entire flow field.

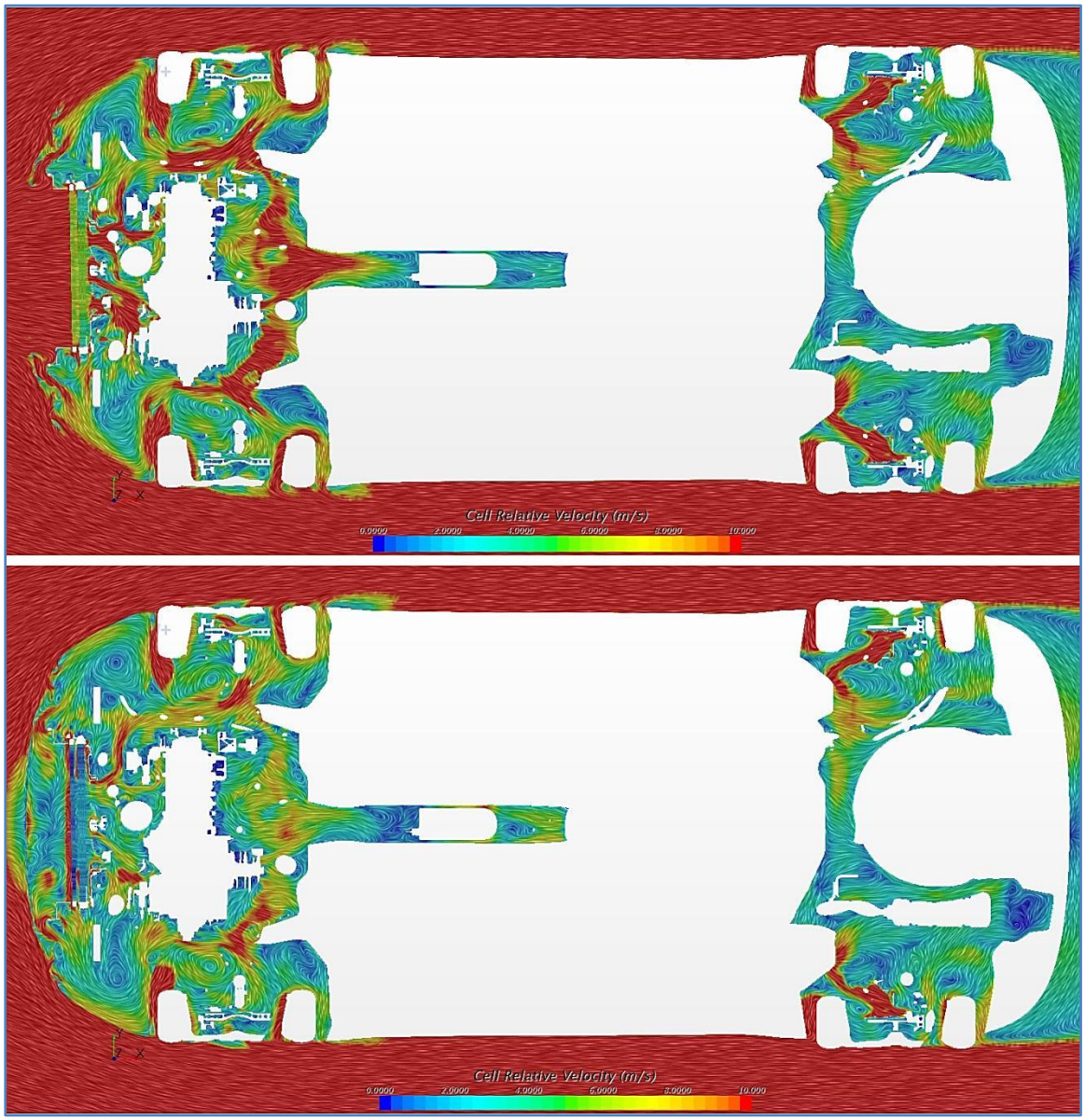

Figure 2.51 - Velocity distribution map over the horizontal plane with coordinates z=+60 mm. Top: baseline; bottom: modified.

Notable differences between the baseline and modified versions take place over a wide range of z positions. In other words, the above maps and the next ones show that the velocity profile is completely different for the two cases even at a big distance in the z direction from the closed inlet. This implies that fairly

dissimilar cooling air flow rates are available to a given component in the two configurations, thus impacting in a non-negligible way on the thermal side.

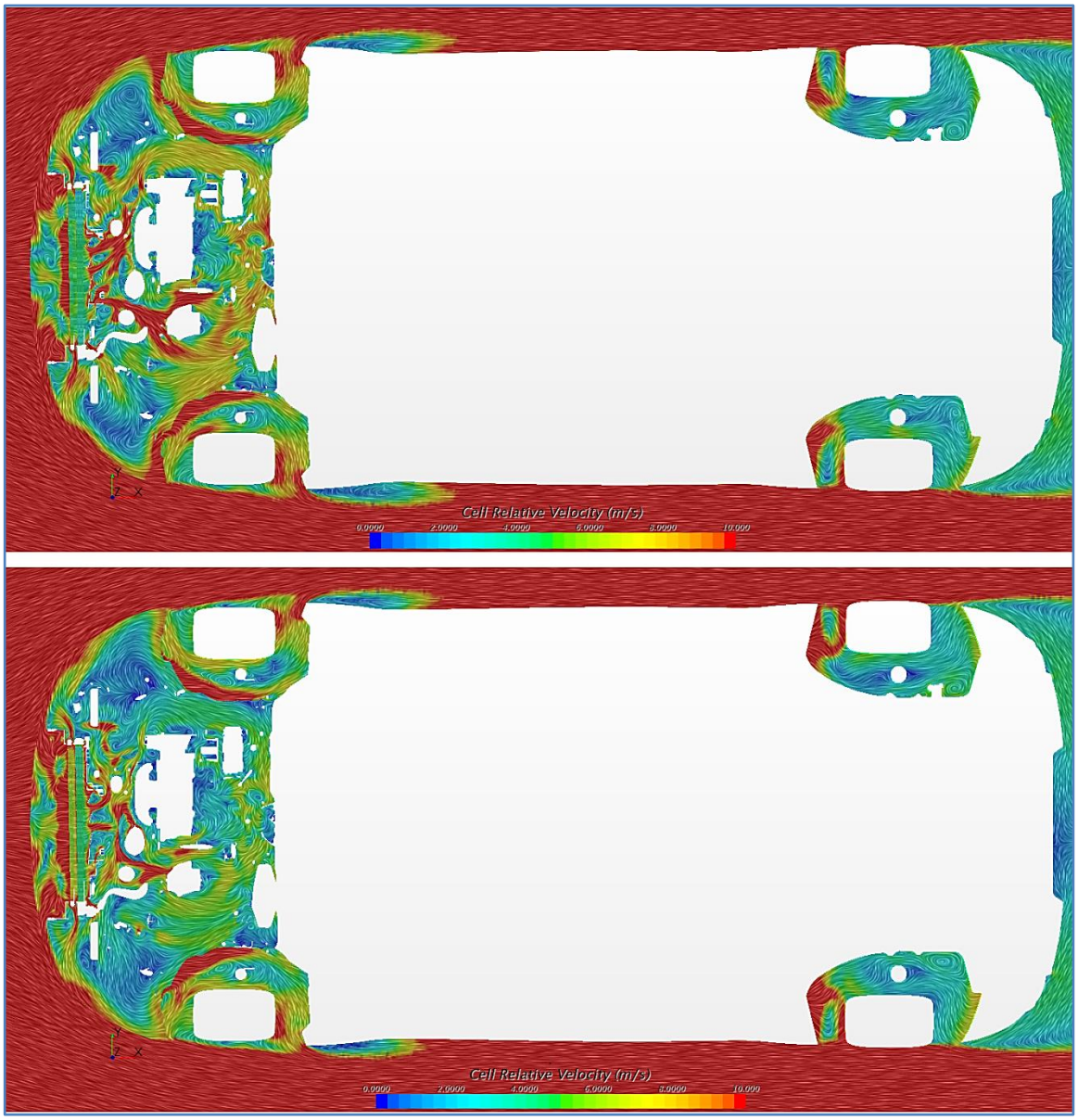

Figure 2.52 - Velocity distribution over the horizontal section plane with coordinates z=+260 mm. Top: baseline; bottom: modified.

Figure 2.53 shows that the underbody flow is absolutely dissimilar for the two configurations, especially if considering the area behind the air dam in proximity of the front axle. Also, it is interesting to notice the reduction in flow separation just downstream of the front wheel-arches for the modified case.

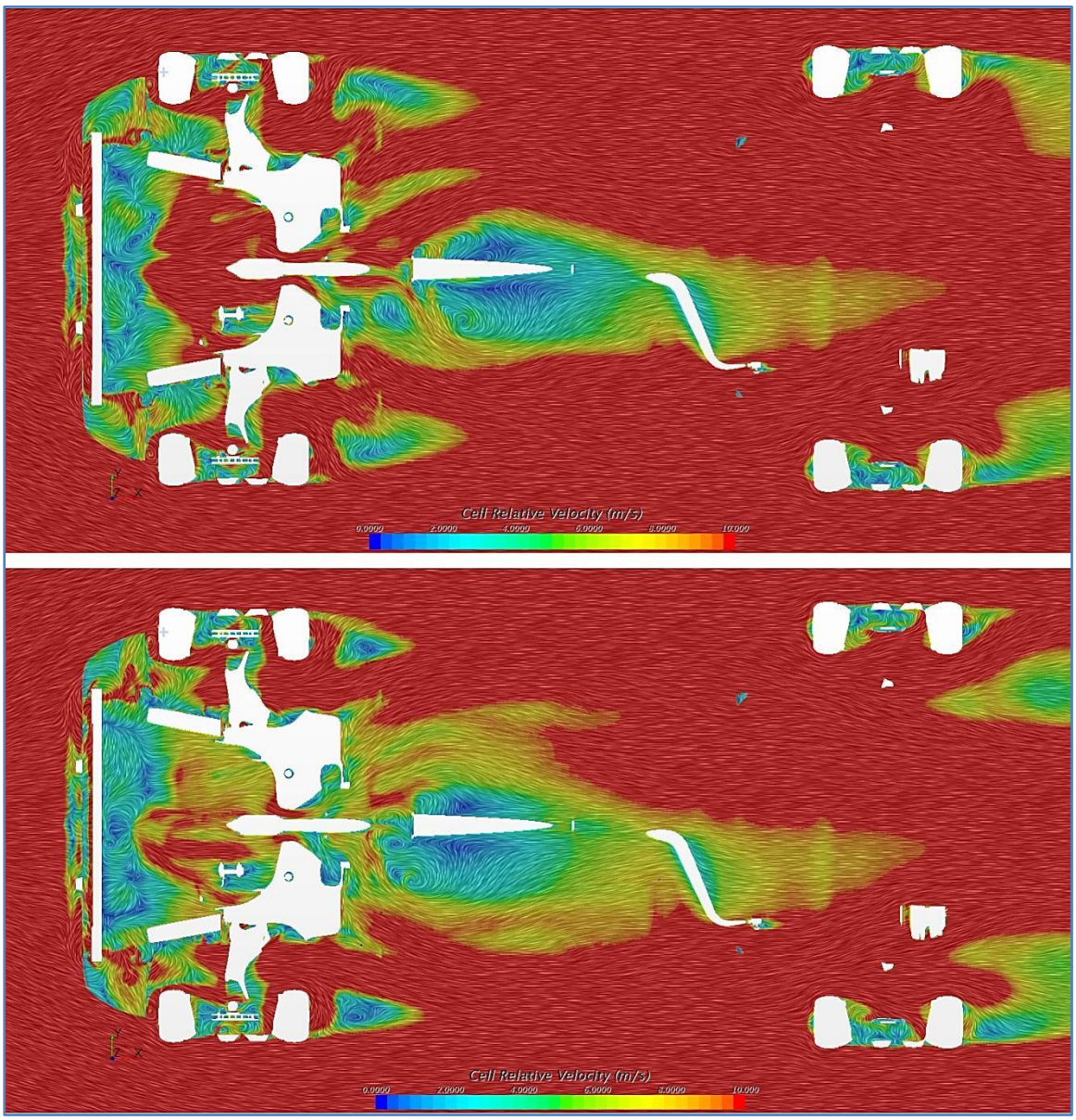

Figure 2.53 - Velocity distribution over the horizontal section plane with coordinates z=-140 mm. Top: baseline; bottom: modified.

The differences in terms of cooling air local velocities are visible also over the vertical section planes slicing the vehicle. Figure 2.54 confirms that the average air velocity in the engine bay is lower for the case with the AGS fully closed. In order to put in evidence the velocity differences of the flow in the underhood and exhaust line area, a variability range has been chosen with speeds varying between 0 m/s and 10 m/s.

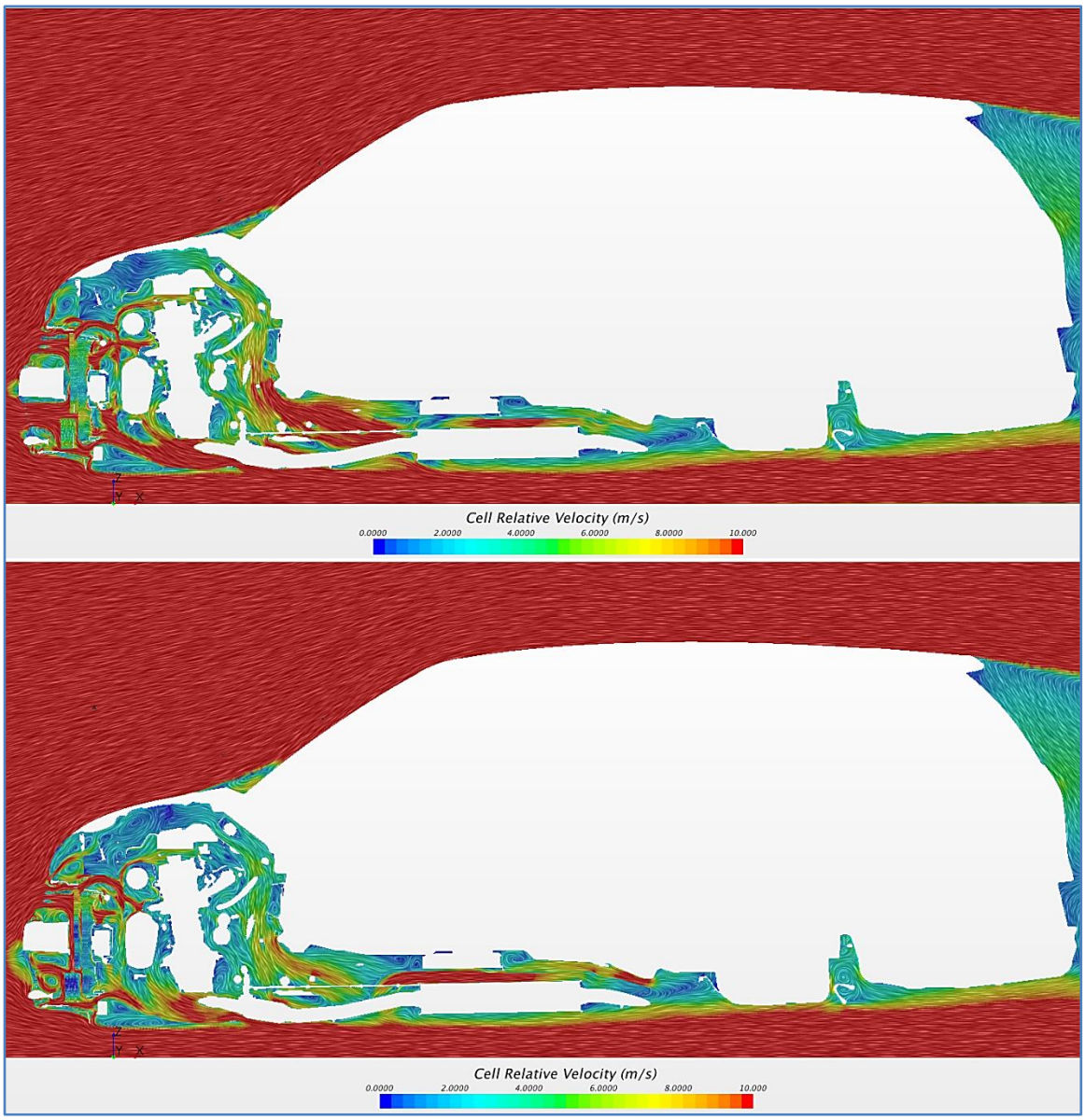

Figure 2.54 -Velocity distribution over the vertical longitudinal mid-plane (y=0 mm). Top: baseline; bottom: modified.

Figure 2.55 shows that by reducing the front inlet opening area, the ram effect available with the baseline version significantly reduces. An indication of this loss is provided by the area circled in black on the map. Here, in fact, it is possible to see how the flow strongly accelerates in proximity of the exit path in the underbody of the vehicle, basically driven by the pressure gradient across the engine bay. This increase in flow speed is much less pronounced in the case with the AGS closed, as clearly visible in the lower part of the figure.

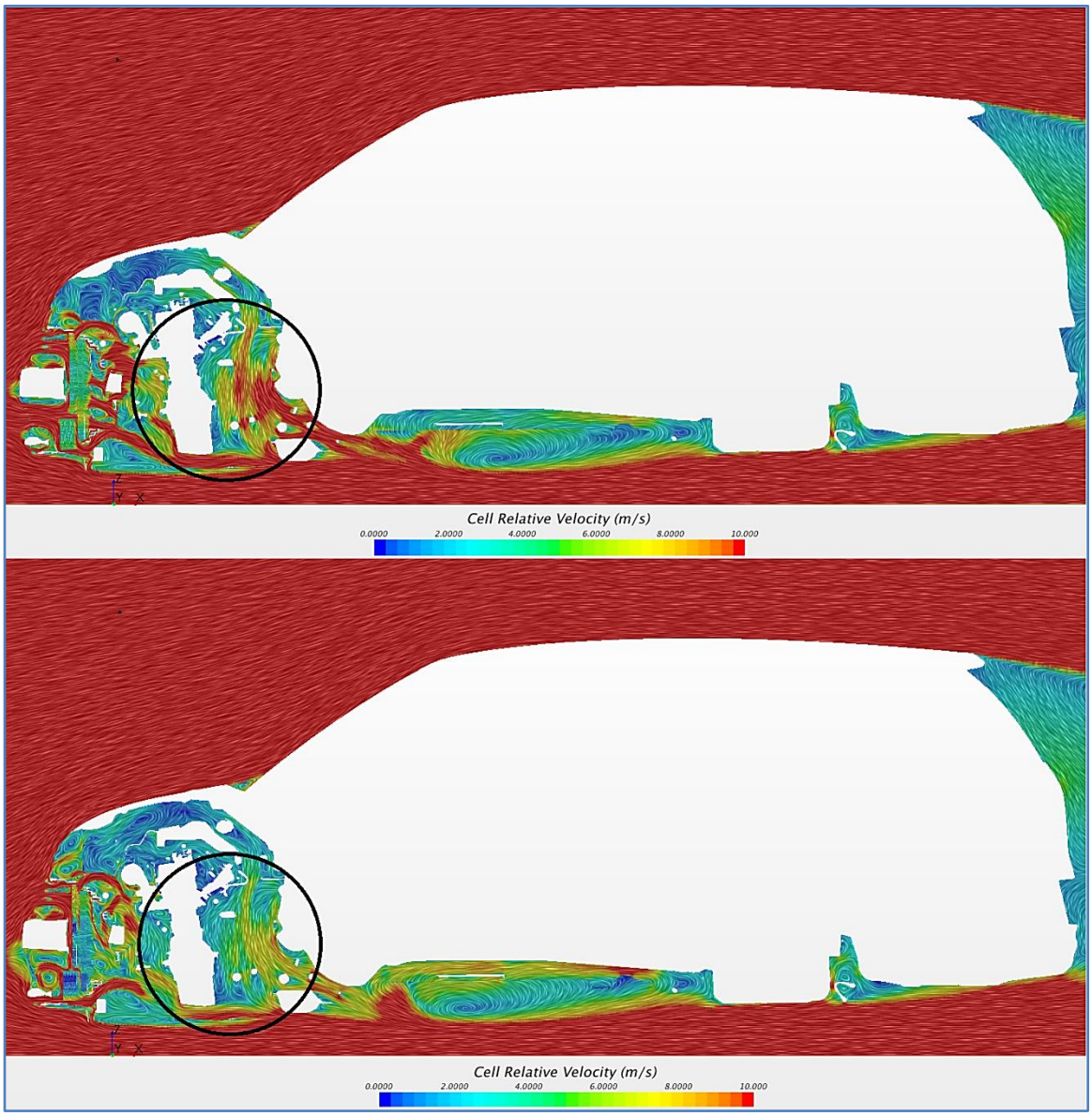

Figure 2.55 - Velocity distribution over the longitudinal vertical section plane with coordinates y=+100 mm. Top: baseline; bottom: modified.

Figure 2.56 shows the reduction in flow separation in proximity of the central muffler. The flow in this area re-attaches to the body surface much earlier than in the baseline case. This local behavior, together with the reduction in flow separation just downstream of the front wheels shown in Figure 2.52, contributes to the reduction in drag highlighted in in the central part of the vehicle in Figure 2.27. Overall, in fact, the decrease in interference drag for the modified case is mostly attributable to the variation of flow field in the central part of the vehicle,

namely to the reduction in flow separation in critical parts of this portion of the car.

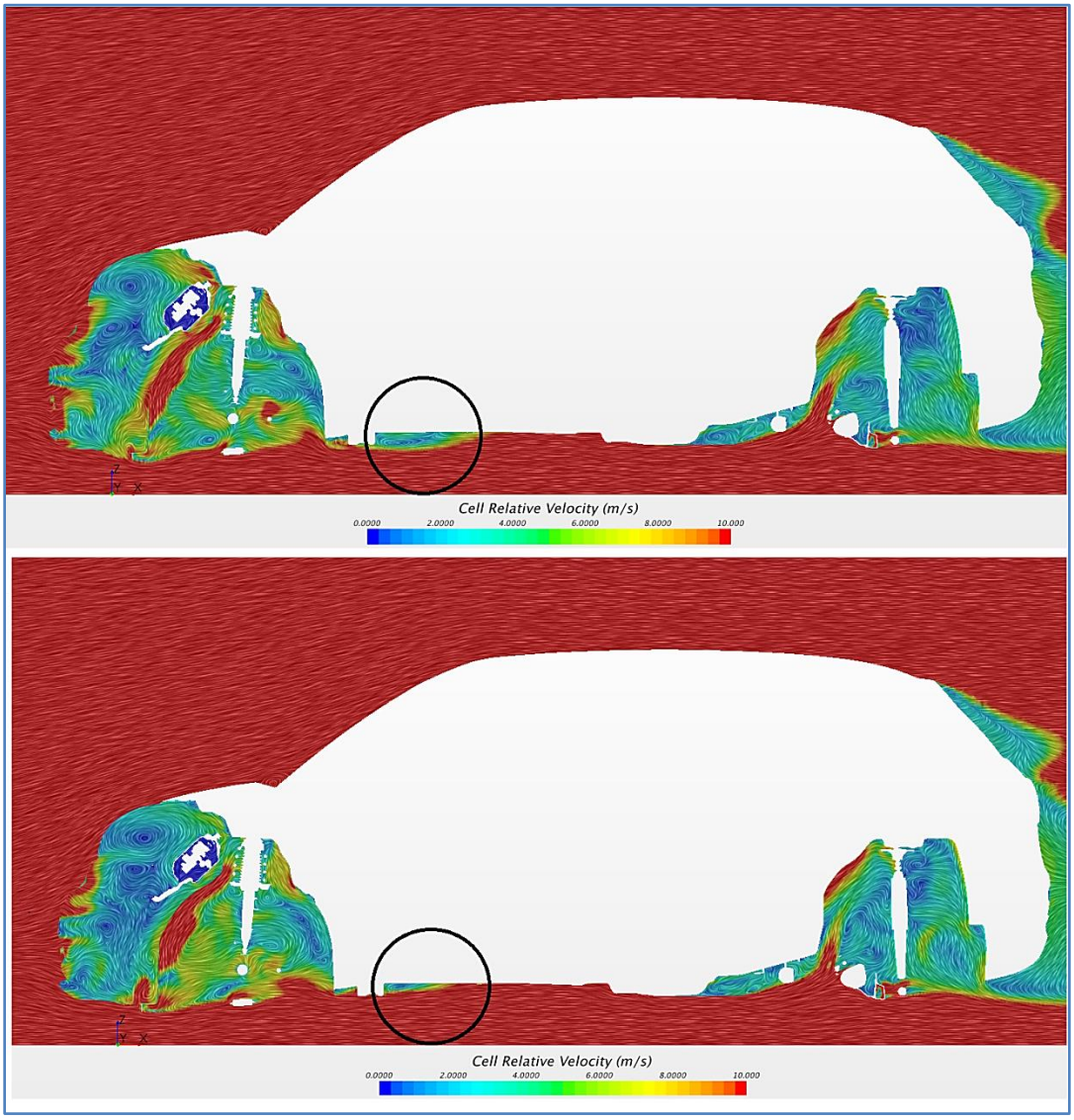

Figure 2.56 - Velocity distribution over the longitudinal vertical section plane with coordinates y=+600 mm. Top: baseline; bottom: modified.

2.2.5.2. ENGINE BAY FLOW FIELD

After considering the whole field surrounding the entire car body, it is now possible to concentrate on the details of the flow in the engine bay.

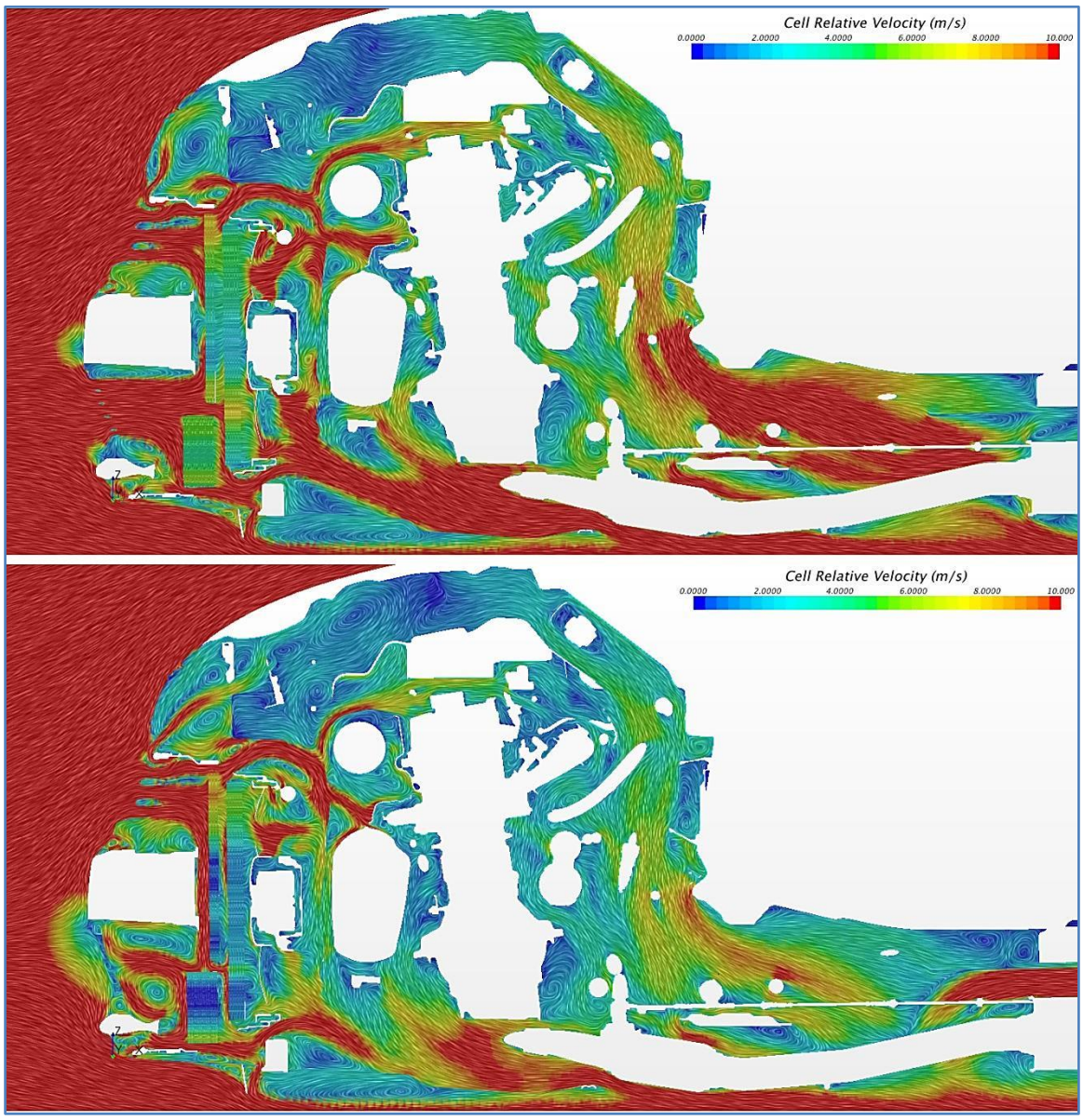

Figure 2.57 - Velocity distribution in the engine bay, vertical longitudinal mid-plane (y=0 mm). Top: baseline; bottom: modified.

On average, the cooling air entering the underhood area moves faster in the baseline case, even though this trend may locally be the opposite. Note, for instance, the area just upstream the muffler and the flow across the exchangers: on this plane here is the location where the main dissimilarities occur between the two versions, as shown in the figure above.

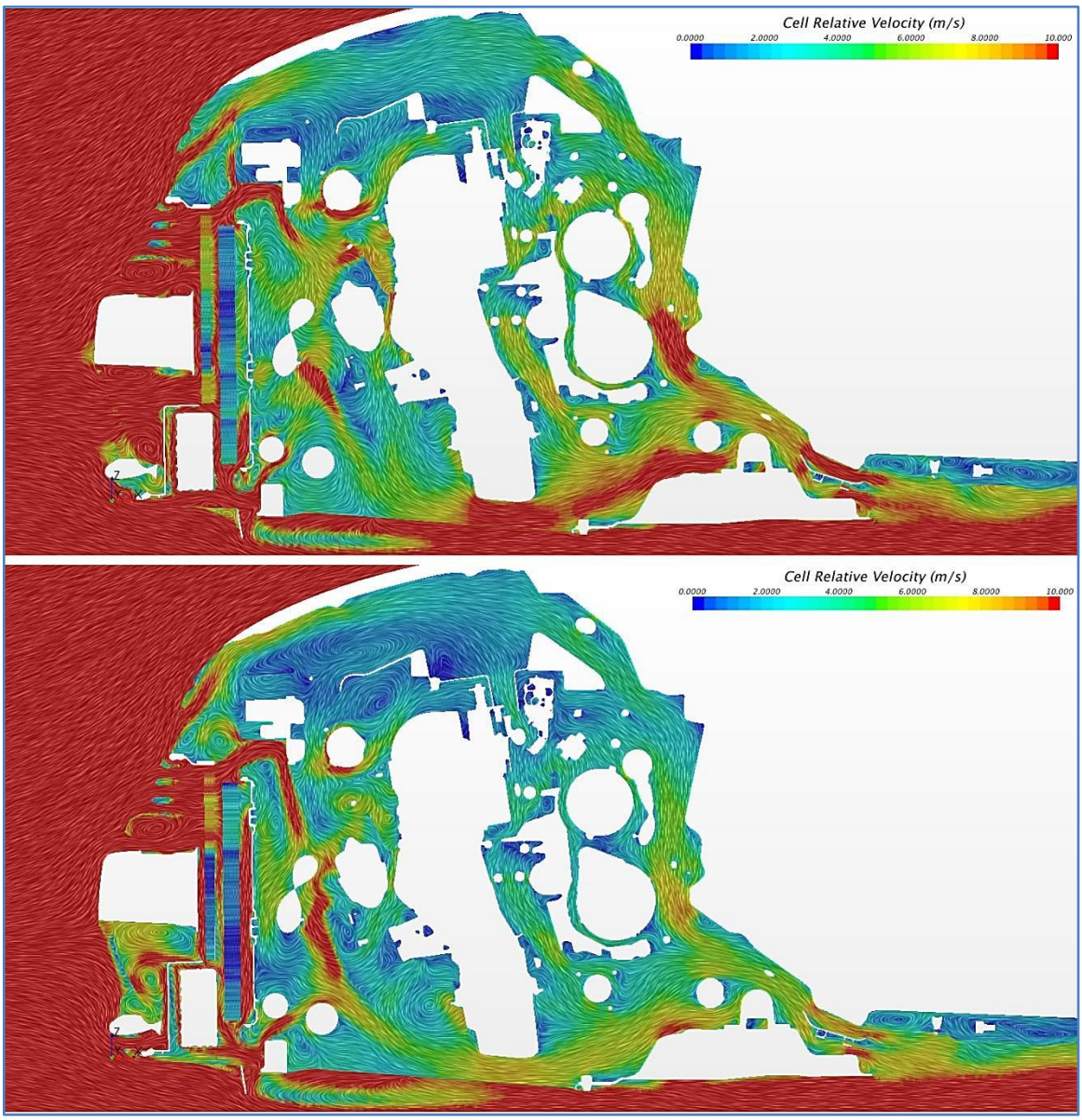

Figure 2.58 - Velocity distribution in the engine bay, vertical longitudinal section plane with coordinates y=+300 mm. Top: baseline; bottom: modified.

The adverse effect of the reduced pressure gradient driving the flow from the front inlet to the outlet in the underbody causes a large recirculation area to appear in the upper part of the engine bay. This is also confirmed by the maps showing the magnitude of the x component of the velocity vector. Figure 2.59 and Figure 2.60 display such maps for the vertical longitudinal section planes with coordinates y=0 mm and y=+300 mm. Large recirculation vortices take place in different areas of the engine bay. Here significant momentum losses

occur which decrease the overall flow energy, thus negatively impacting on the drag performances of the vehicle. Due to the extremely dense packaging of the engine compartment, however, almost no room is left to the aerodynamicist for fitting in an optimal way the underhood components. This constrains a lot the aerodynamic aspect, which is in charge of coping with strict requirements imposed by the powertrain and packaging constraints.

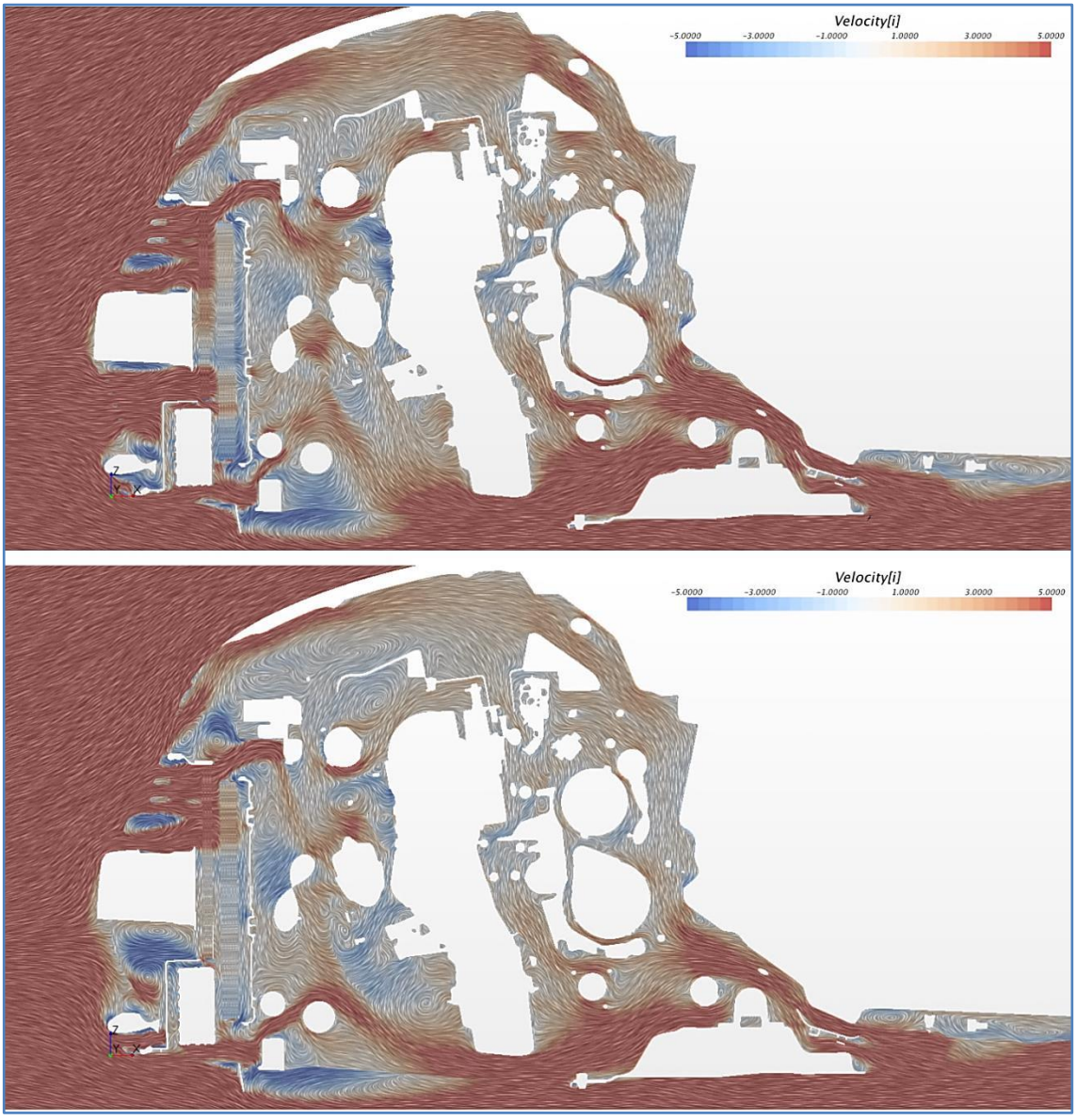

Figure 2.59 - Velocity distribution in the engine bay, vertical longitudinal section plane y=+300 mm. The colors indicate the magnitude of the x component of the vector of the local velocity. Top: baseline; bottom: modified.

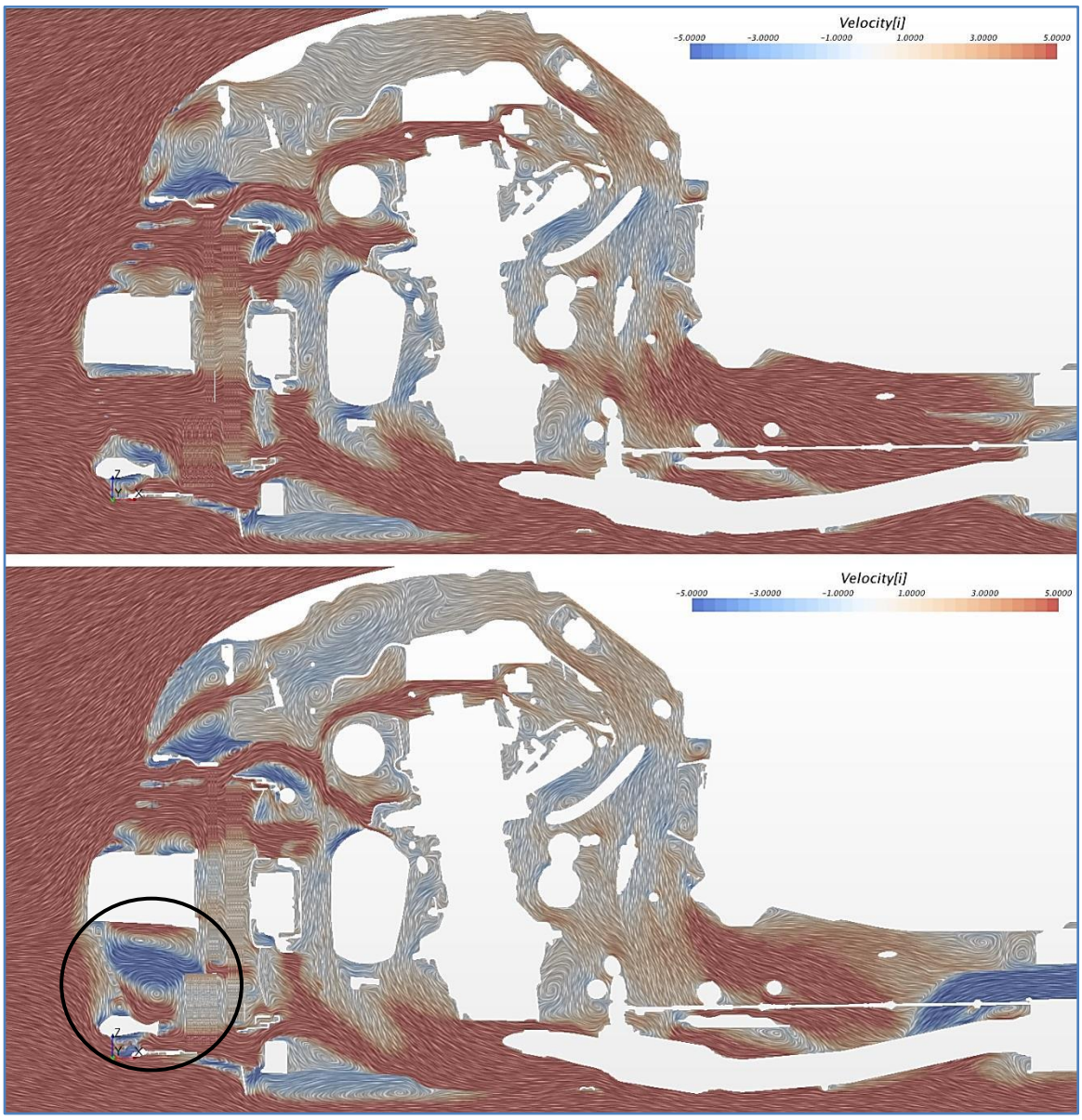

Figure 2.60 - Velocity distribution in the engine bay, detail of the x component of the local velocity vector. Vertical longitudinal mid-plane (y=0 mm). Top: baseline; bottom: modified.

Figure 2.60 indicates a large turbulent area immediately downstream of the closed AGS, where two large vortices form when the two cooling airflow streams incoming from the upper and lower open inlets gather and interact in the suction area just behind the shutter. In fact, for the case with closed AGS, these two flows are driven partially by the pressure gradient across the cooling module, partially from the low pressure area just behind the closed inlet vent. Therefore, a part of each of the two streams gets deviated towards this zone, and when these two

currents meet, two big vortical areas form. These vortex structures are fairly strong and extend over the entire transversal section behind the inlets, for more than 600 mm in the y direction (from -300 mm to +300 mm approximately).

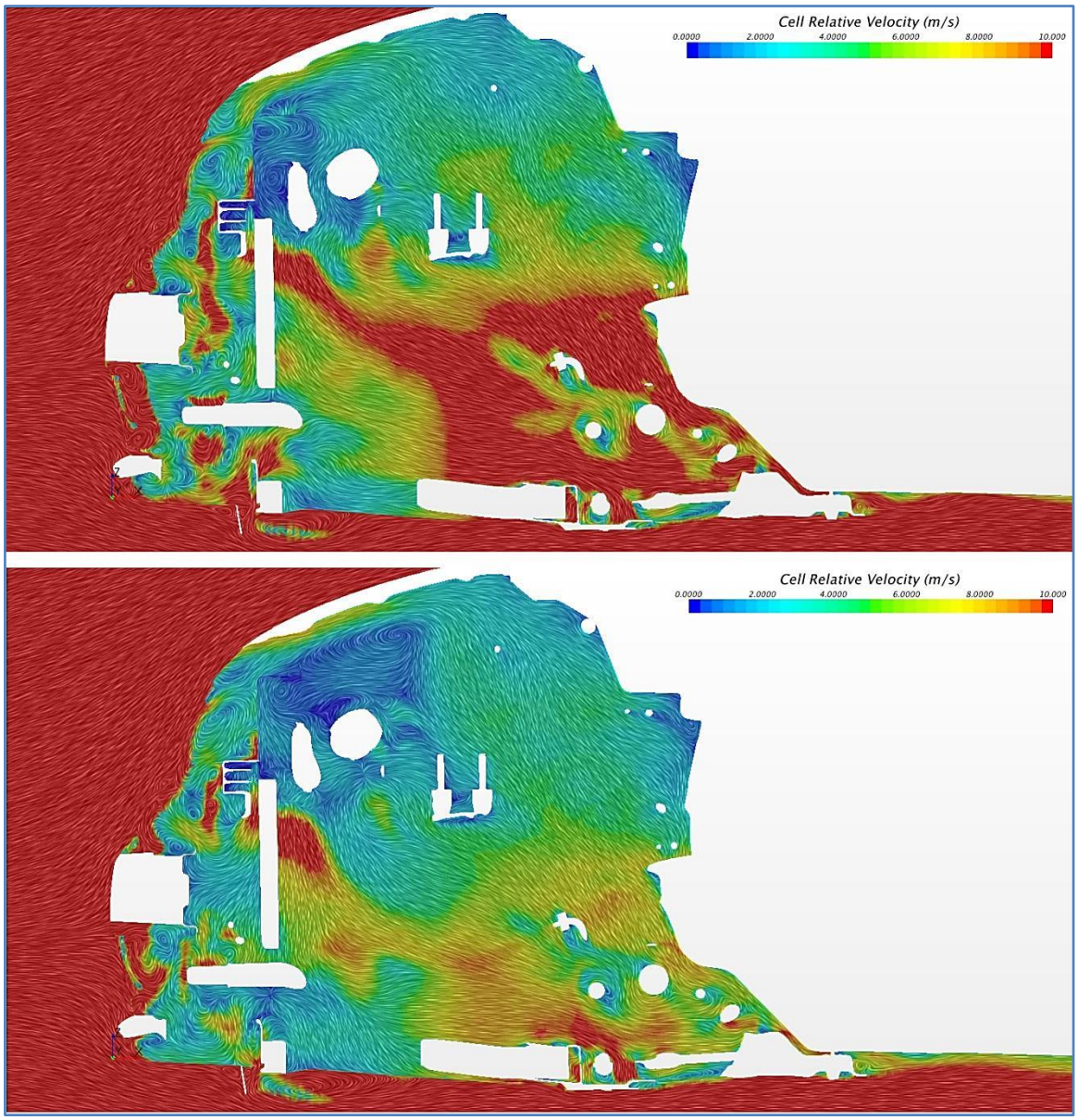

Figure 2.61 - Velocity distribution in the engine bay, vertical longitudinal section plane with coordinates y=+400 mm. Top: baseline; bottom: modified.

Figure 2.61 shows the remarkable variation of local airflow speed between the two configurations even at a large distance from the closed inlet in both x and y direction.

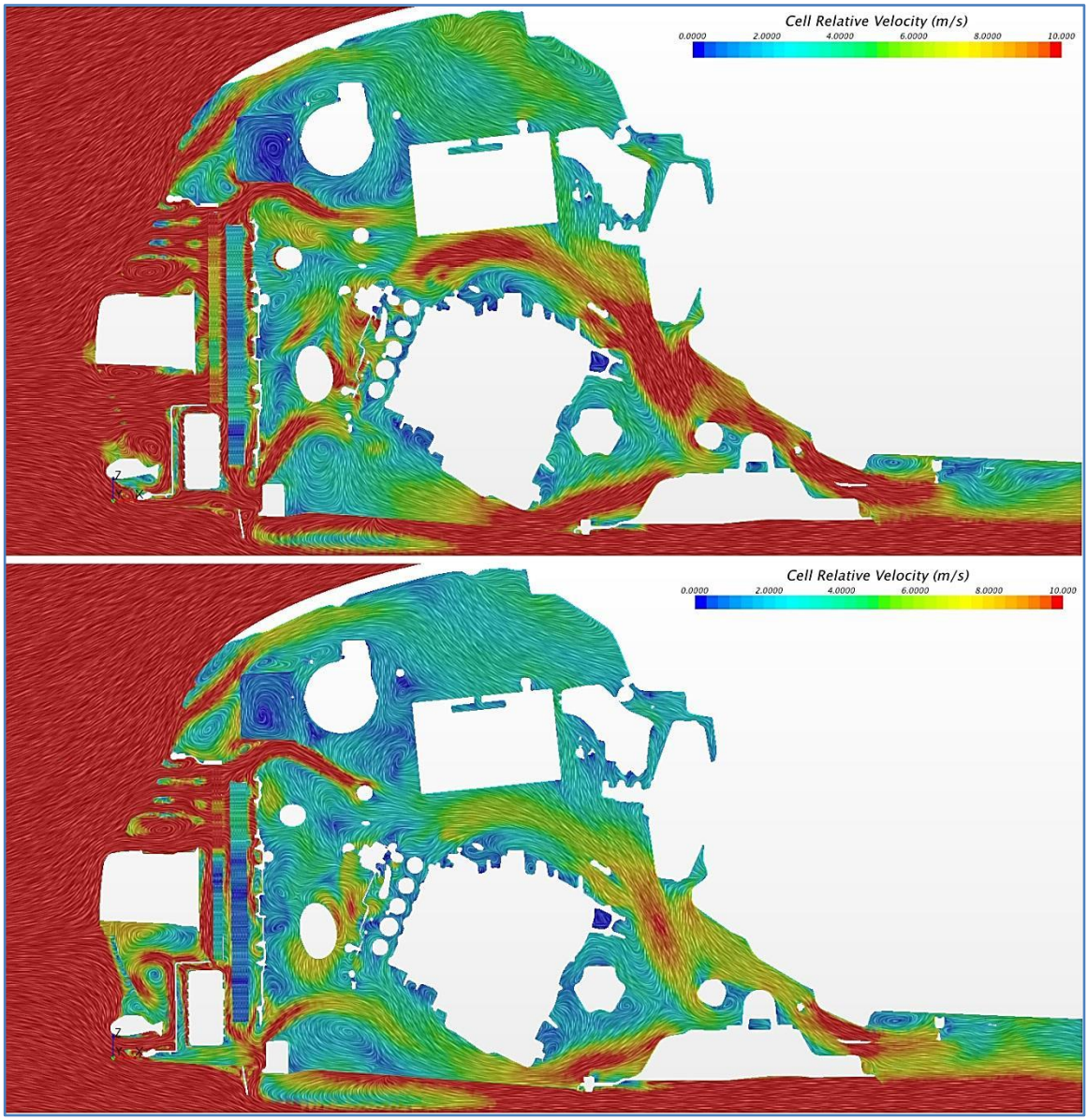

Figure 2.62 - Velocity distribution in the engine bay, vertical longitudinal section plane with coordinates y=-300 mm. Top: baseline; bottom: modified.

Figure 2.62 puts in evidence the reduction in airflow speed around the battery (the square shape on the upper part of the engine bay) and the transmission (the white block just under the battery) when the AGS is fully closed. This will negatively affect the cooling efficacy of the air flowing around these two components, thus resulting in higher temperatures.

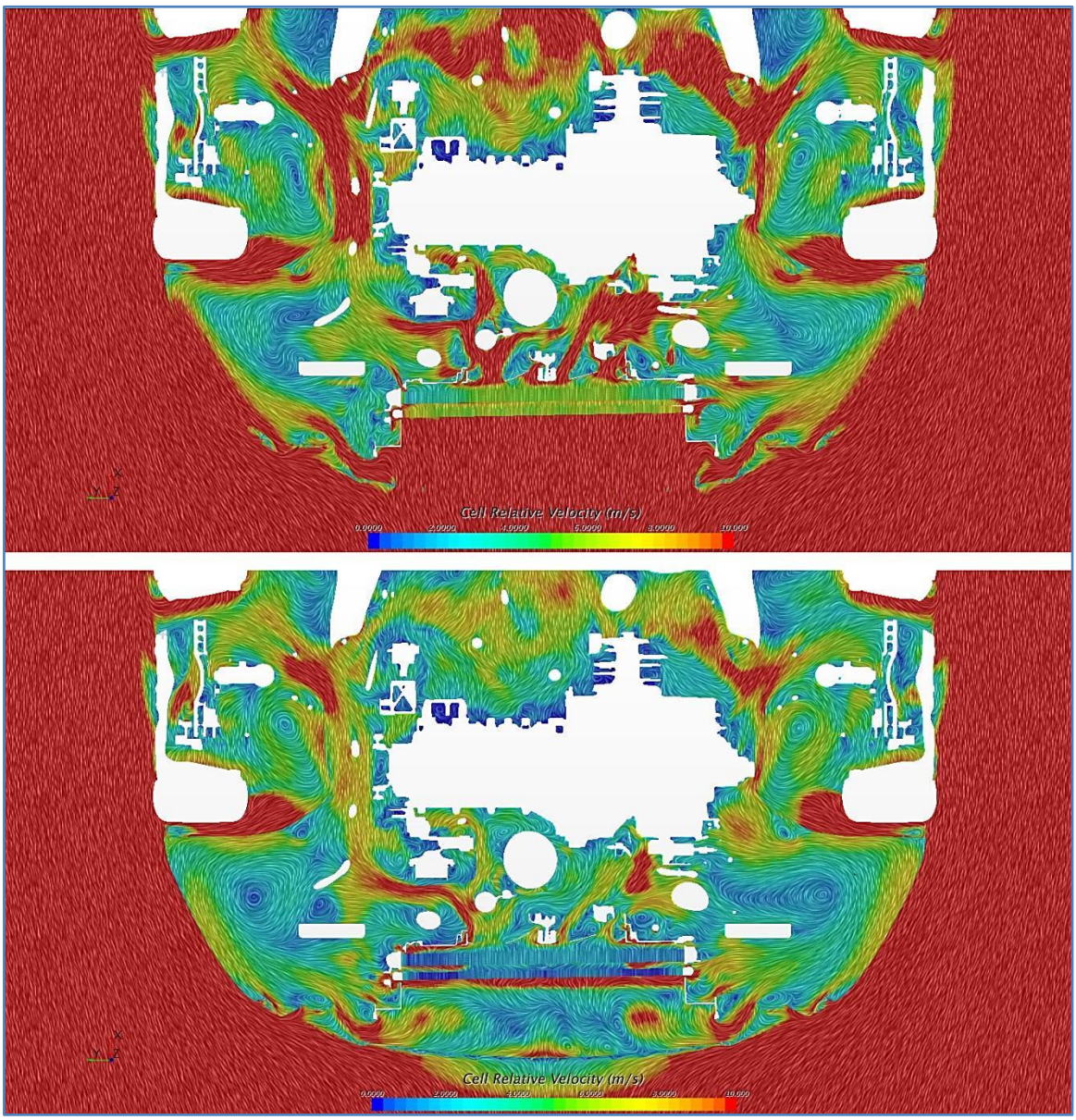

Figure 2.63 - Velocity distribution over the horizontal section plane z=+60 mm, detail of the engine bay. Top: baseline; bottom: modified.

The above picture shows the reduction in air speed downstream of the engine for the case with closed AGS, as well as the direct effect of the shutter in proximity of the closed inlet. Overall, a decrease in the average speed of the cooling air entering the engine bay is observed when the AGS is in fully closed position. This trend is observed not just within the engine bay, but also in

proximity of the outlet area of the cooling air, where the flow is much faster in the baseline case, as shown in the figure below.

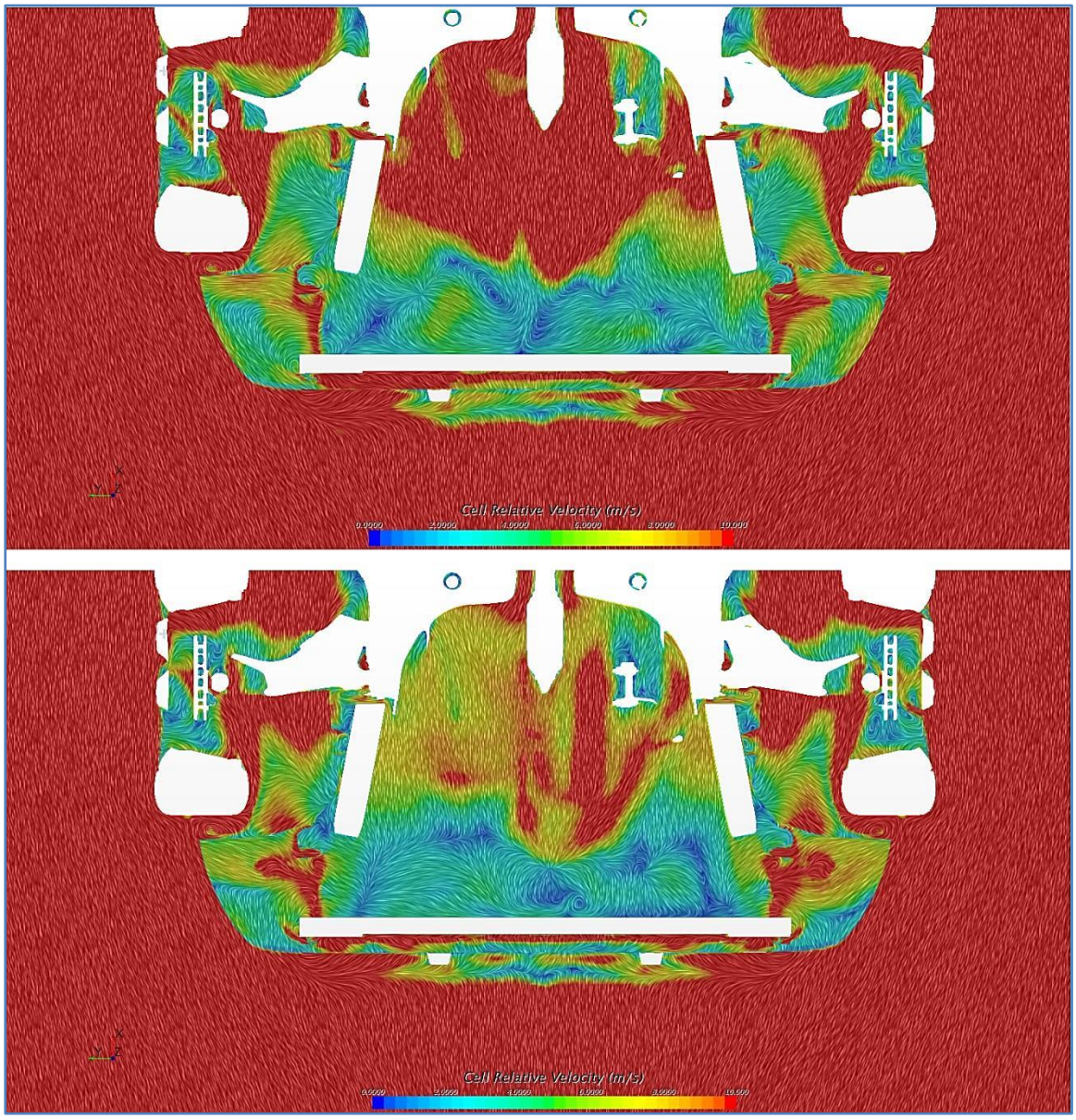

Figure 2.64 - Velocity distribution over the horizontal section plane z=-140 mm, detail of the engine bay. Top: baseline; bottom: modified.

The colors in the map in display the magnitude of the x component of the local velocity vector in the two versions. As can be seen, the slower areas seen in the map above are confirmed by this visualization scene, which also show that larger recirculation areas are present for the closed AGS case.

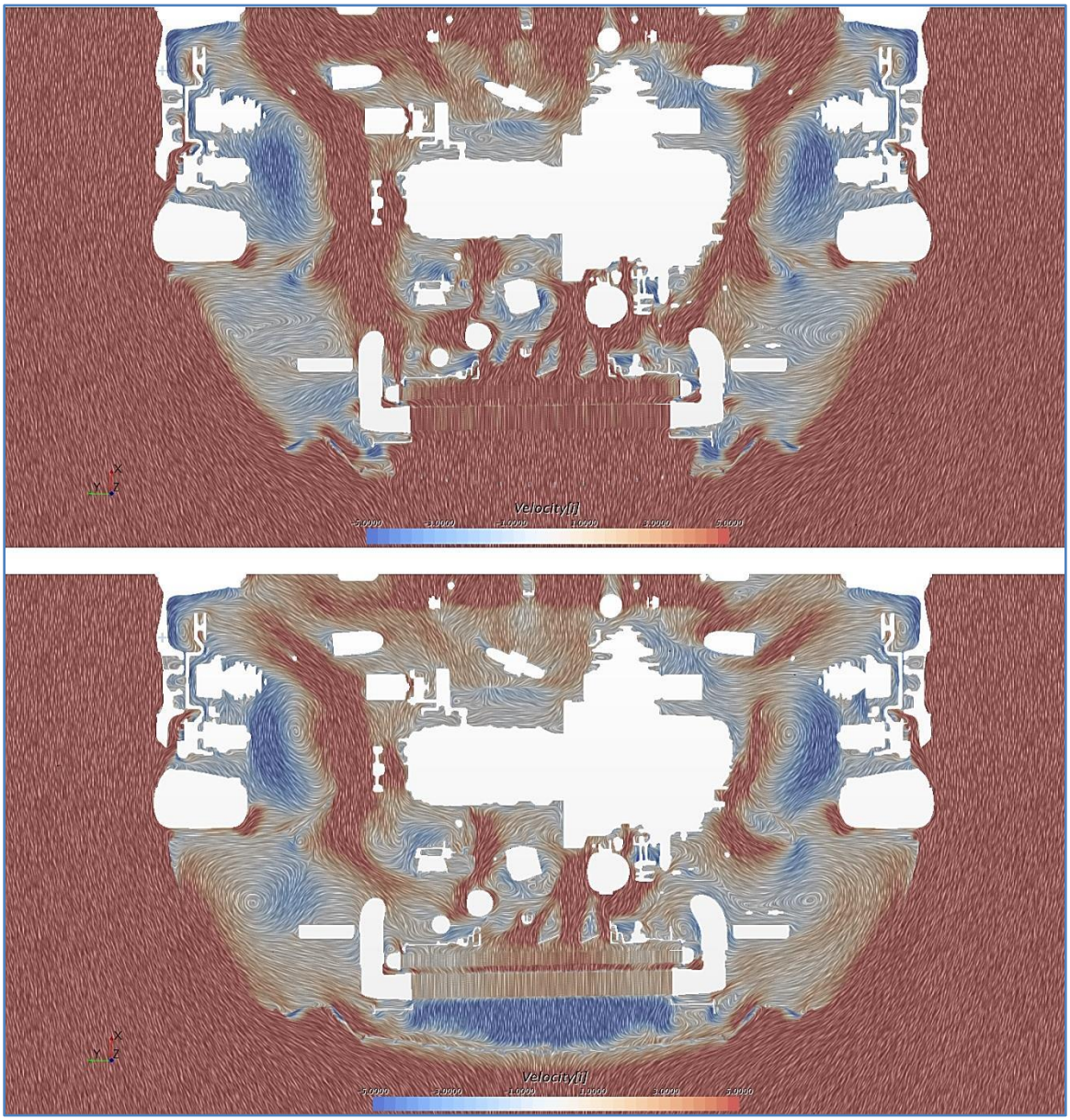

Figure 2.65 - Velocity distribution (colors indicate the magnitude of x component of the local velocity vector) over the horizontal section plane z=+10 mm. Top: baseline; bottom: modified.

The large blue area upstream of the HEXes confirms the presence of a strong transversal vortex where the airflow rolls just behind the shuttered inlet. Clearly, this has a strong impact on the flow crossing the heat exchangers, because the reduction in speed in the exchangers directly affects the thermal performances by worsening the heat transfer process efficiency.

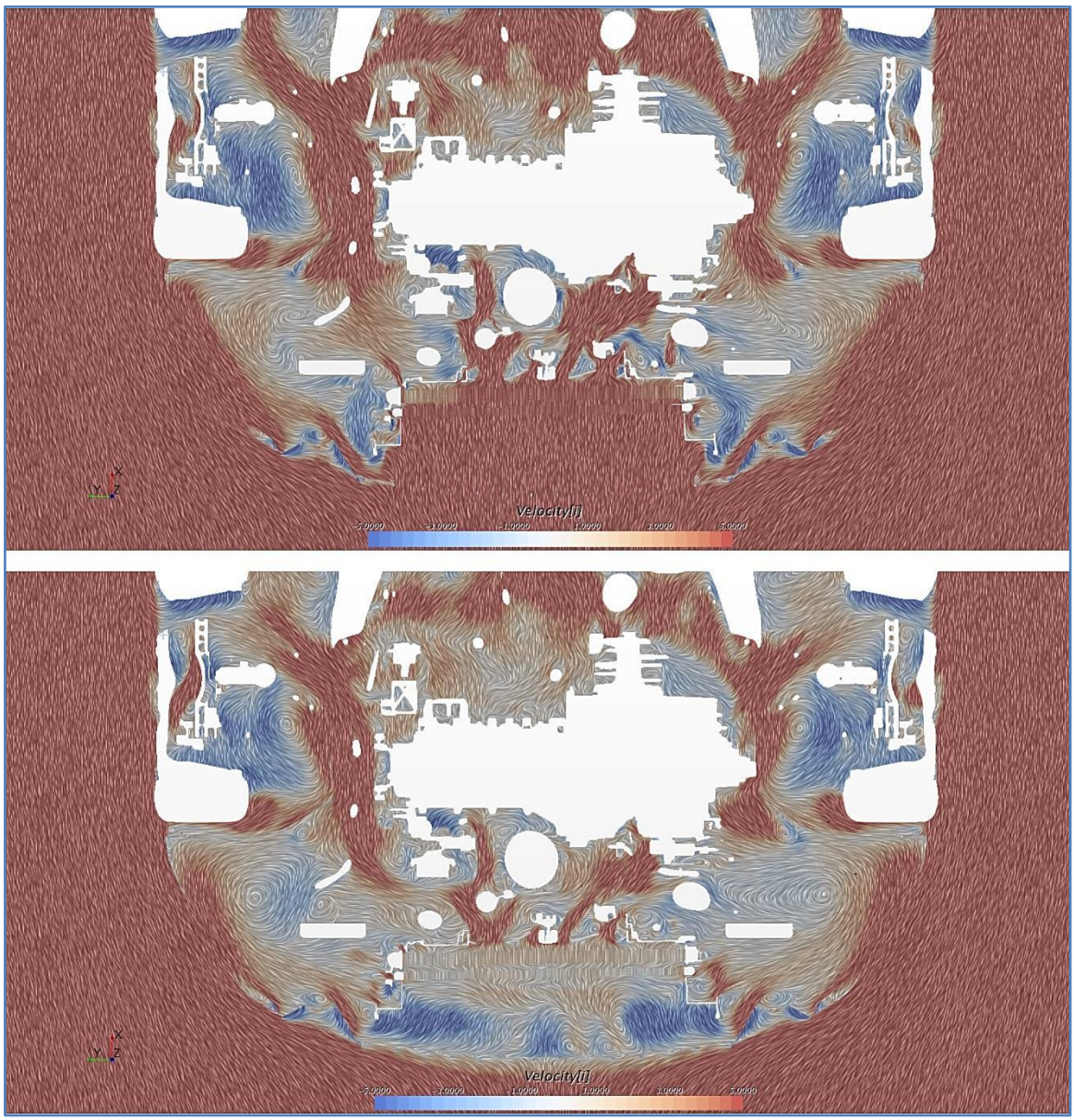

Figure 2.66 - Velocity distribution (colors indicate the magnitude of x component of the local velocity vector) over the horizontal section plane z=+60 mm. Top: baseline; bottom: modified.

Figure 2.66 shows that when closing one of the inlets the flow across the exchangers locally slows down in certain area, even reversing its direction at some points, as indicated by some blue stripes within the radiator and A/C condenser.

The following figures concentrate on the details of the air velocity across the HEXes. They are extremely useful to get an idea about the thermal behavior variation observed when the AGS closes one of the front vents.

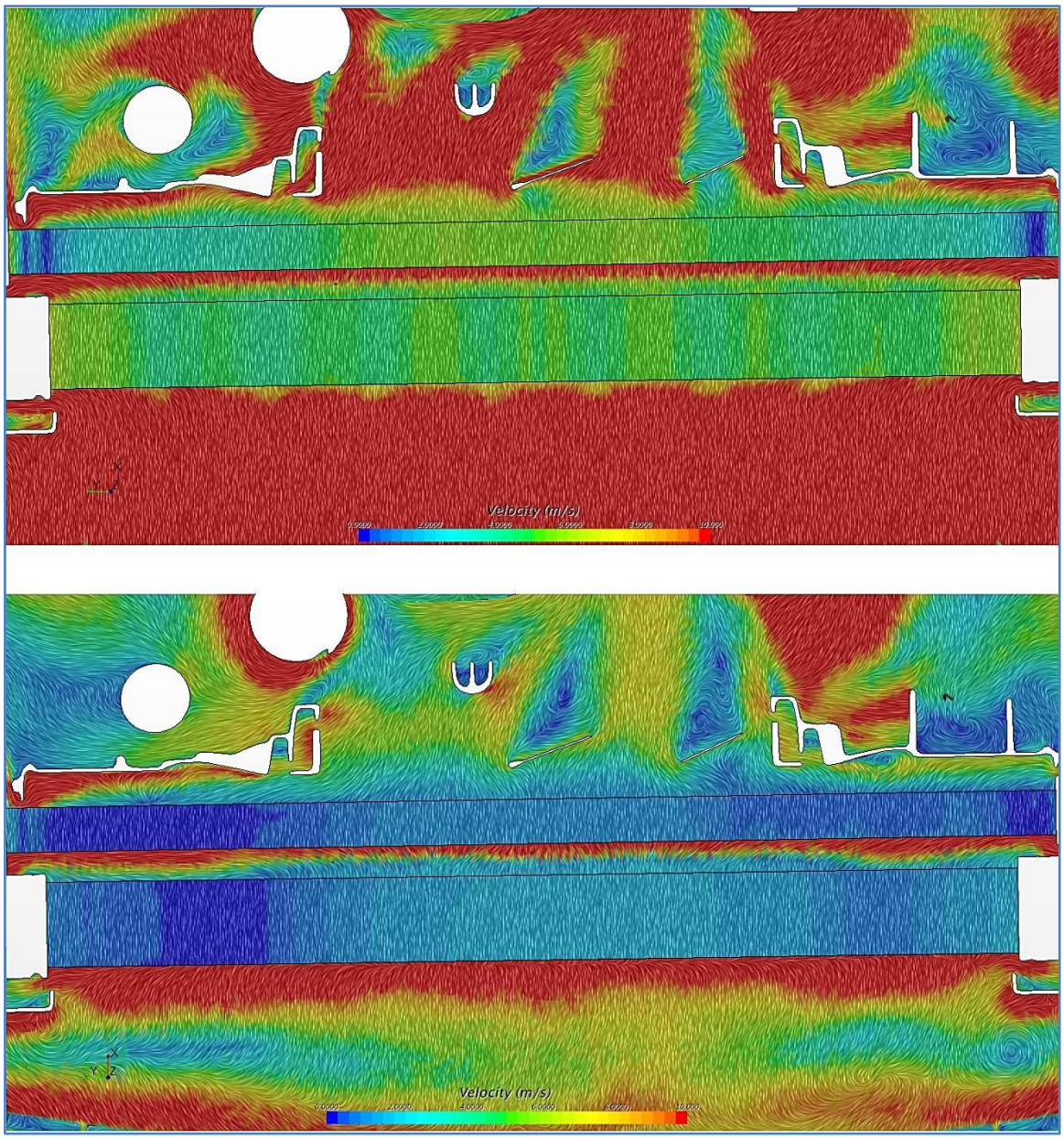

Figure 2.67 - Velocity distribution over the horizontal section plane z=0 mm, detail of the HEXes. Top: baseline; bottom: modified.

The flow velocity in the exchangers is evidently slower in the area just behind the shuttered main central grille for the case fitting the AGS system. This

has a strong reverberation on their thermal power rejection ability, so that countermeasures might be required to avoid engine overheating. However, the cooling system management aspect of the problem goes beyond the scope of this thesis, whose main focus from a thermal point of view is on the temperatures of underhood components. However, the above consideration serves as a reminder that even if some horsepower can be saved when fitting the AGS onboard by reducing the aerodynamic power request at the test speed, some additional horsepower may be required by the cooling system coolant pump and A/C circuit pump in order to circulate more coolant so as to cope with the reduction of cooling air flow rate in order to satisfy a given thermal power dissipation requirement. Also, a proper management of the cooling fan is necessary, so that a smart approach in the control algorithm development is needed in order to avoid designing a system which shuts one of the inlet but then it needs power to turn the fan on in order to draw more air through the exchangers. The control system, however, must be able to understand through the use of temperature sensors (already present in the baseline version) whether too high temperatures are reached for some critical components and for the coolants, so that in case of temporary peaks it can operate the fan for short periods thus getting back to optimal operating values.

Figure 2.68 confirms the above behavior across the heat exchangers, where the flow slows down. In particular, two very slow areas on the sides of the air conditioning condenser are present on the section plane z=+60 mm. These low speed zones, already present in the baseline configuration, are maintained also in the modified setup, but their intensity is even lower, thus worsening the exchanger efficiency in this area.

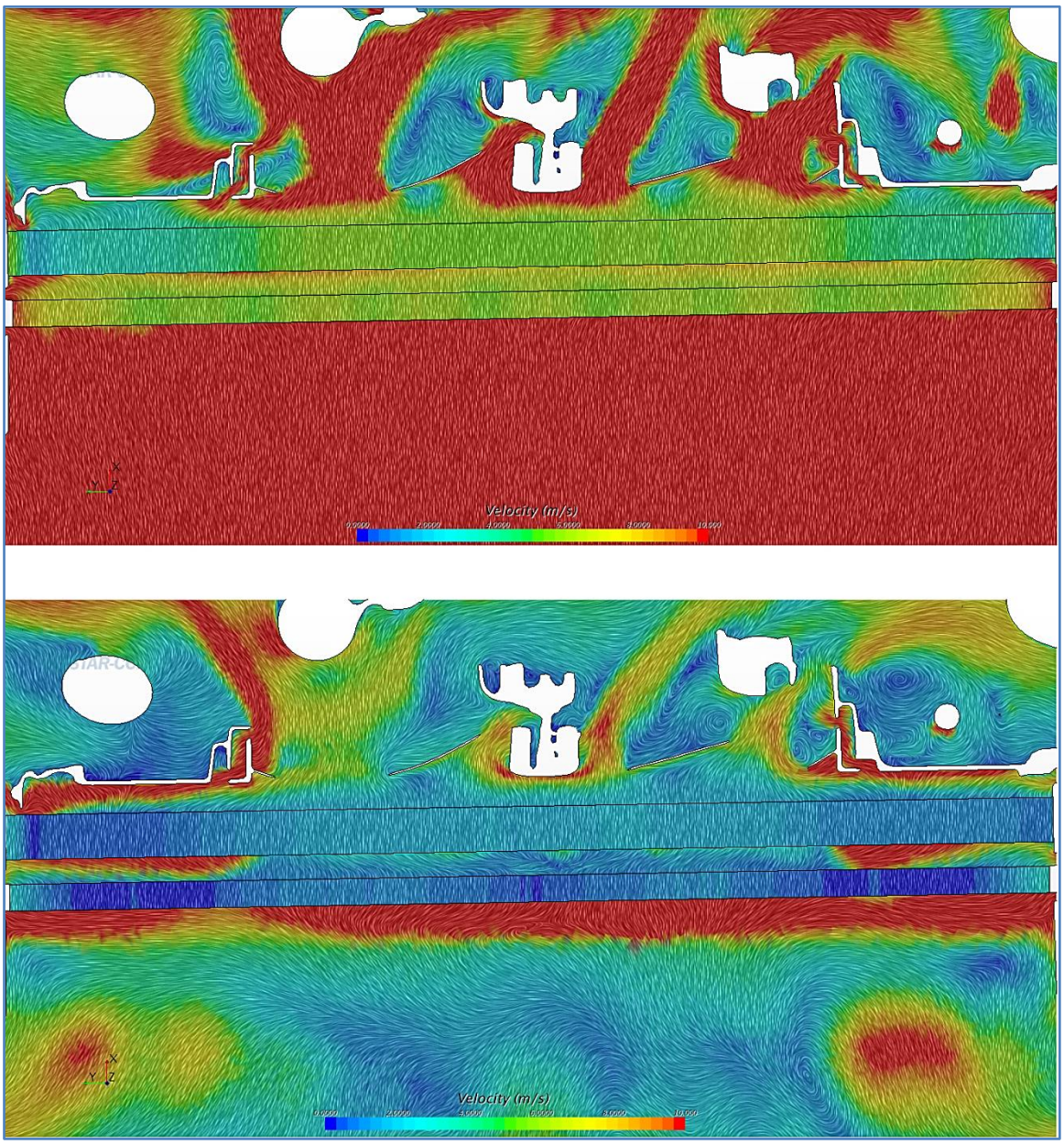

Figure 2.68 - Velocity distribution over the horizontal section plane z=+60 mm, detail of the HEXes. Top: baseline; bottom: modified.

Figure 2.69 shows that the situation becomes particularly critical for the intercooler (the bigger rectangle on the lower part of the figure, just under the radiator in the top view below), thus confirming the reduction of over 58% in the mass flow rate discussed before.

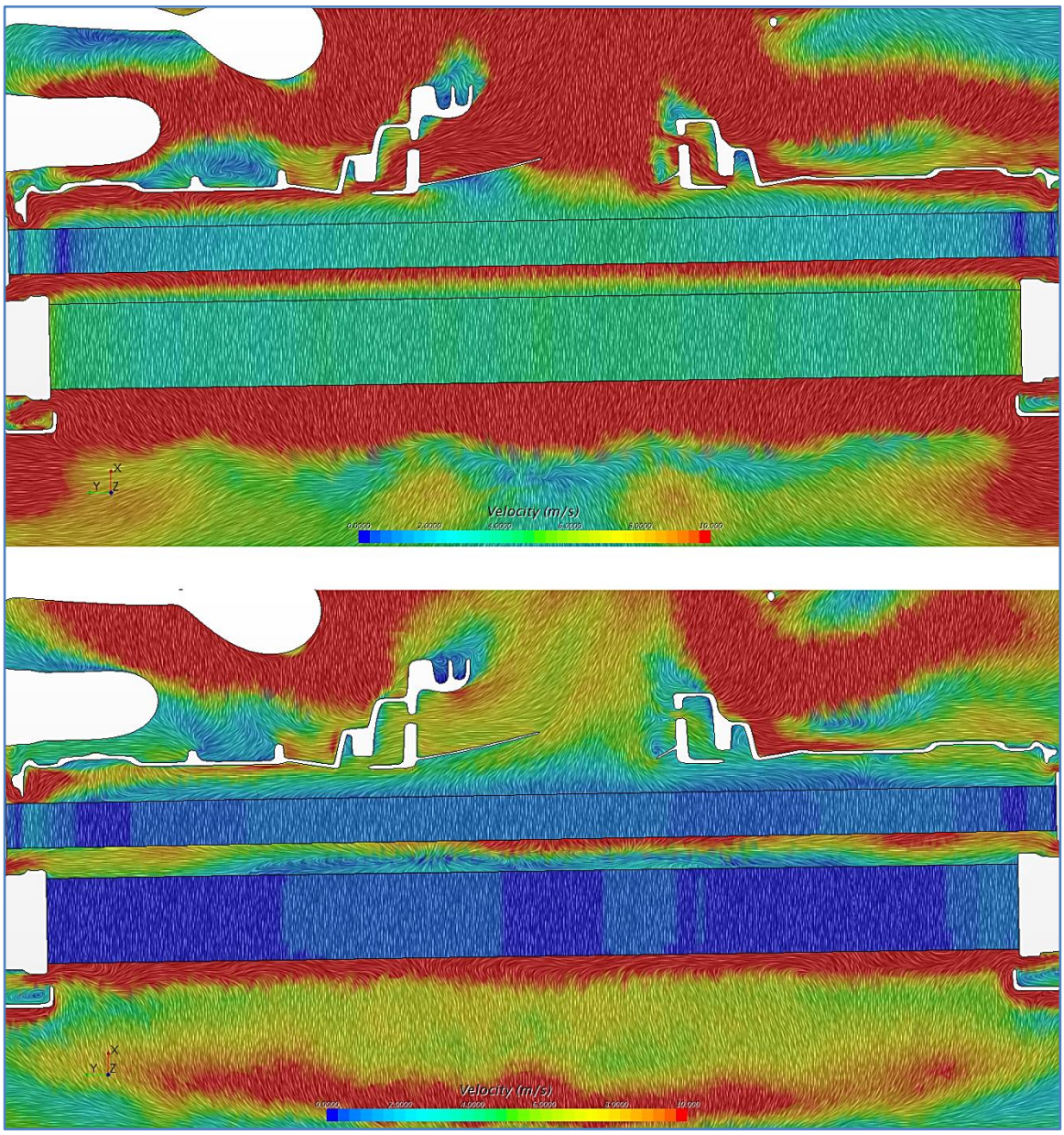

Figure 2.69 - Velocity distribution over the horizontal section plane z=-40 mm, detail of the HEXes. Top: baseline; bottom: modified.

The following maps highlight the velocity distribution in the three heat exchangers composing the cooling module. Differences in the behavior of the flow field in the two configurations are easily spotted. These maps are similar to the one shown above, but isolate the HEXes in order to stress the differences in flow characteristics in this area.

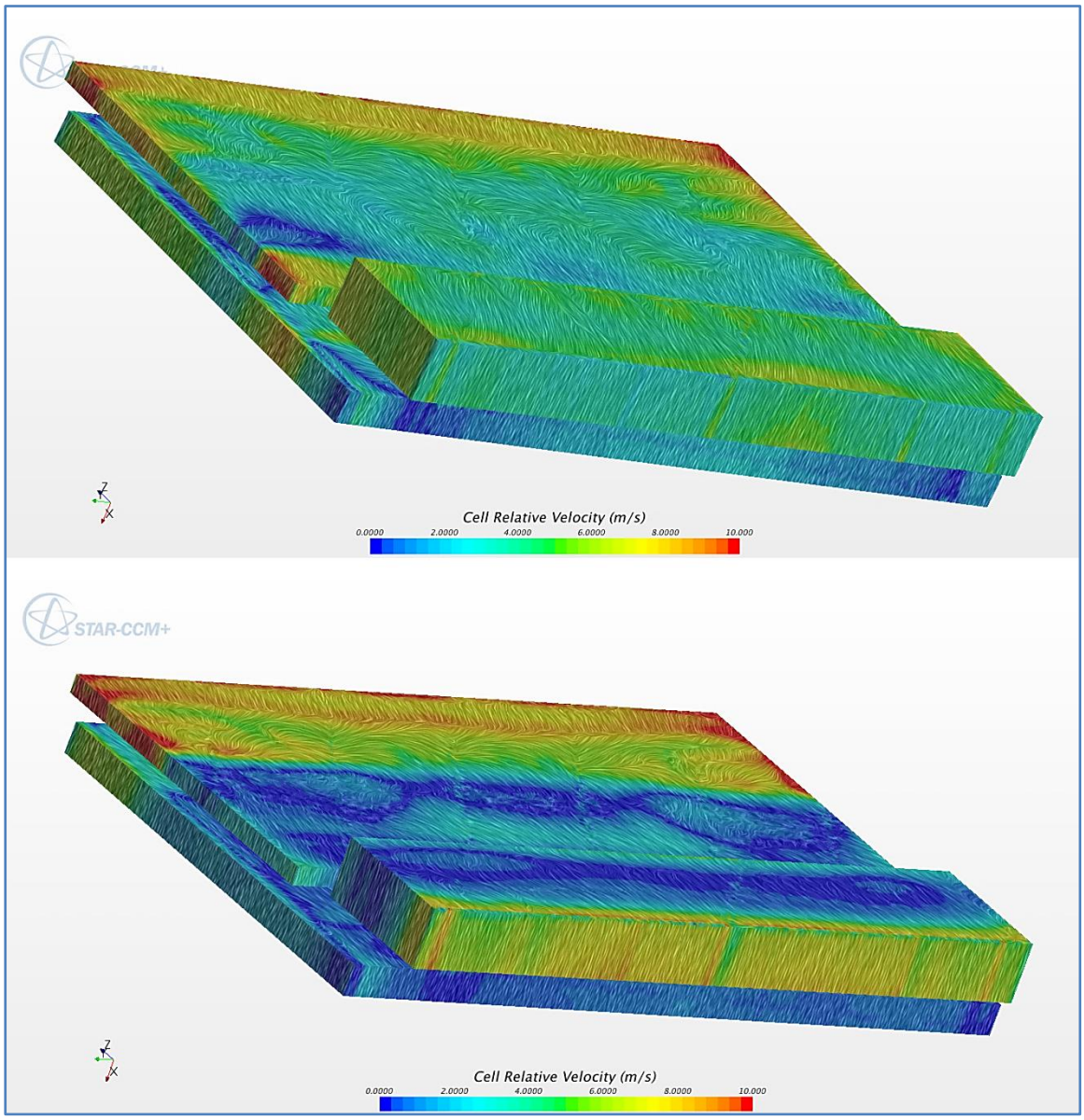

Figure 2.70 - Velocity field in the heat exchangers. Top: baseline; bottom: modified.

A net separation line is visible between the fast moving portion of the flow in the upper part of the cooling module and the slower one on the low side. The effect of the closure is extremely strong, as these pictures show, which visually confirm the simulation numerical results reported before.

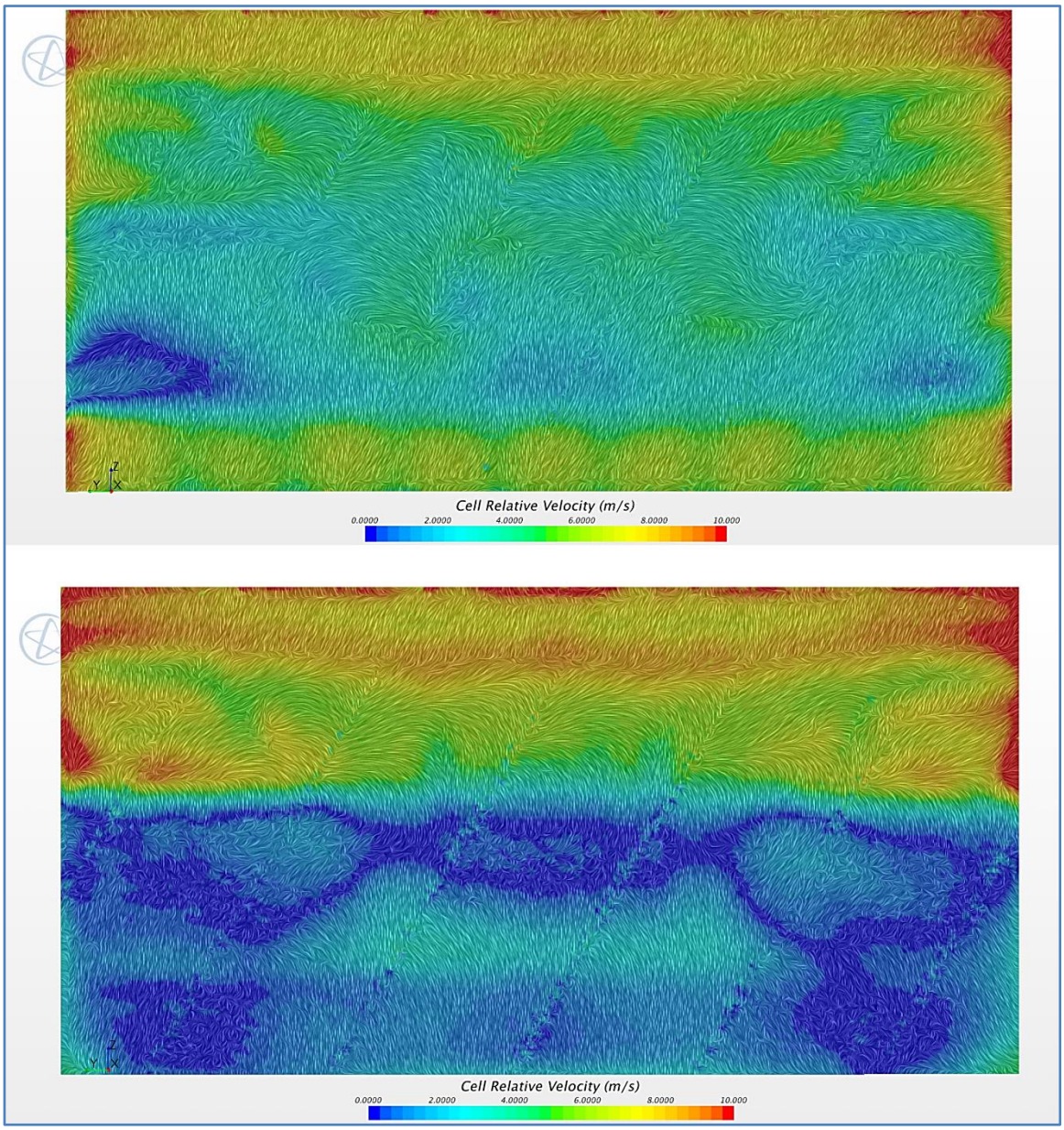

Figure 2.71 - Velocity distribution over the A/C condenser inlet face. Top: baseline; bottom: modified.

Extremely tiny differences in terms of magnitude and direction of the local velocity vector are observed for the inlet and outlet faces of the exchangers, so that for the sake of brevity the outlet faces maps are here omitted.

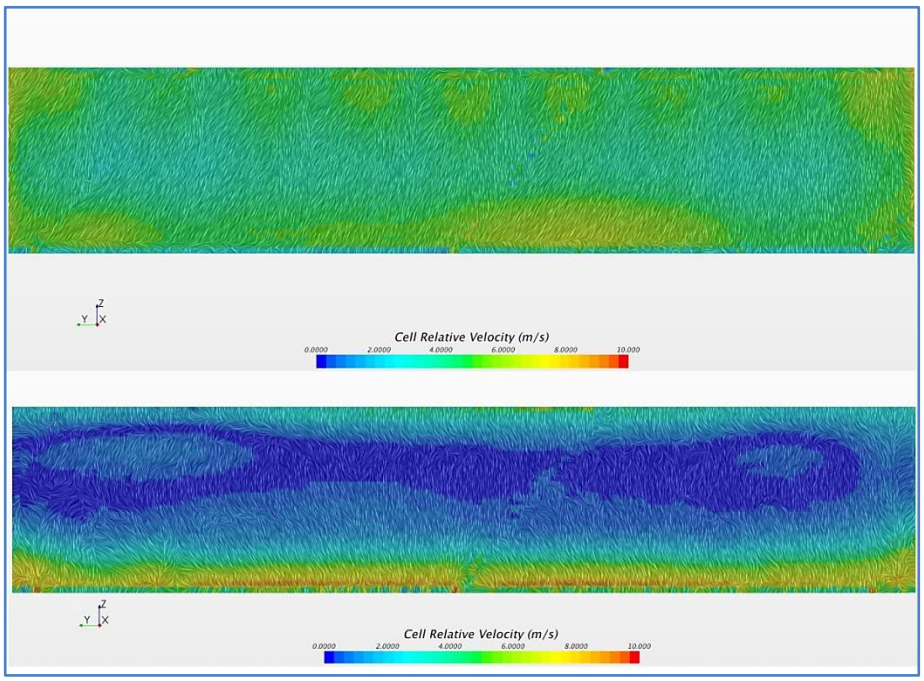

Figure 2.72 - Velocity distribution over the intercooler inlet face. Top: baseline; bottom: modified.

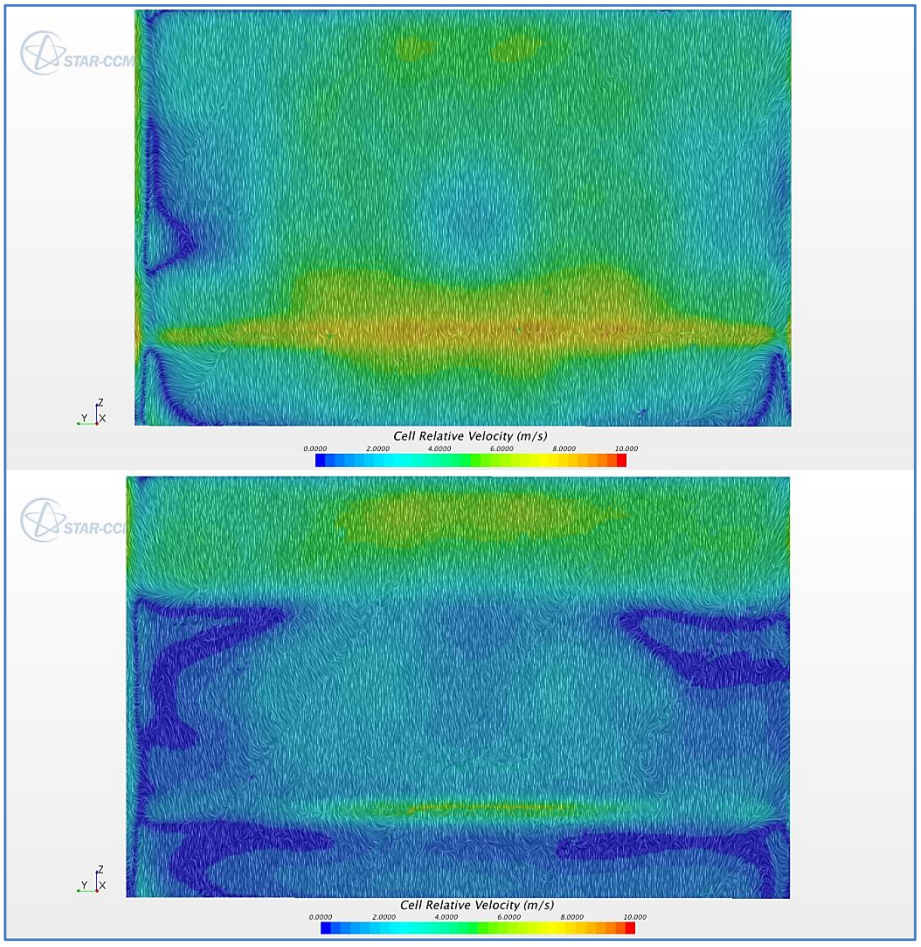

Figure 2.73 - Velocity distribution over the A/C condenser inlet face. Top: baseline; bottom: modified.

After analyzing the aerodynamic characteristics of the flow field around the vehicle, it is now of interest to study the thermal behavior by comparing the performances of the two vehicle configurations. As it has been shown, even though the presence of the fully closed AGS considerably disturbs and alters the flow in the engine bay, a net advantage comes from fitting such system onboard at the specified operating conditions. The drag coefficient remarkable variation is the main numerical indicator quantifying such improvement, whose extent would motivate the adoption of the system. However, as it was explained before, several drawbacks appear when considering the thermal side of the problem. The aim of the next section is to quantify both numerically and visually the deterioration of thermal performances due to the adoption of the AGS, and to evaluate the temperature variation of the underhood components.

I think it is a sad reflection on our civilization that while we can and do measure the temperature in the atmosphere of Venus we do not know what goes on inside our soufflés.

Nicholas Kurti

(Remark made while demonstrating the progress of cooking a Soufflé à la Chartreuse, proving the progress made with thermocouples and chart recorders.)

3. CHAPTER 3

THERMAL ANALYSIS

3.1. CAR VIRTUAL MODEL – GEOMETRY DESCRIPTION

Before getting into the results of the thermal simulation, it is of interest to focus on the geometrical and mesh details of the virtual model used. The geometrical characteristics and feature of the model are exactly the same as the one used for the aerodynamic CFD simulation. However, the mesh size of the thermal model is much coarser due to the higher complexity and computation time required for the solver to reach convergence, especially if considering the adoption of a coupled approach between the aerodynamic and thermal solvers. What is currently done, therefore, is to use the same CAD geometry description used for the CFD (here done with ANSA), and to combine together some cells, thus creating patches where reasonably similar results are expected. This allows considering average values not within single cells but within single patches, thus significantly reducing the elements count and, in turn, speeding up the computation. The automatic procedure developed at CRF automatically performs a mapping of the patches between the H and T values obtained through the Star-CCM+ CFD simulation and the RadTherm model, as long as the PIDs of the two models coincide. In such case, even if the patches are conceptually different in the two solvers, the procedure is able to perform a match which allows the automated script to use and transfer information and results between the two pieces of software. The conceptual difference present in some cases lies in the fact that some parts are defined as "walls" in Star-CCM+, implying that there is a fluid domain only on one side of the part (i.e. only one face faces the fluid domain, while the other faces no domain). On the contrary, each part in RadTherm is two-fold, i.e. it has both an internal and an external

side which are characterized by different thermo-physical conditions. Therefore, the automated macro is in charge of converting all those parts which are defined as walls in Star-CCM+ in two-fold surfaces which can be used in RadTherm to evaluate the thermal properties on both sides.

The following sections provide details of the RadTherm model mesh for both the exteriors and the underhood area.

3.1.1. EXTERIOR BODYWORK MESH

The RadTherm model of the vehicle is discretized as follows:

- Elements: 1,603,247
- Parts: 238
- Trias: 291,816
- Quads: 1,311,431

As can be seen, the total elements count is much lower than in the case of the Star-CCM+ model. As already mentioned above, few cells get combined together into patches, in order to reduce the computational time of both view factors and heat fluxes. A visual example of this strategy is shown in Figure 3.1, which shows the patches created by starting from cells grouped together. Clearly, this has a big impact on the geometrical description ability and on the quality of the surfaces of the discretized model. However, currently this approach represents the best compromise in terms of computational time and required accuracy to get meaningful results. Also, the biggest approximation today in the coupled aero-thermal procedure lies in the fact that only average values are mapped for the H and T values from Star-CCM+ to RadTherm, and that corresponds to the main source of errors. CRF has developed over the last period a procedure which

allows mapping not just average values over the entire surface of a component, but average values cell-by-cell. This allows achieving a much better agreement between experimental and simulated results; however, this procedure is still under intense development and more time consuming, and that is why it was not used for this thesis purposes.

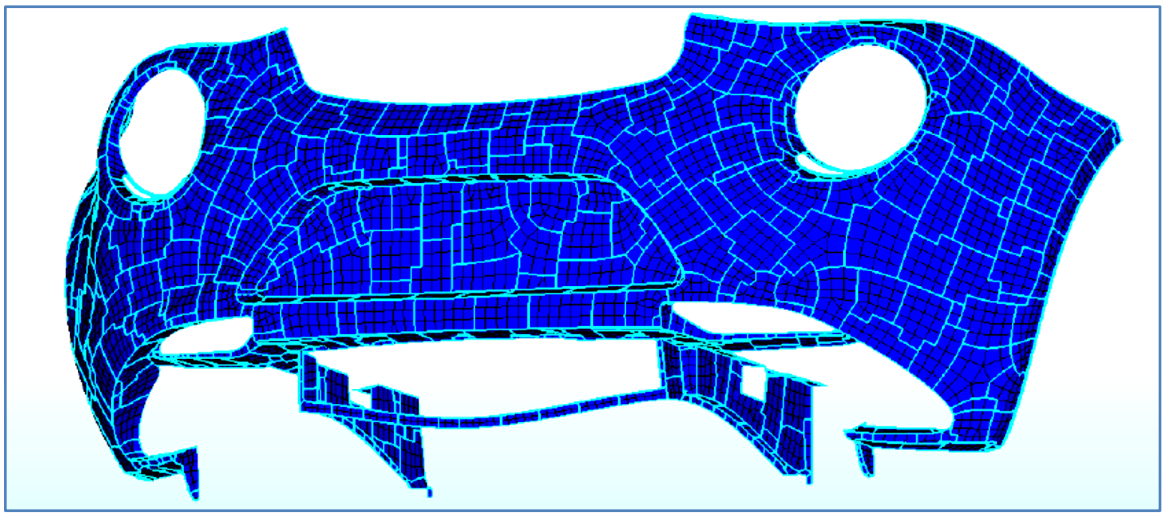

Figure 3.1 - Example of patch creation starting from individual cells grouped together. [24]

Figure 3.2 shows the vehicle model in the RadTherm virtual environment. The coarser surface discretization is immediately evident: note, for instance, the edgy patches on the front bumper and fender. This, however, hardly affects the results, and therefore it is accepted in order to reduce the computation time.

Figure 3.2 - Virtual model of the vehicle in the RadTherm environment.

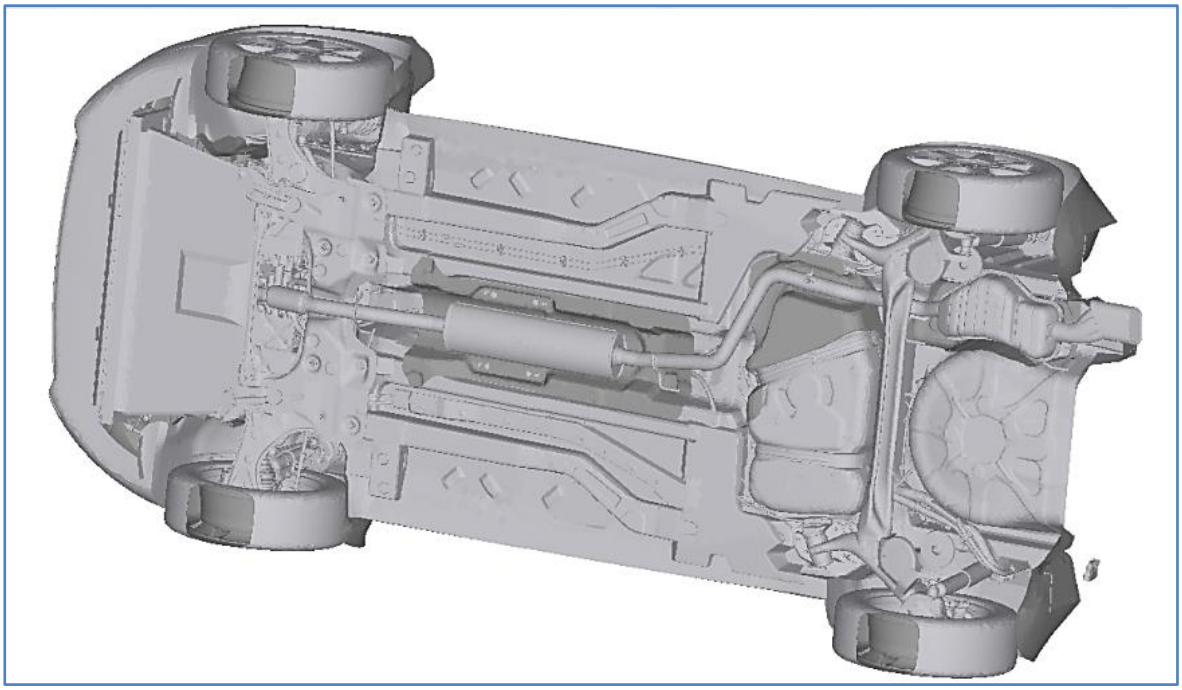

Figure 3.3 - Detail of the underbody geometry as modelled in RadTherm.

Figure 3.4 shows the detail of the surface mesh of the model. The difference with the Star-CCM+ model is remarkable, but this discretization is satisfactory enough to be used for this type of evaluations.

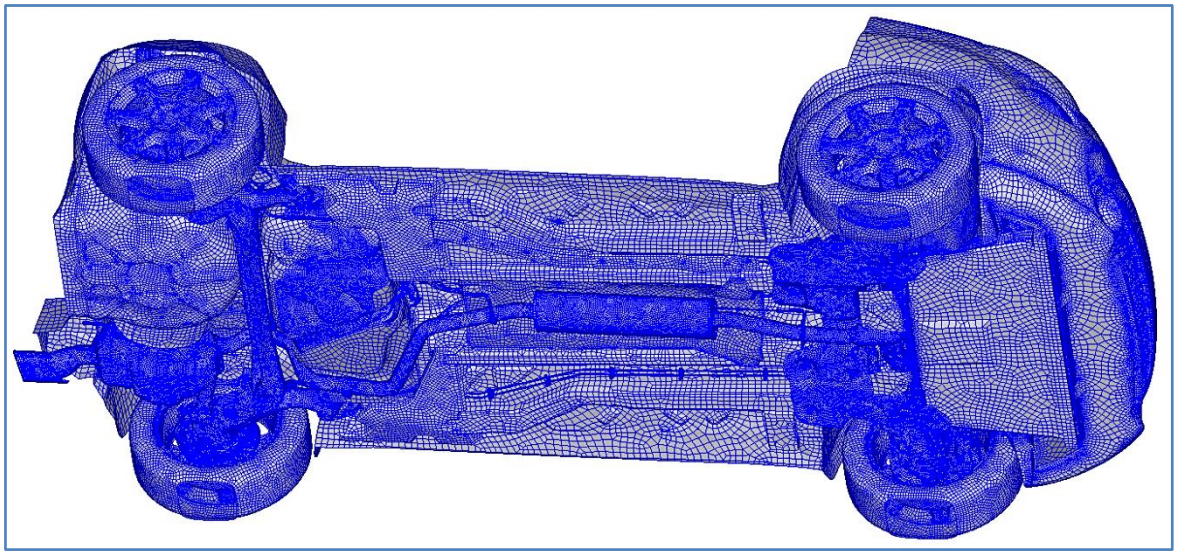

Figure 3.4 - Detail of the mesh of the RadTherm vehicle model.

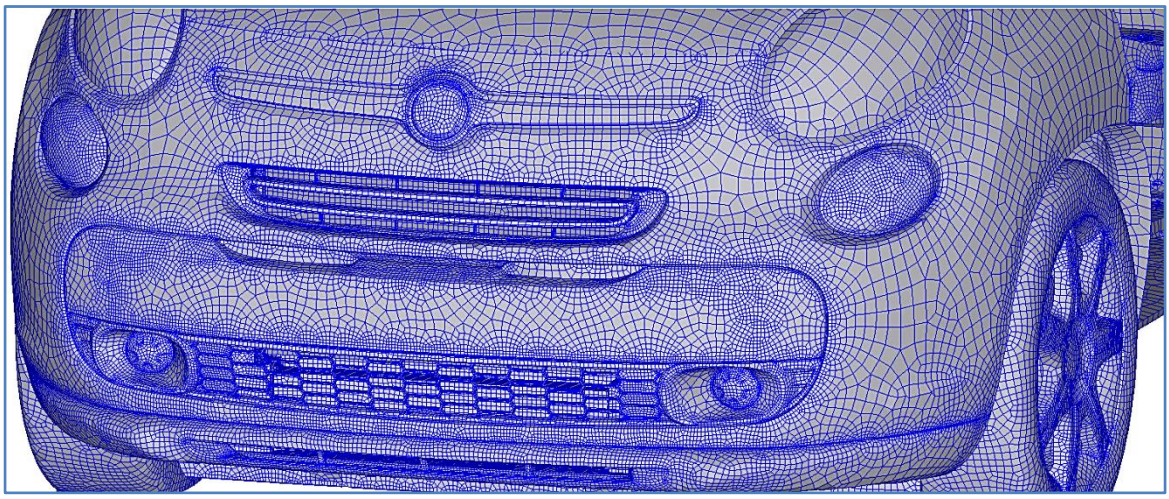

Figure 3.5 - Detail of the mesh of the front-end of the vehicle in RadTherm.

As can be seen from the figure above, the mesh of the model is fairly adequate for describing all the necessary features of the model without losing any relevant information. The models were received by CRF already meshed, due to both time and resources constraints, so that just a check was required to make sure that no issues were present before running the simulations. Of course, a fine mesh was set up for those parts where higher accuracy was needed, like, for instance, the exhaust line and the underhood components. Here, in fact, it is where the attention will focus in terms of thermal behavior, and therefore here is where more accurate temperature distributions are desired.

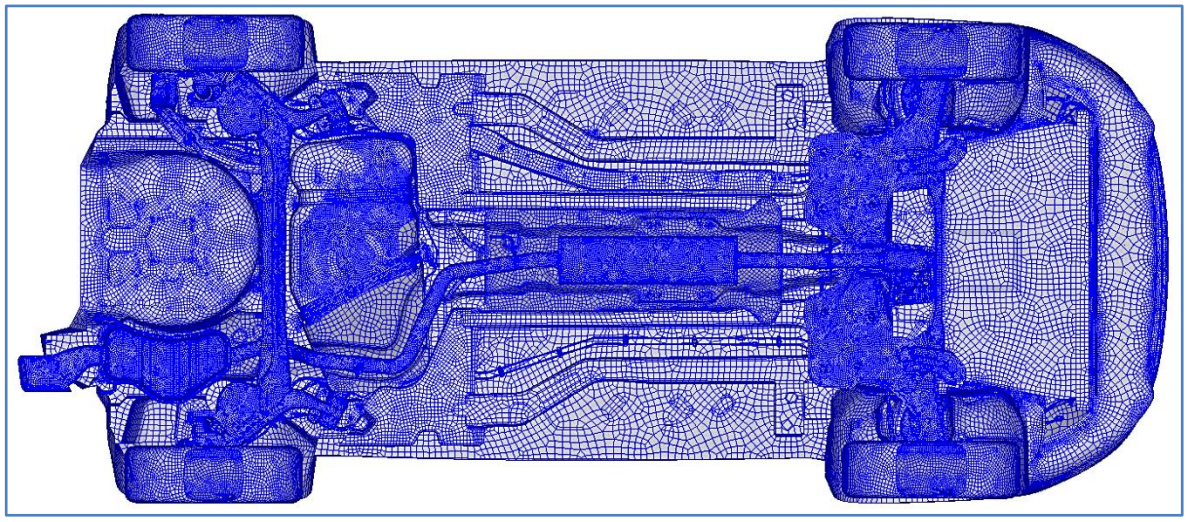

Figure 3.6 - Detail of the mesh of the underbody in RadTherm.

3.1.2. ENGINE BAY MESH

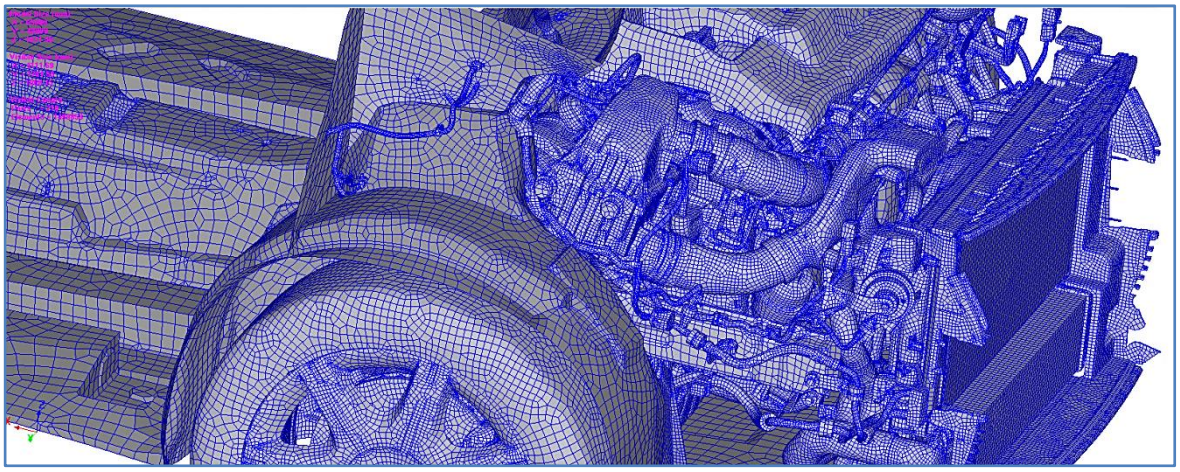

Figure 3.7 - Detail of the engine bay discretization in the RadTherm virtual environment.

The above figure highlights some details of the engine bay components as meshed in RadTherm. The geometrical description is still accurate enough not to lose any relevant information about the thermal behavior of each component, though being less fine than the aerodynamic model one. This is also confirmed by the following figures, in which it is possible to see all the details of the cables and the cooling module.

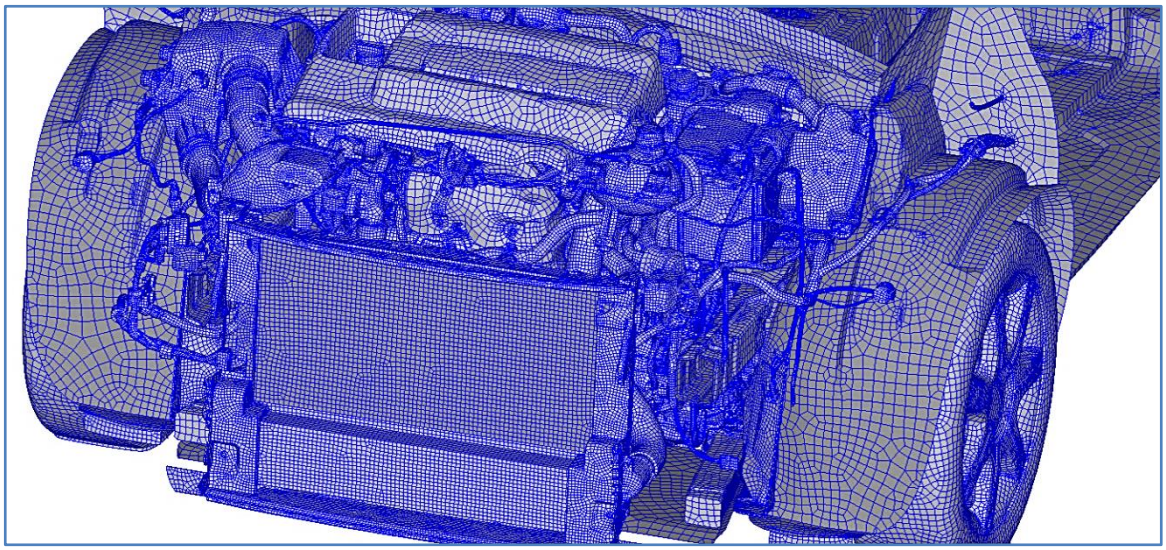

Figure 3.8 - Detail of the engine bay mesh.

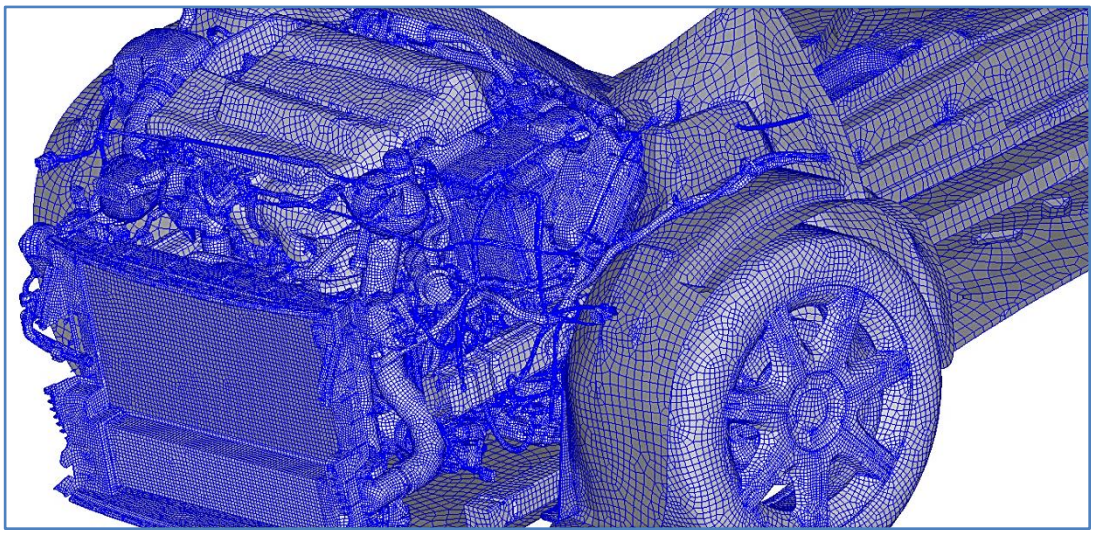

Figure 3.9 - Detail view of the engine bay mesh. Notice the cables and cooling module discretization, still fine enough not to lose any relevant thermal information.

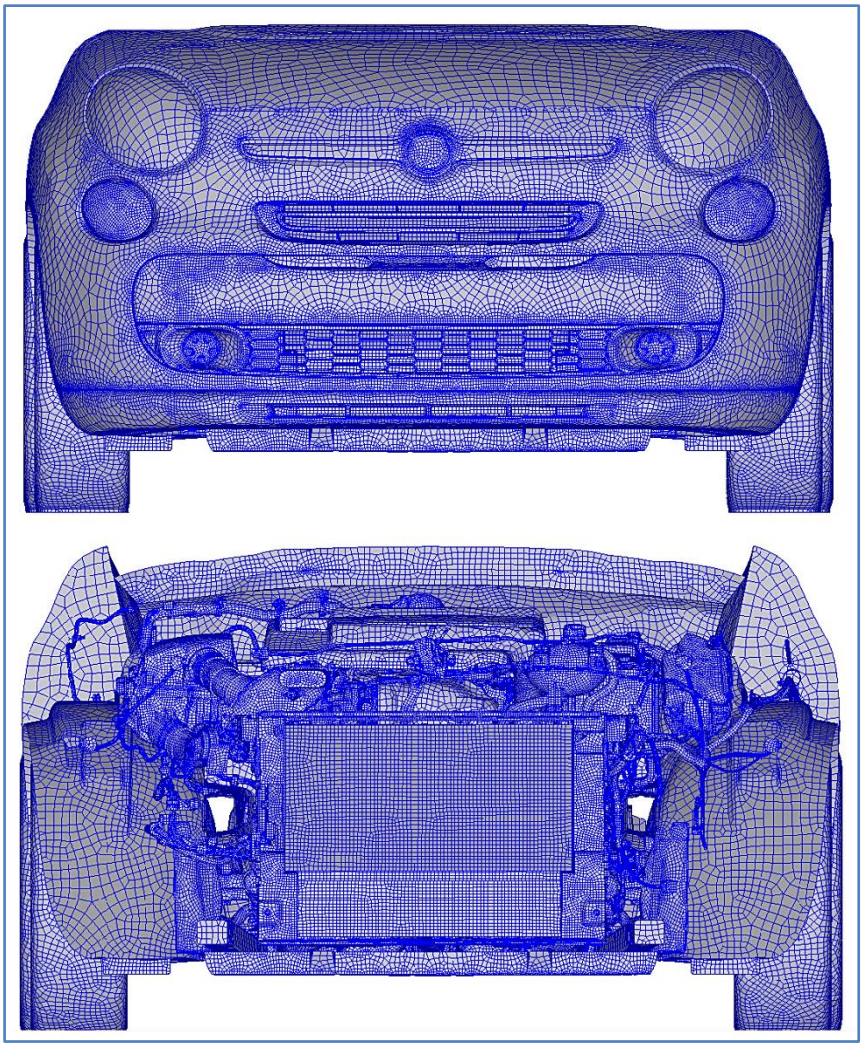

Figure 3.10 - Detail of the front-end mesh, aesthetic parts and detail of the engine bay.

3.2. THERMAL SIMULATION

3.2.1. TESTING CONDITIONS

The following table reports the operating conditions under which the vehicle was tested in the climatic tunnel. More specifically, they represent one of the two most critical conditions from a thermal point of view, namely when the vehicle is at full load, wide open throttle (WOT), top speed gear, and maximum slope (the other one being the heat soak).

Table 3.1 - Thermal test and simulation conditions.

OPERATING CONDITIONS		
SLOPE	[%]	MAX
GEAR ENGAGED		V
TOWING LOAD	[kg]	0
WIND SPEED	[km/h]	139.0
HUMIDITY	[%]	48
TEMPERATURE	[°C]	40.0
ENGINE SPEED	[rpm]	N/A
WHEEL DRUMS SPEED	[km/h]	139.9
TRACTIVE FORCE	[daN]	151.5
SOLAR RADIATION	[W/m^2]	908
POWER AT THE WHEELS	[kW]	58.9
ATMOSPHERIC PRESSURE	[hPa]	986

These conditions were then set as boundary conditions in the numerical solvers so as to replicate the testing conditions of the climatic and wind tunnel.

3.2.2. CONVERGENCE PLOTS

Figure 3.11 shows the convergence plots for the two thermal simulations.

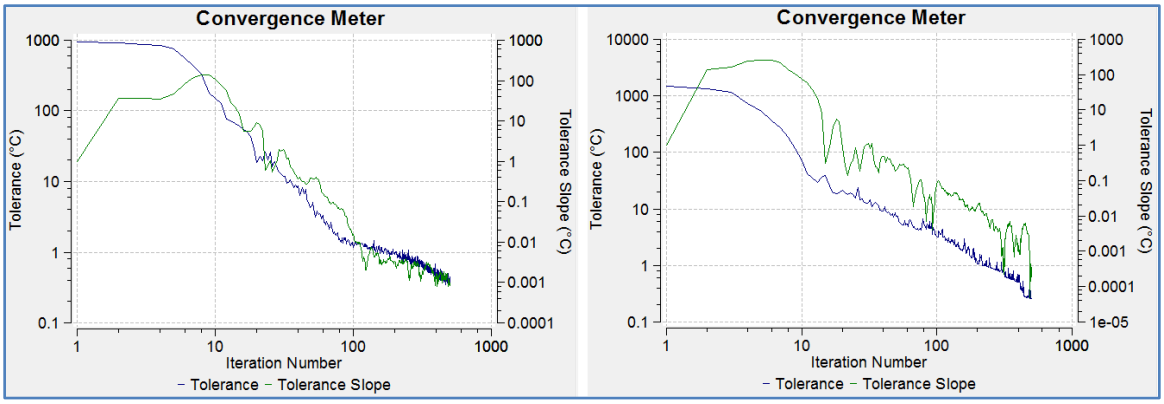

Figure 3.11 - Convergence plot for the thermal simulation. Left: baseline; right: modified.

These plots represent the convergence history of the thermal solution for the baseline and modified models. As in the aerodynamic simulation case, the stopping criterion was imposed in terms of number of iterations, based on past experience for this type of analyses.

3.2.3. THERMAL ANALYSIS RESULTS

Appendix G reports the temperature values for the components under analysis and highlights the variations of the modified version with respect to the baseline. As expected, an increase in cooling air temperature is observed when shutting the main central inlet which affects all of the components in the underhood, especially those directly downstream of the closed grille. Both absolute and percentage changes are shown in the table, in order to get a better understanding of the behavior of the thermal field in the two cases.

The general trend highlights increasing temperatures within the engine bay due to the lower cooling air flow rate through the restricted inlets. In some cases, however, the components exhibit a lower temperature for the modified case. This can be associated to a local increase in the air flow velocity through the remaining available open inlets, as the volume flow rates indicate in Table 2.3. In those locations, in fact, the locally faster flow rate enhances the heat exchange efficacy and more heat is dissipated by the hot underhood components. Also, due to the fact that only average fluid wall temperatures and heat transfer coefficients are mapped for each component from the CFD to the thermal solver, this effect becomes greater and results in values which could be a bit different in a real context. In the vast majority of cases, however, a temperature rise is observed which becomes immediately evident when considering the thermal field maps for the two configurations, which are reported in the next paragraph.

3.2.4. TEMPERATURE DISTRIBUTION MAPS

The objective of this paragraph is to visually understand the numerical results obtained from the simulation. Thanks to the help of the GUI, in fact, it is possible to see how the thermal field is altered by the presence of the closed AGS. In the following, a comparison between the baseline and modified configurations is shown, where maps from similar perspectives are displayed with the same temperature range of variation. This range has been suitably chosen each time in order to underline the differences and allow the reader getting a clear picture of the thermal behavior of the different components involved.

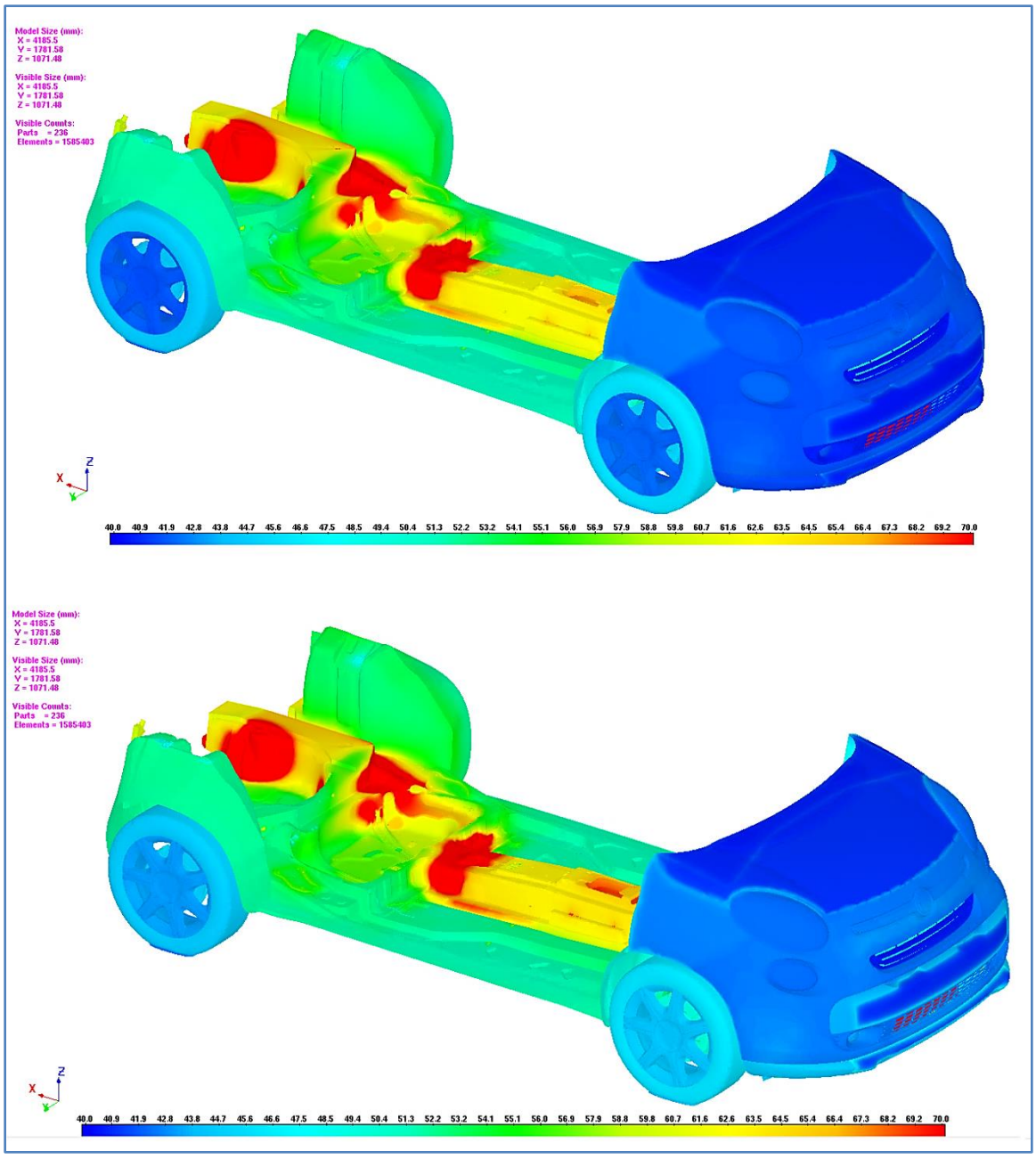

Figure 3.12 - Temperature distribution map of the complete vehicle. Top: baseline; bottom: modified.

Figure 3.12 shows the temperature distribution maps of the two configurations. As expected, no significant variation is observed on the frame, while a slight increase in temperature is visible for the front aesthetic parts (bumper and central grid).

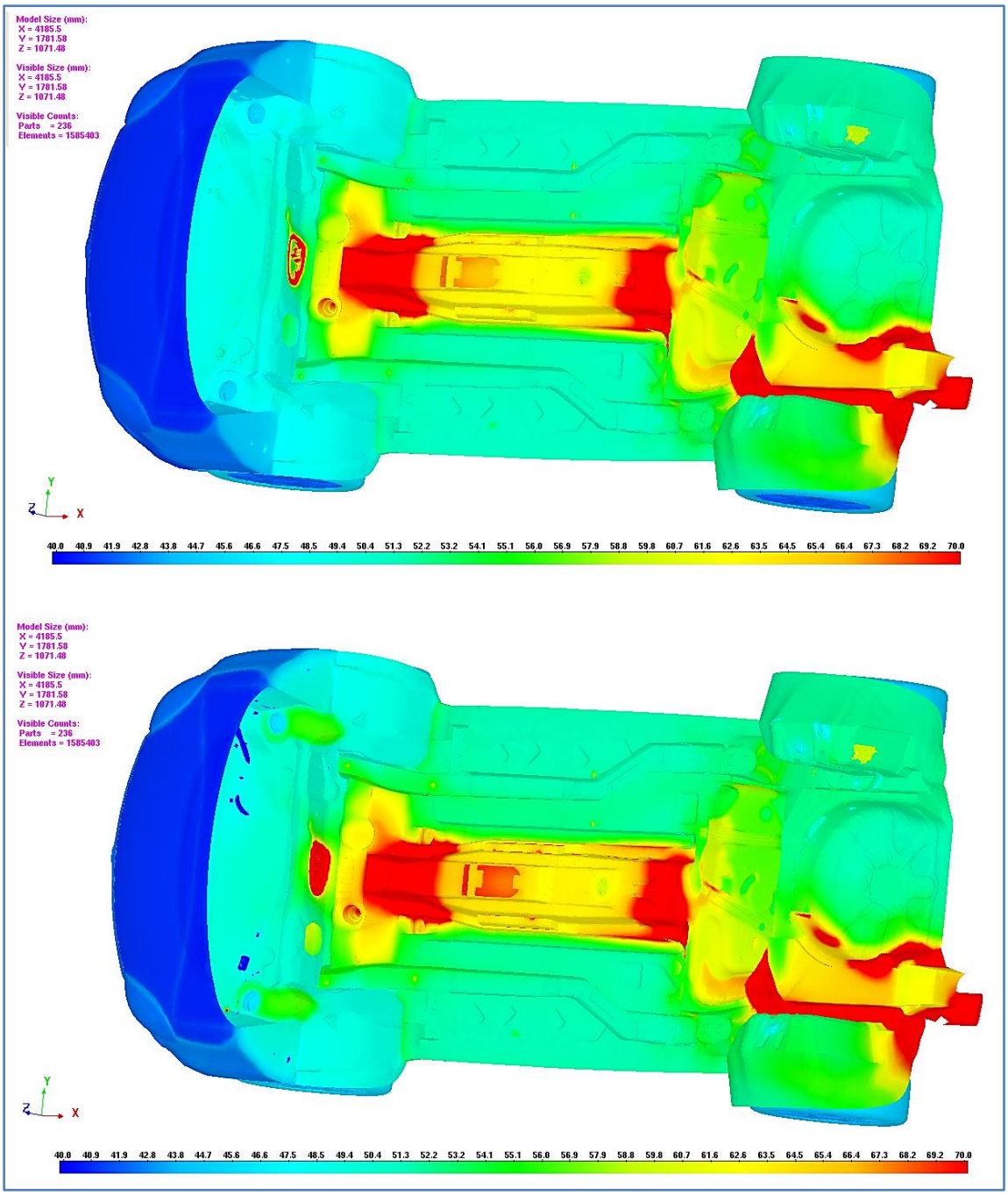

Figure 3.13 - Temperature distribution map of the complete vehicle, view of the upper part of the vehicle body. Top: baseline; bottom: modified.

Figure 3.13 shows the upper part of the vehicle body frame. Again, no significant differences emerge between the two versions, apart from a hotter area in the front-end (on the engine dash panel) for the configuration with closed AGS.

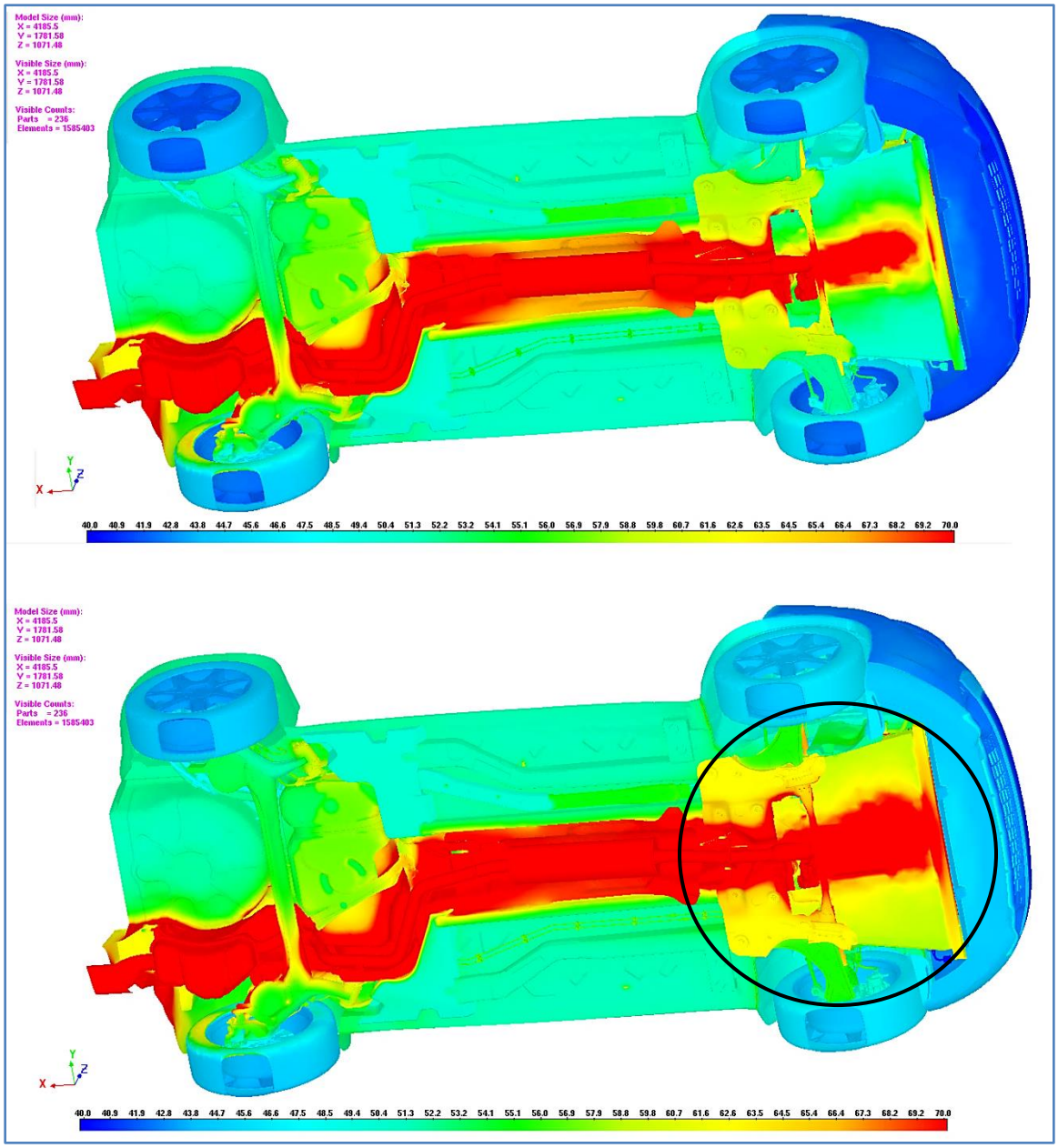

Figure 3.14 - Temperature distribution map, view of the underbody. Top: baseline; bottom: modified.

On the contrary, remarkable differences appear when considering the vehicle underbody. As can be seen in Figure 3.14, in fact, the high temperature area on the front underbody heat shield just under the engine is much more extended in the case with closed AGS, which is a direct result of the higher air temperatures within the engine bay. In particular, the maximum temperature on the inner side (facing the engine bay) passes from 118.8°C to 136.7°C. For plastic

components of this type, the maximum allowed temperature before having thermo-structural degradation is around 120°-140°C, quite close to the value estimated by the simulation. Therefore, the possibility to adopt a different material with a higher acceptable operating temperature for this component should be analyzed before fitting the AGS on-board. Alternatively, the possibility to add aluminized thermal covers should be considered in order to decrease the operating temperature of the plastic component itself. The latter solution allows a lower cost by properly designing the cover only for the high temperature area of the component, so as to partially absorb all the incoming heat flux.

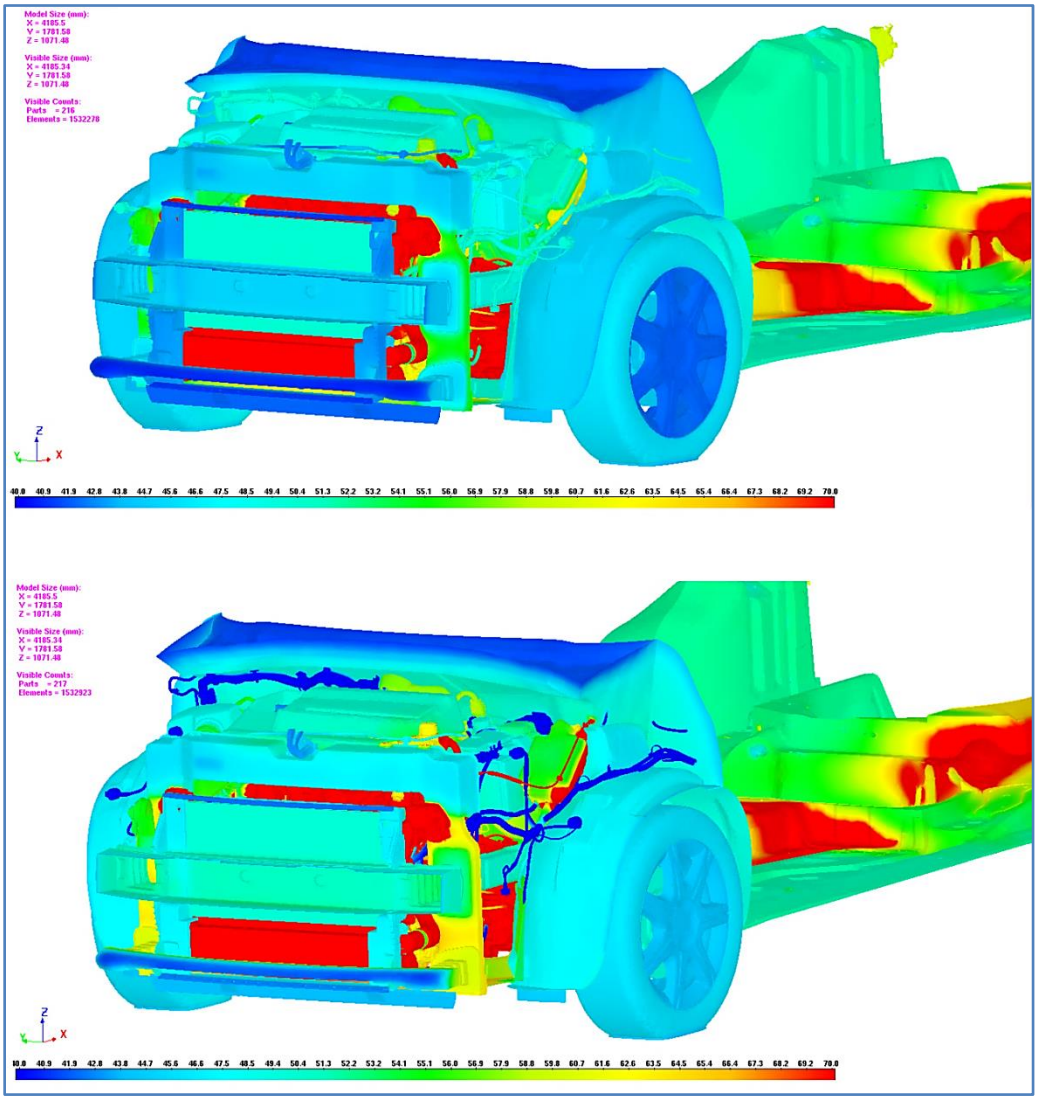

Figure 3.15 - Temperature distribution map, detail of the engine bay. Top: baseline; bottom: modified.

Figure 3.15 highlights the higher temperatures within the underhood area. On average, brighter areas are present in the modified case, showing that higher temperature values are achieved for this configuration, as expected. A different trend is exhibited by the underhood cables, but for this part a large variability was observed over the different co-simulation steps, with average temperatures ranging between 40.6°C and 77.6°C, so that for this component further validation is required (e.g. experimentally).

Overall, however, the vast majority of the underhood components exhibit higher temperature levels for the modified case, the most critical ones being the plastic ones, which may undergo thermo-structural changes which negatively affect their performances.

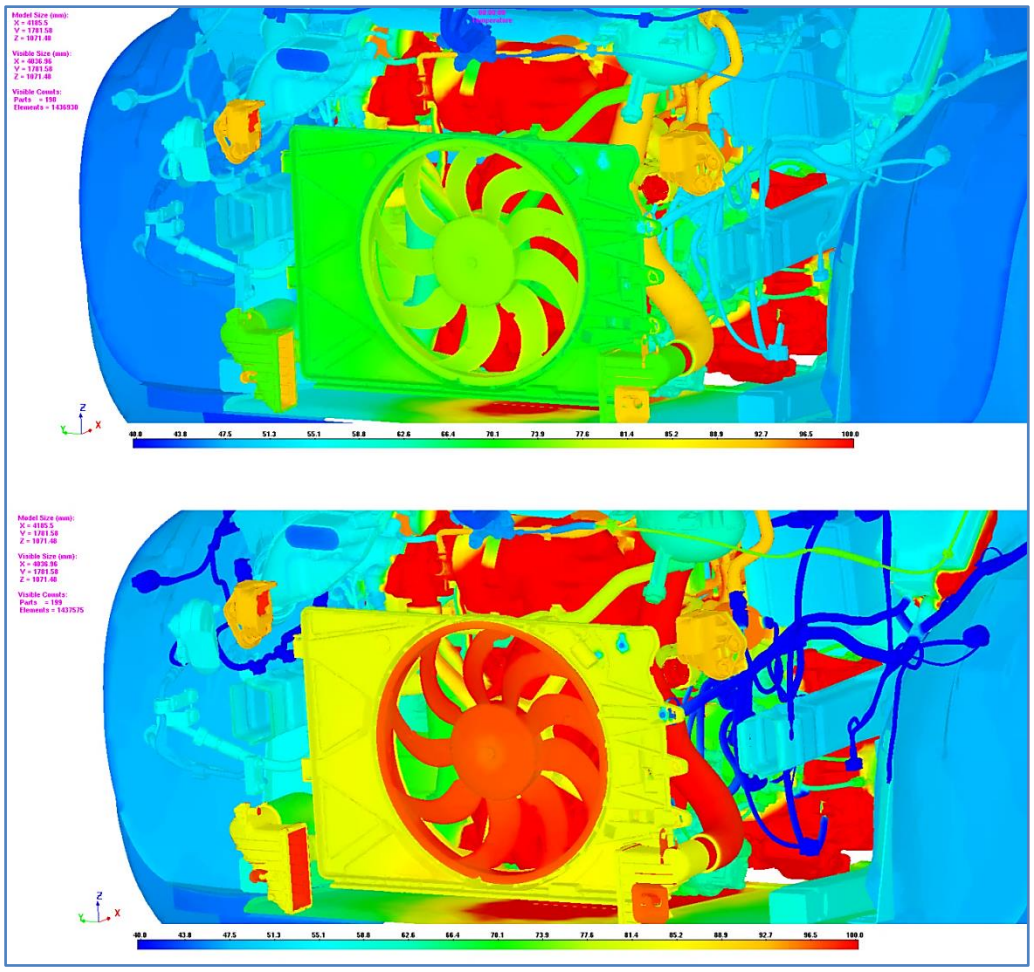

Figure 3.16 - Temperature distribution map, detail of the fan assembly. Top: baseline; bottom: modified.

The above consideration applies especially to the fan assembly, made out of plastic. Also in this case, clear dissimilarities emerge between the two configurations. This visual check confirms the numerical results: for instance, the fan blade average temperature rises from 75.4°C to 98.0°C, and this is directly observed in the above map. The restricted flow results in higher cooling air temperature levels in the engine bay, which, in turn, causes a deterioration of the ability to dissipate heat from the underhood components. The direct consequence of this is evident also in Figure 3.17, where the high temperature red areas are predominant and much wider in the fully closed AGS version.

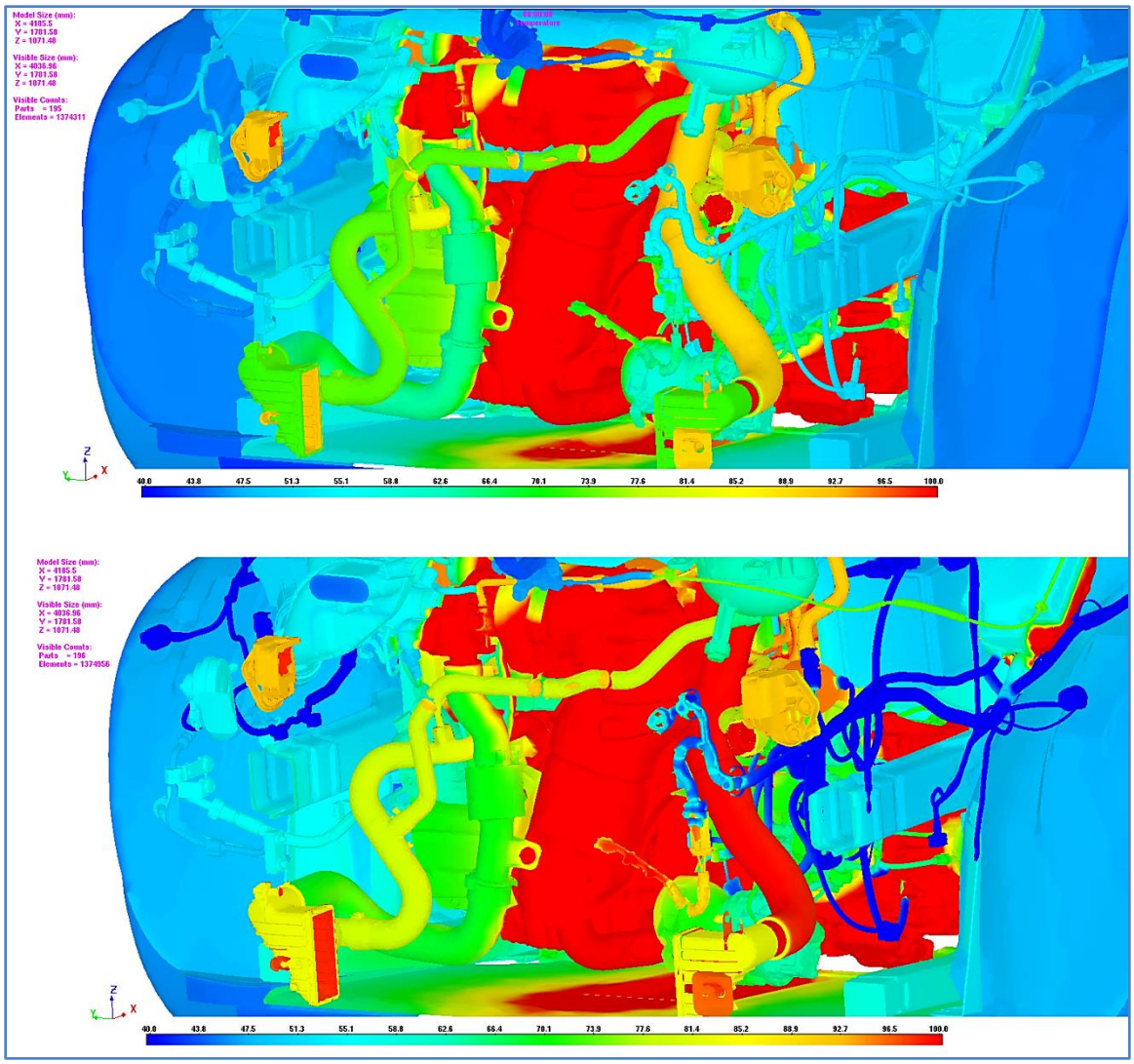

Figure 3.17 - Temperature distribution map, detail of the engine bay. Top: baseline; bottom: modified.

In particular, all the cooling ducts appear hotter in the modified case, especially the one bringing engine air from the intercooler outlet to the engine intake, due to the particular conformation and layout of the engine bay.

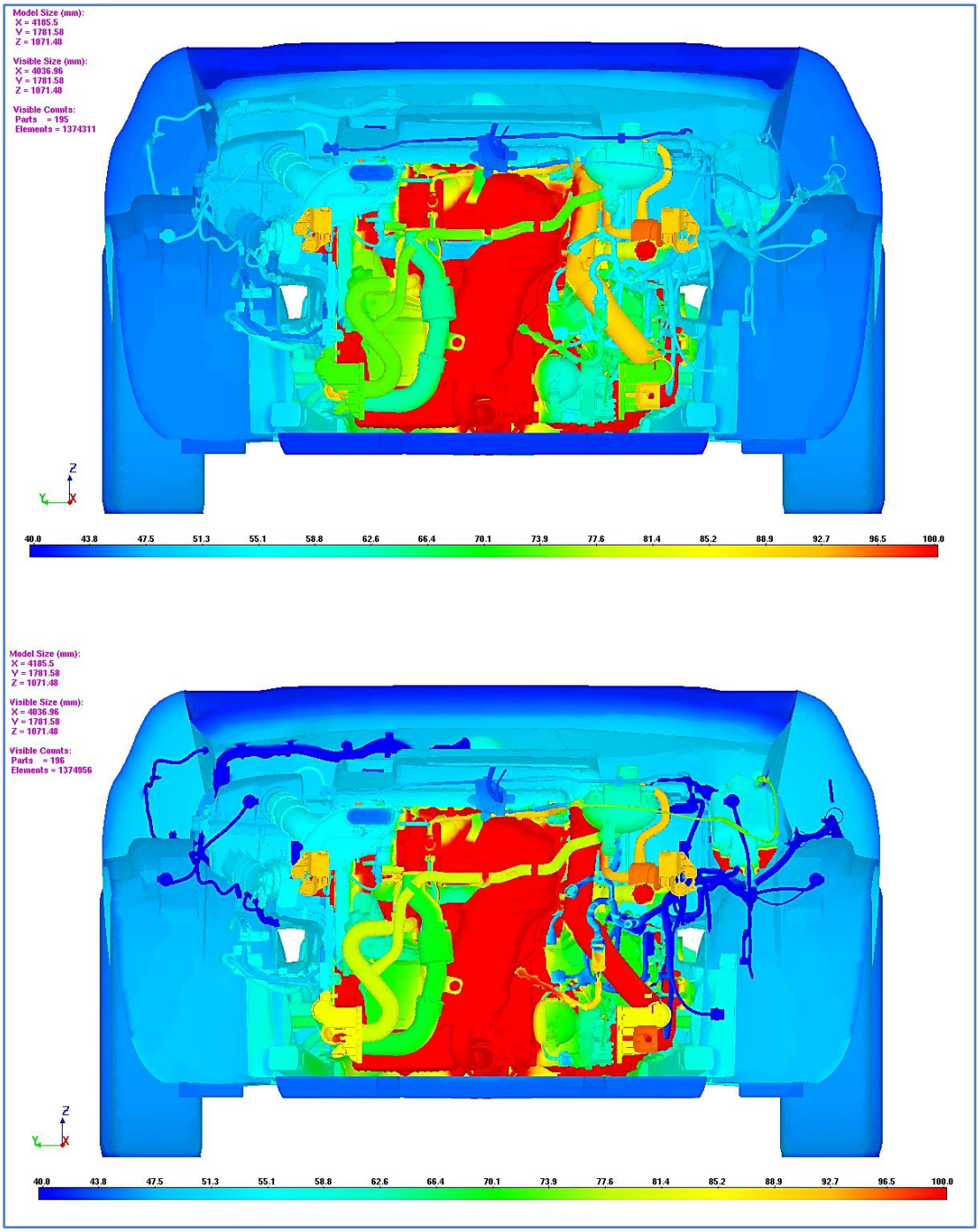

Figure 3.18 - Temperature distribution map, detail of the engine bay from the front. Top: baseline; bottom: modified.

This has a detrimental effect also on engine performances since the increase in temperature of the engine intake air caused by the warmer duct leads to a decrease in density, which, in turn, reduces the engine volumetric efficiency and, as a consequence, the overall engine efficiency. Theoretically, this could be counteracted by locating the engine air inlet in a more favorable position, for instance just downstream of one of the front inlet vents so as to better exploit the ram effect, or even re-tuning the turbocharger unit performances. However, the overall cost of these possible modifications outweighs the potential benefits, so that an estimated increase in average temperature of 9.8°C might be tolerated. However, before further developing the AGS system, a more detailed analysis is recommended for this component, for instance by using the new mapping procedure under development (more accurate) or even performing quick tests in the climatic tunnel to check and validate the simulated results. Using the new simulated or measured data, then, it will be possible to evaluate the variation in engine performances caused by the closure of the inlet, for instance by using virtual simulation tools currently available within the Company to quickly get a numerical quantification of the losses.

An interesting visual analysis can be done by comparing the same sub-groups of the two different versions. The following maps aim at this purpose.

Figure 3.19 compares the fuel lines of the two configurations. In this case, no meaningful difference appears, and both the spatial distribution and the numerical results are very similar to each other. Similarly, no noteworthy dissimilarities are observed for the engine air aspiration assembly, including the dirt and clean air duct and the air filter box. Bigger variations are instead visible for the fuse-box: as can be seen in Figure 3.21, this component achieves significantly higher temperatures in the modified case (especially in the rear part facing the engine), as the color range indicates.

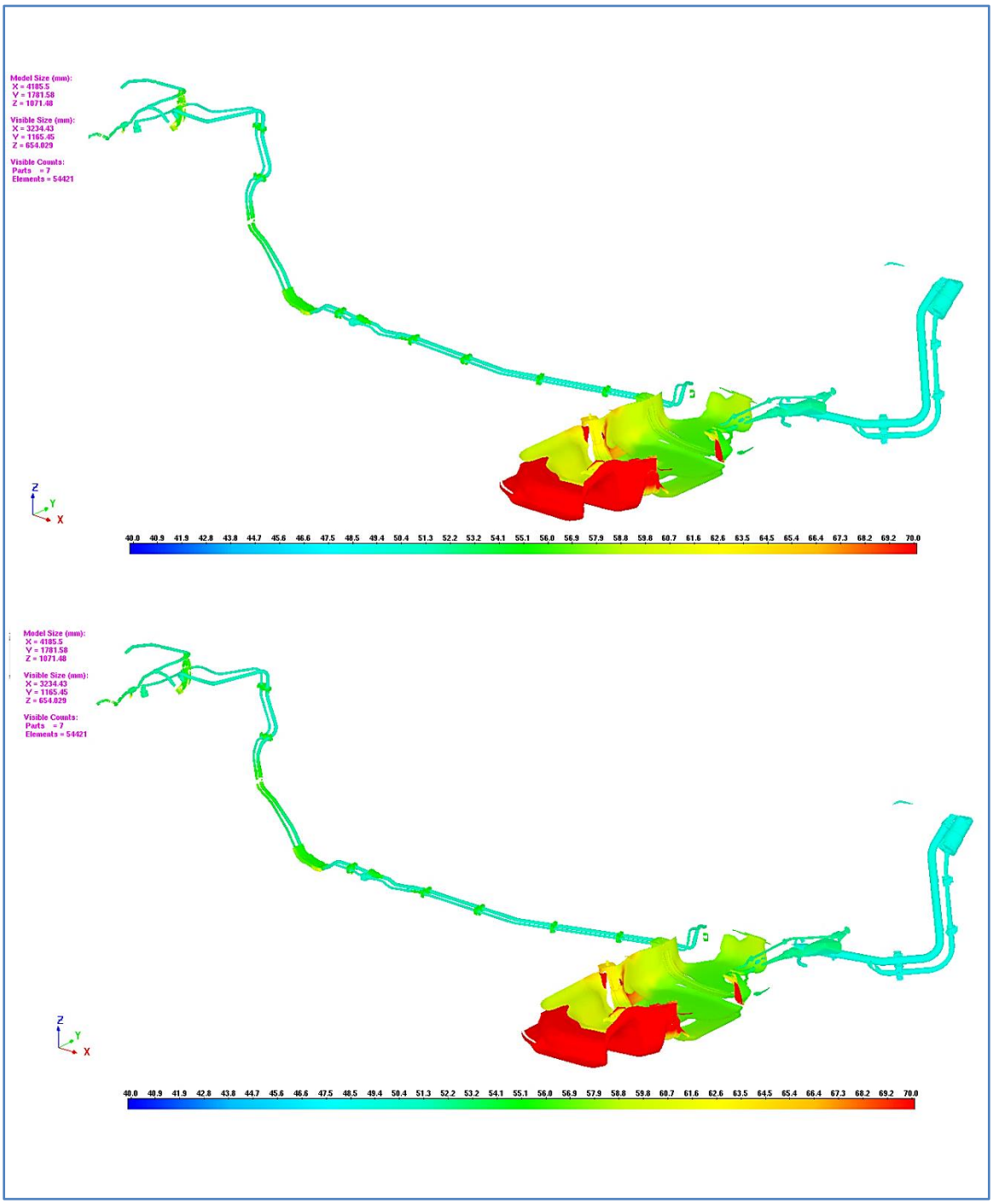

Figure 3.19 - Temperature distribution map, detail of the fuel line. Top: baseline; bottom: modified.

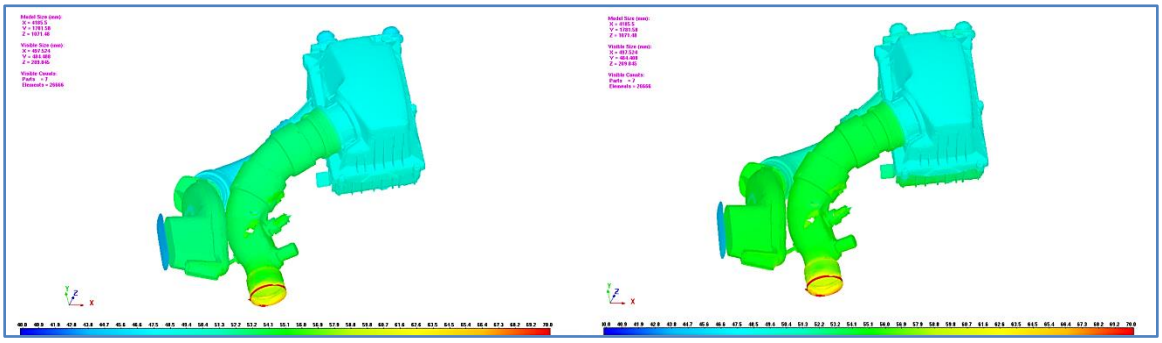

Figure 3.20 - Temperature distribution map, detail of the engine air intake line. Left: baseline; right: modified.

An interesting result is the one associated to the battery: a rise in temperature is observed which is confirmed by the visual check in Figure 3.22, where the wider extension of the red area for the modified case can be seen.

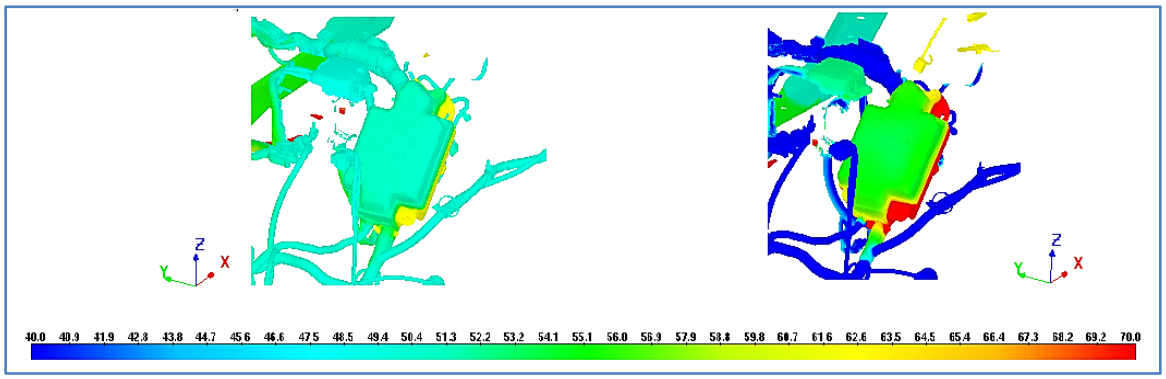

Figure 3.21 - Temperature distribution map, detail of the fuse-box. Left: baseline; right: modified.

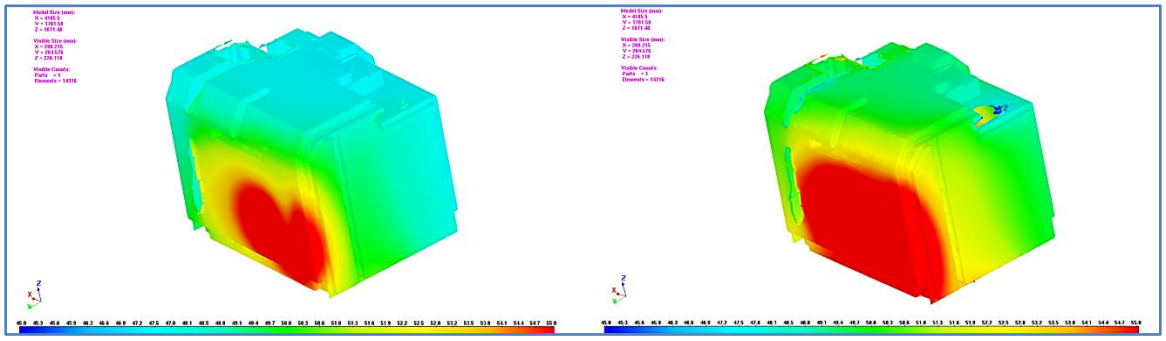

Figure 3.22 - Temperature distribution map, detail of the battery. Left: baseline; right: modified.

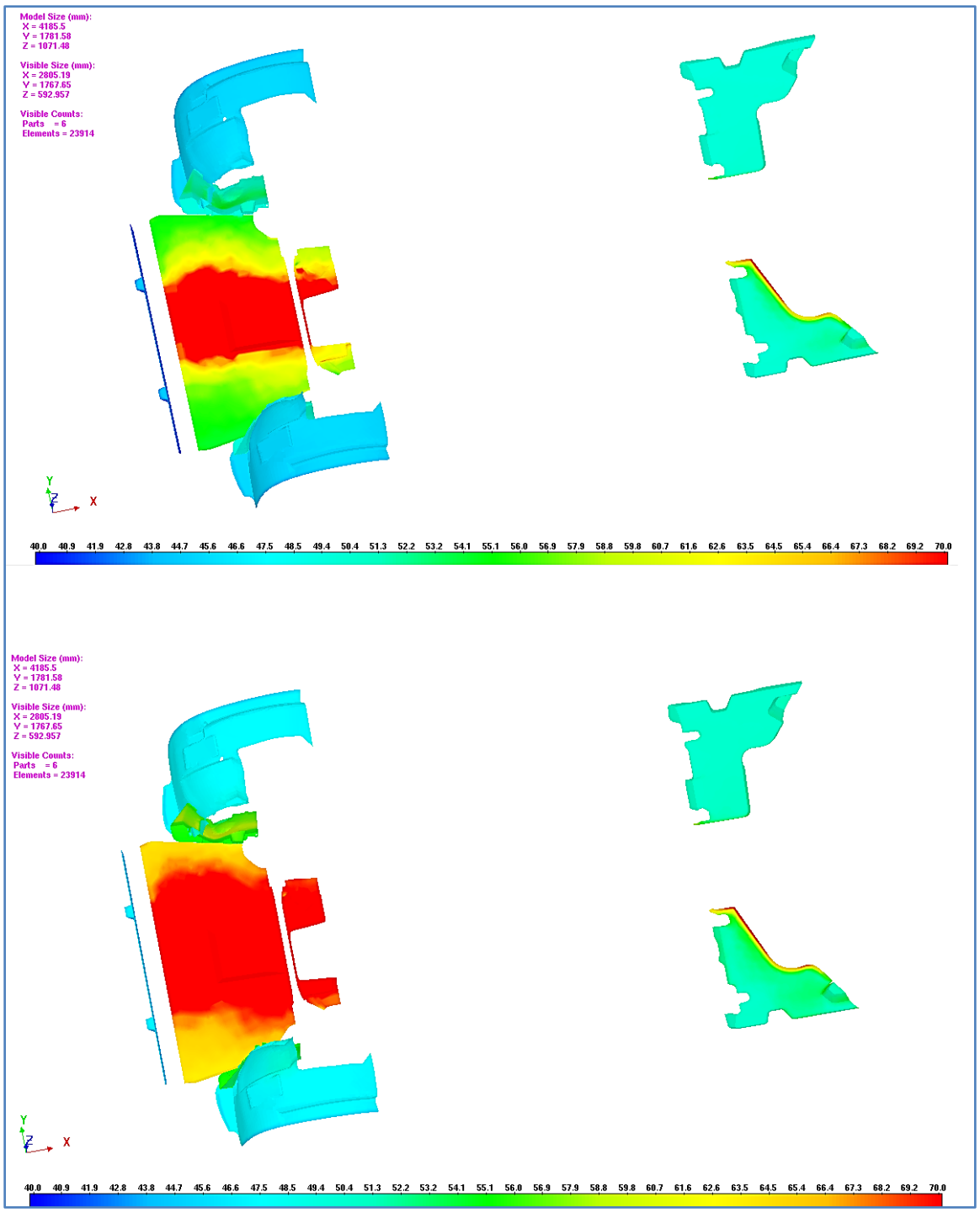

Figure 3.23 - Temperature distribution map, detail of the front lockary and underbody shields. Top: baseline; bottom: modified.

Figure 3.23 shows the increased size of the high temperature area on the front underbody shields just under the engine. This is a clear indicator of the

higher temperature within the engine bay, being the hot zone spread over a much wider surface area of the component.

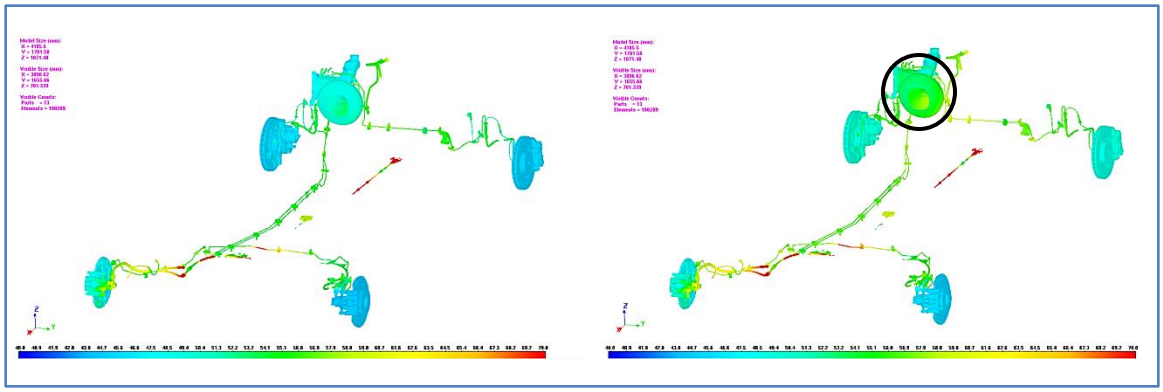

Figure 3.24 - Temperature distribution map, detail of the vehicle body frame. Left: baseline; right: modified.

As for the braking system, no significant difference is detected between the two configurations, with the only minor exception of the booster.

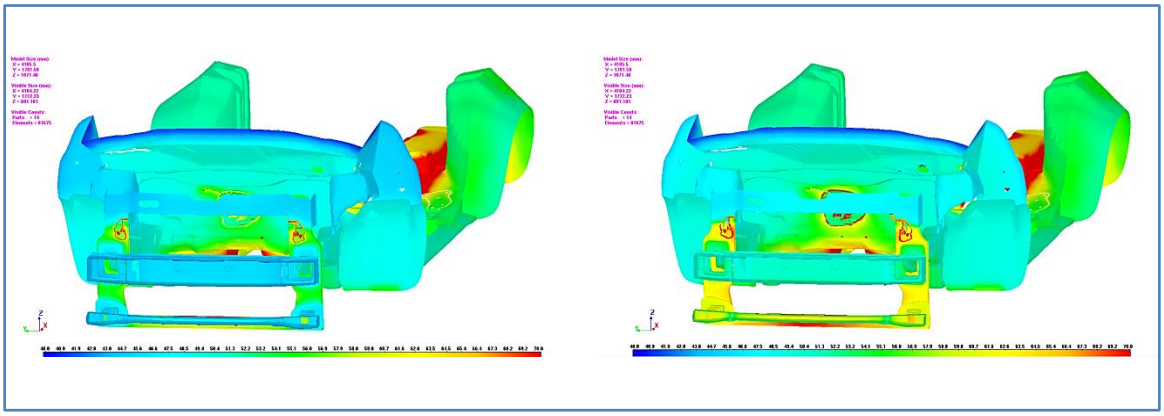

Figure 3.25 - Temperature distribution map, detail of the brakes system. Left: baseline; right: modified.

On the other hand, dissimilarities are observed in the front-end of the vehicle body frame, especially on the lower part of the engine dash panel and the lower front transversal beam. This can be easily spotted both in Figure 3.24 and Figure 3.26, where the front part of this sub-group is circled in black to highlight the area where the biggest differences occur.

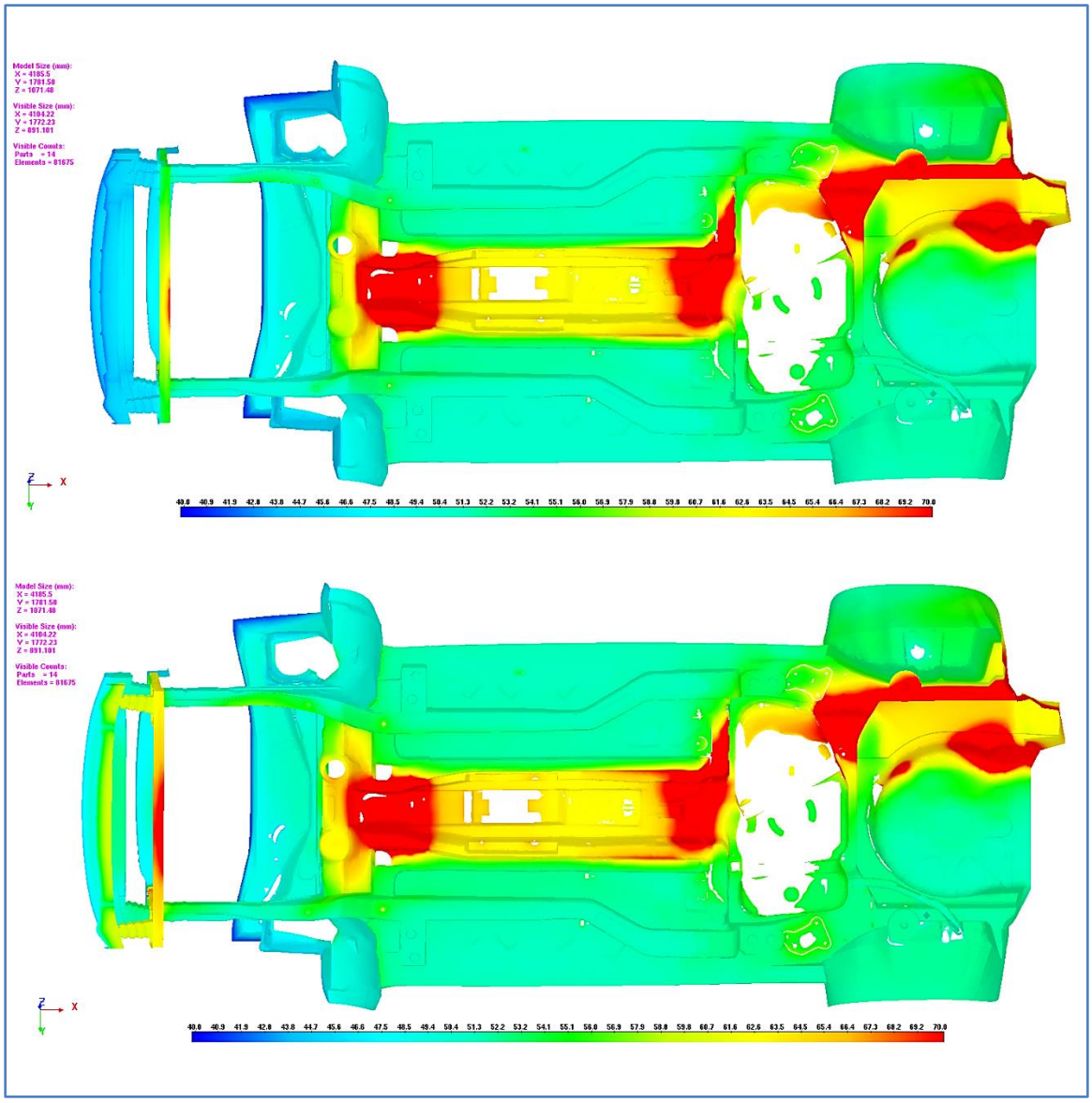

Figure 3.26 - Temperature distribution map, view from above of the vehicle body frame. Top: baseline; bottom: modified.

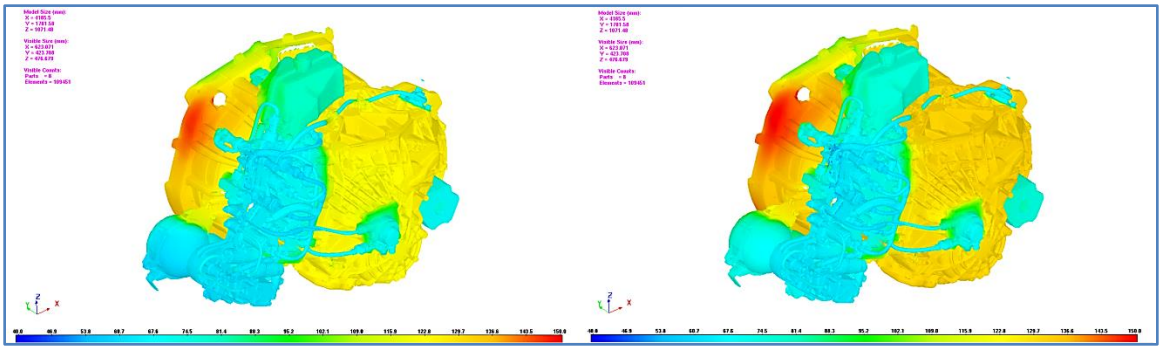

Figure 3.27 - Temperature distribution map, detail of the gearbox assembly. Left: baseline; right: modified.

Higher temperatures are also noticed on the gearbox assembly, as shown in Figure 3.27, especially on the metal block of the gears casing. However, the increase in temperature is far from being an issue from a thermo-structural viewpoint, so that no particular countermeasure needs to be applied.

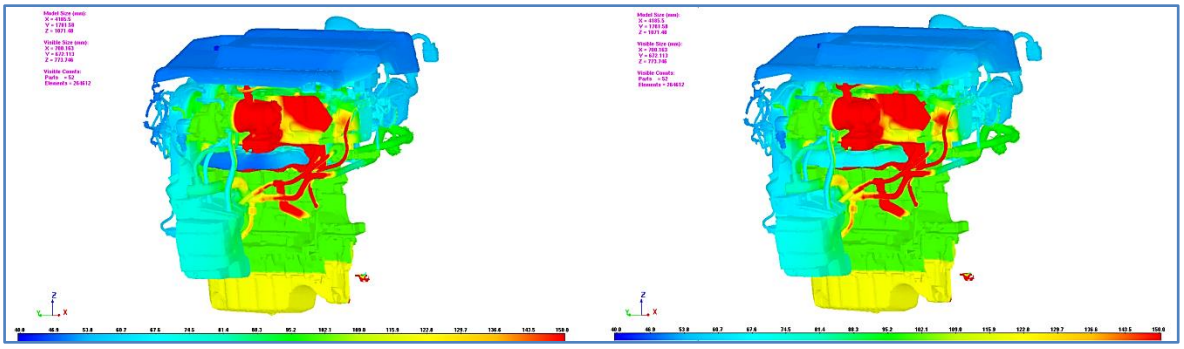

Figure 3.28 - Temperature distribution map, detail of the engine assembly. Left: baseline; right: modified.

The temperature distribution map of the engine does not display substantial alterations in the modified version. This is essentially due to two main reasons: first of all, the involved temperatures are so high that minor changes occur when a cooling air flow rate variation takes place, as important as it could be. Second, some of the surface temperature values were imposed in the CFD as boundary conditions, based on experimental measurements. For those components, in fact, the involved temperatures are so high that a variation in cooling air flow rate, as large as it could be, does not affect them, and they can be treated as heat sources.

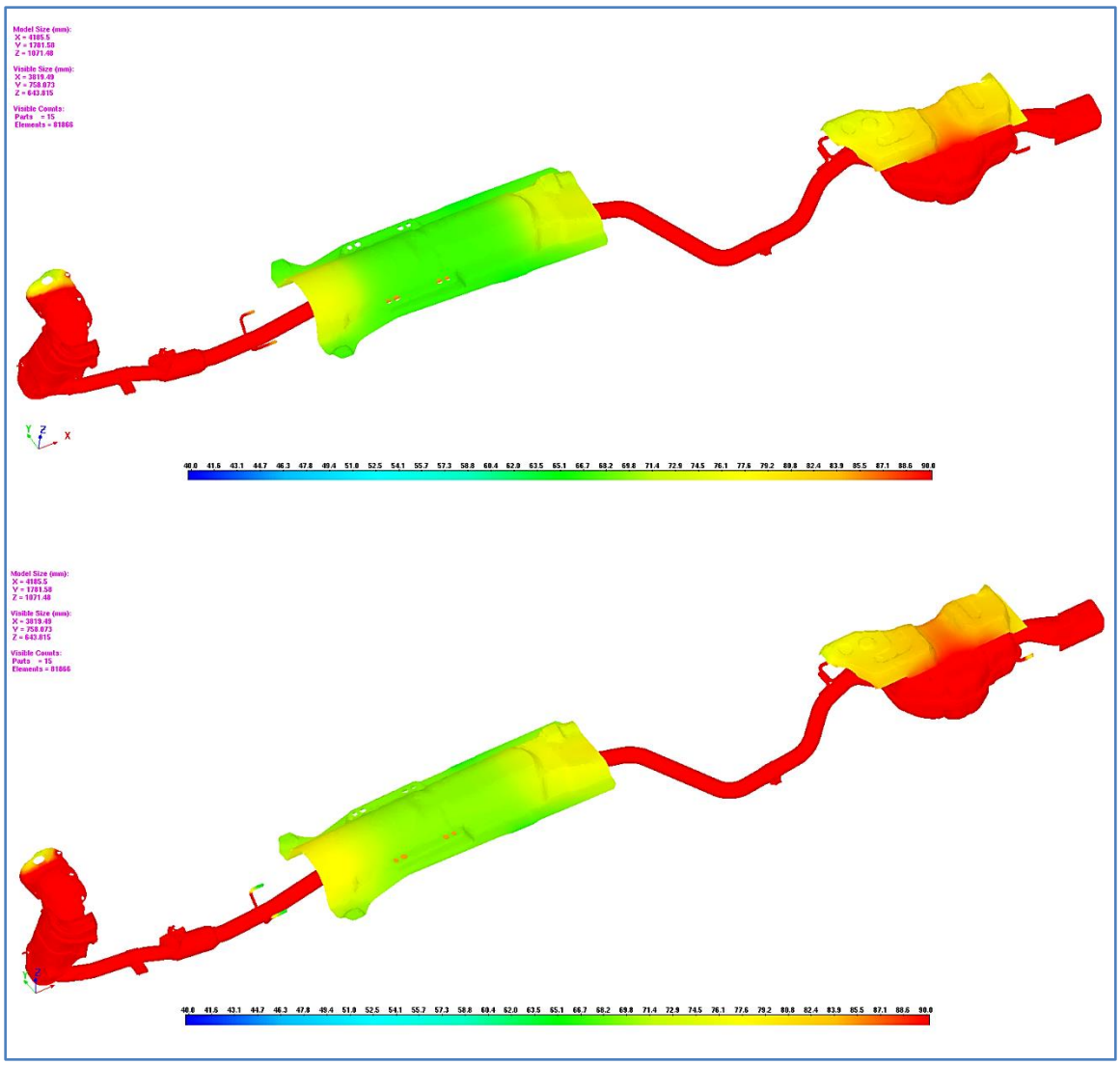

Figure 3.29 - Temperature distribution map, detail of the exhaust line. Top: baseline; bottom: modified.

The same consideration holds true also for the exhaust line, shown in Figure 3.29. Also in this case, in fact, the main components of the exhaust line are heat sources with imposed surface temperatures, while the passive components have temperatures high enough to be barely affected by the presence of the shuttered inlet.

When considering the cooling module components, the situation is definitely different in the configuration with closed shutters, as expected, due to the positioning of these parts just downstream of the closed inlet. Figure 3.30 and Figure 3.31 give a visual extent of the alteration of the thermal field when the

AGS is fully closed. The red, hot area is much wider, and this is numerically quantified in an increase in both the average and maximum temperature of these components. As an example, the fan frame average temperature rises from 69.7°C in the baseline version to 83.0°C in the modified one, with an absolute increase of 13.3°C. The increase is even higher for the very same fan blades, whose temperature rises from 75.4°C to 98.0°C, corresponding to an increase of 22.6°C.

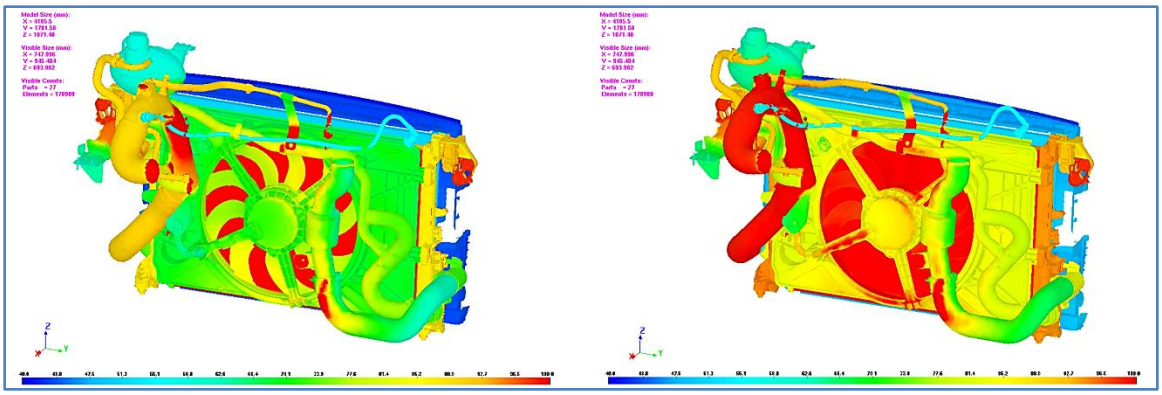

Figure 3.30 - Temperature distribution map, detail of the cooling module. Left: baseline; right: modified.

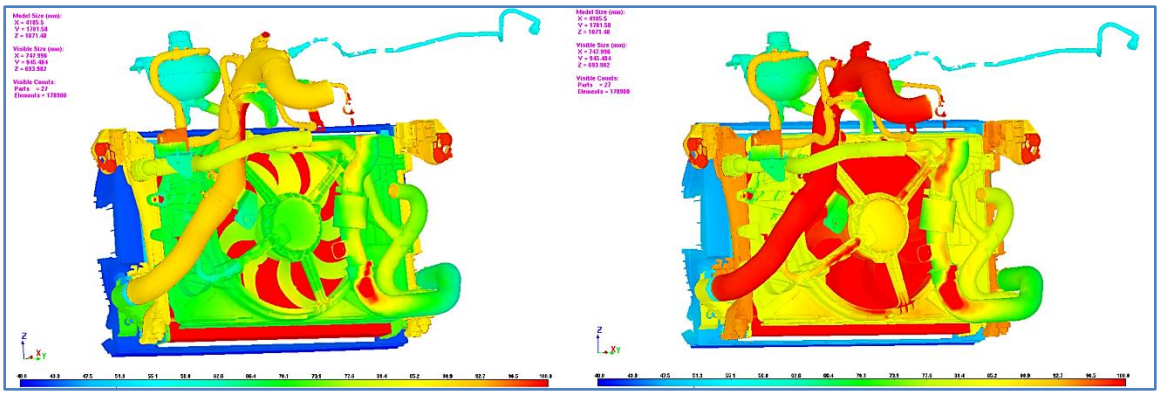

Figure 3.31 - Temperature distribution map, detail of the cooling module. Left: baseline; right: modified.

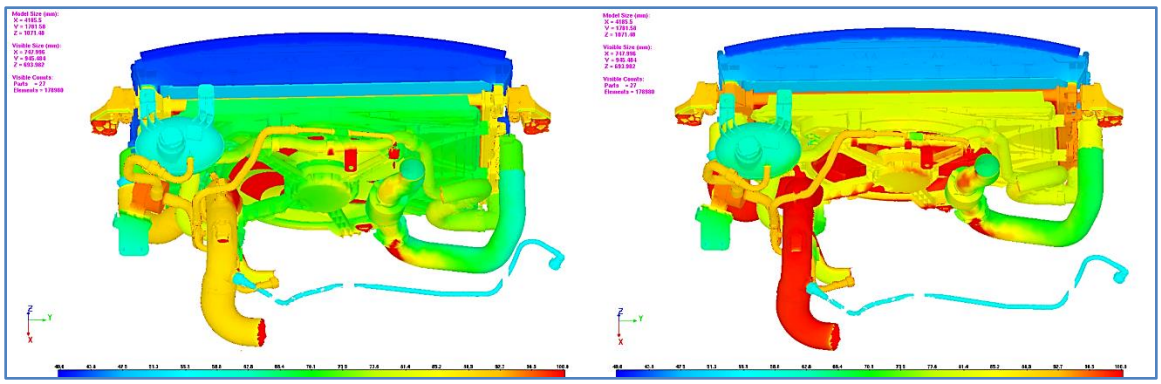

Figure 3.32 - Temperature distribution map, detail of the cooling module. Left: baseline; right: modified.

The effect of the closed shutter propagates further downstream even on the lower part of the front suspension assembly, as shown in Figure 3.33 and Figure 3.34. Here, the red hot central area is much larger in the modified case.

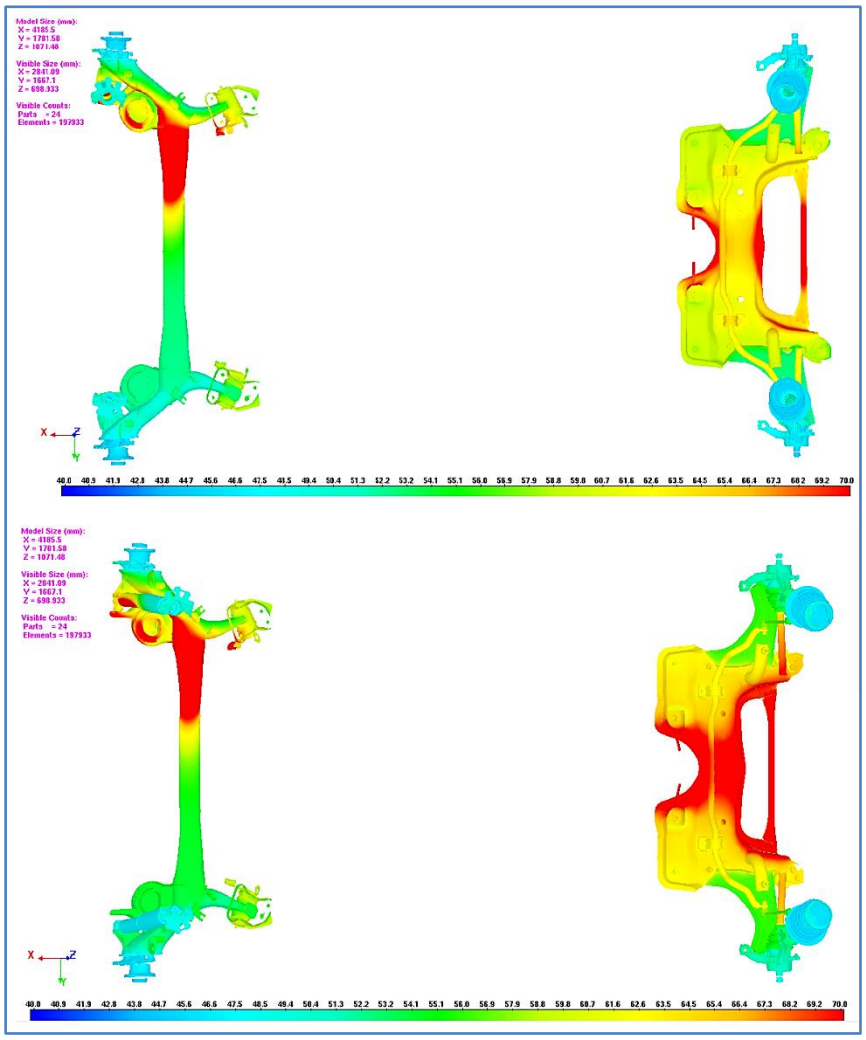

Figure 3.33 - Temperature distribution map, detail of the suspensions sub-group. Top: baseline; bottom: modified.

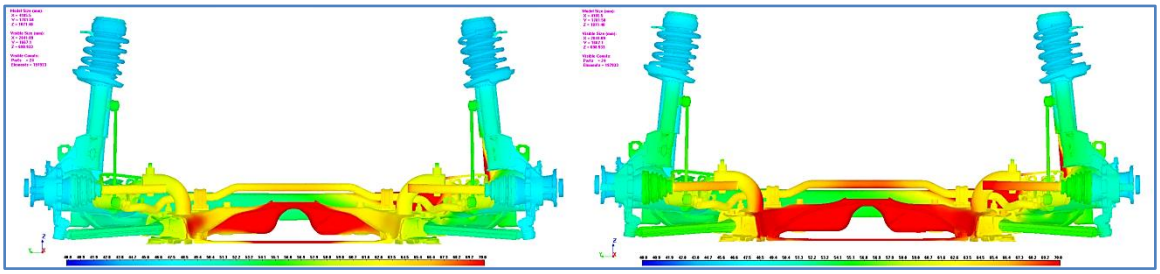

Figure 3.34 - Temperature distribution map, detail of the suspensions sub-group. Left: baseline; right: modified.

The last main sub-group of interest in the underhood area is the steering assembly, displayed in Figure 3.35. Here no big dissimilarities can be spotted between the two cases, as numerically calculated by the solver.

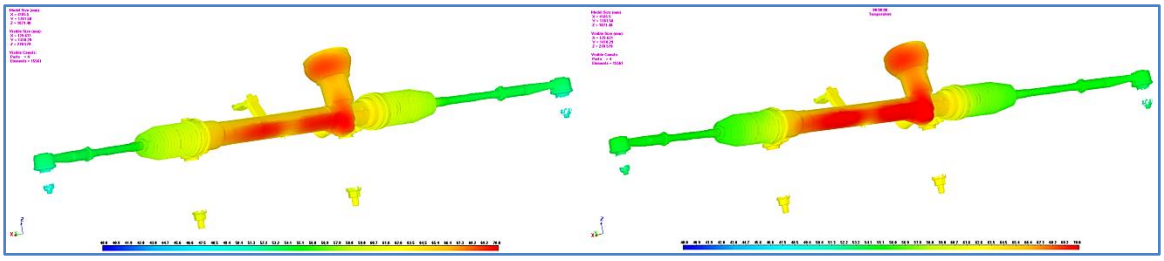

Figure 3.35 - Temperature distribution map, detail of the steering assembly. Left: baseline; right: modified.

3.2.5. SUMMARY OF THERMAL RESULTS

After showing and discussing the thermal results calculated by the numerical simulation, few conclusions can be drawn. Overall, a net increase in temperature is observed for the vast majority of the underhood components, especially those ones directly downstream of the shuttered inlet. Among these, the most remarkable variations are observed for plastic components, like, for instance, the fan assembly. Before fitting the AGS system onboard, a more specific analysis is recommended to be performed component-wise, especially for the mostly affected ones, in order to evaluate potential deterioration of performances when subjected to high temperatures. This is particularly critical

for the plastic components described in the previous section, and a careful sensitivity analysis should be carried out together with the help of the component supplier to investigate if any issue could occur when the AGS is fully closed (worst-case scenario). Only two components were showing an important increase of temperature when the AGS was fully closed: the front underbody shield and the cooling fan blades. Therefore, further analysis is recommended for them, either on a virtual simulation basis using the new, more accurate procedure, or through experimental tests. For these two components, in case the additional analysis confirms the temperature increase evaluated here, few possibilities can be explored. For instance, for the front underbody shield an aluminum cover located on the hot area could absorb part of the heat flux, thus thermally insulating the plastic part and avoiding thermo-structural issues. As for the fan blades, instead, an alternative plastic material to the one currently used can be selected, always respecting the constraints in terms of weight, cost, and mechanical properties. Overall, however, the temperature rise does not seem to be relevant enough to cause any failure or malfunctioning of any system or component, so that this work may represent a starting point for a further development of this device with the final target to install it on-board.

As for the metal parts, the temperature increase recorded by the simulation does not represent an issue. From a thermo-structural point of view, in fact, the temperature increase evaluated by the solver does not affect the performances in any significant way, nor does it from a dimensional stability point of view.

An interesting analysis which could not be carried out in this context is represented by the variation of performances of the cooling system. More specifically, for the purposes of this thesis, a constant power to be dissipated by the heat exchangers has been imposed, equal in the two cases. In the modified case, however, the cooling ability of the cooling air in the engine bay is reduced to an extent which is not negligible, so that an increase of coolant flow rate

would be required for both engine cooling and HVAC purposes. This increase could only be guaranteed by the water and refrigerant pump (in this specific case), which implies that a higher power absorption has to be expected by the latter. Of course, this increase in accessory power absorbed by the pump must not outweigh the reduction in aerodynamic resistance power absorption guaranteed by the AGS system, otherwise the entire purpose of fitting the device on board loses validity.

The numerical solver was able to get the general trend in terms of thermal behavior in the engine bay, even if in some limited cases the temperature values could be not close enough to the real case due to the characteristics of the algorithm followed for the mapping of the T and h results from the CFD to the thermal code. In order to get more reliable results, the new procedure under development at CRF is strongly recommended, which is able to better evaluate the thermal performances of each of the considered components.

Common sense is not so common.

Voltaire, *Dictionnaire philosophique*

4. CHAPTER 4

FINAL CONSIDERATIONS & RECOMMENDATIONS

4.1. OVERALL CONTRIBUTION

This final chapter deals with few final considerations after the completion of the thesis work. More specifically, this paragraph summarizes the overall contribution provided by the author.

First of all, the co-simulation approach used for the aero-thermal analysis was totally new to Chrysler. In particular, this procedure is currently state-of-the-art and even if some automotive manufacturers use it, the readiness, accuracy and development level of this strategy is still at a preliminary stage. In some cases, the simulation results are still too far from the experimental values measured on a physical model, meaning that further margin of improvement is clearly possible. This work served as a starting point for the Company to get acquainted with commercial codes able to address the problem from a global point of view. The main objective for the author was to help the Company implement the co-simulation procedure, thus being a kind of lead user for the identification of those issues which inevitably come up when trying to implement a new process.

From a research point of view, a new, holistic approach was considered where the aerodynamics and thermal problems were addressed in a combined way, and not in a subsequent manner, with virtual simulation tools. In other words, a new aerodynamic solution was devised since the very beginning by keeping directly into account its impact on the thermal performances. This meant that two models were built almost in parallel, one for the fluid-dynamics and one for the thermal simulation. This systematic approach where each new solution is

directly developed and simultaneously evaluated both in its aerodynamic and thermal behavior is extremely recent and sponsored by CFD code developers and very few car manufacturers, but no structured theoretical or research work was done from a scientific or academic point of view.

Finally, based on the current scenario and state-of-the-art procedure, the author was able to provide suggestions about possible evolutions of the current practice, envisioning a process where a DOE approach would speed up the design and development phase of a vehicle in its early stages. Based on the improvements in terms of computational power and codes flexibility and interaction, this innovation is expected to become possible and commercially available within 5-10 years from now.

4.2. MANUFACTURING ISSUES

In the last part of the previous chapter few recommendations were done related to the very co-simulation process in order to get more reliable results from the numerical solver. The objective of this section is to focus on additional issues to be further investigated before fitting the active grille shutter on board the considered vehicle. In particular, the first part of this section addresses those issues related to the *product*, i.e. the AGS system itself, while the focus of the next part is on the *process*, meaning all those steps necessary to proper design and develop the system to be installed on the production vehicle.

The first question to be answered when dealing with a system like the one under analysis is whether the benefits achieved outweigh the complexity and drawbacks caused by the introduction of a new sub-group. As a matter of fact, the analysis carried out here showed that no major issue occurs from a thermal point of view, which still needs to be further validated through a more accurate

co-simulation procedure and/or climatic tunnel experimental tests. Also, an accurate balance should be found between the aerodynamic power reduction guaranteed by the system and the power absorption increase required for increasing the coolants flow rates. In addition to the thermal side, other aspects must be considered. First of all, the complexity of the control algorithm of the AGS should be carefully considered in order to properly match the opening angle of the device blades to the vehicle operating conditions. Here, in fact, only the worst-case scenario was studied to evaluate the worst conditions the engine bay components may encounter, but intermediate cases need to be studied for a proper matching of the device to the vehicle load and speed and external environmental conditions. Only this type of analysis, which could be carried out either in the virtual environment or through physical experimentation, could allow the designers to develop the best control strategy for such device in order to take full advantage in each operating condition.

A second issue associated to the introduction of this system is represented by the weight. It must be remembered that the AGS system is composed by a quite bulky frame and a motor which add a non-negligible weight to the vehicle. In order not to penalize the acceleration and fuel economy/emissions performances, this weight addition should be minimized, meaning that lightweight materials are preferred for this application. The adoption of such materials, in turn, has an effect on the cost, which is one of the main (if not *the* main) factors which come into play when dealing with this type of vehicles, with a mainly urban and extra-urban mission profile. Therefore, cost has to be considered another main element when setting up a development strategy to take this system into production.

In order to reduce the negative impact of cost on the development of the project, an interesting alternative can be suggested. In the newly established FCA group, a mid-size vehicle equipped with an AGS system has already been

developed and is currently available on the market. This is the Dodge Dart, based on the Alfa Romeo Giulietta. Differently from its Italian counterpart, the Dart is equipped with an AGS system which could be carried-over on the FIAT 500L. The author had the chance to take a quick glance at the dimensions of the Dart's AGS system and at the available space in the engine bay of the FIAT 500L, and there seems to be the possibility to fit the device in front of the cooling module of the latter. The possibility to use carry-over parts (if not the entire system, at least parts of it) could dramatically reduce the overall costs of both design and procurement, if properly managed. However, the author did not have the possibility to carefully measure each dimension of the system and the available space in the 500L underhood, and a more accurate analysis is required and recommended (even on the CAD model) before considering this option.

Yet, this alternative could represent an interesting starting point for modularity considerations. In fact, if this system proves effective and reliable, many other models of the Group could be equipped in the near future with this device. As a matter of fact, modularity has become a strong and effective engineering and economic solution in recent years for automotive parts.

One last matter to be addressed in the development of the system corresponds to the underhood packaging of the vehicle. Sufficient space must be available to fit the system in the engine bay, which is particularly critical when dealing with such a compact vehicle with extremely short front overhang. However, thanks to the design studio style requirements to have a vehicle reminiscent of the old FIAT 500L and in line with the present style of the 500 model line, the model was designed with a sufficiently bulged front bumper which allows sufficient space in front of the intercooler to fit an AGS device. However, before commercializing the modified version, the new model must undergo homologation and type approval tests which require specific passive, insurance and pedestrian safety requirements to be satisfied. The fulfillment of

such requirements can be satisfied by properly engineering the system even in a preliminary design stage through virtual simulation tools for crashworthiness. In any event, homologation tests must be done in order to validate the meeting of the safety requirements of the vehicle equipped with the new device.

4.3. WORKFLOW OPTIMIZATION

The aim of this paragraph is to focus on the *process* side of the problem, and to highlight some potential improvement in the workflow organization.

An important consideration is related to the co-simulation procedure in itself. In order to fully exploit the potential of the automated process even on different vehicles and platforms, it is necessary to standardize some steps even upstream of the process. One example of this could be the pre-processing of the models for the CFD and thermal simulations. When assigning the PIDs to the CAD model of the vehicle, it is strongly advisable to use standard names and codes for the same component. For instance, if the standard name "RAD_in" is chosen for the radiator inlet, every time that component is present in a virtual model, it should be identified with this label. Then, by so doing, it will be possible to match in the best possible way the models between different platforms, as could be for instance between Star-CCM+ and RadTherm. Also, by so doing, a complete virtual library database could be developed where to store and retrieve in an easy and fast way a given vehicle model or component CAD model. Also, any time a new version or release of a piece of software is installed, it is necessary to provide the Company users with information about possible differences/incompatibilities with respect to the previous version. In this way, the user knows where to pay attention and/or change a given procedure or command before getting in trouble.

One of the biggest limitations faced during the development of the thesis work was the maximum speed of transfer of simulation files between different networks and between local machines and server. While the former is inevitably constrained by the maximum speed of the transfer protocol used (SFTP – Secure File Transfer Protocol), the latter is essentially due to the strong limitation in terms of bandwidth available at the Chrysler facilities in Canada. Of course, the size of the CFD models to be transferred is quite remarkable (in the order of 10-20 GB), however transfer times of 5-6 hours were not unusual, with peaks up to 10 hours. This puts a huge limit to the useful working time, due to the impossibility to do anything on the transferring files until they get on the server.

Another issue faced during the development of the thesis, this time successfully solved, consisted in the procedure used to post-process the CFD simulation results on the server. Since the available RAM on the local machine was too limited for the model size under study, the server was to be used in order to visualize the flow field maps necessary for the aerodynamic analysis. However, when trying to accomplish this task, some issues arose. Later, a bug in the Star-CCM+ software was found, consisting in a memory leak issue. An alternative way to accomplish the same task without causing the system to crash was then found. In the meantime, the author collaborated with the IT staff at the Chrysler Technical Center in order to setup a post-processing procedure on the backend nodes of the server. This allowed post-processing all the models without any issue and the new procedure was recommended to all CFD users in the Company.

5. REFERENCES/BIBLIOGRAPHY

5.1. SOURCES IN THE TEXT

[1] D. Baeder, T. Indinger, N. Adams and P. Unterlechner, "Aerodynamic Investigation of Vehicle Cooling-Drag," *SAE International,* 16 April 2012.

[2] W.-H. Hucho, Aerodynamics of Road Vehicles, Fourth ed., W. Hucho, Ed., 1998.

[3] D'Ambrosio, Stefano, Politecnico di Torino, *Combustion engines and their application to vehicles,* Torino, 2013.

[4] E. Mühlberg and W. Besslein, "Variable Heiβkühlung beim Fahrzeug-Dieselmotor," *MTZ,* vol. 44, 1983.

[5] H. Reister and W. Bauer, "Simulation Process of the Heat Protection of a Full Vehicle," *SAE International,* 16 April 2012.

[6] R. L. Lietz, "Vehicle Aerodynamic Shape Optimization," *SAE International,* 12 April 2011.

[7] J. McMullough, "U.S. Department of Transportation - Federal Highway Administration," 10 July 2013. [Online]. Available: http://www.fhwa.dot.gov/planning/processes/statewide/practices/ghg_emissions/ghg_webinar/index.cfm. [Accessed 18 January 2014].

[8] "Emission Standards - European Union - Cars and Light Trucks," July 2013. [Online]. Available: http://dieselnet.com/standards/eu/ld.php. [Accessed 18 January 2014].

[9] "Motoring J Style," 11 February 2008. [Online]. Available: http://motoringjstyle.blogspot.com/2008/02/nissan-gtr-graphs-and-aero.html. [Accessed 29 January 2014].

[10] P. Massai, *Aerodynamics lecture notes,* Torino, TO, 2013.

[11] Audi AG, "Audi Future Lab Mobility," 2012. [Online]. Available: http://m.audi-future-lab-mobility.de/en/atp/Body/Aerodynamics-Aeroacoustics/Air-flow-through-the-engine-compartment. [Accessed 30 January 2014].

[12] S. Carmassi, E. Cardile and F. Toni, "Road vehicle provided with a cooling duct for the cooling of a brake". Patent EP20130158043, 6 March 2013.

[13] Chrysler Group, LLC, "2013 Dodge Dart," 2013.

[14] Couture, Justine, "2014 Porsche 911 Turbo and Turbo S first drive gallery," 30 August 2013. [Online]. Available: http://autos.ca.msn.com/reviews/2014/2014-porsche-911-turbo-and-turbo-s-first-drive-gallery?page=7. [Accessed 13 February 2014].

[15] Fartaj, Amir; University of Windsor, *Vehicle Thermal Management,* Windsor, ON, Canada, 2014.

[16] "NetCarShow.com," 2005-2014. [Online]. Available: http://www.netcarshow.com/fiat/2014-500l_us-version/. [Accessed 27 January 2014].

[17] S. Sebben, "Numerical Simulations of a Car Underbody: Effect of Front-Wheel Deflectors," *SAE International,* 2004.

[18] Toyota Motorsport GmbH, "Toyota Motorsport," 2013. [Online]. Available: http://www.toyota-motorsport.com/slideshowpro/albums/album-8/lg/Engine_Calculation1.jpg. [Accessed 18 November 2013].

[19] L. Miretti and E. M. Ribaldone, "Experiences at CRF and FGA in the use of Radtherm for the simulation of underhood components temperatures in unsteady conditions," in *ThermoAnalytics - RadTherm User Group Meeting 2013*, 2013.

[20] "Serious Wheels," [Online]. Available: http://www.seriouswheels.com/pics-2006/2006-Ferrari-P45-Pininfarina-Wind-Tunnel-1920x1440.jpg. [Accessed 6 June 2014].

[21] E. M. Ribaldone, "Best Practices for Thermal Simulations: Introduction," Orbassano, 2012.

[22] The International Council on Clean Transportation (ICCT), "Global Comparison of Light-Duty Vehicle Fuel Economy/GHG Emission Standards," Washington DC - San Francisco - Berlin, 2013.

[23] S.-J. Baek and B. H. J. Lee, "Engine Room Lay-out Study for Fuel Efficiency and Thermal Performance," *SAE International,* 16 April 2012.

[24] W.-H. Hucho, "Threshold strategy - Halving the Drag Coefficient Seems Possible," *ATZ worldwide eMagazines,* vol. 111, January 2009.

6. APPENDICES

6.1. APPENDIX A

EU EMISSIONS STANDARDS FOR PASSENGER VEHICLES

Stage	Date	CO	HC	HC+NOx	NOx	PM	PN
		g/km					*#/km*
Compression Ignition (Diesel)							
Euro 1†	1992.07	2.72 (3.16)	–	0.97 (1.13)	–	0.14 (0.18)	–
Euro 2, IDI	1996.01	1.0	–	0.7	–	0.08	–
Euro 2, DI	1996.01[a]	1.0	–	0.9	–	0.10	–
Euro 3	2000.01	0.64	–	0.56	0.50	0.05	–
Euro 4	2005.01	0.50	–	0.30	0.25	0.025	–
Euro 5a	2009.09[b]	0.50	–	0.23	0.18	0.005[f]	–
Euro 5b	2011.09[c]	0.50	–	0.23	0.18	0.005[f]	6.0×10^{11}
Euro 6	2014.09	0.50	–	0.17	0.08	0.005[f]	6.0×10^{11}
Positive Ignition (Gasoline)							
Euro 1†	1992.07	2.72 (3.16)	–	0.97 (1.13)	–	–	–
Euro 2	1996.01	2.2	–	0.5	–	–	–
Euro 3	2000.01	2.30	0.20	–	0.15	–	–
Euro 4	2005.01	1.0	0.10	–	0.08	–	–
Euro 5	2009.09[b]	1.0	0.10[d]	–	0.06	0.005[e,f]	–
Euro 6	2014.09	1.0	0.10[d]	–	0.06	0.005[e,f]	6.0×10^{11} e,g

* At the Euro 1..4 stages, passenger vehicles > 2,500 kg were type approved as Category N_1 vehicles
† Values in brackets are conformity of production (COP) limits
a. until 1999.09.30 (after that date DI engines must meet the IDI limits)
b. 2011.01 for all models
c. 2013.01 for all models
d. and NMHC = 0.068 g/km
e. applicable only to vehicles using DI engines
f. 0.0045 g/km using the PMP measurement procedure
g. 6.0×10^{12} 1/km within first three years from Euro 6 effective dates

Source: DieselNet.com

6.2. APPENDIX B

US EMISSIONS STANDARDS FOR PASSENGER VEHICLES

Proposed Tier 3 Certification Bin Standards (FTP; 150,000 miles).

Bin	NMOG+NOx	PM	CO	HCHO
	mg/mi			
Bin 160	160	3	4200	4
Bin 125	125	3	2100	4
Bin 70	70	3	1700	4
Bin 50	50	3	1700	4
Bin 30	30	3	1000	4
Bin 20	20	3	1000	4
Bin 0	0	0	0	0

Source: DieselNet.com

Proposed Tier 3 Phase-In of Fleet Average NMOG+NOx FTP Standards.

Vehicle Category	2017*	2018	2019	2020	2021	2022	2023	2024	2025
LDV, LDT1	86	79	72	65	58	51	44	37	30
LDT2, LDT3, LDT4, MDPV	101	92	83	74	65	56	47	38	30
* Starting from MY2018 for vehicles with GVWR above 6,000 lb									

Source: DieselNet.com

6.3. APPENDIX C

CFD MODEL – GEOMETRICAL DESCRIPTION IN STAR-CCM+

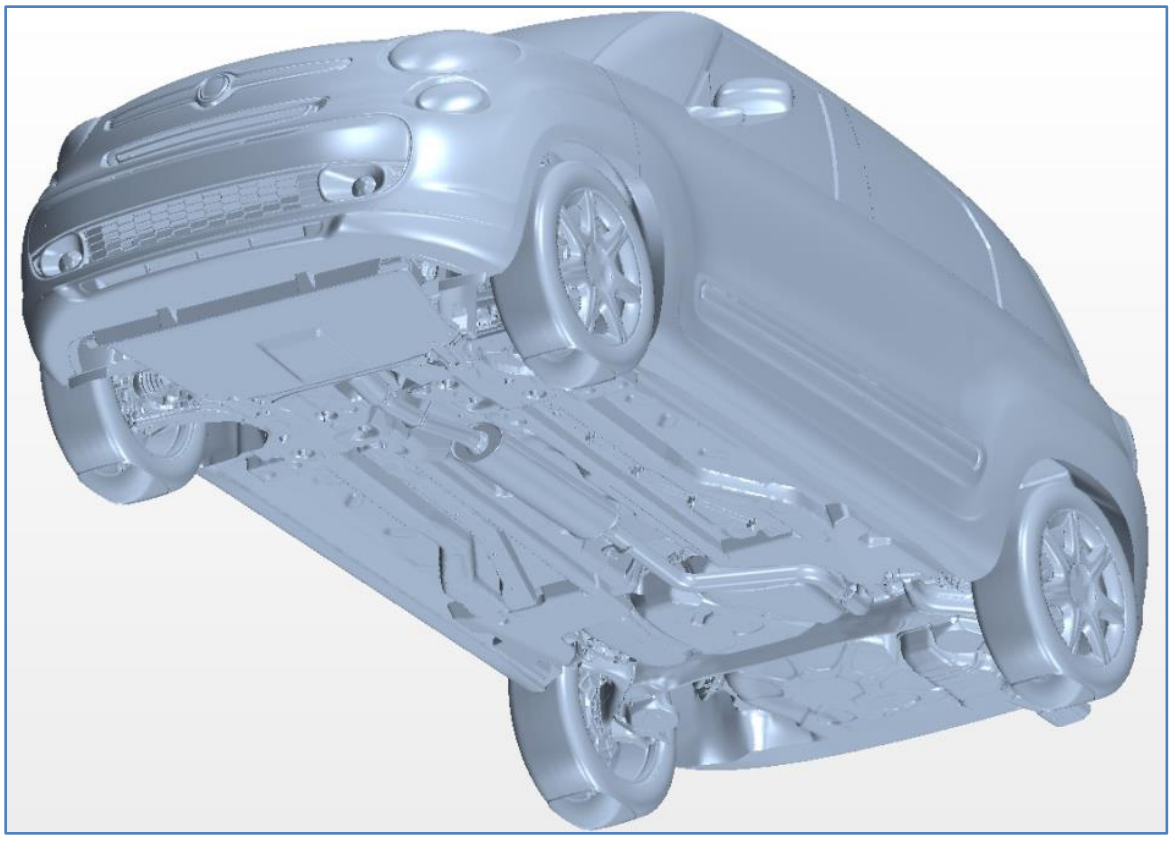

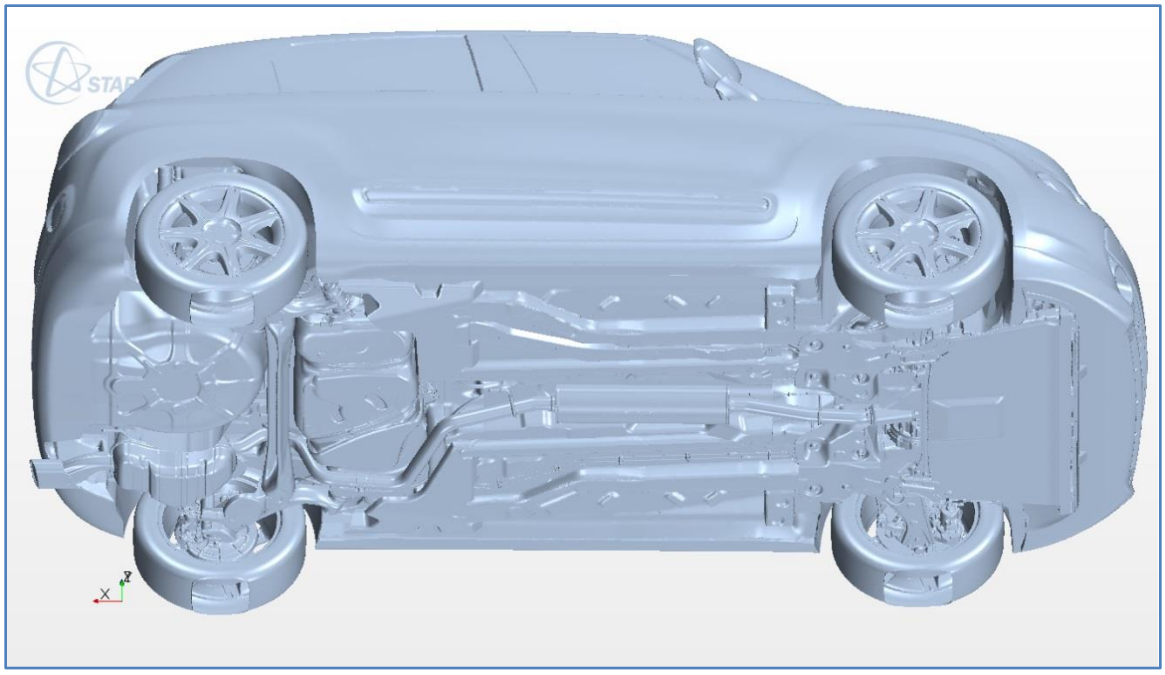

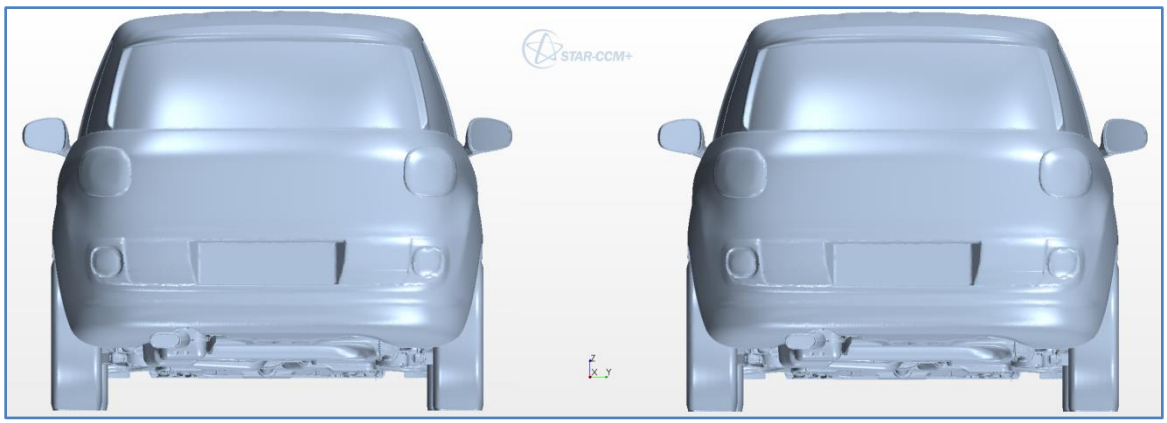

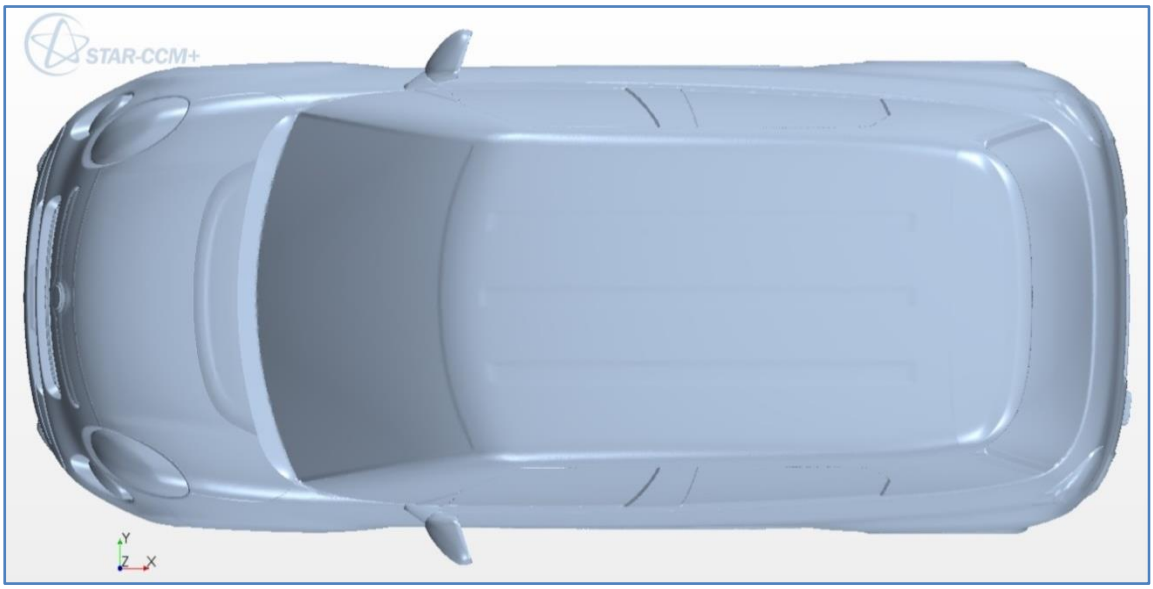
STAR-CCM+

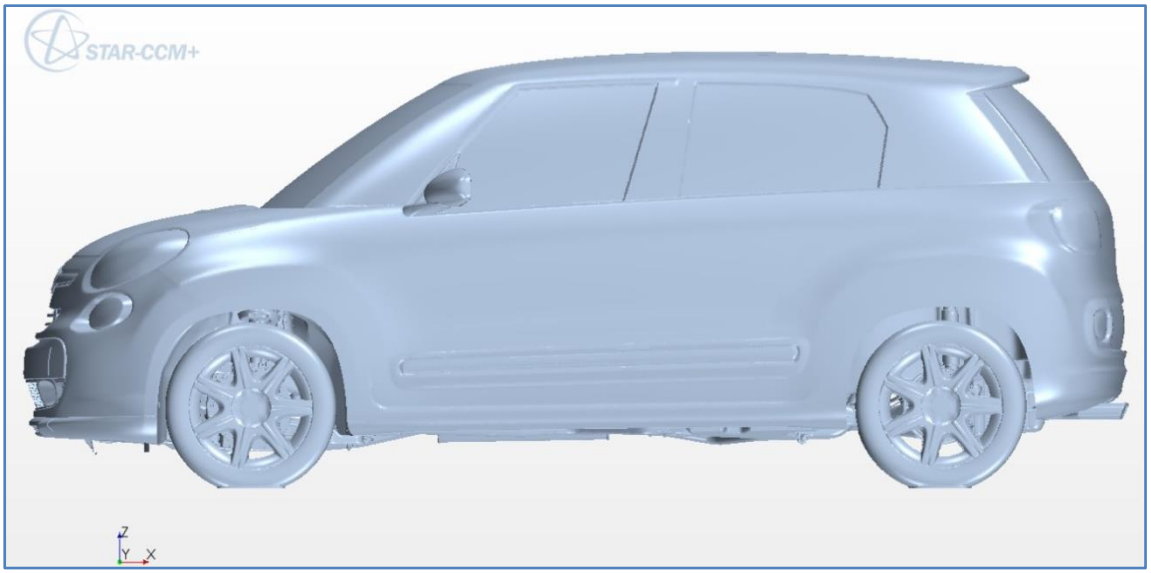
STAR-CCM+

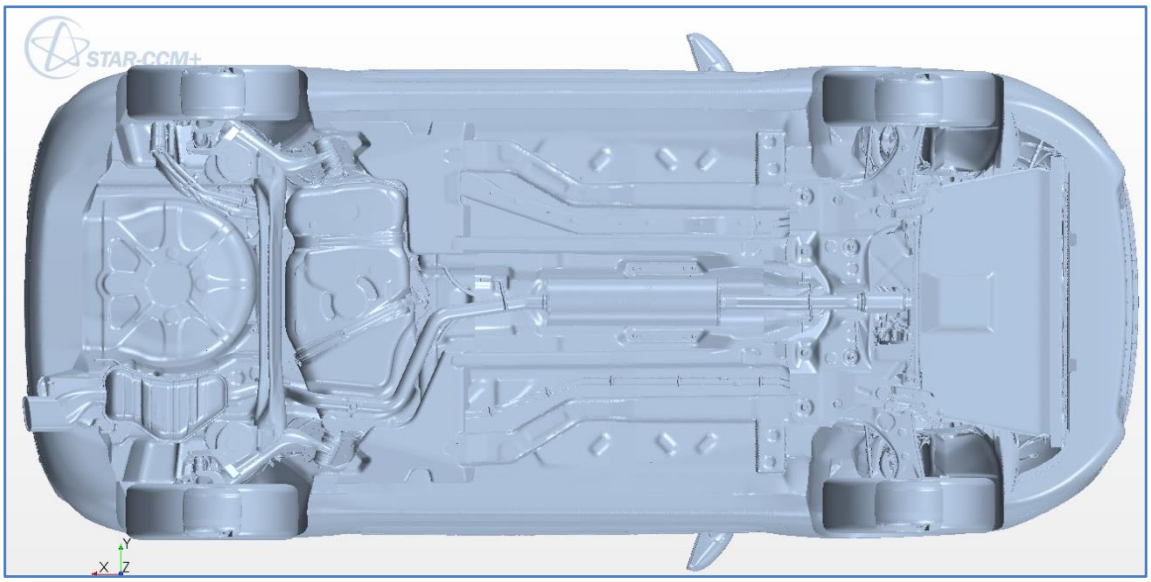
STAR-CCM+

6.4. APPENDIX D

CFD MODEL – VOLUME MESH IN STAR-CCM+

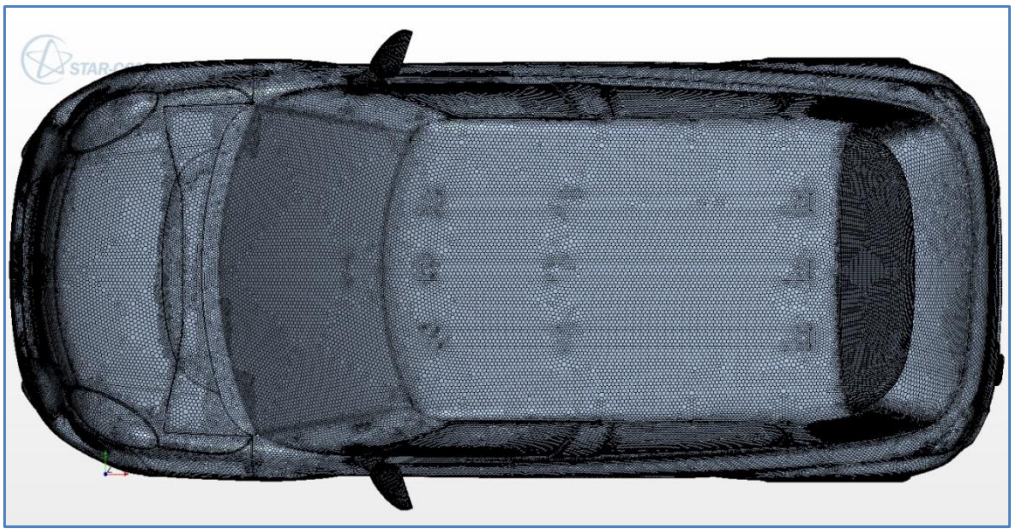

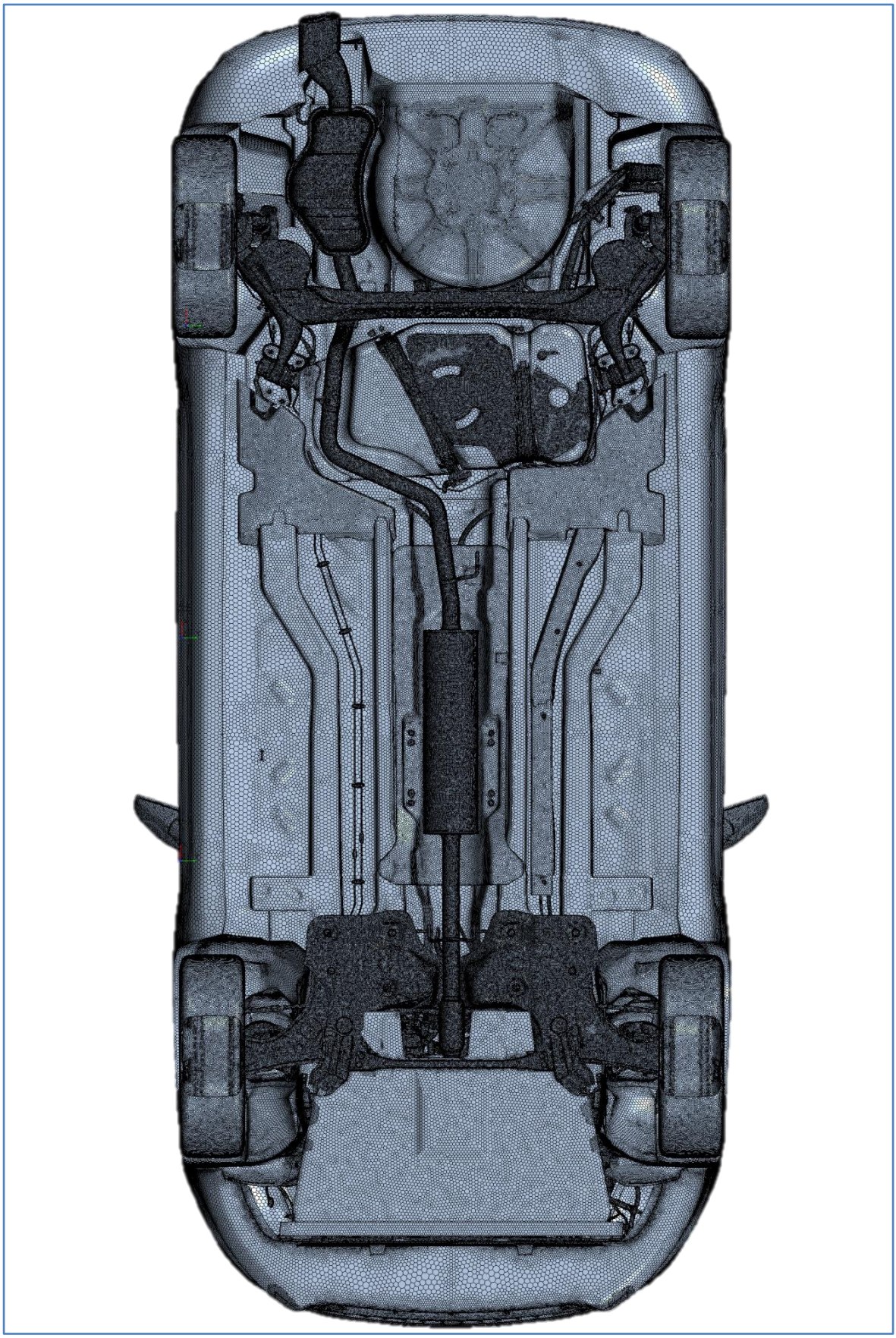

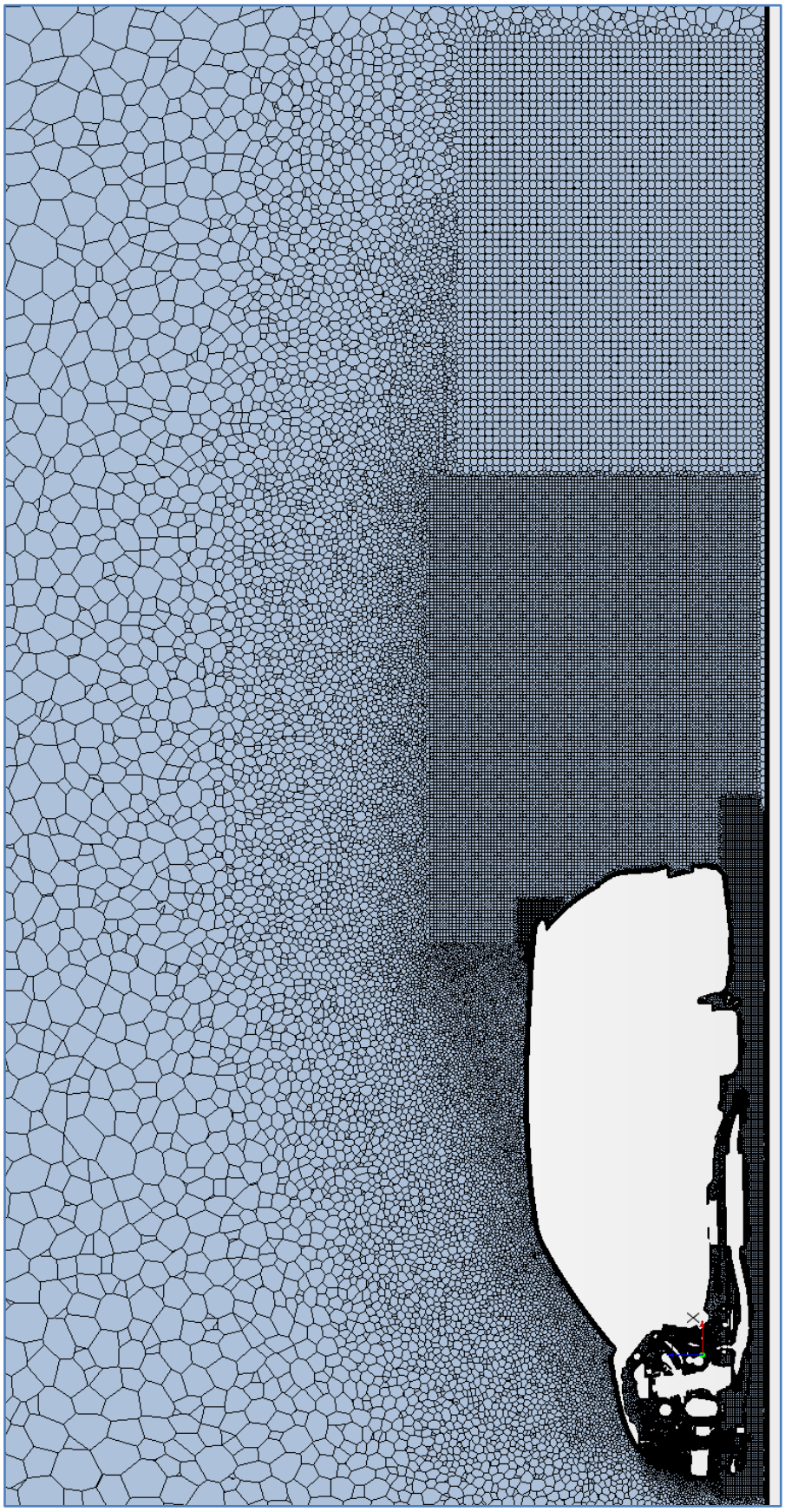

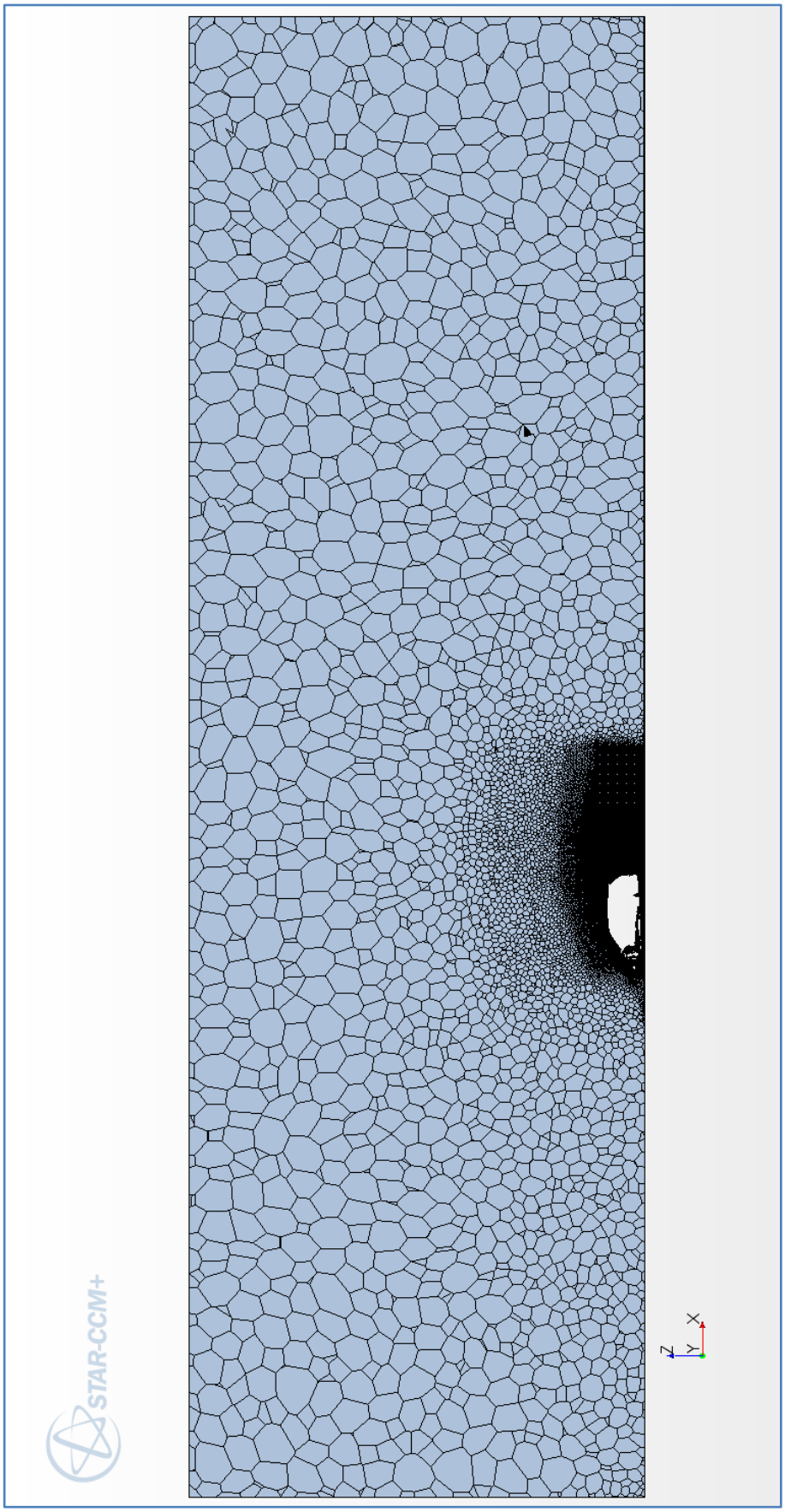
STAR-CCM+
X
Y
Z

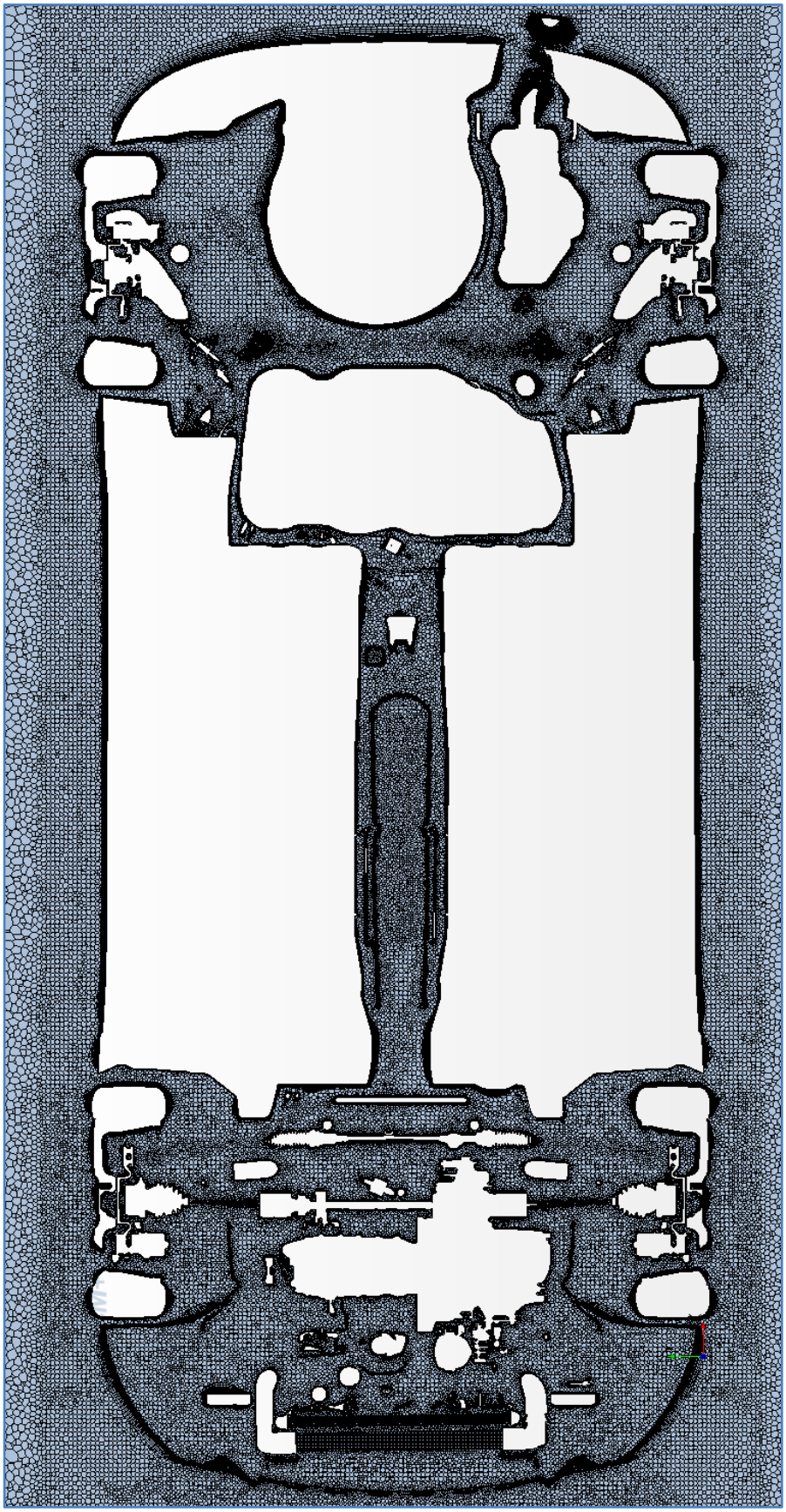

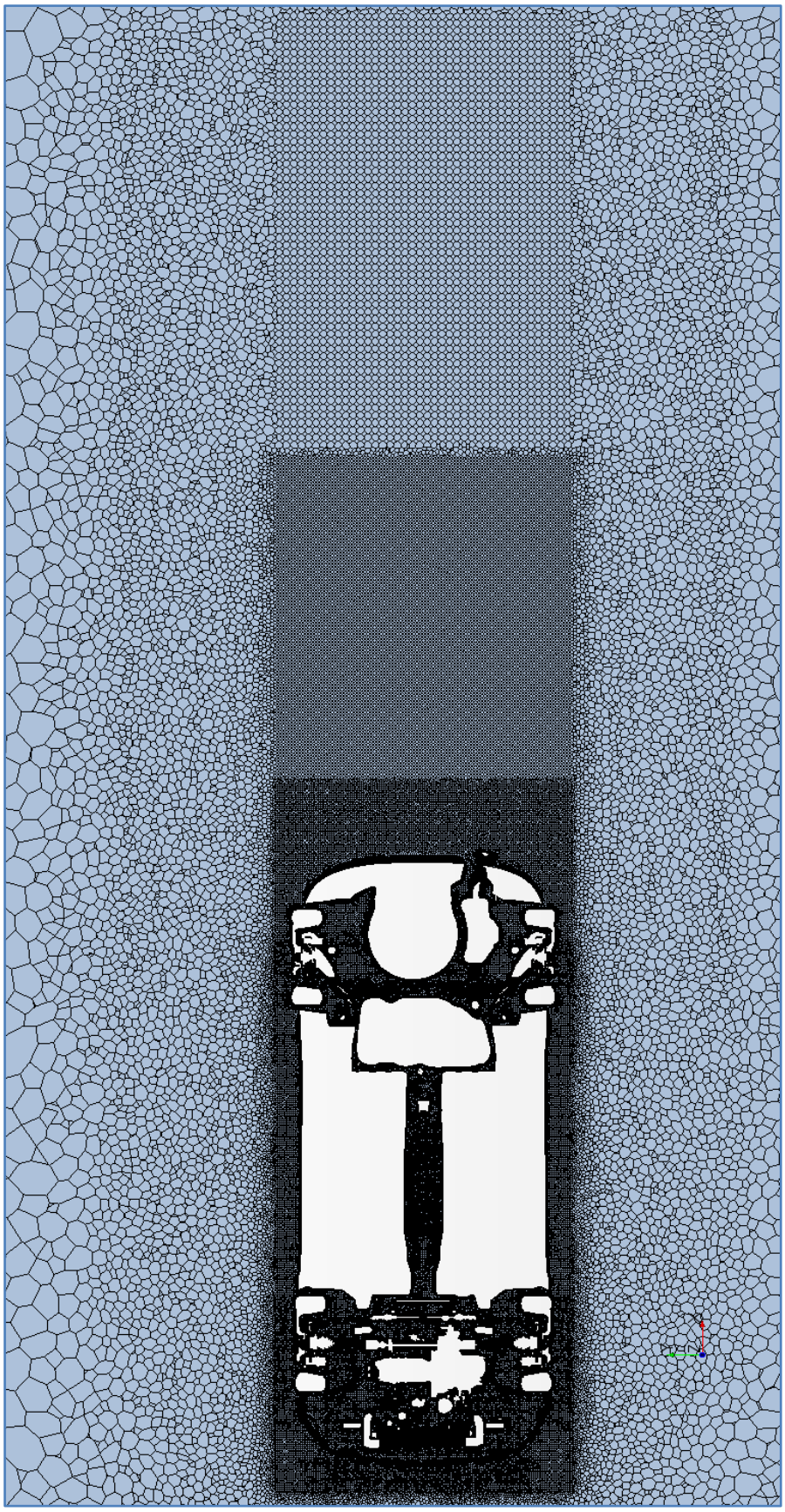

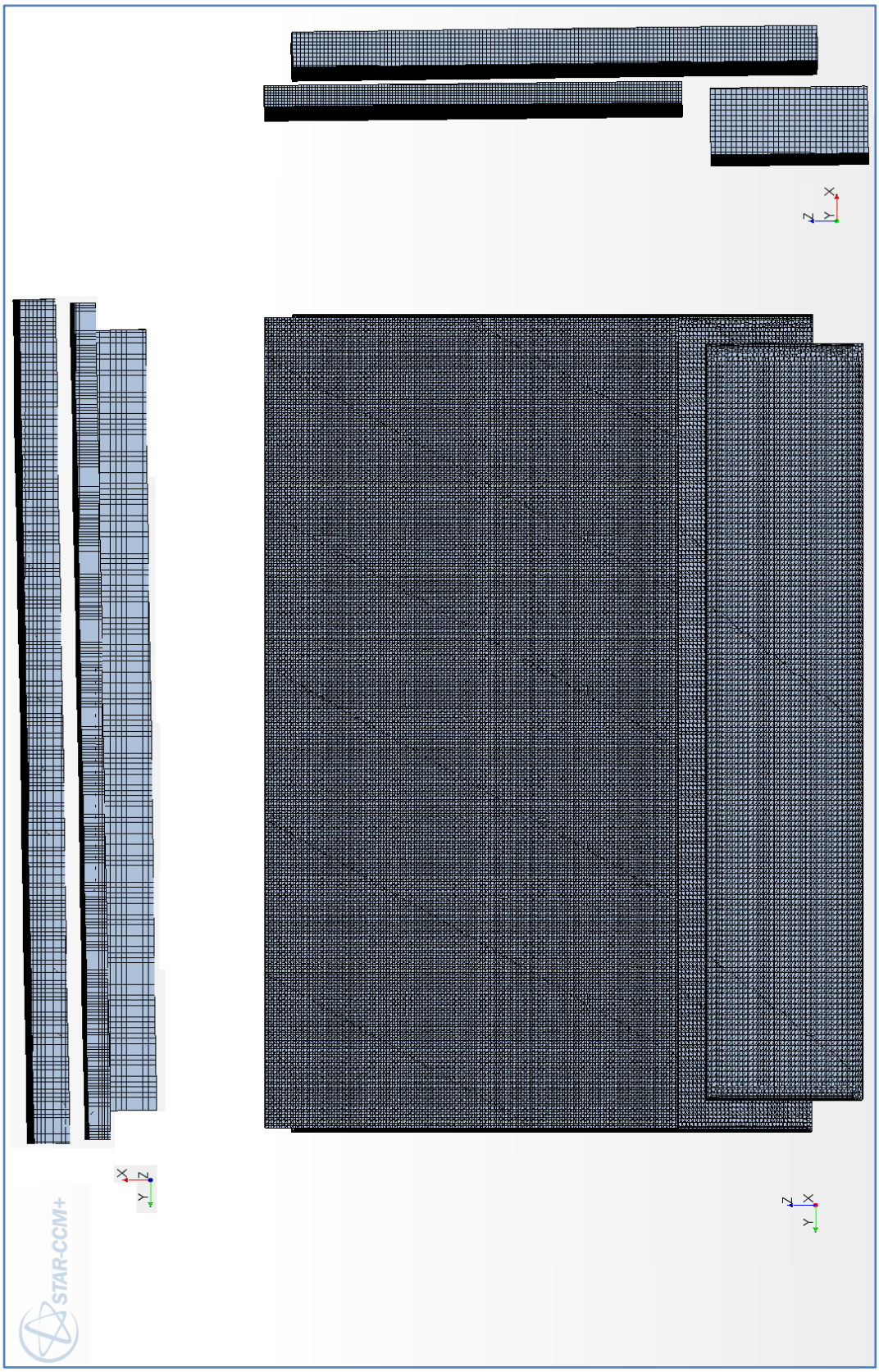
STAR-CCM+

6.5. APPENDIX E

CFD MODEL – PRESSURE DISTRIBUTIONS OVER HEXES FACES

NOTE: unless otherwise specified, the upper maps of the various figures refer to the baseline, while the lower ones to the modified versions.

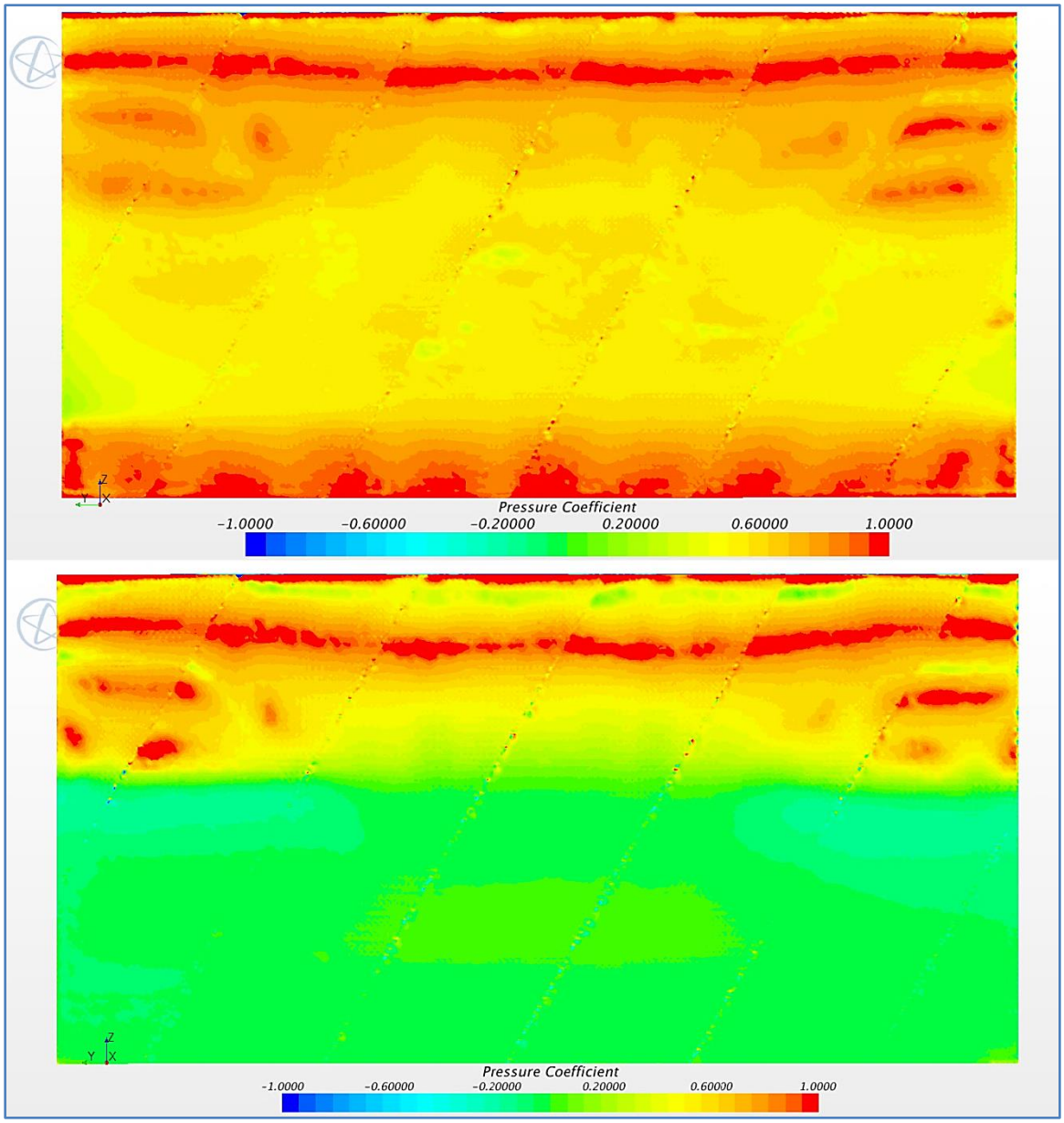

Pressure distribution over the A/C condenser inlet faces.

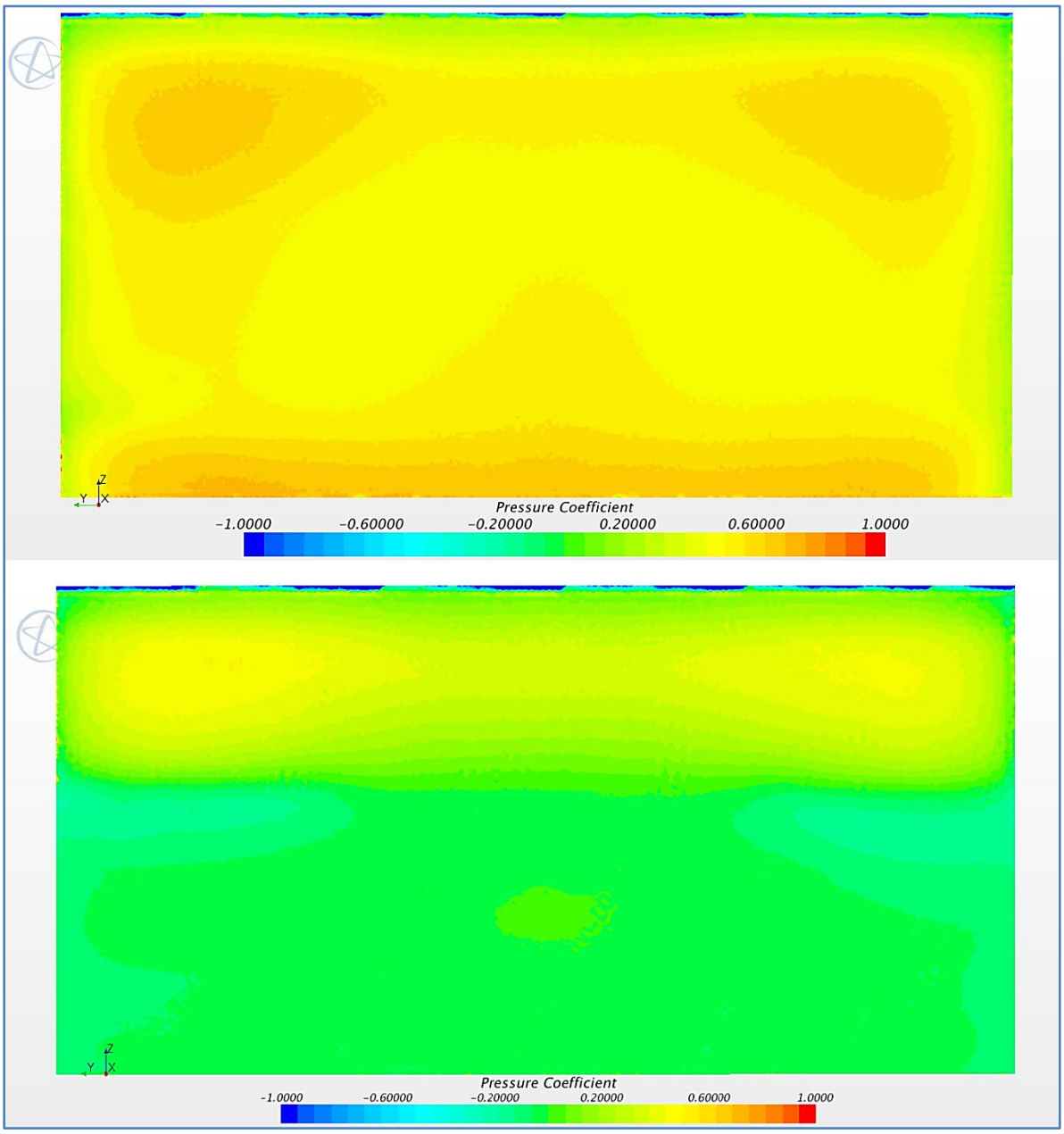

Pressure distribution over the A/C condenser outlet faces.

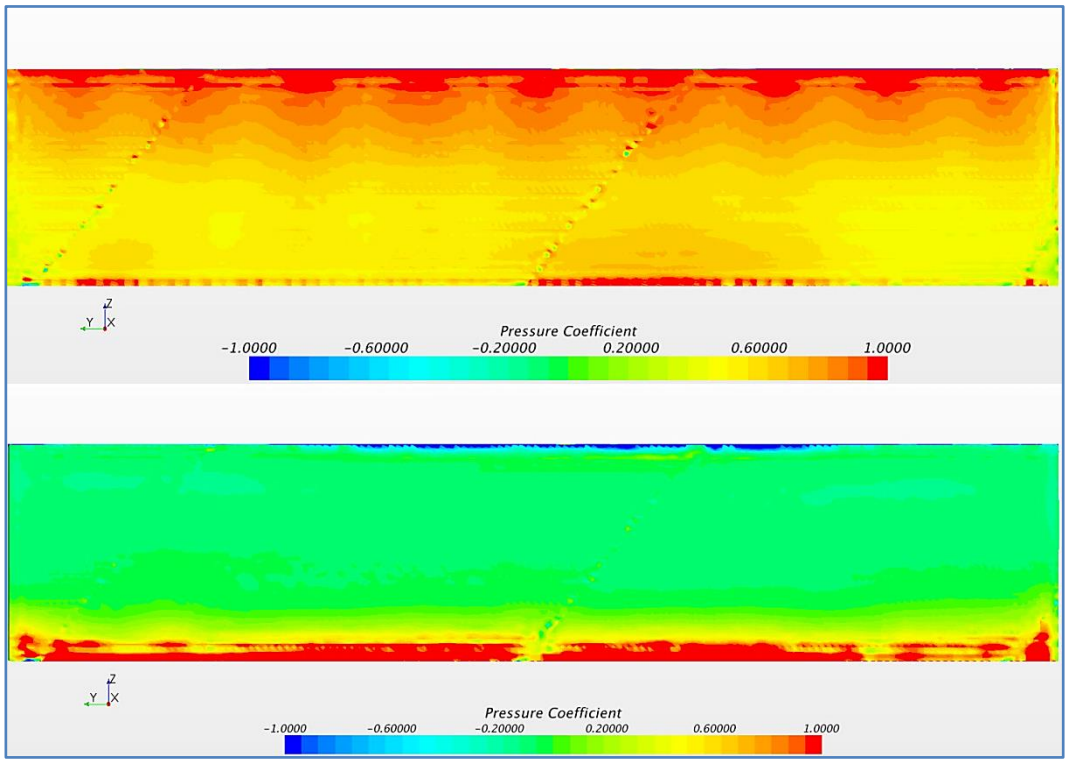

Pressure distribution over the intercooler inlet faces.

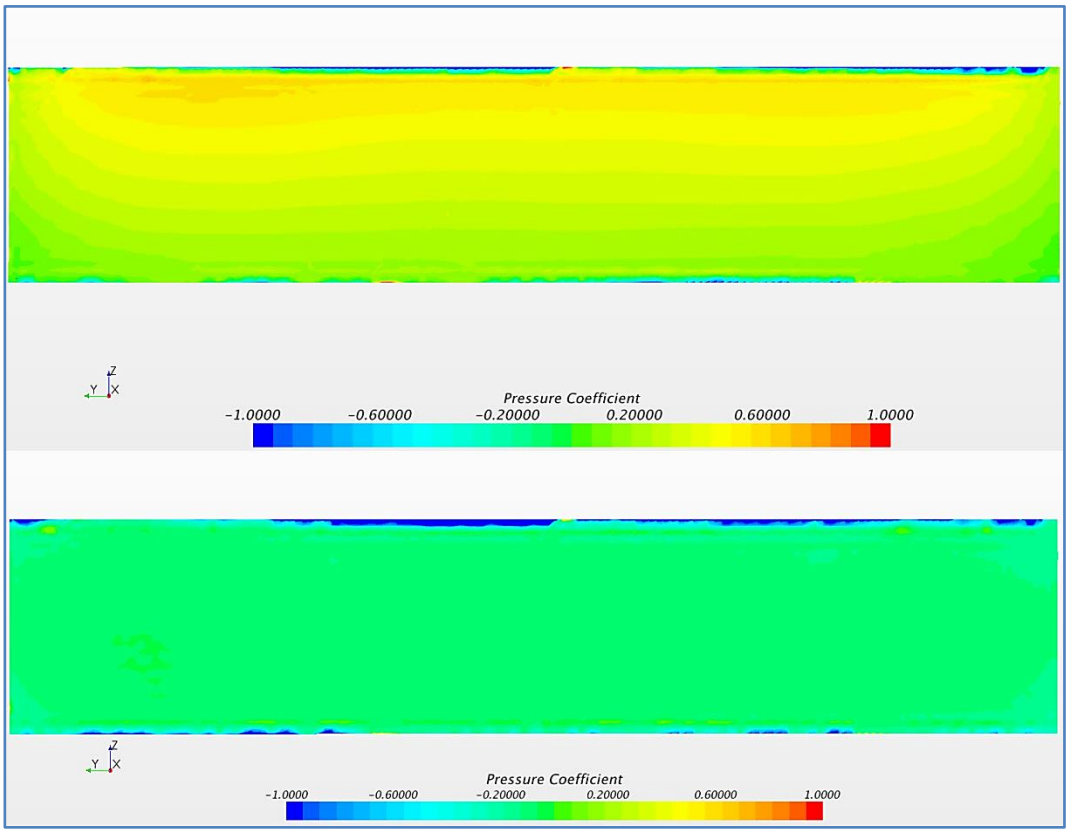

Pressure distribution over the intercooler outlet faces.

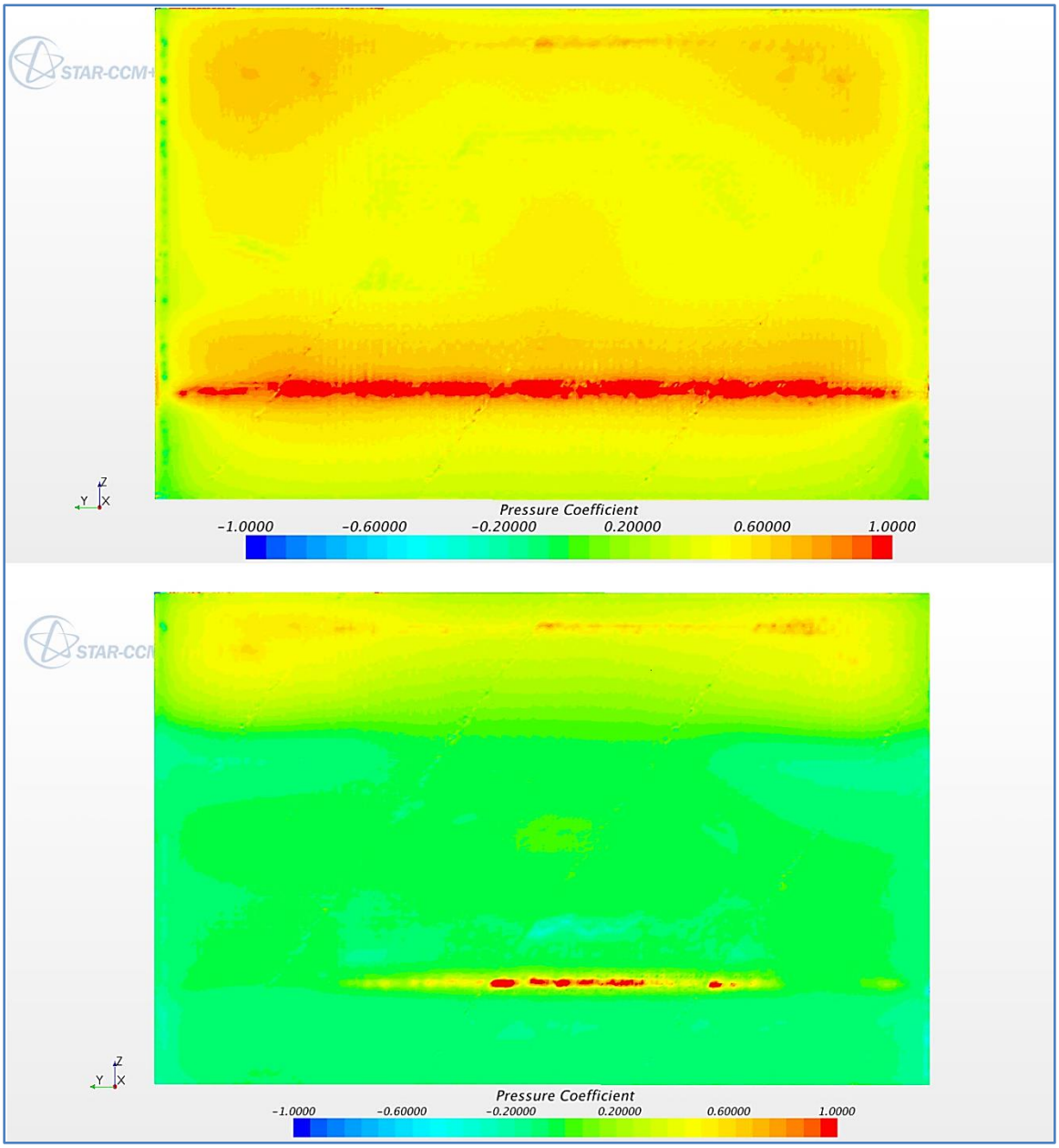

Pressure distribution over the radiator inlet faces.

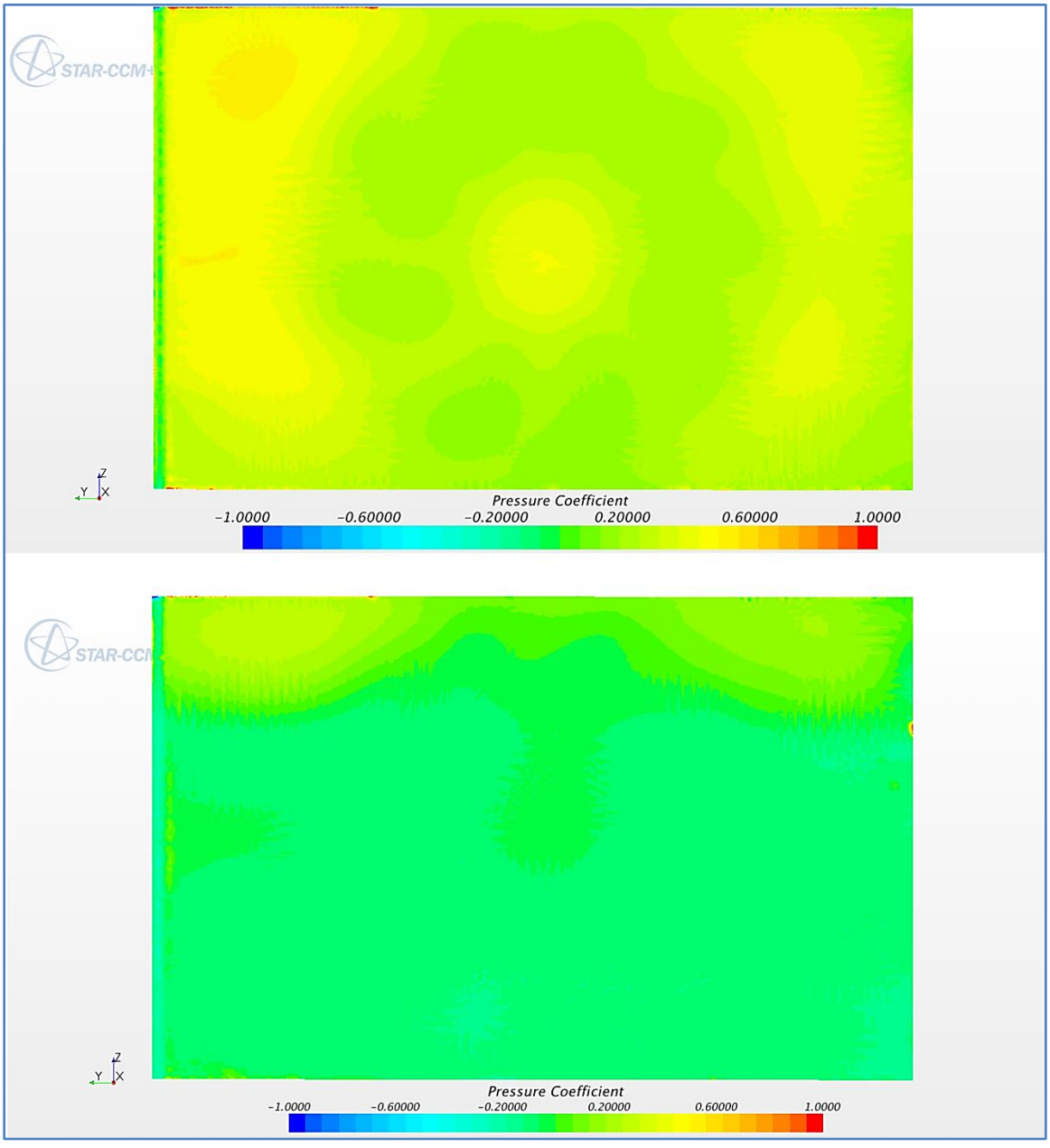

Pressure distribution over radiator outlet faces.

6.6. APPENDIX F

CFD MODEL – PRESSURE DISTRIBUTIONS IN THE ENGINE BAY

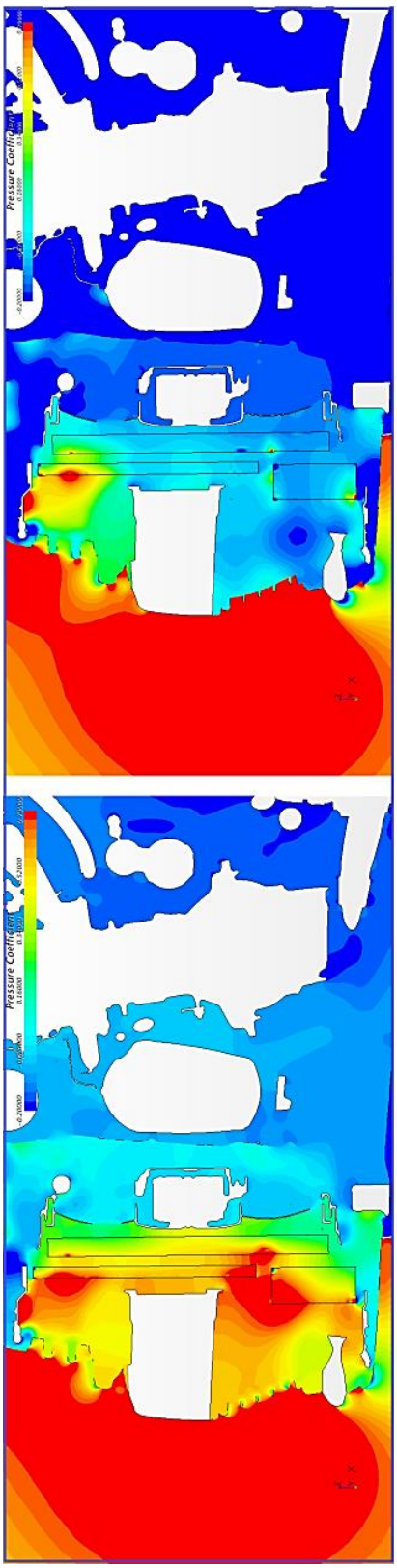

Pressure distribution within the engine bay, longitudinal vertical mid-plane (y=0 mm).
Left: baseline; right: modified.

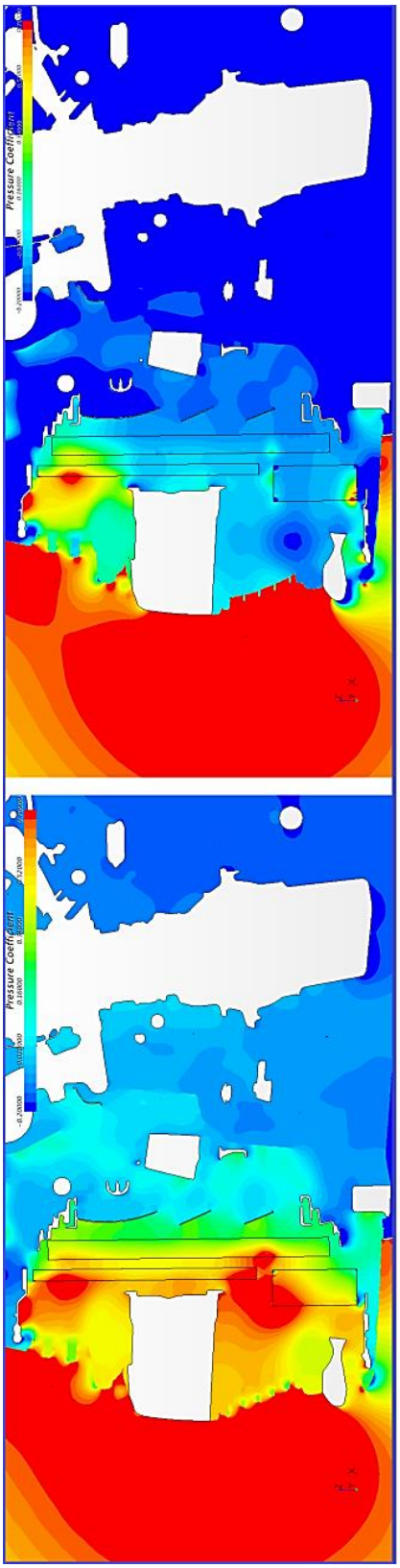

Pressure distribution within the engine bay, longitudinal vertical section plane with coordinates y=+100 mm.
Left: baseline; right: modified.

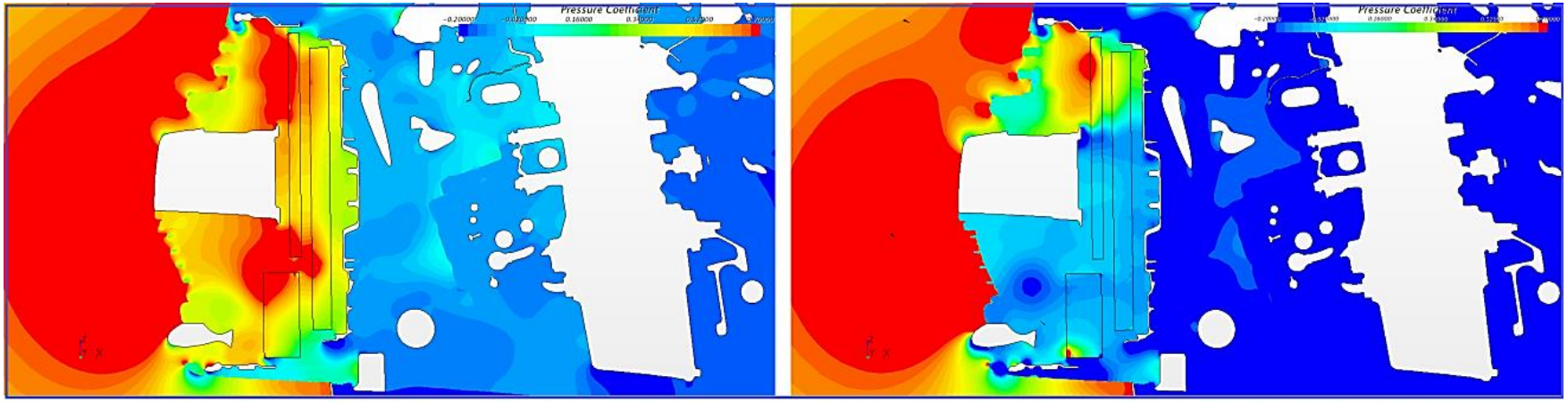

Pressure distribution within the engine bay, longitudinal vertical section plane with coordinates y=+200 mm.
Left: baseline; right: modified.

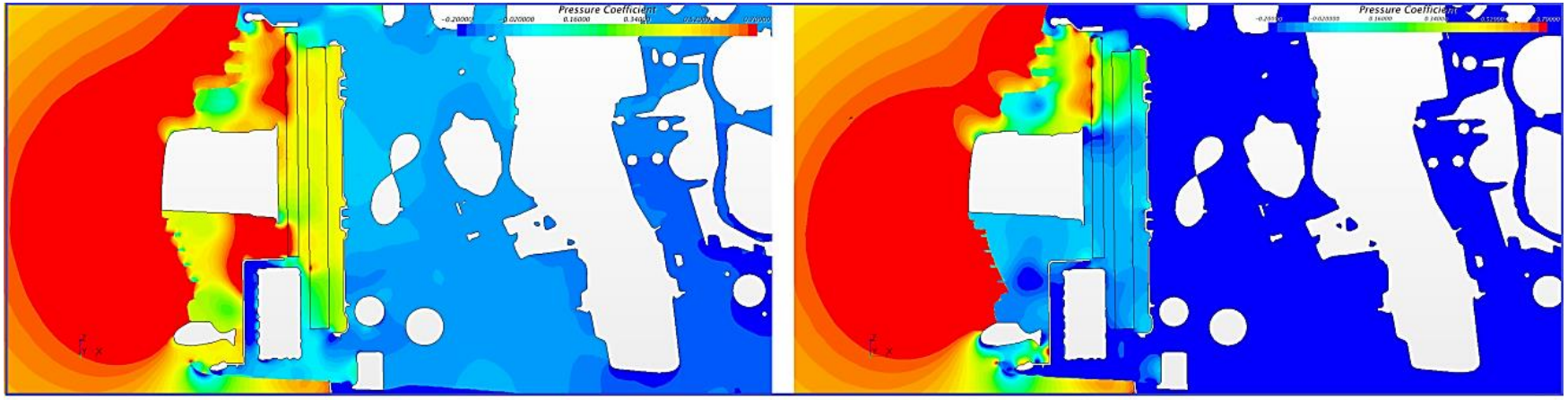

Pressure distribution within the engine bay, longiudinal vertical section plane with coordinates y=+300 mm.
Left: baseline; right: modified.

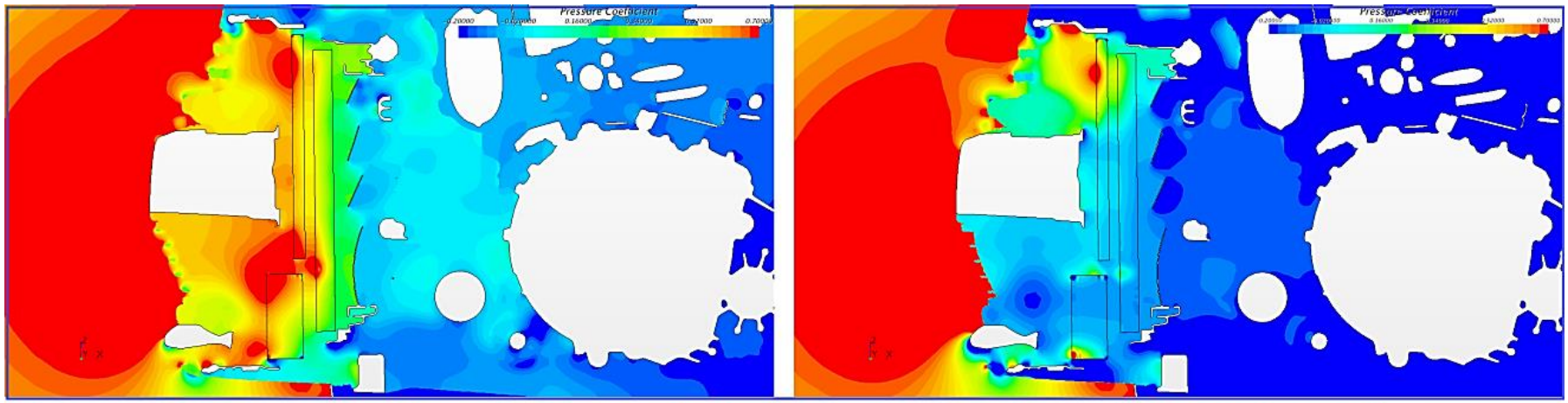

Pressure distribution within the engine bay, longitudinal vertical section plane with coordinates y=-100 mm.
Left: baseline; right: modified.

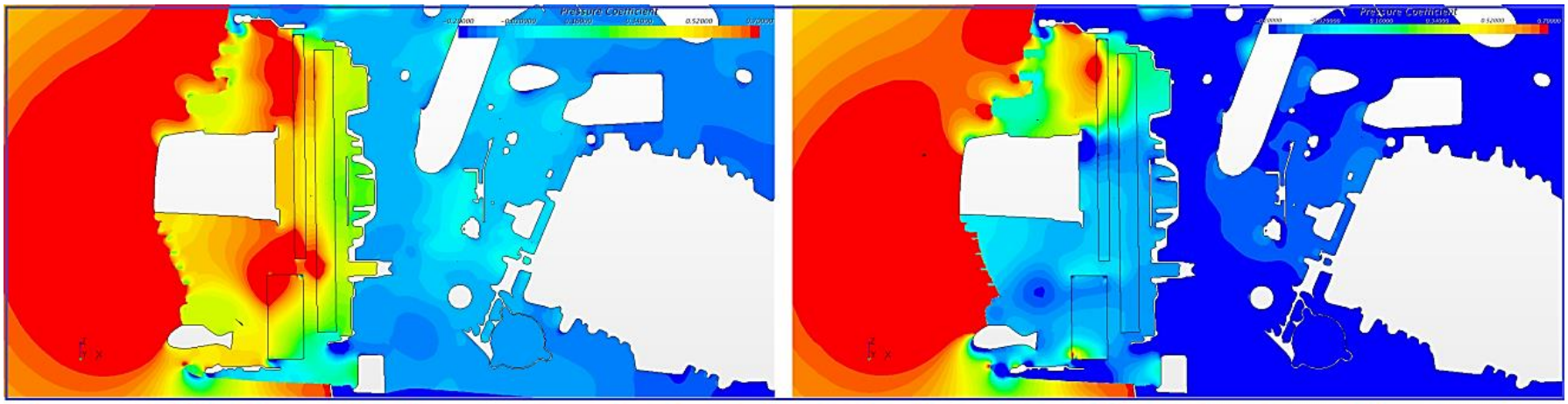

Pressure distribution within the engine bay, longitudinal vertical section plane with coordinates y=-200 mm.
Left: baseline; right: modified.

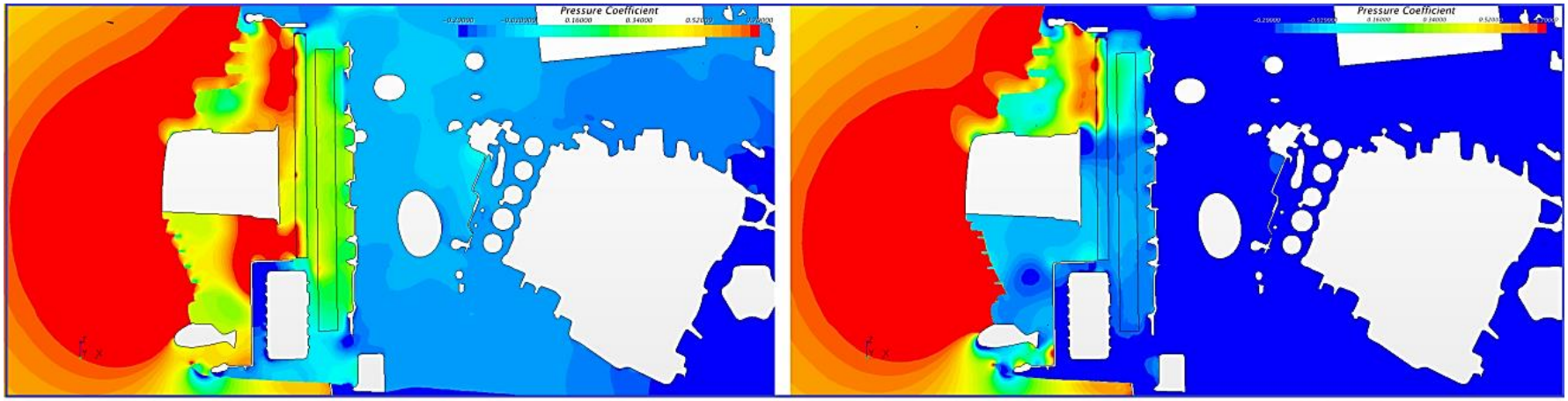

Pressure distribution in the engine bay, longitudinal vertical section plane with coordinates y=-300 mm.
Left: baseline; right: modified.

6.7. APPENDIX G

THERMAL ANALYSIS RESULTS – COMPONENTS TEMPERATURES FOR BASELINE AND MODIFIED VERSIONS

PID	BASELINE		MODIFIED		Δ CFD-BEM MODIFIED-BASELINE			
	T_{ave}	T_{max}	T_{ave}	T_{max}	T_{ave}	T_{max}	T_{ave}	T_{max}
	[°C]	[°C]	[°C]	[°C]	[°C]	[°C]	[%]	[%]
ALI_canister@Front	54.25	80.12	54.74	80.20	0.49	0.08	1%	0%
ALI_fuelPipes@Front	51.04	59.25	51.51	61.99	0.47	2.73	1%	5%
ALI_fuelPipesSupport@Front	55.75	78.79	55.59	81.53	-0.15	2.73	0%	3%
ALI_fuelTank@Front	59.42	80.16	59.30	80.03	-0.12	-0.13	0%	0%
ALI_fuelTankInlets@Front	49.50	53.52	49.15	53.64	-0.36	0.13	-1%	0%
ALI_fuelTankSupports@Front	60.68	79.98	61.14	79.73	0.47	-0.25	1%	0%
ALI_tankShield_ts@Back	87.84	111.19	88.51	111.52	0.67	0.33	1%	0%
ALI_tankShield_ts@Front	87.84	111.18	88.51	111.51	0.67	0.33	1%	0%
ASP_airFilterBottom@Front	48.73	51.44	51.39	54.80	2.66	3.36	5%	7%
ASP_airFilterTop@Front	48.54	51.26	48.86	52.12	0.32	0.86	1%	2%
ASP_inlet@Back	47.55	52.34	52.78	55.72	5.22	3.38	11%	6%
ASP_inletDuct@Front	53.30	56.87	55.01	58.52	1.71	1.65	3%	3%
ASP_outletDuct@Front	53.85	97.45	55.14	97.73	1.29	0.28	2%	0%
ASP_silentBlock@Front	47.13	49.74	49.53	52.94	2.41	3.20	5%	6%
CLI_compressor@Front	46.51	51.73	49.47	56.21	2.97	4.48	6%	9%

CLI_ductLiquidMetal@Front	45.49	50.85	48.89	59.25	3.40	8.40	7%	17%
CLI_ductLiquidRubber@Front	48.47	49.37	52.34	53.56	3.88	4.20	8%	8%
CLI_ductMetal@Front	47.55	52.06	51.49	55.08	3.94	3.02	8%	6%
CLI_ductRubber@Front	56.55	58.34	57.06	57.94	0.51	-0.40	1%	-1%
CLI_ductSupport@Front	52.43	62.79	56.15	68.14	3.72	5.34	7%	9%
CLI_hose@Front	49.42	52.87	51.74	55.90	2.32	3.03	5%	6%
CLI_seal@Front	74.61	91.72	125.90	140.35	51.30	48.63	69%	53%
ELE_batteryContact@Front	49.67	50.15	55.20	57.18	5.53	7.03	11%	14%
ELE_batteryContactCover@Front	49.61	56.46	52.56	57.62	2.95	1.16	6%	2%
ELE_cablesUnderbody@Front	61.24	84.34	61.88	84.81	0.64	0.47	1%	1%
ELE_cablesUnderhood@Front	51.52	119.13	40.55	129.65	-10.97	10.52	-21%	9%
ELE_cover1_ts@Back	50.87	51.43	50.74	51.39	-0.13	-0.03	0%	0%
ELE_cover1_ts@Front	50.82	51.42	50.68	51.37	-0.14	-0.05	0%	0%
ELE_cover2_ts@Back	55.62	57.42	54.95	56.51	-0.67	-0.91	-1%	-2%
ELE_cover2_ts@Front	55.65	57.61	55.08	56.81	-0.57	-0.80	-1%	-1%
ELE_fuseBox@Front	62.67	65.05	106.95	122.57	44.28	57.52	71%	88%
ELE_fuseBoxCover@Front	52.34	61.42	58.51	105.80	6.16	44.39	12%	72%
ELE_horn@Front	55.34	57.13	55.17	60.07	-0.17	2.94	0%	5%
ENE_batteryWalls@Front	49.36	57.32	51.83	61.35	2.48	4.03	5%	7%
ENE_starterMotor@Front	70.56	119.25	73.18	123.56	2.62	4.31	4%	4%
FIE_centralDam@Front	42.26	44.54	44.31	47.19	2.05	2.65	5%	6%
FIE_engineCover_ts@Back	69.57	118.78	81.24	136.70	11.67	17.92	17%	15%
FIE_engineCover_ts@Front	57.85	84.10	67.81	98.49	9.96	14.39	17%	17%
FIE_frontWheelDam@Front	43.86	44.25	44.54	45.25	0.68	0.99	2%	2%
FIE_frontWheelIntCover_ts@Back	49.39	51.92	53.43	56.05	4.04	4.13	8%	8%
FIE_frontWheelIntCover_ts@Front	51.09	55.01	56.82	61.15	5.73	6.14	11%	11%

FIE_lokary_ts@Back	45.33	48.82	47.54	51.99	2.21	3.17	5%	6%
FIE_lokary_ts@Front	45.06	47.58	46.66	49.79	1.61	2.21	4%	5%
FIE_suspCover_ts@Back	51.39	72.28	52.27	74.16	0.88	1.88	2%	3%
FIE_suspCover_ts@Front	50.81	75.55	51.70	77.44	0.89	1.89	2%	3%
FIP_hoodHook@Front	43.77	45.59	45.21	47.74	1.43	2.15	3%	5%
FIP_hoodHookCable@Front	47.75	52.99	73.67	80.53	25.92	27.54	54%	52%
FIP_hoodPiece@Front	70.57	86.75	77.82	99.44	7.24	12.69	10%	15%
FIP_hoodStick@Front	43.21	44.35	47.84	49.48	4.64	5.13	11%	12%
FRE_asmSensor@Front	106.39	477.70	114.60	478.11	8.20	0.42	8%	0%
FRE_booster@Front	50.66	54.65	55.18	59.90	4.52	5.25	9%	10%
FRE_brakeCoverFront@Front	45.65	46.59	51.04	51.54	5.39	4.96	12%	11%
FRE_brakeCoverRear@Front	45.84	52.72	46.25	52.52	0.42	-0.20	1%	0%
FRE_brakeDiscFront@Front	44.98	45.93	49.59	50.94	4.61	5.00	10%	11%
FRE_brakeDiscRear@Front	45.08	51.86	45.63	52.30	0.55	0.44	1%	1%
FRE_caliperFront@Front	45.35	49.51	50.19	53.12	4.85	3.60	11%	7%
FRE_caliperRear@Front	47.59	63.56	48.68	64.51	1.09	0.94	2%	1%
FRE_ecuSupport@Front	47.54	51.74	51.53	55.58	3.99	3.84	8%	7%
FRE_elStabCU@Front	49.40	52.27	53.60	55.57	4.20	3.30	9%	6%
FRE_oilTank@Front	47.47	51.96	50.77	57.29	3.31	5.34	7%	10%
FRE_pipes@Front	55.51	84.92	57.69	86.17	2.18	1.24	4%	1%
FRE_pipesSupports@Front	56.26	84.01	58.10	84.00	1.84	-0.01	3%	0%
PIA_arresterWall@Front	50.49	70.39	52.29	121.38	1.81	50.99	4%	72%
PIA_crashBox@Front	45.06	51.46	50.93	58.96	5.87	7.50	13%	15%
PIA_crossImpact@Front	45.37	54.38	58.22	65.85	12.85	11.47	28%	21%
PIA_frontEnd@Front	59.07	89.65	67.26	100.38	8.19	10.73	14%	12%
PIA_frontEnd_ts@Back	45.95	60.78	47.92	62.90	1.97	2.11	4%	3%

PIA_frontEnd_ts@Front	45.95	60.78	47.92	62.89	1.97	2.11	4%	3%
PIA_leftWall@Front	44.78	46.86	48.24	51.13	3.46	4.27	8%	9%
PIA_shockTower_ts@Back	45.67	49.20	47.53	51.09	1.86	1.89	4%	4%
PIA_shockTower_ts@Front	45.67	49.19	47.53	51.09	1.86	1.89	4%	4%
PIA_tankLeft@Front	65.18	82.31	65.66	81.76	0.48	-0.55	1%	-1%
PIA_tankRight@Front	55.51	74.84	55.86	75.58	0.35	0.74	1%	1%
PIA_underbody@Front	69.97	143.88	70.44	141.39	0.48	-2.50	1%	-2%
PIA_underfloor@Front	54.36	130.04	54.68	127.74	0.32	-2.30	1%	-2%
PIA_wheelarchFront@Front	48.70	52.46	49.78	53.63	1.07	1.17	2%	2%
PIA_wheelBuffle_ts@Back	54.36	55.34	55.77	56.86	1.41	1.52	3%	3%
PIA_wheelBuffle_ts@Front	54.36	55.34	55.77	56.86	1.41	1.52	3%	3%
PIM_centralHood@Front	45.11	49.03	46.15	51.26	1.05	2.22	2%	5%
PIM_sideHood@Front	44.20	46.63	45.87	49.00	1.67	2.37	4%	5%
PIT_gearCable@Front	60.20	74.84	61.69	82.52	1.49	7.68	2%	10%
PIT_gearCableSupport@Front	52.62	60.66	57.03	63.94	4.40	3.28	8%	5%
PIT_gearFork@Front	70.60	78.18	72.79	82.96	2.19	4.78	3%	6%
PIT_gearForkSupport@Front	87.34	117.71	89.16	127.72	1.82	10.01	2%	9%
PIT_itcSupport@Front	66.73	68.07	68.61	70.05	1.88	1.98	3%	3%
PIT_shaft@Front	70.18	140.36	73.08	164.84	2.90	24.48	4%	17%
PIT_support@Front	73.67	212.80	79.32	253.80	5.65	41.00	8%	19%
PWC_cables@Front	69.47	120.14	69.87	130.78	0.41	10.64	1%	9%
PWC_csc@Front	82.42	116.90	85.46	125.52	3.05	8.63	4%	7%
PWC_diffShaft@Front	79.31	119.55	87.08	127.46	7.76	7.90	10%	7%
PWC_gearBox@Front	127.15	572.14	132.95	572.22	5.79	0.08	5%	0%
PWC_hydrActPressReservoir@Front	73.45	123.44	84.55	129.65	11.09	6.21	15%	5%
PWC_hydrActPump@Front	67.86	90.55	81.45	109.09	13.59	18.54	20%	20%

PWC_hydrActTank@Front	85.64	121.15	81.47	122.44	-4.18	1.29	-5%	1%
PWC_hydraulicActuator@Front	68.75	123.90	71.36	130.87	2.61	6.97	4%	6%
PWM_alternator@Front	48.59	98.28	53.62	98.56	5.04	0.28	10%	0%
PWM_aspirationFlange@Front	50.29	53.58	52.26	54.68	1.97	1.10	4%	2%
PWM_auxiliary@Front	46.85	48.72	48.47	51.47	1.62	2.75	3%	6%
PWM_base@Front	100.00	100.00	100.00	100.00	0.00	0.00	0%	0%
PWM_beautyCover@Front	50.44	94.36	52.56	94.50	2.12	0.14	4%	0%
PWM_beltPulley@Front	51.98	52.66	53.25	54.24	1.27	1.58	2%	3%
PWM_beltTightener@Front	55.58	72.81	58.03	76.34	2.45	3.53	4%	5%
PWM_cabMultiair@Front	58.65	249.22	61.12	270.44	2.47	21.22	4%	9%
PWM_cabSupport@Front	60.58	93.49	63.22	93.85	2.64	0.36	4%	0%
PWM_camshaftCover@Front	95.00	95.00	95.00	95.00	0.00	0.00	0%	0%
PWM_carter@Front	61.42	106.51	59.12	107.20	-2.29	0.70	-4%	1%
PWM_connectorCover@Front	85.38	93.74	115.42	136.12	30.04	42.38	35%	45%
PWM_coolantPipes@Front	100.49	210.11	101.90	228.20	1.41	18.09	1%	9%
PWM_coolantValve@Front	100.00	100.00	100.00	100.00	0.00	0.00	0%	0%
PWM_cylinderHead@Front	100.00	100.00	100.00	100.00	0.00	0.00	0%	0%
PWM_ductSupport@Front	47.34	48.63	50.39	50.95	3.05	2.33	6%	5%
PWM_electrCables@Front	61.08	477.32	64.57	477.81	3.49	0.49	6%	0%
PWM_engineCover1_ts@Back	77.25	88.59	66.28	81.39	-10.97	-7.20	-14%	-8%
PWM_engineCover1_ts@Front	77.25	88.59	66.28	81.39	-10.97	-7.20	-14%	-8%
PWM_engineCover2_ts@Back	79.87	88.98	78.38	89.26	-1.49	0.28	-2%	0%
PWM_engineCover2_ts@Front	79.87	88.98	78.38	89.27	-1.49	0.29	-2%	0%
PWM_engineCover3_ts@Back	78.96	93.89	80.42	94.02	1.46	0.13	2%	0%
PWM_engineCover3_ts@Front	78.96	93.88	80.42	94.01	1.46	0.13	2%	0%
PWM_engineCover4_ts@Back	102.03	187.07	119.27	221.68	17.25	34.61	17%	18%

PWM_engineCover4_ts@Front	102.03	187.07	119.27	221.68	17.25	34.61	17%	19%
PWM_engineMount@Front	78.94	100.00	88.29	100.00	9.35	0.00	12%	0%
PWM_enginePulley@Front	73.77	109.60	68.92	109.61	-4.85	0.01	-7%	0%
PWM_engineSupport@Front	59.77	99.94	64.16	99.95	4.39	0.02	7%	0%
PWM_exhaust@Front	267.37	368.37	283.20	386.28	15.83	17.92	6%	5%
PWM_exhaustHeatShield@Front	57.26	136.74	77.48	159.35	20.23	22.61	35%	17%
PWM_flanges@Front	80.57	181.06	83.20	202.86	2.63	21.80	3%	12%
PWM_greenFilter@Front	76.95	111.70	72.19	118.51	-4.75	6.81	-6%	6%
PWM_heatShield@Front	130.19	289.83	137.36	323.14	7.17	33.31	6%	11%
PWM_ignCoil1@Front	74.49	94.01	70.08	93.92	-4.41	-0.10	-6%	0%
PWM_ignCoil2@Front	75.90	94.88	73.56	94.88	-2.34	0.00	-3%	0%
PWM_ignCoil3@Front	76.90	94.86	80.73	94.92	3.83	0.06	5%	0%
PWM_ignCoil4@Front	56.94	90.75	60.83	91.73	3.89	0.97	7%	1%
PWM_inaModule@Front	82.19	94.80	84.66	94.85	2.47	0.05	3%	0%
PWM_inaModuleCables@Front	60.15	96.07	41.63	98.06	-18.52	1.99	-31%	2%
PWM_jacket@Front	100.00	100.00	100.00	100.00	0.00	0.00	0%	0%
PWM_oilCap@Front	44.83	90.68	46.53	91.88	1.70	1.20	4%	1%
PWM_oilPump@Front	110.00	110.00	110.00	110.00	0.00	0.00	0%	0%
PWM_oilSump@Front	120.00	120.00	120.00	120.00	0.00	0.00	0%	0%
PWM_separator@Front	54.40	86.43	61.81	102.00	7.41	15.58	14%	18%
PWM_serpentineBelt@Front	54.13	89.29	53.44	90.07	-0.69	0.77	-1%	1%
PWM_sideSupport@Front	100.00	100.00	100.00	100.00	0.00	0.00	0%	0%
PWM_turbochargerBody@Front	100.00	100.00	100.00	100.00	0.00	0.00	0%	0%
PWM_turbochargerCompressor@Front	100.00	100.00	100.00	100.00	0.00	0.00	0%	0%
PWM_turbochargerCoolant@Front	72.95	115.34	68.11	122.68	-4.83	7.34	-7%	6%
PWM_turbochargerSensor@Front	63.92	98.50	61.31	98.35	-2.61	-0.15	-4%	0%

PWM_turbochargerTurbine@Front	325.83	639.51	344.90	639.58	19.07	0.07	6%	0%
PWM_turbochargerWgate@Front	69.48	96.45	70.14	96.58	0.66	0.12	1%	0%
PWM_vacuumPump@Front	98.43	143.18	102.03	153.73	3.60	10.55	4%	7%
PWM_wgVacuumPipes@Front	55.64	66.20	56.57	68.49	0.93	2.29	2%	3%
PWM_wgVacuumValve@Front	61.75	98.99	63.56	99.08	1.82	0.09	3%	0%
RAF_cacPipeIn@Front	70.07	531.87	75.42	535.36	5.35	3.49	8%	1%
RAF_cacPipeOut@Front	92.01	133.22	101.80	148.86	9.79	15.63	11%	12%
RAF_conveyor@Front	43.35	61.34	47.40	65.51	4.05	4.17	9%	7%
RAF_fanBlades@Front	75.38	87.30	98.04	112.11	22.66	24.81	30%	28%
RAF_fanFrame@Front	69.66	105.64	83.03	122.80	13.37	17.17	19%	16%
RAF_fanMotor@Front	71.60	72.23	98.22	99.01	26.62	26.78	37%	37%
RAF_fanMotorCable@Front	65.84	75.32	91.80	103.83	25.96	28.52	39%	38%
RAF_flanges@Front	73.23	385.46	78.65	408.16	5.42	22.70	7%	6%
RAF_frameCond@Front	50.00	50.00	50.00	50.00	0.00	0.00	0%	0%
RAF_frameIntercooler@Front	120.00	120.00	120.00	120.00	0.00	0.00	0%	0%
RAF_frameSupport@Front	91.87	93.03	91.99	93.88	0.12	0.86	0%	1%
RAF_inletCond@Front	50.00	50.00	50.00	50.00	0.00	0.00	0%	0%
RAF_inletIntercooler@Front	120.00	120.00	120.00	120.00	0.00	0.00	0%	0%
RAF_inletRad@Front	100.00	100.00	100.00	100.00	0.00	0.00	0%	0%
RAF_nourice@Front	59.88	83.64	64.53	86.64	4.66	3.00	8%	4%
RAF_nouricePipIn@Front	90.41	101.23	92.17	104.31	1.76	3.08	2%	3%
RAF_outletCond@Front	50.00	50.00	50.00	50.00	0.00	0.00	0%	0%
RAF_outletIntercooler@Front	120.00	120.00	120.00	120.00	0.00	0.00	0%	0%
RAF_outletRad@Front	100.00	100.00	100.00	100.00	0.00	0.00	0%	0%
RAF_radFrame@Front	87.44	90.14	94.35	96.01	6.91	5.86	8%	7%
RAF_radPipeIn@Front	83.68	126.68	82.59	132.21	-1.09	5.53	-1%	4%

RAF_radPipeOut@Front	74.94	90.77	80.36	97.68	5.42	6.91	7%	8%
RAF_radTankIn@Front	72.51	74.26	83.40	85.30	10.89	11.04	15%	15%
RAF_sensorCable@Front	55.64	97.55	56.57	104.26	0.93	6.71	2%	7%
RAF_sideframCond@Front	50.00	50.00	50.00	50.00	0.00	0.00	0%	0%
RAF_Trimming@Front	41.26	42.79	42.71	46.41	1.46	3.61	4%	8%
RAF_waterPump@Front	95.64	96.01	95.32	95.73	-0.33	-0.29	0%	0%
SCA_aestheticEnd@Front	134.00	134.00	134.00	134.00	0.00	0.00	0%	0%
SCA_catIn@Front	640.00	640.00	640.00	640.00	0.00	0.00	0%	0%
SCA_catOut@Front	640.00	640.00	640.00	640.00	0.00	0.00	0%	0%
SCA_catSkin@Front	580.00	580.00	580.00	580.00	0.00	0.00	0%	0%
SCA_exhaustCover1_ts@Back	89.34	604.86	91.37	604.46	2.03	-0.41	2%	0%
SCA_exhaustCover1_ts@Front	89.34	604.87	91.37	604.47	2.03	-0.41	2%	0%
SCA_exhaustCover2_ts@Back	119.36	611.49	130.22	613.41	10.86	1.92	9%	0%
SCA_exhaustCover2_ts@Front	119.35	611.45	130.21	613.37	10.86	1.93	9%	0%
SCA_exhBtwMufflers@Front	430.00	430.00	430.00	430.00	0.00	0.00	0%	0%
SCA_exhColdEnd@Front	134.00	134.00	134.00	134.00	0.00	0.00	0%	0%
SCA_exhDet@Front	480.00	480.00	480.00	480.00	0.00	0.00	0%	0%
SCA_exhFlexCoupler@Front	500.00	500.00	500.00	500.00	0.00	0.00	0%	0%
SCA_exhHtEnd@Front	580.00	580.00	580.00	580.00	0.00	0.00	0%	0%
SCA_exhMufflerIn@Front	500.00	500.00	500.00	500.00	0.00	0.00	0%	0%
SCA_mufflerFirst@Front	85.00	85.00	85.00	85.00	0.00	0.00	0%	0%
SCA_mufflerSecond@Front	400.00	400.00	400.00	400.00	0.00	0.00	0%	0%
SCA_supports@Front	216.14	498.24	207.24	498.29	-8.90	0.05	-4%	0%
SOV_drivingAxle@Front	63.36	67.59	67.04	73.07	3.69	5.48	6%	8%
SOV_flangeHub@Front	45.42	48.39	46.08	49.39	0.66	1.00	1%	2%
SOV_fronAddMounts@Front	69.12	74.51	73.92	79.83	4.80	5.32	7%	7%

SOV_fronBananaStrut@Front	52.67	57.26	56.04	61.27	3.37	4.02	6%	7%
SOV_front_CVJoint@Front	45.77	46.76	50.35	51.24	4.59	4.48	10%	10%
SOV_frontChassisSupport@Front	60.86	66.89	63.41	71.72	2.56	4.82	4%	7%
SOV_frontCoil@Front	44.80	45.66	45.25	46.28	0.45	0.62	1%	1%
SOV_frontConRod@Front	55.18	59.24	56.27	60.09	1.09	0.85	2%	1%
SOV_frontCVJGasket@Front	50.50	60.70	55.07	64.27	4.57	3.57	9%	6%
SOV_frontMainStrut@Front	47.24	51.69	51.61	55.25	4.37	3.56	9%	7%
SOV_frontMount@Front	45.91	54.46	46.28	55.56	0.37	1.10	1%	2%
SOV_frontRBMount@Front	63.48	65.04	63.37	65.00	-0.10	-0.05	0%	0%
SOV_frontRollBar@Front	62.77	68.56	64.15	71.67	1.38	3.11	2%	5%
SOV_frontShAbsGasket@Front	45.15	47.48	46.12	51.51	0.97	4.03	2%	8%
SOV_frontShockAbs@Front	50.62	54.61	52.99	55.70	2.36	1.09	5%	2%
SOV_frontTransvBeam@Front	64.59	124.56	70.23	141.96	5.64	17.41	9%	14%
SOV_hubBolts@Front	44.78	45.20	45.42	45.56	0.64	0.36	1%	1%
SOV_rearChassisMount@Front	59.31	75.80	59.86	77.55	0.55	1.76	1%	2%
SOV_rearMainStrut@Front	46.72	54.39	47.14	55.14	0.42	0.75	1%	1%
SOV_rearShockAbs@Front	51.94	83.70	52.48	86.23	0.53	2.53	1%	3%
SOV_rearUpperBushing@Front	49.59	51.70	49.47	51.66	-0.12	-0.04	0%	0%
SOV_rearUpperGasket@Front	47.52	49.55	47.86	49.47	0.34	-0.08	1%	0%
SOV_trailingArm@Front	53.09	70.37	55.09	72.16	2.00	1.78	4%	3%
SOV_twistBeam@Front	56.99	97.96	58.78	100.22	1.79	2.27	3%	2%
STE_gasket@Front	58.70	64.02	56.89	63.92	-1.81	-0.10	-3%	0%
STE_rackPinion@Front	63.63	70.33	64.18	72.20	0.55	1.86	1%	3%
STE_rubberSeal@Front	65.79	68.92	65.97	69.38	0.18	0.46	0%	1%
STE_steeringArms@Front	53.57	56.26	54.75	55.73	1.18	-0.53	2%	-1%
STY_fender_ts@Back	41.97	43.18	43.04	49.05	1.08	5.88	3%	14%

STY_fender_ts@Front	41.66	42.67	42.49	48.26	0.83	5.59	2%	13%
STY_fenderWheels_ts@Back	42.41	43.47	42.64	44.33	0.24	0.86	1%	2%
STY_fenderWheels_ts@Front	42.40	43.47	42.64	44.33	0.24	0.86	1%	2%
STY_fogLight_ts@Back	44.03	44.30	44.37	44.67	0.34	0.37	1%	1%
STY_fogLight_ts@Front	42.03	42.11	42.21	42.29	0.18	0.18	0%	0%
STY_frontContactPatch@Front	44.01	45.57	44.22	45.80	0.21	0.23	0%	1%
STY_frontEnd_ts@Back	45.34	50.94	48.78	55.33	3.44	4.39	8%	9%
STY_frontEnd_ts@Front	45.34	50.94	48.78	55.32	3.44	4.39	8%	9%
STY_frontLights_ts@Back	43.01	43.21	43.90	44.15	0.89	0.93	2%	2%
STY_frontLights_ts@Front	41.77	41.84	42.20	42.29	0.43	0.45	1%	1%
STY_frontTyre@Front	46.18	48.05	46.19	48.07	0.01	0.02	0%	0%
STY_frontWheelRim@Front	42.08	44.21	44.21	45.22	2.13	1.01	5%	2%
STY_gridStructure_ts@Back	41.79	42.23	43.71	44.69	1.92	2.46	5%	6%
STY_gridStructure_ts@Front	41.79	42.23	43.71	44.68	1.92	2.45	5%	6%
STY_grilleLower_ts@Back	41.21	42.19	44.89	46.02	3.67	3.83	9%	9%
STY_grilleLower_ts@Front	40.70	41.42	42.52	43.32	1.82	1.90	4%	5%
STY_grilleUpper_ts@Back	40.50	40.99	40.68	41.24	0.18	0.25	0%	1%
STY_grilleUpper_ts@Front	40.45	40.83	40.61	41.05	0.16	0.22	0%	1%
STY_hoodCover_ts@Front	40.91	42.61	41.04	43.75	0.12	1.14	0%	3%
STY_hoodEdge_ts@Back	43.55	44.17	44.82	45.80	1.26	1.63	3%	4%
STY_hoodEdge_ts@Front	43.55	44.17	44.82	45.80	1.26	1.63	3%	4%
STY_hoodGap_ts@Back	42.08	42.85	42.62	43.93	0.54	1.08	1%	3%
STY_hoodGap_ts@Front	42.08	42.84	42.62	43.93	0.54	1.08	1%	3%
STY_hoodInner_ts@Front	40.72	41.21	40.82	41.37	0.10	0.16	0%	0%
STY_light_ts@Back	43.36	43.56	46.73	47.04	3.38	3.48	8%	8%
STY_light_ts@Front	41.50	41.60	43.13	43.26	1.63	1.66	4%	4%

STY_lowerFender@Front	41.26	43.52	43.37	52.45	2.11	8.93	5%	21%
STY_outerHood@Front	40.71	42.62	40.83	43.78	0.12	1.16	0%	3%
STY_plasticHood@Front	40.62	41.00	40.64	41.11	0.02	0.11	0%	0%
STY_rearTyre@Front	45.71	64.38	45.61	63.03	-0.10	-1.35	0%	-2%
STY_rearWheelRim@Front	41.96	42.72	43.35	44.39	1.40	1.67	3%	4%
STY_splitter_ts@Back	43.02	46.74	51.58	56.06	8.56	9.32	20%	20%
STY_splitter_ts@Front	41.59	42.75	44.53	47.63	2.95	4.89	7%	11%
STY_upperFender@Front	40.76	42.29	41.61	44.90	0.85	2.61	2%	6%
STY_wheelhouse@Front	50.96	60.07	58.88	68.47	7.92	8.40	16%	14%

6.8. APPENDIX H

THERMAL ANALYSIS RESULTS – MAPS

NOTE: unless otherwise specified, all maps show the baseline version at the top (left) and the modified one in the bottom (right).

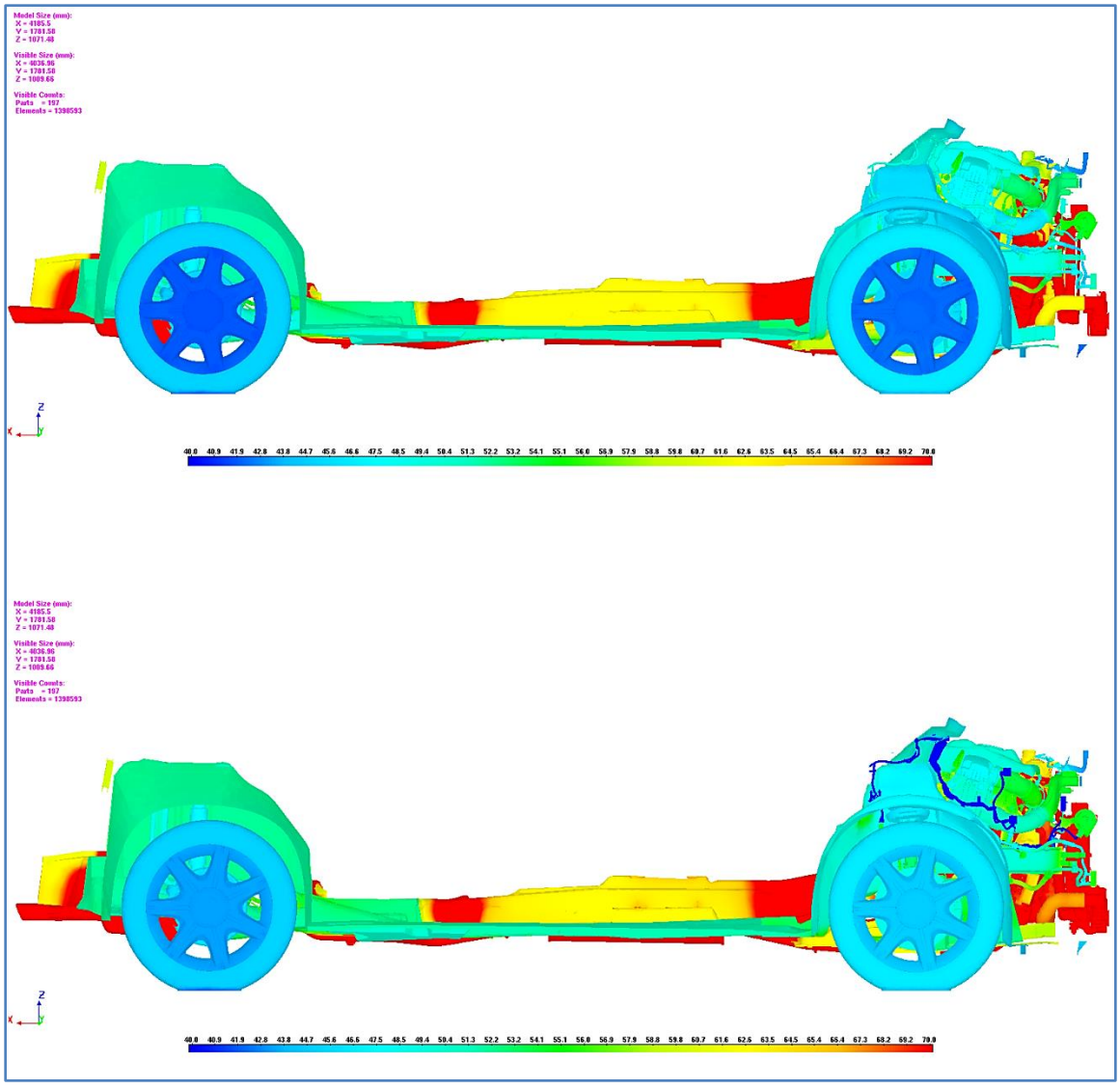

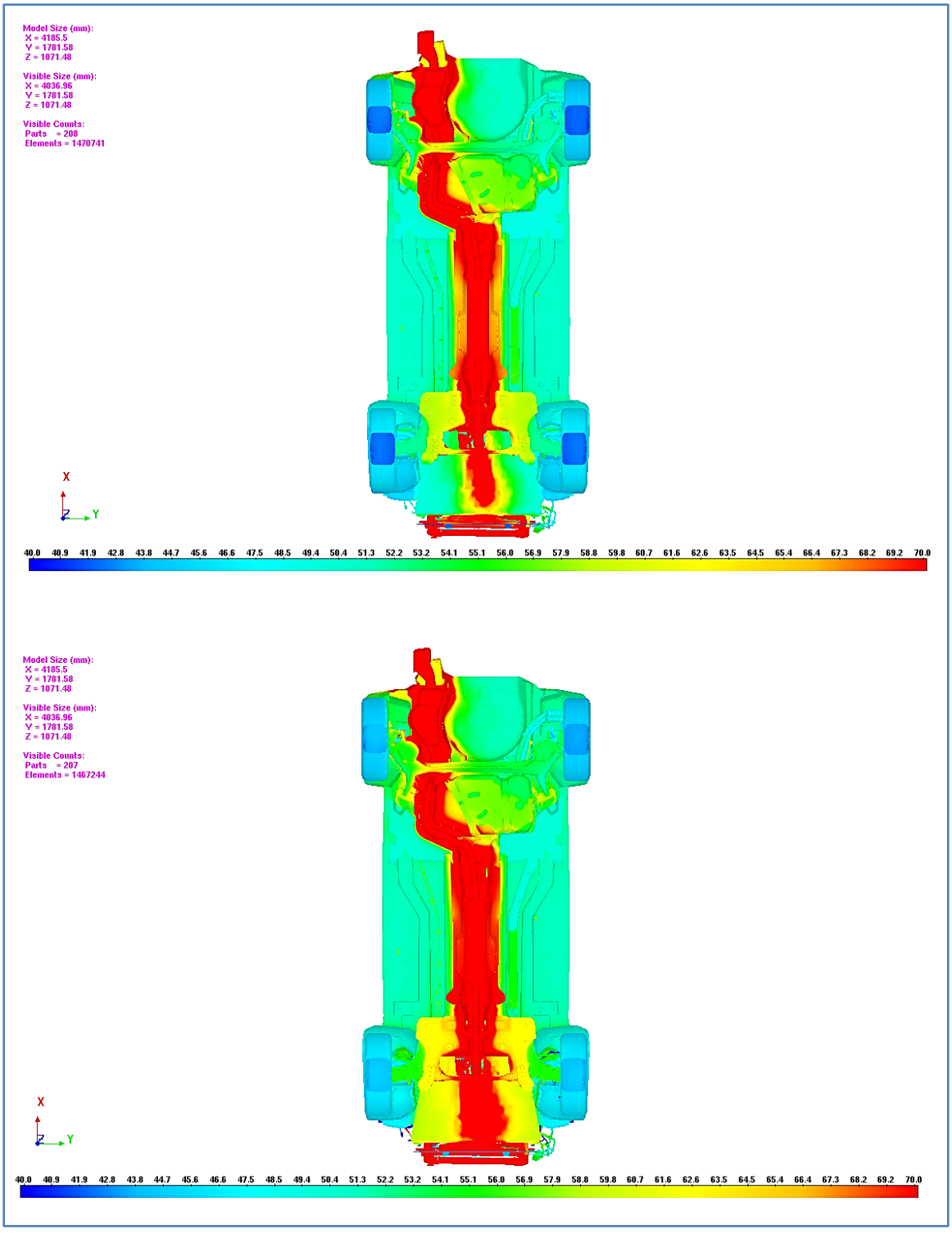
Model Size (mm):
X = 4185.5
Y = 1781.58
Z = 1071.48
Visible Size (mm):
X = 4036.96
Y = 1781.58
Z = 1071.48
Visible Counts:
Parts = 208
Elements = 1470741
X
Z
Y
40.0 40.9 41.9 42.8 43.8 44.7 45.6 46.6 47.5 48.5 49.4 50.4 51.3 52.2 53.2 54.1 55.1 56.0 56.9 57.9 58.8 59.8 60.7 61.6 62.6 63.5 64.5 65.4 66.4 67.3 68.2 69.2 70.0
Model Size (mm):
X = 4185.5
Y = 1781.58
Z = 1071.48
Visible Size (mm):
X = 4036.96
Y = 1781.58
Z = 1071.48
Visible Counts:
Parts = 207
Elements = 1467244
X
Z
Y
40.0 40.9 41.9 42.8 43.8 44.7 45.6 46.6 47.5 48.5 49.4 50.4 51.3 52.2 53.2 54.1 55.1 56.0 56.9 57.9 58.8 59.8 60.7 61.6 62.6 63.5 64.5 65.4 66.4 67.3 68.2 69.2 70.0

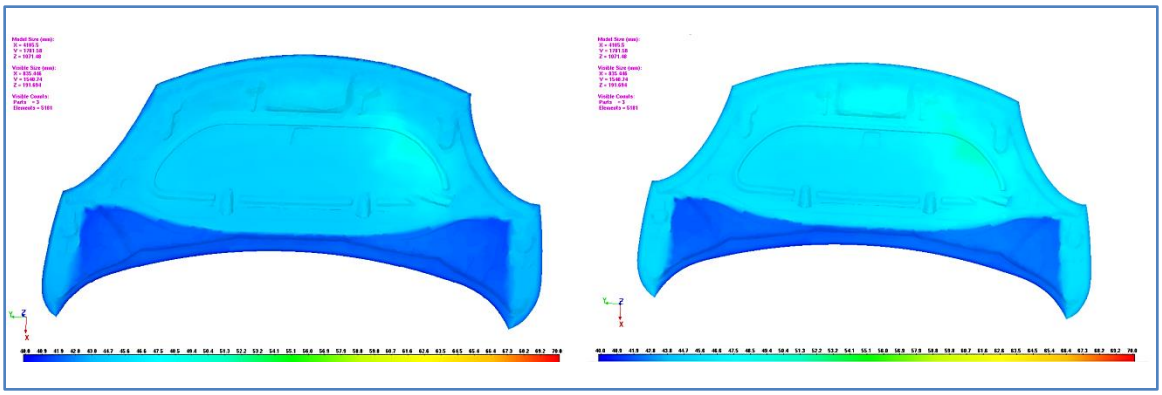

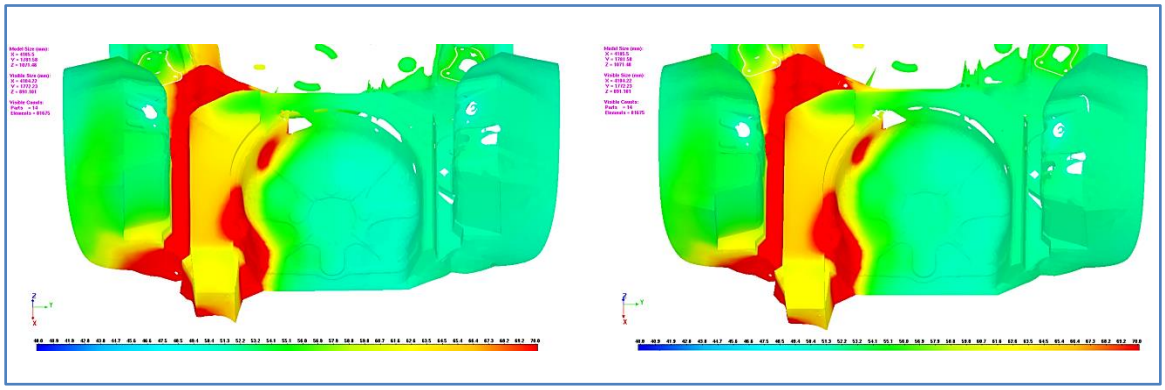

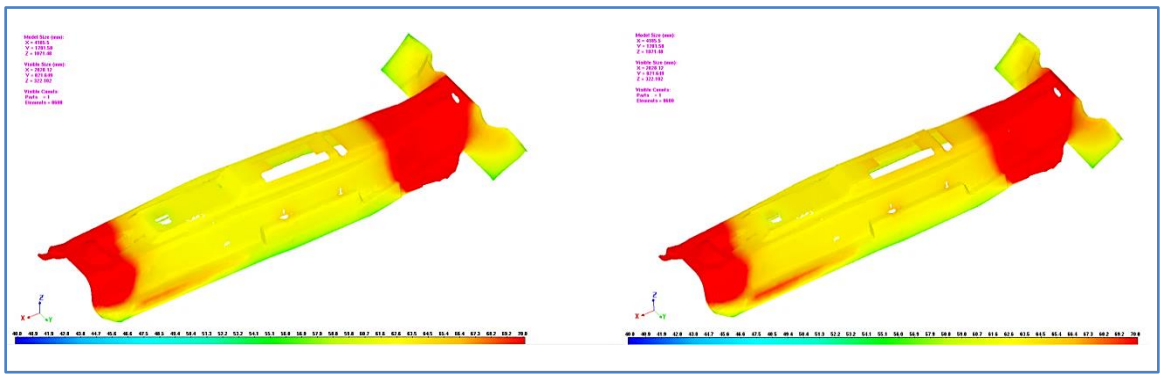

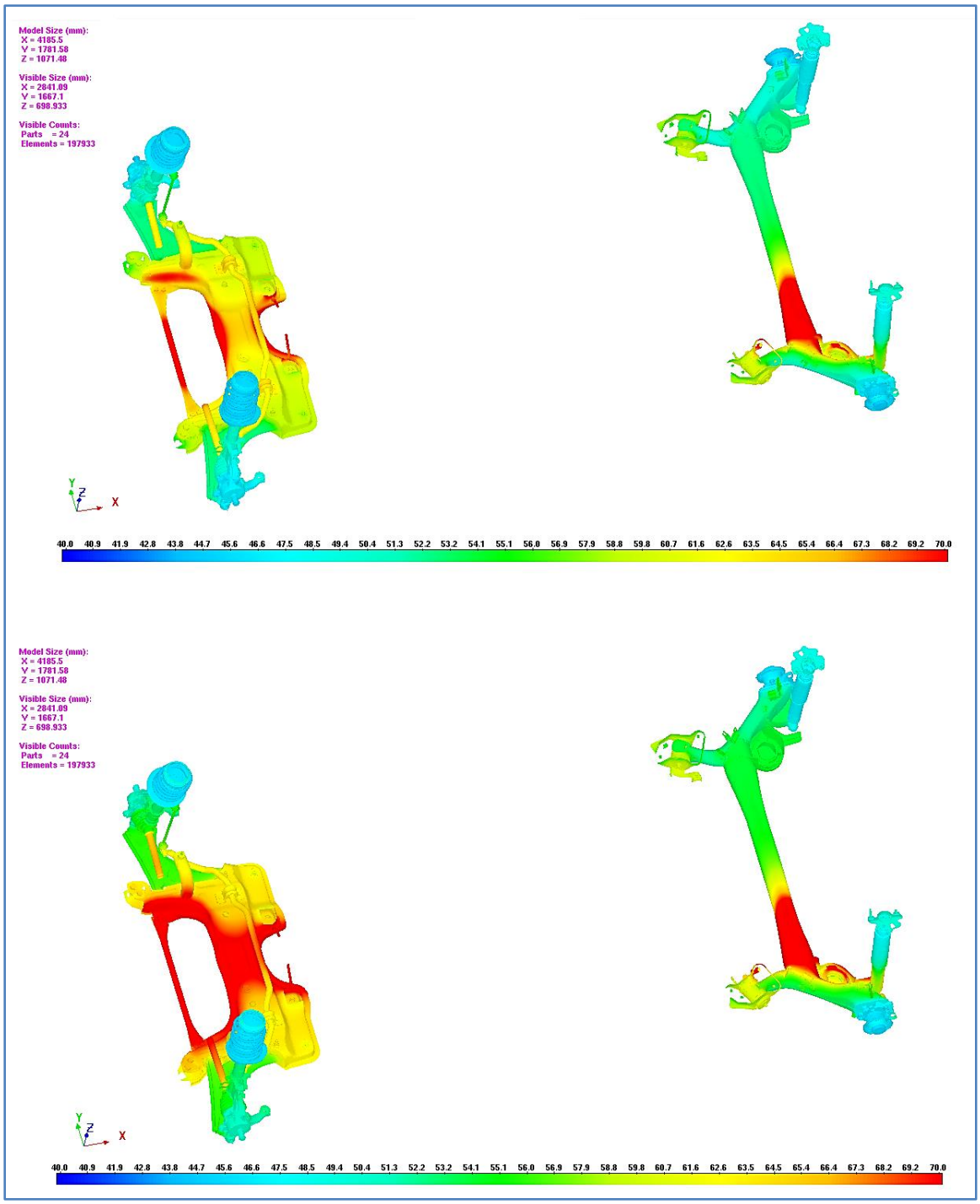
Model Size (mm):
X = 4185.5
Y = 1781.58
Z = 1071.48
Visible Size (mm):
X = 2841.89
Y = 1667.1
Z = 698.933
Visible Counts:
Parts = 24
Elements = 197933
Y
Z
X
40.0 40.9 41.9 42.8 43.8 44.7 45.6 46.6 47.5 48.5 49.4 50.4 51.3 52.2 53.2 54.1 55.1 56.0 56.9 57.9 58.8 59.8 60.7 61.6 62.6 63.5 64.5 65.4 66.4 67.3 68.2 69.2 70.0
Model Size (mm):
X = 4185.5
Y = 1781.58
Z = 1071.48
Visible Size (mm):
X = 2841.89
Y = 1667.1
Z = 698.933
Visible Counts:
Parts = 24
Elements = 197933
Y
Z
X
40.0 40.9 41.9 42.8 43.8 44.7 45.6 46.6 47.5 48.5 49.4 50.4 51.3 52.2 53.2 54.1 55.1 56.0 56.9 57.9 58.8 59.8 60.7 61.6 62.6 63.5 64.5 65.4 66.4 67.3 68.2 69.2 70.0

7. VITA AUCTORIS

NAME: Federico De Medio

PLACE OF BIRTH: Torino, Italy

YEAR OF BIRTH: 1990

EDUCATION: Vanderbilt University, SECAC exchange programme, Nashville, TN, USA, 2011

Politecnico di Torino, B.Sc., Torino, Italy, 2012

University of Windsor, M.A.Sc., Windsor, ON, Canada, 2014

Politecnico di Torino, M.Sc., Torino, Italy, 2014